Tiago Czelusniak

Influence of laser sintering parameters on SLS of PA12 and carbon fiber reinforced PA12: from microstructural and crystallization evolution to modelling and optimization

Curitiba

2020

Tiago Czelusniak

Influence of laser sintering parameters on SLS of PA12 and carbon fiber reinforced PA12: from microstructural and crystallization evolution to modelling and optimization

Doctoral thesis submitted to the Mechanical Engineering Graduate Program at Pontifical Catholic University of Paraná in partial fulfilment for the award of the Doctor degree.

Pontifical Catholic University of Paraná - PUCPR
Polytechnic School
Mechanical Engineering Graduate Program - PPGEM

Supervisor: Prof. Dr. Eng. Fred Lacerda Amorim

Curitiba
2020

To my lovely wife Lais and my little girl Mariana.

Acknowledgements

I would like to thank all the people who supported me, in whichever way, during the period of this work. First of all, my greatest thanks to my advisor Prof. Fred Amorim, not only for giving me the opportunity to make my Master and Doctorate degree in this fascinating area, but also for his personal friendship, support and encouragement during the whole work. Special thanks to Prof. Paulo Soares for his support with characterization and valuable discussions.

Thanks to Prof. Franciso Serbena from State University of Ponta Grossa (UEPG) for his support in conducting DSC measurements. Special thanks to technicians Rogerio, Claudio and Leonardo from PUC-PR for their support with measurements and testing. I would also like to express my gratitude to Jessica for her great support with SEM, XRD and FTIR characterization.

This research would not have been possible without the financial support from CAPES (Coordenação de Aperfeiçoamento de Pessoal de Nível Superior) and FINEP (Financiadora de Estudos e Projetos).

I am also thankful to my wife Lais, for her valuable support and comprehension during the whole period of this work and to my little daughter Mariana, who gave me the final energy to finish this thesis. At last I wish to thank my parents Paulo Roberto and Nalu, and my brother Diego for their unconditional support.

"The world breaks everyone, and afterward,
many are strong at the broken places"
(- Ernest Hemingway)

Abstract

Additive Manufacturing (AM) refers to the physical modelling of prototypes, components and products from their CAD designs using digitally driven layer-wise material additive processes. A common characteristic of these technologies is the additive approach used on the parts manufacturing, enabling the fabrication of very complex geometries without the necessity of specific tooling and without increasing the cost of the part. From the AM technologies available, Selective Laser Sintering (SLS) ranks among the most successful due to its the ability to generate complex parts without the need of a support structure. In theory, any material in powder form can be processed by SLS, however the complex laser material interaction and consolidation mechanism occurring in SLS limits the range of materials available to date. Therefore, the research on laser material interaction is important to improve the knowledge on material consolidation mechanisms at different laser sintering parameter combinations and for process optimization. To this aim, this work provides an in-depth investigation on the influence of laser sintering parameters on mechanical, surface and dimensional properties of PA12 and carbon fiber reinforced PA12 parts manufactured by selective laser sintering (SLS). A space filling DOE was used to conduct the experimental trials in order to cover a wide range of laser sintering parameters. Consolidation mechanism was evaluated by microstructural and crystallization evolution of the samples produced at different energy densities, supported by mechanical testing, scanning electron microscopy (SEM), X-ray diffraction (XRD), differential scanning calorimeter (DSC) and infrared spectroscopy (FTIR). For the first time in SLS applications Gaussian process ($\mathcal{GP}$) supervised learning was used to model the interaction between laser sintering parameters and important quality criteria. Stochastic optimization via Evolutionary algorithm (EA) was employed to obtain trade-off solutions for several optimization tasks. Laser energy density had major influence on physical and mechanical properties, exhibiting a complex and non-linear behavior for both polymer and polymer composite materials evaluated. Fracture mechanism occurred at interlayer region or interface between carbon fiber and PA12 or between unmolten PA12 particles, depending on the energy density applied. XRD and DSC analysis revealed a decrease in crystal fraction with increasing energy density, whereas FTIR measurement suggested that polymer degradation at high energy densities could be present by both polymer chain scission (for PA12 and PA12-CF) and oxygen functional group decomposition and gas release upon laser heating of carbon fiber (for PA12-CF), resulting in lower mechanical properties. Gaussian process ($\mathcal{GP}$) modelling of the laser sintering parameters could be successfully applied for both materials, presenting very good model quality for the majority of quality variables evaluated. Multi-objective optimization with EA could be deployed for several optimization tasks, showing a wide range of optimized laser sintering parameters depending on the trade-off objective desired.

Keywords: Additive Manufacturing, Laser Sintering, Polymers, Polymer Composites, space filling DOE, Gaussian process modelling, stochastic optimization.

Resumo

A Manufatura aditiva (AM) refere-se a modelagem física de protótipos, componentes e produtos a partir de seus desenhos digitais obtidos por modelagem em CAD, utilizando processos de adição de material em camadas. Uma característica comum a estas tecnologias é a abordagem aditiva usada na fabricação de peças, que possibilita a fabricação de geometrias extremamente complexas sem a necessidade de ferramental específico e sem aumentar o custo da peça. Das tecnologias AM disponíveis, a Sinterização seletiva a laser (SLS) está entre as mais bem-sucedidas devido à capacidade de gerar peças complexas sem a necessidade de uma estrutura de suporte. Em teoria, qualquer material na forma de pó pode ser processado pela SLS, no entanto, o complexo mecanismo de interação e consolidação do material a laser que ocorre durante a sinterização a laser limita a variedade de materiais disponíveis. Neste contexto, a pesquisa sobre a interação do laser material é importante para melhorar o conhecimento dos mecanismos de consolidação do material em diferentes combinações de parâmetros de sinterização a laser e otimização do processo. Para contribuir com este objetivo, este trabalho fornece uma investigação aprofundada sobre a influência dos parâmetros de sinterização a laser nas propriedades mecânicas, superficiais e dimensionais das peças PA12 e PA12 reforçadas com fibra de carbono fabricadas por sinterização seletiva a laser (SLS). Uma abordagem de DOE foi utilizada para conduzir os ensaios experimentais, a fim de cobrir uma ampla gama de parâmetros de sinterização a laser. O mecanismo de consolidação foi avaliado pela evolução microestrutural e de cristalização das amostras produzidas em diferentes densidades de energia, suportadas por ensaios mecânicos, microscopia eletrônica de varredura (MEV), difração de raios X (DRX), calorimetro diferencial de varredura (DSC) e espectroscopia no infravermelho (FTIR). Pela primeira vez em aplicações SLS, o aprendizado supervisionado via processo Gaussiano foi usado para modelar a interação entre os parâmetros de sinterização a laser e importantes critérios de qualidade. A otimização estocástica via algoritmo evolutivo (EA) foi empregada para obter soluções para várias tarefas de otimização. A densidade de energia do laser teve grande influência nas propriedades físicas e mecânicas, exibindo um comportamento complexo e não linear para os materiais polímeros e compósitos poliméricos avaliados. O mecanismo de fratura ocorreu na região entre camadas ou na interface entre a fibra de carbono e o PA12 ou entre as partículas de PA12 não fundidas, dependendo da densidade de energia aplicada. A análise por e DRX e DSC revelou uma diminuição na fração de cristal com o aumento da densidade de energia, enquanto a medição por FTIR mostrou que a degradação de polímeros em altas densidades de energia pode estar presente tanto pela cisão da cadeia do polímero (para PA12 e PA12-CF) quanto pela decomposição do grupo funcional de oxigênio e liberação de gás pelo aquecimento da fibra de carbono (para PA12-CF), resultando em propriedades mecânicas mais baixas. A modelagem dos parâmetros de sinterização a laser via processo gaussiano pode ser aplicadacom sucesso a ambos os materiais, apresentando alta qualidade do modelo para a maioria das variáveis analisadas. A otimização estocástica com múltiplos objetivos pode ser implementada para vários critérios, apresentando um amplo espectro de soluções ótimas dependendo do objetivo desejado.

Palavras-chave: Manufatura Aditiva, Sinterizacao a Laser, Polímeros, Compósitos poliméricos.

List of Figures

List of Tables

List of abbreviations and acronyms

3D	Three Dimensional
3DP	Three Dimensional Printing
AM	Additive Manufacturing
BJ	Binder jetting
CAD	Computer aided design
CDLP	Continuous digital light processing
CNT	Carbon Nano-tube
CT	Computer Tomography
DLP	Digital light processing
DOD	Drop on demand
DOE	Design of Experiments
DSC	Differential scanning salorimeter
EA	Evolutionary algorithm
EBM	Electron beam melting
EOS	Electro Optical Systems
FDM	Fused deposition modeling
FTIR	Fourier-transform infrared spectroscopy
GP	Gaussian process
LENS	Laser engineering net shaping
LOM	Laminated object manufacturing
LS	Laser sintering
LPS	Liquid phase sintering
MJ	Multi jet

MJF	Multi-Jet fusion
NPJ	Nano particle jetting
PMC	Polymer Matrix Composites
RP	Rapid Prototyping
RM	Rapid Manufacturing
RT	Rapid Tooling
SEM	Scanning electron microscopy
SLA	Stereolithography
SLS	Selective laser sintering
SLM	Selective laser melting
TE	Tissue engineering
TEM	Transmission electron microscopy
UV	Ultra violet
XRD	X-Ray Difraction

List of symbols

ψ	Volumetric Energy per unit of Single Processing Track
τ	Exposure Time
ε	Error between observed and modelled values
ϑ	Normalized manufacturing time
d	Laser Beam Spot Size
D	Training dataset
$\mathbb{E}$	Expectation
$\mathcal{GP}$	Gaussian process
$f(x)$	Gaussian process function values
h	Scan Line Spacing
H_c	Heat of melting
H_{100}	Heat of melting of a 100 % crystalline sample
$I(r)$	Radial Intensity Distribution
$k(x, x')$	Covariance (or kernel) function evaluated at x and x'
l	Laser Line Length
l_c	Characteristic length-scale
$m(x)$	The mean function of a Gaussian process
O	Degree of Overlapping
N_t	Number of Total Exposures
P	Laser Power
r	Radial Distance from the Center of the Laser Spot
$RMSE$	Root mean square error
R^2	Coefficient of determination

R	Laser Beam Radius
t	Delay Period
T_g	Glass Transition Temperature
T_m	Melting Temperature
v	Laser Scanning Speed
w	Layer Thickness
X_c	Crystal fraction
y	Observed output value

Contents

1 Introduction

Additive manufacturing (AM) encompasses a group of layer based technologies which have the potential to overcome the limitations from traditional manufacturing methods. AM technologies provide the possibility of the direct fabrication of complex shaped objects from three-dimensional CAD models, reducing the lead time and processing costs (GIBSON; ROSEN; STUCKER, 2010). The key feature of AM is the additive approach, where a CAD design of the parts is first sliced by software into many thin layers. These layers are then used as templates to build a solid model, layer-by-layer until the object is built. The main benefit from this approach is the ability to produce parts of virtually any geometric complexity without the need for tooling, reducing dramatically the process planning.

From the wide variety of AM techniques available, Selective Laser Sintering (SLS) emerges as one of the most successful additive manufacturing technologies. SLS is a powder bed fusion technique that creates parts layer-by-layer by consolidating successive layers of loose powder (GU et al., 2006). Consolidation is obtained by selectively fusing or sintering each layer using the thermal energy supplied by a focused laser beam (KRUTH et al., 2003) which scans the layers according to the sliced CAD model.

SLS ranks among the most successful additive manufacturing techniques, due to its ability to generate complex parts using powdered materials, which can be accomplished most times without the need of a support structure. A wide range of materials can be processed by LS compared to other AM processes (AGARWALA et al., 1995). Also, the process is very fast when compared to other AM techniques, because the powder is bonded together in a thermal process and there is no need of a secondary curing (DAS et al., 1998). At last, it offers great potential to expand its application scope to the production of tools and functional parts (KIMBLE, 1992).

Polymers were the first and are still the most applied materials in SLS. Interestingly, only a few powder materials are available on the market, and most of these materials are based on polyamide 12 (PA12), which is a typical nylon grade easily processable by SLS (Goodridge et al., 2012; Kruth et al., 2008). The high success of using PA12 in SLS is generally ascribed to a complex combination of materials properties and material-laser-interaction properties that are fulfilled in order to turn a polymer into an SLS processable polymer powder.

Laser sintering consolidation mechanism of PA12 has been studied considering all aspects described before. Dupin et al. (2012) studied pore distribution and amount of unmolten particles during laser sintering of PA12 at different energy densities and found a great influence of energy density on pore morphology and amount of nascent particles. Stichel et al. (2017), Stichel et al. (2018) conducted a similar work but using a Round Robin methodology. The authors observed a correlation of highest ductility of PA12 samples with low pore concentration, absence of coplanar pores and high degree of particle melting. Schmid et al. (2017) studied different PA12 powder systems with pronounced powder characteristics. The authors investigated powder differences based on particle size distribution, thermal analysis, XRD, mechanical analysis and melt volume rate. It was found a high influence of the powder characteristics such as particle shape, sintering window, powder distribution and chain termination on mechanical properties and surface roughness. A similar study was performed by Verbelen et al. (2016) with extended research to PA11 and PA6. Crystallization behavior of PA12 during SLS was studied in more detail by other authors, who found that partial melting of PA12 is the main mechanism occurring during SLS, with a full melting of the particles surfaces and unmolten particle core. The authors observed a correlation of mechanical properties with crystal fraction, where improved elongation at break was achieved with decreasing crystal fraction of PA12 (ZARRINGHALAM et al., 2006; MAJEWSKI; ZARRINGHALAM; HOPKINSON, 2008; GRIESSBACH; LACH; GRELLMANN, 2010)

SLS parameters are generally related to the energy delivered to the powder bed and influence important quality factors such as the geometrical, surface and mechanical properties of parts produced. Work has been dedicated to study the influence of the energy density on mechanical properties.Caulfield, McHugh & Lohfeld (2007) studied the influence of energy density and build orientation on mechanical properties of PA12. The authors and found a positive correlation of laser power with mechanical properties, although an optimum energy input was found.Wegner & Witt (2012) used response surface modelling to study the effect of laser speed, laser power, scan line spacing, pre-heating temperature and layer thickness on density and tensile properties of PA12 parts. The authors also observed an optimal energy input existing to result in best mechanical properties. Usher, Gornet & Starr (2013) employed fractional factorial design and Weibull growth modelling to study the influence of build orientation and laser sintering parameters on yield strength and elongation at break of PA12 samples processed by SLS. Hofland, Baran & Wismeijer (2017) also used a fractional factorial design to investigate the influence of individual laser sintering parameters on density and tensile properties of PA12. Sensitivity analyses showed that the most important process variables were scan spacing and layer thickness.

An interesting field of research concerns the improvement of polyamide 12 properties to meet the requirements of more demanding applications. SLS of polymer matrix composite materials is based on the rationale of combining two or more materials to improve properties unachievable by the single materials (KUMAR; KRUTH, 2010). The most common method to produce composites by LS is the combination of matrix and reinforcement powders. Reinforcement powders are generally used in particulate form or in the form of small sized fibers. The combination of powders can be made by simply mixing the matrix and reinforcing powder, using a single composite powder, or coating reinforcement material with the polymer matrix, which helps overcome problems associated with non-uniform mixing of powders, yielding a uniform spread of composite components.

Extensive research has been made to improve the mechanical properties of polymer laser sintered parts by reinforcing them with micron-sized inorganic fillers (PARANDOUSH; LIN, 2017; WANG et al., 2017; GOODRIDGE; TUCK; HAGUE, 2012), most of these works focusing on reinforcing PA12 or PA11. Aluminum was added to PA12 by means of direct mixing to produce composite parts resulted in accurate parts and with increased mechanical strength compared to pure PA12 (MAZZOLI; MORICONI; PAURI, 2007). Silicon carbide was mixed with PA12 to produced composite parts by SLS and an investigation on the effect of sintering parameters was performed (HON; GILL, 2003). PA12 was also mixed with limestone for laser sintering processing (GUO; JIANG; BOURELL, 2014). Glass beads reinforced PA12 have been studied (NEGI; DHIMAN; SHARMA, 2015), showing limited mechanical properties of parts manufactured with these systems. Nanomaterials have also been combined to polymer for SLS processing.

The SLS of carbon fibers reinforced PA12 composites have recently received attention by research community. Yan et al. (2011) prepared carbon fibers by surface modification in order to improve interface adhesion with PA12 and further mixing CF with PA12 by dissolution-precipitation method. Mechanical properties were greatly enhanced by the preparation method when compared to pure PA12. More recently, carbon fiber surface modification via HNO_3 treatment was performed to improve adhesion with PA12 via direct mixing (JING et al., 2017). Porosity of mechanically mixed PA12-CF samples manufactured in different building directions was studied by means of computed tomography (JANSSON; PEJRYD, 2016). Fracture mechanism of PA12-CF material processed by SLS was recently studied (LIU et al., 2019).

SLS of PA12 is a well known topic to the scientific community and much research has been conducted to investigate different aspects of PA12 consolidation during SLS and influence of energy density on density and mechanical properties. Nevertheless, few studies have been conducted so far on the modelling of individual laser sintering parameters and important quality variables such as dimensional accuracy, surface and mechanical properties. Also, the works previously conducted is based on fractional factorial design space which gives poor space coverage for modelling purposes and does not give a complete picture on the behavior of output parameters based on variation of laser sintering input parameters. This is therefore the main contribution of this work for PA12, to perform an in depth investigation on modelling of individual laser sintering parameters and the most relevant quality criteria for laser sintering of PA12 and also perform optimization tasks considering the frequently conflicting criteria that needs to be met when producing a SLS part.

From the literature review on SLS of polymer composites and more specifically on SLS of PA12-CF, most of the research carried out so far in laser sintering of PA12-CF materials is focused on material aspects, without taking into consideration the influence of laser sintering parameters on quality properties. No research has been conducted to investigate the effect of laser sintering parameters which influence the energy density delivered to the powder bed. Therefore, the goal of this research study is to investigate the influence of energy density on important quality criteria such as surface properties, dimensional accuracy, density and mechanical properties. Additionally and consequently, there is no modelling of the individual laser sintering parameters existing. Also the modelling and optimization of individual laser sintering parameters is performed and a multi-objective optimization is performed for the first time for PA12-CF.

The work is divided in the following chapters: chapter 2 details the Additive Manufacturing and selective laser sintering (SLS) process, presenting the phenomena behind the process, major process parameters and materials used. Furthermore, a review on selective laser sintering of polymers and polymer composites is given; chapter 3 presents the experimental methodology proposed whereas chapter 4 presents the results obtained for PA12 and chapter 5 . At last chapter 6 presents the conclusions drawn from the present work as well as further research directions.

2 Additive Manufacturing

This chapter provides an overview of Additive Manufacturing (AM). The main technologies are given and the manufacturing process chain is described. Furthermore, the Selective Laser Sintering (SLS) process is introduced, detailing its main features, materials used in the process and also a physical description of the process including a theoretical discussion on the influence of the main SLS parameters. At last a review on the application of SLS for processing of polymers and polymer composites is presented.

2.1 Overview

Additive Manufacturing (AM) is defined by ASTM Standard F2792-12a (2012) as the "process of joining materials to make objects from three-dimensional (3D) model data, usually layer upon layer, as opposed to subtractive manufacturing technologies" . It refers to the physical modelling of a design using digitally driven additive processes. AM systems quickly produce models and prototype parts, tools, patterns and functional parts from 3D computer-aided design (CAD) data, computer tomography (CT) and magnetic resonance imaging (MRI) scans, and data from 3D digitizing systems. Using an additive approach, AM systems join liquid, powder, or sheet materials to form physical objects. Layer by layer, AM machines process plastic, paper, ceramic, metal, and composites from thin, horizontal cross sections of a computer model (WOHLERS, 2004).

The development of the first AM process emerged in 1987 with Stereolithography from 3D Systems, a process that solidifies thin layers of ultraviolet light-sensitive liquid polymer using a laser (WOHLERS, 2007). As the technologies initially were used only to produce prototypes, the term Rapid Prototyping (RP) was given to embrace all AM technologies. Since then, many techniques have been developed and evolved in such way that, recently, improvements in the quality of the output from these techniques made possible to shift towards the use of RP processes for the manufacture of tools (Rapid Tooling, RT) and end-use functional parts (Rapid Manufacturing, RM) (GIBSON; ROSEN; STUCKER, 2010). As the term Rapid Prototyping was misleading and overlooked the principle of these technologies, the term Additive Manufacturing (AM) was created to embrace all these technologies. Synonymous of AM, besides the one cited above, are additive fabrication, additive process, direct digital manufacturing, layer manufacturing and freeform fabrication.

A common feature of all AM processes is the additive approach used to produce parts. The main benefit gained from this is the ability to produce parts of virtually any geometric complexity without the need for tooling, reducing significantly the process planning, production and lead times and costs (HOPKINSON; HAGUE; DICKENS, 2006). Another interesting characteristic is the wide range of materials that can be used, from polymers, metals and ceramics to composites.

As in Additive Manufacturing complex shapes are built with little/no form restriction, it increases the potential for different design methodologies focused on the 'Manufacture for Design' rather than 'Design for Manufacture' philosophy used by conventional manufacturing processes, which represent one of the most restrictive factors for product development (HOPKINSON; HAGUE; DICKENS, 2006).

For many years, the additive manufacturing industry lacked categories for grouping AM technologies, which made it challenging educationally and when communicating information in both technical and non-technical settings. The ASTM committee defined 7 additive manufacturing groups which enabled the discussion of a category of machines, rather than needing to explain an extensive list of commercial variations of a process methodology (ASTM Standard F2792-12a, 2012).An overview of the main processes according to ASTM F2792-12a is given in Tab. 2.1 (ASTM Standard F2792-12a, 2012).

In Vat photopolymerization a liquid photopolymer in a vat is selectively cured by light-activated polymerization. Examples of processes include Stereolithography (SLA), which consolidate a liquid photocurable resin by selective exposure to a UV light, and digital light processing (DLP), which is similar to SLA, except that instead of laser vector scanning, it projects a bitmaps onto the photocurable resin using a projector and curing a layer at once.

Example of material extrusion is Fused deposition modelling (FDM), where a molten polymer filament is fed by a nozzle onto a substrate by means of a moving head.

In material jetting, material is selectively dispensed through a nozzle or orifice. Examples include Material Jetting process, where photopolymer droplets are deposited on a layer by means of a nozzle and cured with UV light. Drop on demand (DOD) process uses a similar process but using molten wax which is deposited via a nozzle.

Binder jetting is an AM process in which a liquid bonding agent is selectively deposited to join powder materials. Most common process example is Binder jetting or Three-dimensional Printing (3DP), in which the part is built in a powder bed and an ink jet printing head is used to spray a liquid binder in the powder layer, which solidifies to form the solid layer.

Powder based AM processes are focused on the application of material in powder form and the consolidation of the part is performed by a heat source to build each layer. Examples include Laser Sintering (LS) or Selective Laser Sintering (SLS$^{\text{TM}}$), where the powder is spread in a layer and selectively scanned by a laser. This process uses partial melting or liquid phase sintering (LPS) as the consolidation method and is focused on

Table 2.1 – Overview of the main additive manufacturing processes (ASTM Standard F2792-12a, 2012)

Group	Process	Material Preparation	Layer Technique	Materials
Vat photopolymerization	SLA	Liquid resin in vat	Laser scanning	UV curable resin, ceramic suspension
	DLP	Liquid resin in vat	UV projector	UV curable resin
	CDLP	Liquid resin in vat	Continuous UV projector	UV curable resin
Material extrusion	FDM	Filament melted in nozzle	Continuous extrusion and deposition	Thermoplastics, wax
Material jetting	MJ	Liquid polymer in jet	Droplet deposition and laser scanning	UV curable resin
	DOD	Liquid wax in jet	Droplet deposition	Wax
	NPJ	Liquid resin with metal nanoparticles	Droplet deposition	Metals
Binder jetting	BJ	Powder in bed	Droplet deposition joined with bonding agent	Sand, Metals
Powder bed fusion	SLS^{TM}/LS	Powder in bed	Laser scanning	Thermoplastics, wax, composites
	SLM	Powder in bed	Laser scanning	Metals
	EBM	Powder in bed	Electron Beam scanning	Metals
	MJF	Powder in bed	Fused with agent and energy	Polymers
Direct energy deposition	LENS	Powder feed	Laser scanning	Metals
Sheet lamination	LOM	Laser cutting	Binding of sheets with adhesive	Paper, plastics, metals

processing polymers or more than one phase polymer composites. Selective Laser Melting (SLM) was derived from SLS and developed to process metals by full melting instead of partial melting. A similar technology is Electron Beam Melting (EBM), which uses the same approach of SLM but uses an electron beam as a heat source, instead of a laser.

Direct energy deposition technologies include Laser Engineered Net Shaping (LENS), which fully melt metal powders by means of a laser, similarly to SLM. The main difference is that instead of using a powder bed, the powder is fed by a nozzle.

The main sheet lamination process available is Laminated Object Manufacturing (LOM), where a solid sheet of material is attached to the previous one, and a hot roller compresses the sheet and activates a heat-sensitive adhesive (GUO; LEU, 2013).

All commercialized AM machines to date use a layer-based approach. The ways they differ are in the materials that can be used, how the layers are created and how the layers are consolidated. Such differences determine factors such as the time to produce a part, the accuracy of the part and its material properties (GIBSON; ROSEN; STUCKER, 2010).

2.2 Additive Manufacturing Process Chain

Additive Manufacturing creates physical parts from their CAD data in a layerwise fashion. Although there will be some variations depending on which technology is being used, the general AM process chain is composed of a sequence of seven steps, described below (GIBSON; ROSEN; STUCKER, 2010) and represented in Fig. 2.1.

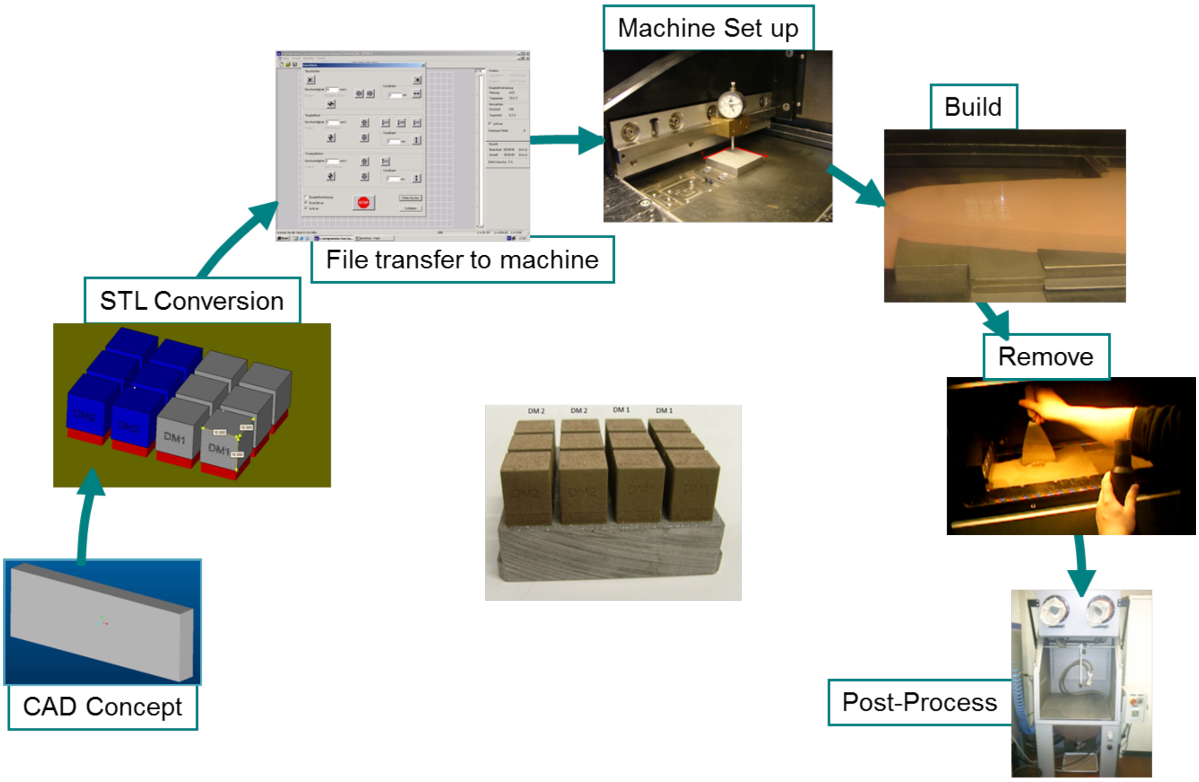

Figure 2.1 – Additive Manufacturing process chain.

1. Conceptualization and CAD: A generic AM process must start with 3D CAD information from the product. There is a variety of ways as how the 3D data can be created, such as 3D sensors (laser, sonic or optical digitized). Most of 3D CAD systems are solid modeling systems with surface modeling components. This step is usually the most time consuming of the entire process chain, since many factors contribute to the model quality, for example the software quality, orientation of the part, need for supports, complexity of the part, use of thin walls, small holes and slots.

2. Conversion to STL: Nearly all AM processes uses the STL format, which is a simple description of its CAD model in terms of its geometry alone. Aspects such as construction data and historic modeling are neglected and the surfaces of the model are approximated using triangles facets. The triangle size is calculated in terms of the distance between the plane represented by the triangle and the surface it is supposed to represent. Combined to this is a vector normal to the surface indicating the direction of the triangle, inside vs. outside the part. This process of converting to STL is automatic in most of the CAD software but errors might occur during this transition and a STL repair software may be needed to correct problems with the file generated by the CAD. Common software used is MAGICS from the Belgium Company Materialise.

3. Transfer to AM machine and file manipulation: Once the STL file is created it can be sent directly to the AM machine. At this step it is necessary to check if the part is correct. Normally AM machines have software for visualization that allows the user to view and manipulate the part. Here the user can reposition the part, change the orientation direction to better allocate it, chose to build more than one part when possible.

4. Machine setup: All AM machines have a setup of parameters that must be adjusted and that are specific to that machine or process. For example, some machines may process only one or two materials and have a fixed layer thickness, resulting in setup changes. Others may be designed to run with a variety of materials and need optimization of the parameters to best suit the part to be built, requiring a numerous setup options. In such cases, it is normal to define default values to help speed up the machine setup and to prevent mistakes being made.

5. Build: Once these steps are completed, the process switches to the computer-automated building phase, taking place the layer-based manufacturing concept. Generally the AM machines will have a similar sequence of layer control, using an adjustable platform, material deposition and layer cross-section formation. This process will be repeated until either the build is completed or there is no feeding material remaining.

6. Removal and cleaning: At this stage, it is expected that the parts will require additional effort for removal and cleaning, since the parts must be either separated from a building platform on which the part was produced or removed from excess build material surrounding it. This is specially the case for processes where a support structure is used, to prevent the part from collapsing or warping during its manufacturing. Different AM processes will require different clean-up requirements.

7. Post-Process: The final step in the AM process chain is the post-processing which refers to the stage of finishing (usually manual) the parts for application purposes. It may involve polishing and sandpapering to improve surface finish and aesthetic appearance, coating application, binder removals, post curing for liquid based AM process (CHUA; LEONG; LIM, 2010).

2.3 Selective Laser Sintering

Selective Laser Sintering (SLS) is a powder-based layer-additive manufacturing process that allows the manufacturing of three-dimensional (3D) complex parts directly from their CAD models (DAS et al., 1998; KRUTH, 1991). The LS technique creates parts layer-by-layer by consolidating successive layers of loose powder (GU; SHEN, 2006). Consolidation is obtained by selectively fusing or sintering each layer using the thermal energy supplied by a focused laser beam (KRUTH et al., 2003; KRUTH et al., 2005) which, by means of a mirror deflection system (SCHUEREN; KRUTH, 1995), scans the layers according to the cross section of the object's mathematically sliced CAD model. Figure 2.2 gives a representation of the machine.

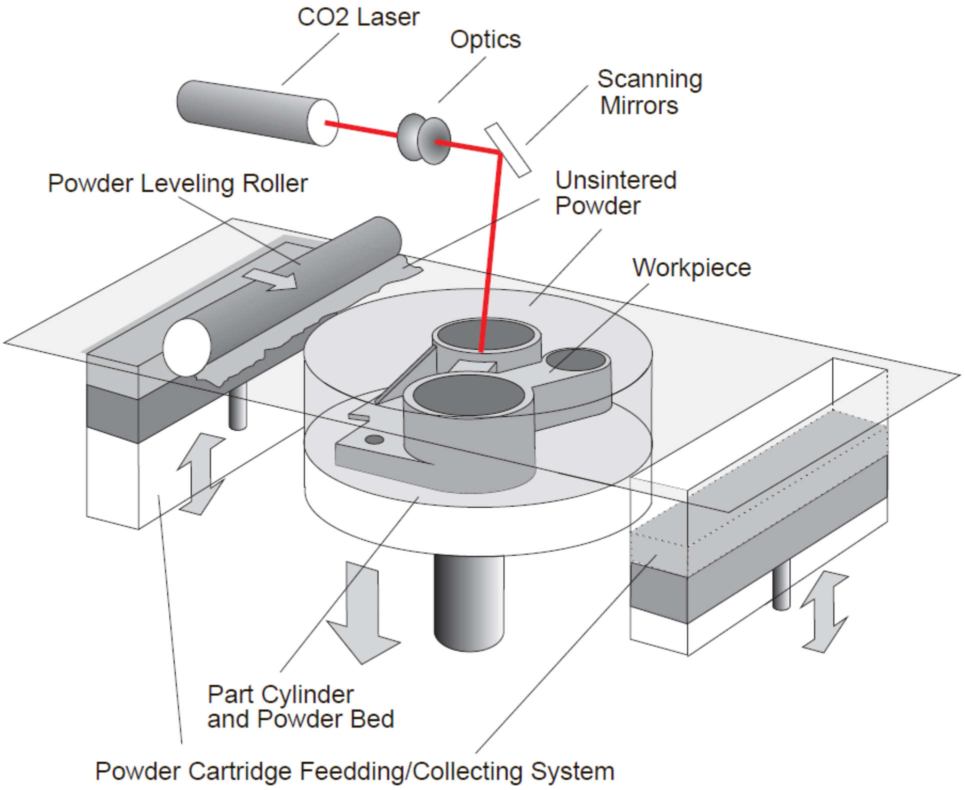

Figure 2.2 – Schematic representation of an SLS machine (DOLENC, 1994).

SLS ranks among the most successful additive manufacturing techniques, due to its unique characteristics: the ability to generate very complex parts using powdered materials, which can be accomplished most times without the need of a support structure since the powder acts as a natural support structure during the process; wide range of materials can be processed by LS compared to other AM processes; the process is very fast when compared to other AM techniques, because the powder is bonded together in a thermal process and there is no need of a secondary curing; great potential to expand its application scope to the production of tools and functional parts (KIMBLE, 1992).

Initially, SLS was developed as manufacturing process for single use functional prototypes (DECKARD, 1989). Recent developments in SLS machines and process made possible a shift to the direct manufacturing of tools (Rapid Tooling) (RADSTOK, 1999) and end-use functional parts (Rapid Manufacturing) (KARAPATIS et al., 1998).

The additive manufacturing steps in the SLS process can be described in the following way (Figure 2.3):

- Initially the dosing platform is raised to add new material on the building platform (Fig. 2.3a);
- next, a blade or roller is moved across the process chamber and new powder is spread and leveled on the building platform (Fig. 2.3b);
- after this the laser beam (Nd:YAG or CO_2) scans the powder layer according to the cross-section of the part's mathematically sliced CAD model, resulting in the consolidation of the particles (Fig. 2.3c). The underlying layer provides support to the subsequent layers of material while the surrounding powder that did not interact with the laser acts as a support structure for the consolidated layer, eliminating, occasionally the need to model and build a support structure;
- in the last step, the building platform is moved one layer size down, while the dosing platform moves down a certain distance to prevent the blade/roller from carrying powder when it moves to the other end of the process chamber (Fig. 2.3d);
- the cycle is repeated again until all layers are processed and the whole part is finished.

2.3.1 Laser Sintering Processing Parameters

Several parameters influence the SLS manufacturing of adequate parts, with the desired physical and geometrical properties. Understanding how these parameters affect the process is therefore important not only for the process control and automation but also for selecting appropriate parameters prior to processing. The parts quality is directly related to the densification behaviour of the material, whose response is influenced by many processing parameters and material characteristics. The first are addressed in this section whereas materials characteristics are addressed in section 2.3.2.

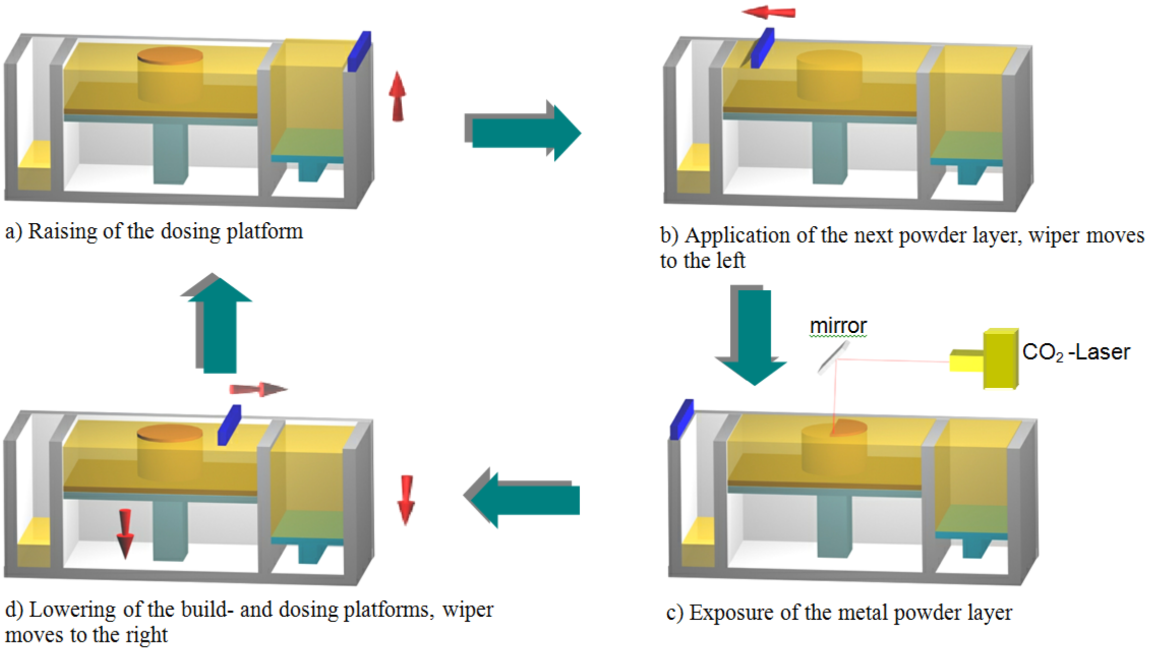

Figure 2.3 – Description of the SLS process.

Processing parameters are defined variables that influence and control the SLS process. These parameters are generally related to the energy delivered to the powder bed and influence the response parameters such as the geometrical and mechanical properties of the parts produced. The amount of energy delivered to the surface during the laser-material interaction period is dependent on the laser intensity of the laser irradiation, the period of a single exposure, the number of total exposures and the time between each exposure (WILLIAMS; DECKARD, 1998).

The parameters that are most influential on the energy delivered to the powder bed surface with a layer thickness (w) are the laser power (P), laser beam spot size (d), laser scan speed (v), scan line spacing or hatch distance (h) and the scanning strategy applied, including the laser line length (l) and the method of irradiation between successive layers. The laser irradiation is related to the laser power and the laser beam spot size:

$$P = \int_0^R I(r) 2\pi r dr \tag{2.1}$$

where $I(r)$ is the radial intensity distribution, r the radial distance from the center of the laser spot and R the laser beam radius. The exposure time τ is related to the laser beam spot size and the laser scan speed through the following:

$$\tau = \frac{d}{v} \tag{2.2}$$

Lower laser scan speed values lead to higher exposure times, increasing the amount of heat delivered to the powder bed and resulting in a deeper and wider melting pool and a better consolidation of the powders. Regarding the laser beam spot size, its increase results in a larger exposure area, increasing the number of exposures and the exposure period. Consequently it has a significant effect on the densification behavior of the part. On the other side the higher spot size decreases the temperature of the powder bed surface, for a given laser power. If, despite this temperature decrease, the temperature achieved is still enough for consolidation, it is preferred to use higher laser spot sizes. The number of total exposures is defined as the ratio between the laser beam spot size and the scan line spacing:

$$N_t = \frac{d}{h} \tag{2.3}$$

This definition comes from the overlapping scanning pattern during SLS, where the same region is exposed to the laser irradiation several times. This pattern can be expressed by (WILLIAMS; DECKARD, 1998):

$$O = 1 - \frac{d}{h} \tag{2.4}$$

Where O represents the degree of overlap occurring. Overlap is achieved whenever the distance between scan lines is less than the laser spot diameter ($h<d$). This parameter has a significant effect on the densification of the part, as it measures the degree at which adjacent scan lines superpose and are reprocessed. The amount of energy stored at the surface is related to the time between exposures. The longer this time, the longer period in which the molten pool loses heat by conduction to the powder bed and by radiation and convection at its surface. This delay period depends on the scan line length and the laser scan speed:

$$t = \frac{l}{v} \tag{2.5}$$

Increase in the scan line length results in longer delay periods which may increase the cooling time and probably decrease the maximum temperature reached. Consequently, it is expected a worse powder consolidation and densification of the part. Scan line length also influences the development of thermal stresses and the higher this parameter the higher tendency to develop these stresses (POHL et al., 2001) and to cause parts curling, loss of edge tolerances and even parts delamination. Therefore short scan line length are always preferable (SIMCHI; PETZOLDT; POHL, 2003). Directly related to the scan line vector is the scanning strategy applied, which affects the inter-layer bonding (LI; SHI; LIU, 2009).

Another important parameter is the layer thickness w. Although not related to the energy delivered to the powder bed surface, it affects the volumetric amount of energy absorbed. Smaller layer thickness generally yields higher densities, as the heat provided by the laser is better absorbed by the underlying layers, resulting in a better inter-layer bonding. On the other hand there is a minimum value for the layer thickness which is dependent on the particle size distribution of the material. Below this value, the process might become unstable since the blade or roller mechanism will tend to scratch the previously processed layers, leading to part damage. It should be noted also that higher layer thicknesses speed up the SLS process, so that there is always a compromise between these factors.

The combination of laser power, laser scan speed, scan line spacing and layer thickness gives an indication of the volumetric energy per unit of single processing track:

$$\psi = \frac{P}{vhw} \tag{2.6}$$

2.3.2 Physical aspects in Selective Laser Sintering of polymers and PMCs

The physical processes associated with laser sintering are of complex nature (DAS, 2003). As the laser scans the powder layer, a part of the light energy from the laser is converted to thermal energy, heating the powder. This conversion is strongly dependent on the interaction laser-material, as the material absorbs a certain quantity of energy from the laser (WANG et al., 2002). Part of this generated heat will subsequently be transferred along the powder bed, and the way this heat transfer occurs depends on the thermophysical properties of the powder, such as thermal conductivity, specific heat and thermal diffusivity. After the powder is heated by the laser, it undergoes densification by different consolidation mechanisms such as partial melting and liquid phase sintering. Aspects such as the wetting, capillary instability and thermocapillary effects such as Marangoni flow must be kept in mind in order to promote an adequate densification. For high input energies, phenomena such as evaporation of material, oxidation and polymer degradation may take place. At last, due to the processing chamber being kept at near the melting temperature of the polymer, the slow and localized cooling and solidification of the material govern its final microstructural characteristics.

Figure 2.4 shows the different polymer properties which are important to achieve SLS promising materials. They are divided in optical, thermal and rheological properties and also in particle and powder properties.

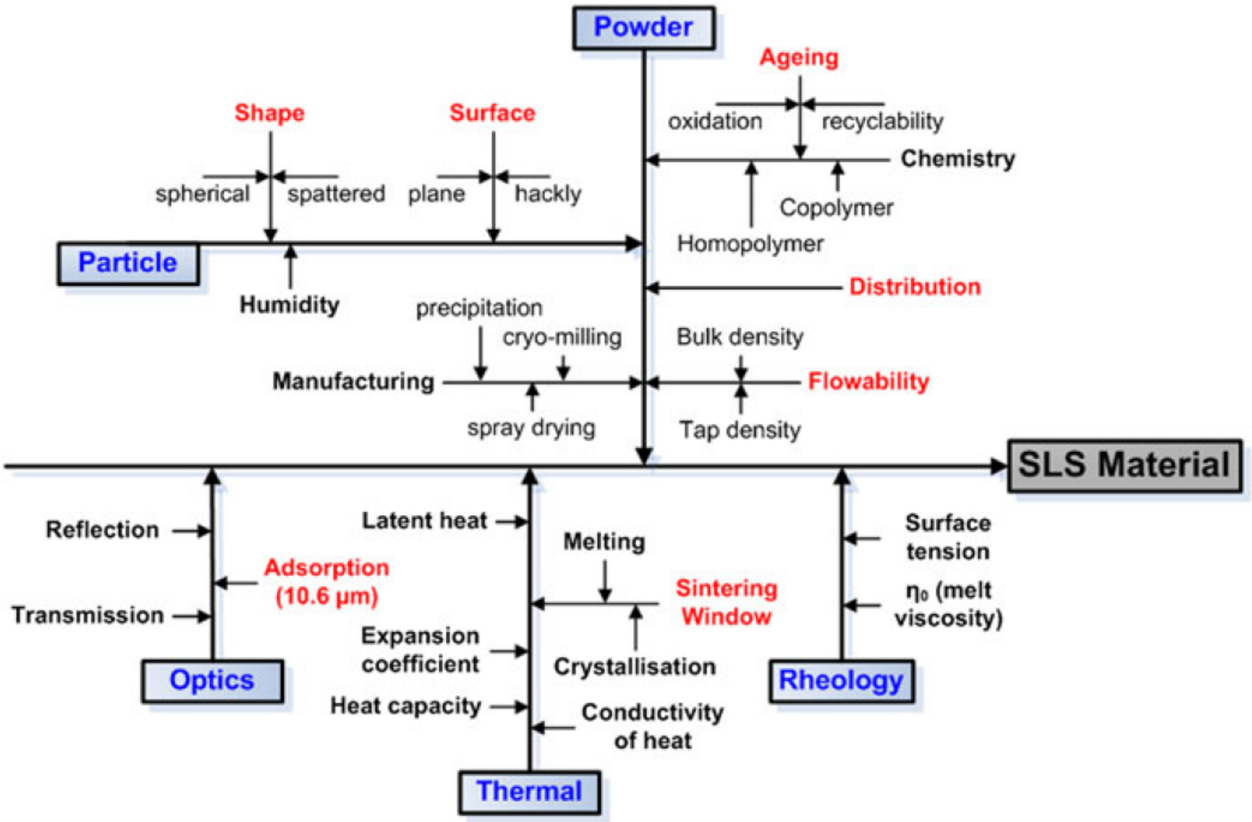

Figure 2.4 – Main variables affecting the SLS process.

2.3.2.1 Optical properties

Optical properties are related to the ability of the polymer to absorb the energy delivered by the laser wave length. As CO_2 lasers (wavelength of 10.6 μm) are normally used to process polymer powders, polymers present a good absorption of the radiation in this spectrum. In powder beds the scatter of radiation is observable, which is a process that does not remove energy from the radiation field, but redirect it, generating multiple reflections in the powder bed and consequently higher absorptions values than bulk materials (LAUMER et al., 2016).

2.3.2.2 Thermal properties

During SLS, polymer powders are heated up to high temperatures and are subject to a change from a hard structure to a softer one and finally to a viscous flowing melt. The way and the temperature at which this transformation will occur are dependent on the polymer type and have a significant influence of the laser sinterability of the material. Semi-crystalline polymers have glass transition temperatures T_g normally between room temperature or below, and a melting temperature T_m normally above 100 °C. This class of polymers rapidly changes from solid to viscous liquid when sufficient heat is applied. On the other hand, these materials present a high degree of shrinkage during cooling from their T_m. In contrast, amorphous polymers do not have a clear melting temperature range. They have a T_g normally around 100 °C above which the material will gradually change to rubbery and liquid state without clear transitions (KRUTH et al., 2008).

In order to process these materials, specially semi-crystalline polymers, it is imperative to keep the powder bed with constant heating. For semi-crystalline the heating temperature should be just below its melting point and for amorphous polymers just below its T_g. This temperature is important to minimize effects of part shrinkage and distortion during and after laser processing.

Another thermal aspect related to the polymer properties is the so called "sintering window" of the material, which is the temperature range between its melting and crystallization temperature. This SLS temperature range for a specific polymer is normally obtained by performing a Differential Scanning Calorimeter (DSC) of the material, as shown in Fig. 2.5. Ideally a suitable polymer material for SLS processing should possess a narrow melting peak in the heating curve of the DSC and also non-overlapping melting and re-crystallization peaks. The first condition provides a fast melting of the material without excess energy and the second condition gives the material more time in its liquid state during the cooling phase, delaying crystallization during the build process. Polymers whose DSC heating and cooling curves are superposed crystallize quickly during cooling, provoking shrinkage and distortion of the part (GOODRIDGE; TUCK; HAGUE, 2012).

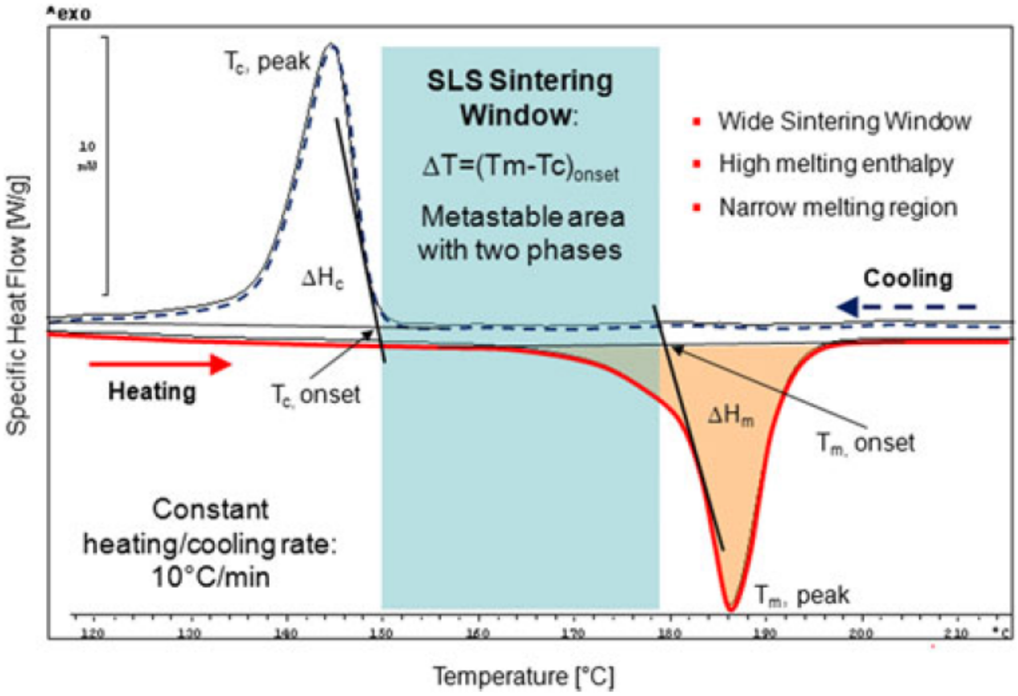

Figure 2.5 – DSC showing the "sintering window" of SLS processing (GOODRIDGE; TUCK; HAGUE, 2012)

2.3.2.3 Rheological properties

Besides the thermal and optical properties, low viscosity and low surface tension of the polymer melt are important for successful SLS processing. Low viscosity is important to allow full spreading of the molten polymer within the process time scale. On the other hand low viscosity also contributes to part shrinkage and lower accuracy (KRUTH et al., 2003). Additionally, thermocapillary forces are generated in molten pools with non-uniform temperature, such as the ones created during SLS. Due to this non-uniform temperature distribution, surface tension gradients are formed, generating a convective flow, called Marangoni flow, from regions of low to high surface tension. The strength of thermocapillary flow is determined by the Marangoni number Ma, which depends on properties such as the surface tension temperature gradient, viscosity and diffusivity of the molten pool (TSOTRIDIS; ROTHER; HONDROS, 1989).

The consolidation phenomena during SLS plays a major role in processing polymers and polymer composites. Two types of consolidation mechanisms are of main importance in SLS: Liquid phase sintering and partial melting. Liquid phase sintering is a consolidation mechanism where part of the powder material is melted (binder phase) while the other remains solid (structural phase). The liquid phase flows between the solid particles very quickly, driven by capillary forces, therefore no need of pressure is required, as the magnitude of these forces are comparable to the external pressures used in pressure based sintering processes (GERMAN, 1985). Three overlapping stages can be identified during LPS. The first is the rearrangement stage the liquid is formed and there is a rapid initial densification due to the capillary forces exerted by the wetting liquid in the solid particles. Concurrently to this there is dissolution and reprecipitation, controlled by diffusion processes. At last solid state sintering occurs. It must be mentioned that the kinetics of the first step is so fast that the other events may be overshadowed (GERMAN, 1985). For SLS applications, only a limited range of the rearrangement stage occurs, due to the very short interaction times involved (ANESTIEV; FROYEN, 1999). The drawback of this is that the porosity of SLS parts is higher than with normal LPS. The SLS through LPS is by far the most used process and there are different ways for consolidating the structural and binder phase: mixture of two-component powders; coating of the binder in the structural material; use of composite powder particles and the use of materials where no distinction between structural and binder phase can be done.

Partial melting occurs when no distinct binder and structural phase are used, as is the case when processing single polymers only. During partial melting, only the shell of the particle is melted, whereas the core of the grain remains solid. The molten shell of the particle forms necking structures with neighbouring particles, acting as a binder of non-molten particle cores (KRUTH et al., 2007).

2.3.2.4 Powder and particle properties

The particle and powder properties are also of great importance for SLS processing. Spherical particles are preferable for SLS, as this form induces a better flowing behavior during the process and a better compacting of the powders during the roller or blade passage. Most of today's available SLS powders are not perfectly spherical, they rather have a "potato" shape originated from the precipitation process. Particles obtained from cryogenic milling are normally not adequate for SLS due to inferior flowability characteristics and poor powder bed formation (SCHMID; AMADO; WEGENER, 2014).

Particle size distribution directly influences the SLS processability of polymers. For instance, the mean particle size is generally used as a lower limit for the definition of the layer thickness, since smaller layer thickness's can provoke the interference between the blade/roller and the part. For polymer processing, some researchers have concluded that an adequate particle distribution is between 45 and 90 μm (GOODRIDGE; DALGARNO; WOOD, 2006), whereas other found smaller values, between 20 and 80 μm (SCHMID; AMADO; WEGENER, 2014). Smaller particles normally provide a better densification, part accuracy and surface quality. However if the particles are too small the spreading of the particles may be difficult and there is a higher probability of particle coalescence due to the heating applied in the powder bed.

Another aspect that must be considered during SLS of polymers is the powder degradation and reuse. As all the powder of the processing chamber is heated during the process, the supporting powder undergoes a significant thermal cycle, which causes thermal degradation of the polymer. The long exposure to heat leads to an increase in the molecular weight of the polymer and a consequent increase in the viscosity, resulting in problems in the densification of the powder, mechanical properties and part quality. Normally it is not possible to re-use 100 % of the polymer powder, being necessary to mix the used powder with new powder.

2.3.3 Laser Sintering of Polymers

In theory, any material can be processed by SLS, provided that it is available as powder and the particles tend to melt or sinter when heat is applied. However, practice shows that consolidation problems occur on the processing of many powder materials, influencing the part density, mechanical properties and final quality, therefore limiting the materials processed by SLS. The materials processed by SLS can be waxes, polymers, metals and composites. Since polymers and PMCs are the main focus of this work, a discussion on the SLS processing of polymers, polymer matrix composites and nanocomposites is given in the next sub-headings.

2.3.3.1 Laser Sintering of PA12

Polymers were the first and are still the most applied materials in SLS. On the other hand, only a few powder materials are available on the market, and most of these materials (95 %) are based on polyamide 12 (PA12), i.e., a typical nylon grade is easy processable by SLS (KRUTH et al., 2008). Research is being carried out in new materials and materials such as PEEK and Polystyrene are appearing, but to date none of them has achieved the success of PA12. This limited success of using other materials in SLS is generally ascribed to a complex combination of materials properties and material-laser-interaction properties that must be fulfilled in order to turn a polymer into an SLS processable polymer powder.

The requirements necessary for polymer powders processed by SLS are very stringent and are a reason for the limited availability of commercial powders for SLS. As explained above, PA12 is the most successfully applied powder in the SLS market and the reason for this is a combination of historical reasons and because of important properties of PA12 that make this material suitable for SLS processing. One of these properties is related to the sintering window of PA12 for SLS purposes. The PA12 developed for SLS presents a wide gap between melting and crystallization. This is done intentionally for SLS, since PA12 for injection molding purposes does not present such stretched gap. The shift of the melting point to higher values and the crystallization point to lower values are also provoked in order to diminish the effect of a second heating run of the material, very common during SLS processing (KRUTH et al., 2008).

SLS of PA12 is also favoured by its particle shape and size distribution. LS PA12 presents a potato shape particles, which favours flowability of the powders and as a consequence improves the densification during processing. The molecular structure of SLS PA12 also plays an important role in the process. To obtain the PA12 powder the chemical reaction ends up in the polymer chain forming well defined end-groups, usually one carboxylic group (COOH) and one amide group (-NH2). This open structure with unblocked chain ends combined with the nitrogen atmosphere of the chamber creates ideal conditions for solid state condensation reaction, and the polymer chain ends have enough time to meet reaction partner by molecular movement. This provokes an increase on the molecular weight of the polymer chain, which results in increased mechanical properties and interlayer bonding. Unfortunately this reaction also occurs in nonsintered particles on the chamber, which increases their melt viscosity and can have effect on further processing, compromising surface quality (SCHMID; AMADO; WEGENER, 2014).

Laser sintering consolidation mechanism of PA12 has been studied considering all aspects described before. Dupin et al. (2012) studied pore distribution and amount of unmolten particles during laser sintering of PA12 at different energy densities and found a great influence of energy density on pore morphology and amount of nascent particles. Stichel et al. (2017) and Stichel et al. (2018) conducted a similar work but using a

Round Robin methodology. The authors observed a correlation of highest ductility of PA12 samples with low pore concentration, absence of coplanar pores and high degree of particle melting. Schmid et al. (2017) studied different PA12 powder systems with pronounced powder characteristics. The authors investigated powder differences based on particle size distribution, thermal analysis, XRD, mechanical analysis and melt volume rate. It was found a high influence of the powder characteristics such as particle shape, sintering window, powder distribution and chain termination on mechanical properties and surface roughness. A similar study was performed by Verbelen et al. (2016) with extended research to PA11 and PA6. Crystallization behavior of PA12 during SLS was studied in more detail by other authors, who found that partial melting of PA12 is the main mechanism occurring during SLS, with a full melting of the particles surfaces and unmolten particle core. The authors observed a correlation of mechanical properties with crystal fraction, where improved elongation at break was achieved with decreasing crystal fraction of PA12 (ZARRINGHALAM et al., 2006; MAJEWSKI; ZARRINGHALAM; HOPKINSON, 2008; GRIESSBACH; LACH; GRELLMANN, 2010).

SLS parameters are generally related to the energy delivered to the powder bed and influence important quality factors such as the geometrical, surface and mechanical properties of parts produced. Work has been dedicated to study the influence of the energy density on mechanical properties. Caulfield, McHugh & Lohfeld (2007) studied the influence of energy density and build orientation on mechanical properties of PA12. The authors used a DTM Sinterisation machine with increasingly laser power inputs and found a positive correlation of laser power with mechanical properties, although an optimum energy input was found.

In a more extensive study, Wegner & Witt (2012) used response surface modelling to study the effect of laser speed, laser power, scan line spacing, pre-heating temperature and layer thickness on density and tensile properties of PA12 parts. The authors also observed an optimal energy input existing to result in best mechanical properties. Based on sensitivity analysis, laser power was found to have lowest influence on mechanical properties, whereas layer thickness and scan line spacing resulted in highest influence.

Usher, Gornet & Starr (2013) studied the influence of build orientation and laser sintering parameters on yield streght and elongation at break of PA12 samples processed by SLS. A fractional factorial design with 2 levels was employed and the results modelled with a non-linear regression model based on Weibull-growth modelling to predict the response variables based on energy density. The authors found very good model quality for both output variables chosen and a high influence of part build orientation and energy density on mechanical properties.

Hofland, Baran & Wismeijer (2017) used a fractional factorial design to investigate the influence of individual laser sintering parameters on density and tensile properties of PA12. The authors used response surface modelling to study the effect of laser speed, laser power, scan line spacing, pre-heating temperature and layer thickness. The fractional factorial design used 5 variables with 2 levels each. Sensitivity analyses showed that the most important process variables were scan spacing and layer thickness, followed by laser speed, pre-heating temperature and laser power.

The previous studies provide interesting results for both influence of energy density and individual laser sintering parameters. Nevertheless, previous works conducted were approached based on response surface modelling using fractional factorial design space coverage, which normally gives poor design space coverage for more in depth studied on response surface modelling of individual laser sintering parameters. For instance, fractional factorial design involves two or three levels variations for each input variable, which for sensitivity purposes may be adequate but for modelling purposes may result in poor model quality, specially at input points away from the ones defined in the design space.

2.3.3.2 Laser Sintering of other polymers

As described before, most of the polymers available for SLS process are based on polyamides (PA12 and PA11). Nevertheless new materials are being launched as the challenging requirements for the powders are met. Examples include polystyrene and PEEK, recently released by Electro Optical System (EOS) and also a thermoplastic elastomer released by Advanced Laser Materials (ALM).

Increasing research is being carried out to increase the range of polymer materials available for SLS. Most of this research is focused on polyamide-based materials, blends or reinforced with other materials or nanofillers. However, few works are being conducted in new polymers. Polyoxymethylene (POM) powders were successfully produced by cryogenically milling, with mechanical properties and surface quality even superior to commercial PA12 (PA2200 from EOS) (RIETZEL; WENDEL; FEULNER, 2008). Research on high temperature laser sintering of PEK showed a good repeatability of manufacturing, low porosity and good bonding between the layers (GHITA et al., 2014).

The SLS of amorphous polymers like polycarbonate and Bish-phenol-A polycarbonate (NELSON et al., 1993) produces parts with very good dimensional accuracy and surface finish, although they cannot be used as functional parts due to the only partially consolidation of the powder particles caused by their lower flow and sintering rate. Due to their shrinkage characteristics during SLS, these materials have potential in the SLS of patterns for producing molds. Interesting works on the SLS of polycarbonate are the works of Berzins, Childs & Ryder (1996) and Ho, Cheung & Gibson (2002).

Leite et al. (2010) studied the SLS of amorphous polymers, polystyrene and PMMA blends. The authors observed a high porosity of the samples, suggesting the tissue engineering and drug delivery as potential applications for the material.

An increasing field of application is the use of polymers in medical applications. Goodridge, Hague & Tuck (2010) conducted a research on the SLS of ultra-high molecular weight polyethylene (UHMWPE), evaluating the effect of various sintering parameters. The authors claimed a successful production of parts with the material, however a very small processing window for the material was observed, limiting the commercial use of it.

Laser sintering focusing on non-load bearing medical applications such as tissue engineering (TE) are gaining increasing attention. Particularly challenging is the choice of adequate biomaterials that are capable of meet the TE requirements and also the geometry complexity associated with the manufacturing of scaffolds (TAN et al., 2005). The last aspect ranks AM and SLS as promising in the automated manufacturing of scaffolds. Water-soluble and non-biodegradable biocompatible polymers are being researched. Water soluble biopolymers include polyvinyl alcohol (PVA) (SHUAI et al., 2013), poly-ε-caprolactone (PCL) (YEONG et al., 2010), poly(L-lactide) (PLLA) (ZHOU et al., 2008) and poly(L-lactide-co-glycolide) (PLGA) (SIMPSON et al., 2008). Non-biodegradable polymers include PEEK (TAN et al., 2005) and polyethylene (HAO et al., 2006).

2.3.3.3 Laser Sintering of Polymer Matrix Composites and Nanocomposites

Laser sintering of polymer matrix composite materials is based on the rationale of combining two or more materials to improve properties unachievable by the single materials. The most common method to produce composites by SLS is the combination of matrix and reinforcement powders. Since continuous fibers raise problems in SLS manufacturing due to the formation of a non-smooth powder bed, reinforcement powders are generally used in particulate form or in the form of small sized fibers. The combination of powders can be made by simply mixing the matrix and reinforcing powder or using a single composite powder, which helps overcome problems associated with non-uniform mixing of powders, yielding a uniform spread of composite components.

The physical aspects involved during SLS of composites are similar to the ones described for polymers. The consolidation mechanism associated is liquid phase sintering (LPS), where the matrix phase is melted while the reinforcement phase remains solid (KUMAR; KRUTH, 2010).

Commercial examples of composite materials used in SLS are glass-filled polyamide 12 (EOS PA 3200 GF and 3D Systems Duraform GF), aluminum-filled polyamide 12 (EOS Alumide and 3D Systems Duraform AF) and short carbon fiber filled polyamide 12 (EOS CarbonMide). These materials consist of single composite powders, with each particle being composed of matrix and reinforcing material.

Many attempts have been made to improve the mechanical properties of polymer laser sintered parts by reinforcing them with micron-sized inorganic fillers (GOODRIDGE; TUCK; HAGUE, 2012), most of these works focusing on reinforcing PA12 or PA11. The work of Burning (1998), combined PA12 with copper particles by standard mixing to produce composites via SLS. The author found interlayer segregation phenomena due to differences in particle weight and size, creating mechanical defects on the samples and compromising strength of the material. In contrast, the direct mixing of Al with PA12 to produce composite parts, resulted in accurate parts and with increased mechanical strength compared to pure PA12 (MAZZOLI; MORICONI; PAURI, 2007).

Hon & Gill (2003) produced composite parts by SLS using a powder mixture of SiC and PA12 and performed an investigation on the effect of sintering parameters. They found a strong relation between sintering parameters and tensile strength, and also a strong sensitivity of the system to the PA12 content.

Recently Guo, Jiang & Bourell (2014) developed a new type of composite material based on PA12 and limestone for SLS processing. The authors mechanically mixed the powders at different ratios of filler/matrix and studies the effect of sintering parameters such as pre-heating and laser power. They observed an uniform dispersion of the limestone material on the matrix and also an increase in the mechanical strength of the material in comparison to pure PA12. Increased laser powder improved the mechanical properties and part bed temperature had a significant influence on the processing, with lower temperatures showing curling of the part and higher temperatures showing caking.

Also using direct mixing, Aldahsh (2011) combined PA12 and cement to fabricate composite parts by SLS. The author found that the addition of cement, under right SLS processing conditions, produced parts with increased mechanical properties than pure PA12, although with reduced impact strength. Parts with good surface quality were achieved for a ratio of 30 wt.% of cement.

Other matrix materials were used to fabricate PMCs by SLS. For instance, the work of Fan, Cheung & Gibson (2008), used acrylic-styrene copolymer (TrueForm from 3D Systems) as matrix and silicon dioxide powder as filler to prepare composite powders via dry mixing and melt extrusion processes. The authors studied different particle sizes of SiO_2 powder and also surface treatment methods on the filler such as silane. The volume fraction of SiO_2 used was 30 vol.%. The authors used an engraving laser machine instead of a commercial SLS, therefore all experiments were conducted on ambient conditions. The authors found that reducing the particle size of the filler had a negative effect on the sintering behavior of the material, resulting in weaker parts. The surface treatment used slightly improved the strength of the material. The blending methods applied had a significant effect on the sintering behavior of the material, with the melt blending technique generating a better contact between polymer and ceramic particles, but the increase in viscosity of the blend resulted in poor densification.

Ho, Cheung & Gibson (2002) studied the effect of adding graphite on the laser sintering behavior of polycarbonate. The authors blended the graphite and PC and evaluated the effect of the temperature distribution on the processing chamber. They found that the surface temperature was greatly increased by the addition of small amounts of graphite, addressing this behavior to the higher laser absorption of the graphite material.

Laser sintering is also a promising technology for the fabrication of scaffolds for tissue engineering, as it promotes design flexibility, the customization of the pore structure of the scaffold and reproducibility. The use of biocompatible composites in scaffold fabrication is increasing and involves the use of biodegradable or bioinert materials. In particular biodegradable materials present interesting properties in implant for tissue engineering as they eliminate the need of second surgery for removing implants and improve the match of the mechanical properties between bone and implants. Most composites fabricated by SLS for tissue engineering applications uses hydroxyapatite (HA) as the filler as this material has properties very similar to bone and improves the osteoconductivity of the biocomposite. SLS of composites with HA include PEEK/HA (TAN et al., 2003), PVA/HA (CHUA et al., 2004), PLLA/HA (ZHOU et al., 2008), PCL/HA (WIRIA et al., 2007), PLG/HA (SIMPSON et al., 2008), PE/HA (ZHANG et al., 2008), PA/HA (SAVALANI, 2006) and HDPE/HA (HAO et al., 2006).

The SLS of carbon fibers reinforced PA12 composites have recently received attention by research community. Yan et al. (2011) prepared carbon fibers by surface modification in order to improve interface adhesion with PA12 and further mixing CF with PA12 by dissolution-precipitation method. Mechanical properties were greatly enhanced by the preparation method when compared to pure PA12. More recently, carbon fiber surface modification via HNO3 treatment was performed to improve adhesion with PA12 via direct mixing (JING et al., 2017). Improved mechanical properties were obtained after surface modification of CFs but only when treated in nitrogen atmosphere. Porosity of mechanically mixed PA12-CF samples manufactured in different building directions was studied by means of computed tomography (JANSSON; PEJRYD, 2016). Highly porous structures were observed, concentrated between the layers manufactured, leading to highly anisotropic mechanical properties. Fracture mechanism of PA12-CF material processed by SLS was recently studied (LIU et al., 2019). Crack growth was found to initiate at the interface between carbon fiber and PA12.

2.3.3.4 Laser Sintering of Polymer Matrix Nanocomposites

The addition of nanomaterials in AM and SLS is a recent field of research which has the potential for the creation of a new class of composite materials with unique properties. Limited research has been carried out in combining SLS with nanomaterials, but the literature published so far reports that the introduction of nanostructures such as carbon nanotubes and ceramic nanoparticles can significantly improve the sintering behavior and properties of parts manufactured (IVANOVA; WILLIAMS; CAMPBELL, 2013). The main advantage of combining SLS and nanocomposites is that the addition of very small amounts of nanofillers can have a significant improvement on the properties of the composites, as nanofillers have a very high surface to volume ratio and also in some cases the high aspect ratio (GOODRIDGE; TUCK; HAGUE, 2012).

Kim & Creasy (2004) evaluated the thermal and rheological behavior of nanoclay reinforced PA6 nanocomposites for use in SLS. The authors found that the addition of nanoclay increases the melting point of the material as well as its viscosity. The authors also observed that the addition of nanoclay reduces the crystallization peak width during the DSC experiments. The authors concluded that the pre heating temperature during SLS of nanoclay PA6 composites may require higher pre heating temperature and laser power than pure PA6 powder for SLS processing. As a final remark the authors stated that high nanoclay contents in the nanocomposite may not be applicable for SLS because of its low final density.

Wang, Shi & Huang (2005) used organically modified rectorite (OREC, which is a different kind of nanoclay) and PA12 to produce nanocomposites by SLS. The authors used mechanical mixing to generate the powder systems (pure PA12; PA12-2.5 wt.% OREC and PA12-5 wt.% OREC) and evaluated the thermal behavior of the powder using DSC analysis and also measured mechanical properties such as tensile and flexural strength and impact resistance. The authors found that the addition of rectorite increased the crystallization temperature of PA12 and narrowed the width of the crystalline peak. Tensile and flexural strength was improved by the addition of the nanofiller and less laser power was required to achieve enhanced mechanical properties.

Jain, Pandey & Rao (2009) performed an experimental investigation on the laser sintering of PA and nanoclay. The authors used surface modified nanoclay (montmorillonite) as the nanofiller and PA12 as polymer matrix and mechanically mixed the powders. The authors studied different powder blends without nanoclay, with 2 and 5 wt.% of nanoclay and used Taguchi Orthogonal array analysis as DOE method to study the influence of the SLS parameters with minimum experiments. The authors observed that the nanoclay was not uniformly dispersed in the polymer matrix, forming agglomeration of particles and hindering the formation of a nanocomposite. Mechanical properties were also deteriorated at increasing filler content.

Athreya, Kalaitzidou & Das (2010) used nanosized carbon black powder and PA12 for SLS. The authors used zirconia grinding media to ball mill the carbon black pellets in a rotary tumbler and sieved the ball-milled carbon black using a mesh of 106 μm opening. The sieved carbon black was mixed with the PA12 in a rotary tumbler for 24h. The SLS parameters varied were laser power and laser scan speed, with the remaining parameters kept constant. The authors used characterization techniques such as SEM and XRD to evaluate the morphology and crystallinity of the samples produced, DSC for thermal analysis and UTS machine to evaluate the mechanical properties. The nanocomposite produced presented crystallization characteristics similar to the pure PA12. SEM analysis showed segregation of the carbon black on the polymer matrix, which was credited to decrease the mechanical properties of the nanocomposite in comparison to the pure PA12 processed by the same method. Electrical conductivity was improved by a factor of 5 with the addition of carbon black.

Carbon nanofibers were also used as filler for PA12 (GOODRIDGE et al., 2011). The authors used 3 wt.% of carbon nanofibers and prepared nanocomposite powders using melt-mixing and cryogenic milling techniques. For comparison, the same melt mixing technique was applied to produce PA12 powders and also as supplied PA12 was used as reference. Mechanical analysis of the parts produced was carried out. The authors found that the as supplied PA12 had the highest modulus and the addition of carbon nanofibers in the matrix increased in 22 % the modulus when compared to melt-mixed PA12. The authors observed that the decrease in the properties of the nanocomposite in comparison to as supplied PA12 was due to the cryogenic milling process applied, which produced powders with not suitable morphology for SLS processing. Therefore alternative processing methods for powder manufacturing were considered as necessary to explore the potential of these nanocomposites.

Nylon 11 (PA11) was reinforced with silica nanoparticles to produce functionally graded materials with SLS (CHUNG; DAS, 2008). The powders were mixed in a rotary tumbler at varying silica contents, ranging from 2 vol.% up to 10 vol.%. To optimize the SLS parameter a two level factorial design of experiments (DOE) was adopted. The output variable was density. Microstructure of the samples produced were evaluated by TEM and tensile and compressive strength were measured. The optimization of the SLS variables led to a part density of >90 % for different silica contents. Tensile modulus also increased with increasing silica loads but the materials also became more brittle.

Wahab et al. (2010) used different approaches to produce nanocomposite powders for SLS. In their study, solution blending followed by spray drying process were applied. The matrix used was PA6. Two different reinforcements were used: Hectorite clay and yttrium stabilized zirconia (YSZ). The spray drying process involved the atomization of the solution containing the matrix and the nanofillers followed by drying with hot air in a drying chamber. Different solution concentrations were applied to evaluate its effect on the powder formation. The authors could procedure nearly spherical composite particles by the method for both reinforcing materials used. TEM observations showed an evenly distribution of the nanofiller on the matrix. SLS of the composite powder led to near full dense parts, but the mechanical properties of the parts was reduced in comparison to pure PA6 material. The authors ascribed this reduction to the spray drying process applied, as the sintered materials contained voids probably generated from the trapped gases of the residual solvent.

Koo et al. (2005) conducted a research to improve PA11 for SLS purposes. Three nanofiller were studied: chemically modified montmorillonite (MMT) clay, nanosilica and carbon nanofibers. The nanofillers were added to the PA11 powder by means of a melt blending process (extruder) and subsequently injection molded. Different contents of nanofillers were tested. The most suitable injection molded materials were then cryogenically ground into fine powders for SLS processing. TEM and SEM analysis were performed to evaluate interfacial aspects and morphology. After SLS processing the most suitable composite was PA11 filler with carbon nanofibers, whereas powder flow of the nylon 11 clay nanocomposites was not adequate, which led to a poor powder deposition and processing issues.

Bai et al. (2013) added multi walled carbon nanotubes on PA12 to manufacture nanocomposites by SLS. The authors claimed a new method to manufacture near spherical shape powders composed of PA12 and MWNCT. The effect of the addition of carbon nanotubes on the thermal and mechanical properties of PA12 was evaluated. The authors found that the CNT were uniformly dispersed on the polymer matrix. There was no apparent increase on the powder bed temperature with the addition of CNT and the processing of the nanocomposite powder by SLS occurred smoothly. Thermal conductivity increased slightly with the addition of CNT, whereas significant improvements were achieved in dimensional stability of the part. An increase in 44.5 % on tensile modulus and 7 % in tensile strength was observed with the addition of CNT.

In more recent studies, Bai et al. (2014a), evaluated the nanostrucural characteristics of SLS carbon nanotubes reinforced PA12 by 3D-TEM.The 3D imaged obtained by the characterization technique revealed that the CNTs were agglomerate free in the PA-CNT parts. In another study at the same year the authors studied the rheological properties of CNTs reinforced polyamide manufactured by SLS (BAI et al., 2014b). The authors used dynamic oscillatory shear tests to measure the rheology of the pure PA12 and CNT-PA12 powders.

Also using PA12 as matrix, Yang, Shi & Yan (2010) proposed a new method for preparing PA12 reinforced with titanium potassium titanium whiskers (PTW) for SLS processing. The method included a dissolution-precipitation process where the PA12 and PTWs were added to a high pressure reactor together with a solvent and additives. The mixture was stirred when the temperature was 150 °C and then cooled down until 105 °C, until the PA12 started to precipitate. The resulting PTWs-filled PA12 powder was then mechanically mixed with PA12 powder at different contents (10, 20 and 30 wt.% of PTWs filled PA12).The powders were then processed in a SLS machine Morphological, mechanical and thermal properties of the powders were evaluated. For comparison, glass filed PA12 were also processed by SLS and their mechanical properties were evaluated. Results showed that the particles had a spherical shape with an narrow particle distribution centered at an average particle size of 36.7 μm (10 wt.% of PTWs). Higher amounts of PTWs led to t uniform particle distributions. DSC results showed little modification on the melting and crystallization temperatures with the addition of PTWs on PA12. Mechanical properties were significantly improved. For instance, using 20 wt.% of PTWs increased the tensile strength, bending strength and bending modulus by 55, 118 and 158 % respectively, in comparison to pure PA12.

Besides PA12 and PA11, polystyrene PS was used as matrix for nanocomposites applications, as reported in the work of Zheng et al. (2006). The authors used nano-Al2O$_3$ particles coated with PS by emulsion polymerization. The authors compared the sintering behavior and mechanical properties of PS coated particles with uncoated particles, obtained by direct mixing of PS with 5 wt.% of nano-Al2O$_3$, and pure PS. It was found that the coated nano-alumina powders had a more even dispersion on the matrix when compared to uncoated particles. In addition, the absorptance of the powder system improved with the use of coated nanofillers, which promoted a better adhesion of the filler on the matrix. At last the authors the addition of nanofillers on the matrix promoted toughening and strengthening of the PS.

2.4 Summary and present work contribution

Considering the aforementioned literature review, laser sintering of PA12 is a well known topic to the scientific community and extensive research has been conducted to investigate different aspects of PA12 consolidation during SLS and influence of energy density on density and mechanical properties. Nevertheless, few studies have been conducted so far on modelling of individual laser sintering parameters on important quality variables such as dimensional accuracy, surface and mechanical properties. Also the work previously conducted is based on fractional factorial design space which gives poor space coverage for modelling purposes and does not give a complete picture on the behavior of output parameters based on variation of laser sintering input parameters. This is therefore the main contribution of this work for PA12, to perform an in depth investigation on modelling of individual laser sintering parameters on the most relevant quality criteria for laser sintering of PA12 and also perform optimization tasks considering the frequently conflicting criteria that needs to be met when producing a SLS part.

From the literature review on SLS of polymer composites and more specifically on SLS of PA12-CF, most of the research carried out so far in laser sintering of PA12-CF materials was focused on material aspects, without taking into consideration the influence of laser sintering parameters on quality properties. To the authors knowledge, no research has been conducted to investigate the effect of laser sintering parameters which influence the energy density delivered to the powder bed. Additionally and consequently, there is no modelling of the individual laser sintering parameters existing. Therefore, the goal of this research study is to investigate the influence of energy density on important quality criteria such as surface properties, dimensional accuracy, density and mechanical properties. Also the modelling and optimization of individual laser sintering parameters is performed for the first time for PA12-CF. More details on the methodology applied to achieve these goals are given in Chapter 3.

3 Methodology and Experimental Approach

This chapter presents the methodology and experimental approach used in this work for the laser sintering investigation of PA12 and PA12-CF. A systematic framework was developed aiming a better orientation during the research. It starts with a description of the materials selected for the investigation, followed by the laser sintering approach to manufacture the samples, DOE technique applied, modelling technique used for response surface analysis and optimization method used. At last, properties measurement and characterization details are presented.

3.1 Overview

A systematic framework shown in Fig. 3.1 was created to provide an overview of the main steps associated with the laser sintering investigation. The framework started with materials selection used to perform the investigation. To perform the laser sintering trials, a Design of Experiments (DOE) approach was followed to include the main laser sintering process input variables and reduce the number of experiments necessary. The next step involved measurement of output data selected for further evaluation, including dimensional analysis, surface roughness measurements, mechanical properties, density and manufacturing time. The framework is then divided in two mains parts: one involving an investigation on the influence of energy density on the output parameters measured including here a further characterization of the materials employed to evaluate microstrcture and crystallisation behavior of the materials; the other part involves the response surface modelling of the input and output variables using for the first time in SLS applications a method based on supervised learning regression analysis and further multi-objective optimization using a stochastic method. A detailed description of the experimental methodology is given in the next sections.

3.2 Materials

Two materials were chosen to manufacture the laser sintered specimens: standard PA2200 material (PA12) and a composite material based on PA-12 and carbon black, commercially known as Carbon Mide (PA12-CF)(EOS, 2020).

PA12 is a nylon graded polymer white powder well known in AM and SLS because of its favorable properties to be processed by SLS. Some properties of PA12 taken from the manufacturer's datasheet are shown in Table 3.1 (EOS, 2020). Its tensile strength and modulus are comparable to their injection molded counterparts, whereas the elongation

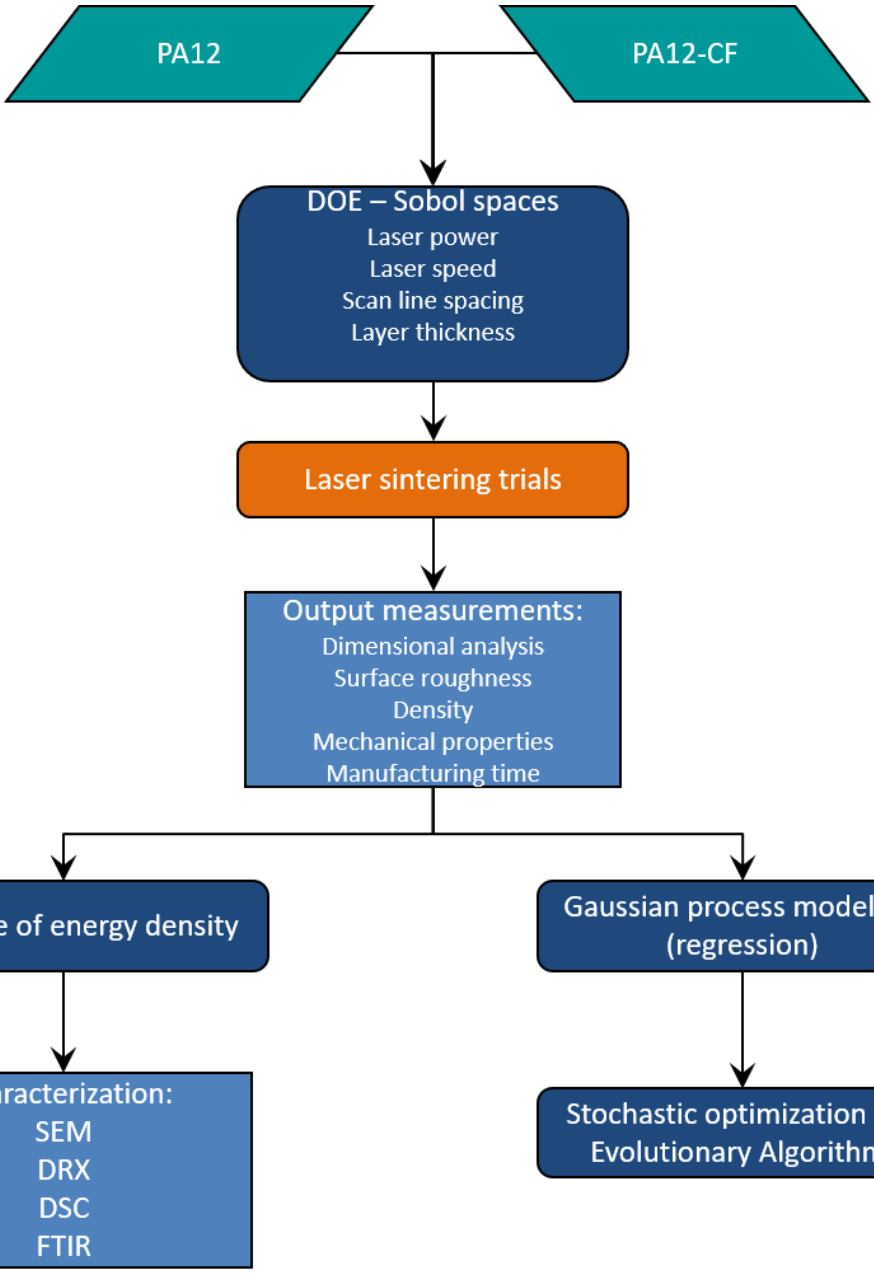

Figure 3.1 – Framework developed for laser sintering investigation.

at break is still inferior. Due to the layer-by-layer nature of the additive manufacturing process, the mechanical properties of the parts manufactured by LS are non-isotropic. Figure 3.2a-b shows SEM images of PA12 powder at 200x and 1000x magnification. PA12 powder particles present a "potato" shaped morphology, which contributes to powder spreading during LS process.

The other material chosen to perform the experiments is commercially known as Carbon Mide (PA12-CF), a composite material composed by anthracite black carbon fiber reinforced PA12. Figure 3.2c-d shows SEM images of PA12-CF powder at 200x and 1000x magnification. PA12 particle shape is the same as described before, whereas carbon fiber has a "stick" morphology, presenting a high aspect ratio.

Table 3.1 – Properties of LS materials (EOS, 2020).

Property	PA2200 (PA12)	Carbon Mide (PA12-CF)
Tensile Modulus X Direction (MPa)	1650	6100
Tensile Modulus Y Direction (MPa)	1650	3400
Tensile Modulus Z Direction (MPa)	1650	2200
Tensile Strength X Direction (MPa)	48	72
Tensile Strength Y Direction (MPa)	48	56
Tensile Strength Z Direction (MPa)	42	25
Elongation at brake X Direction (%)	18	4.1
Elongation at brake Y Direction (%)	18	6.3
Elongation at brake Z Direction (%)	4	1.3

Its properties are presented in table 3.1. This material was chosen due to its improved stiffness and strength-to-weight ratio properties, which can be valuable for the manufacturing of load bearing applications. Compared to PA12, PA12-CF has superior modulus in all directions and tensile strength in two directions, whereas its elongation at break is considerably lower than PA12 in all directions. The process related orientation of the fibers make the PA12-CF powder more anisotropic than the PA12 powder.

3.3 Laser sintering and DOE

To perform the experiments, an EOS P396 laser sintering machine was used, equipped with a 70 W continuous wave Gaussian CO_2 laser (wavelength 10.6 μm). To produce the LS samples for modelling and optimization, standard type I dumbbell shaped (165 x 19 x 3.2 mm) (ASTM Standard D638-02a, 2002) and rectangular flexion bar (127 x 12.7 x 3.2 mm) (ASTM Standard D790-02, 2002) samples were manufactured. All samples were positioned in the building platform in X direction (same direction as recoater blade moving direction). Figure 3.3 shows the parts positioning in the building platform of EOS P396.

To evaluate the influence of the main SLS parameters (laser power, laser scan speed, scan line spacing, layer thickness) a Design of Experiments (DOE) approach was adopted. In order to get a good compromise between number of experiments and number of input variables a space filling DOE was adopted. Space filling DOE techniques are based on quasi-random number generators, which are a mathematical series of generating sets of numbers which are able to pass randomness tests. One main advantage of space filling DOE techniques is the flexibility to use the design space and chose the number of experiments. In the present study the so called Sobol spaces were used, which is a base

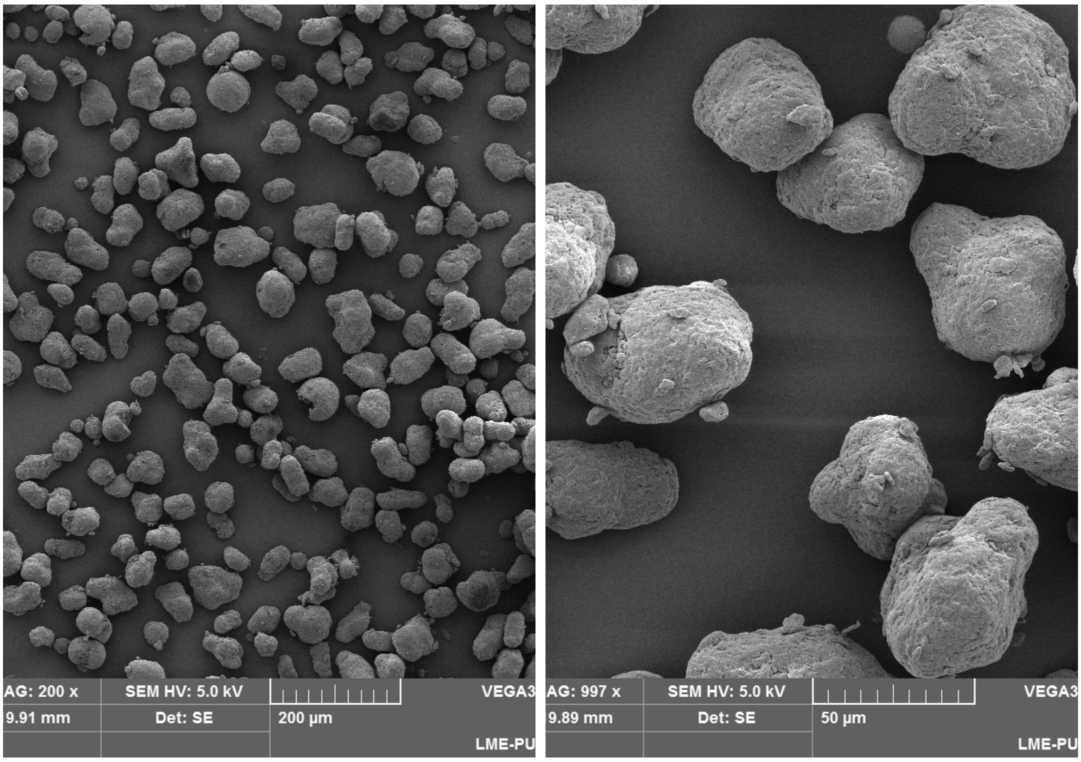

(a) PA12 x200 (b) PA12 x1000

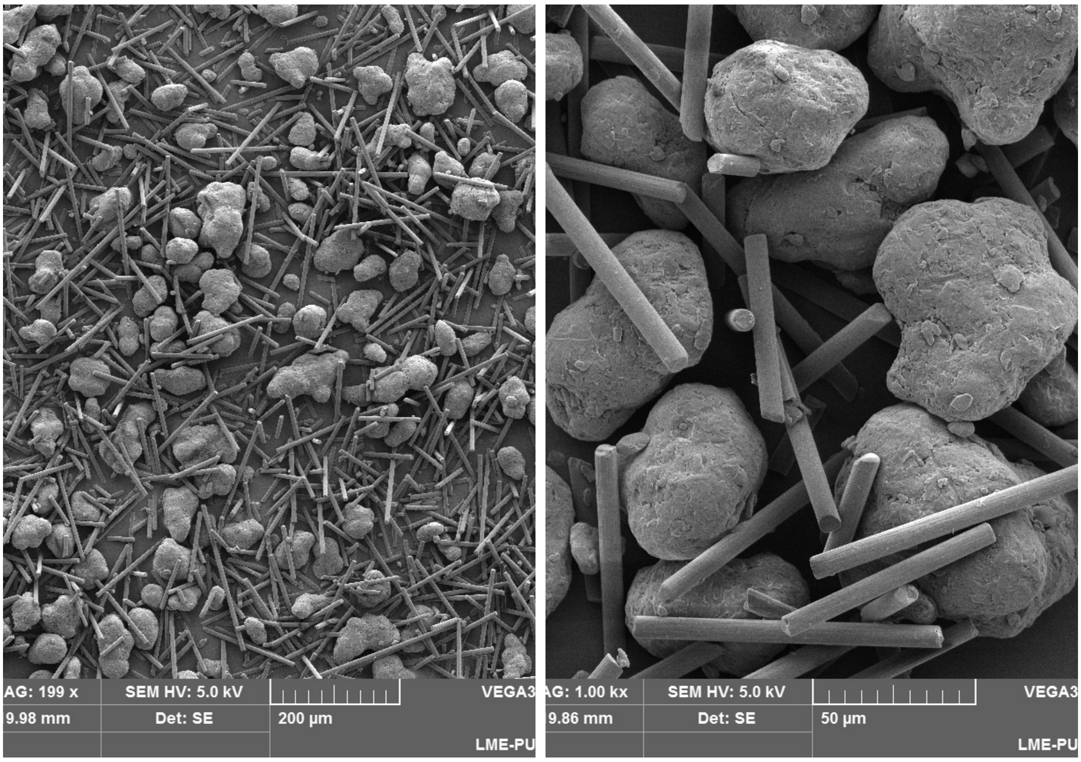

(c) PA12-CF x200 (d) PA12-CF x1000

Figure 3.2 – SEM images of PA12 and PA12-CF.

2 digital sequence that provide a highly uniform space coverage and flexible number of experiments. (CAVAZZUTI, 2013).

Using this methodology, for PA12 laser power was varied from 30-45 W, laser

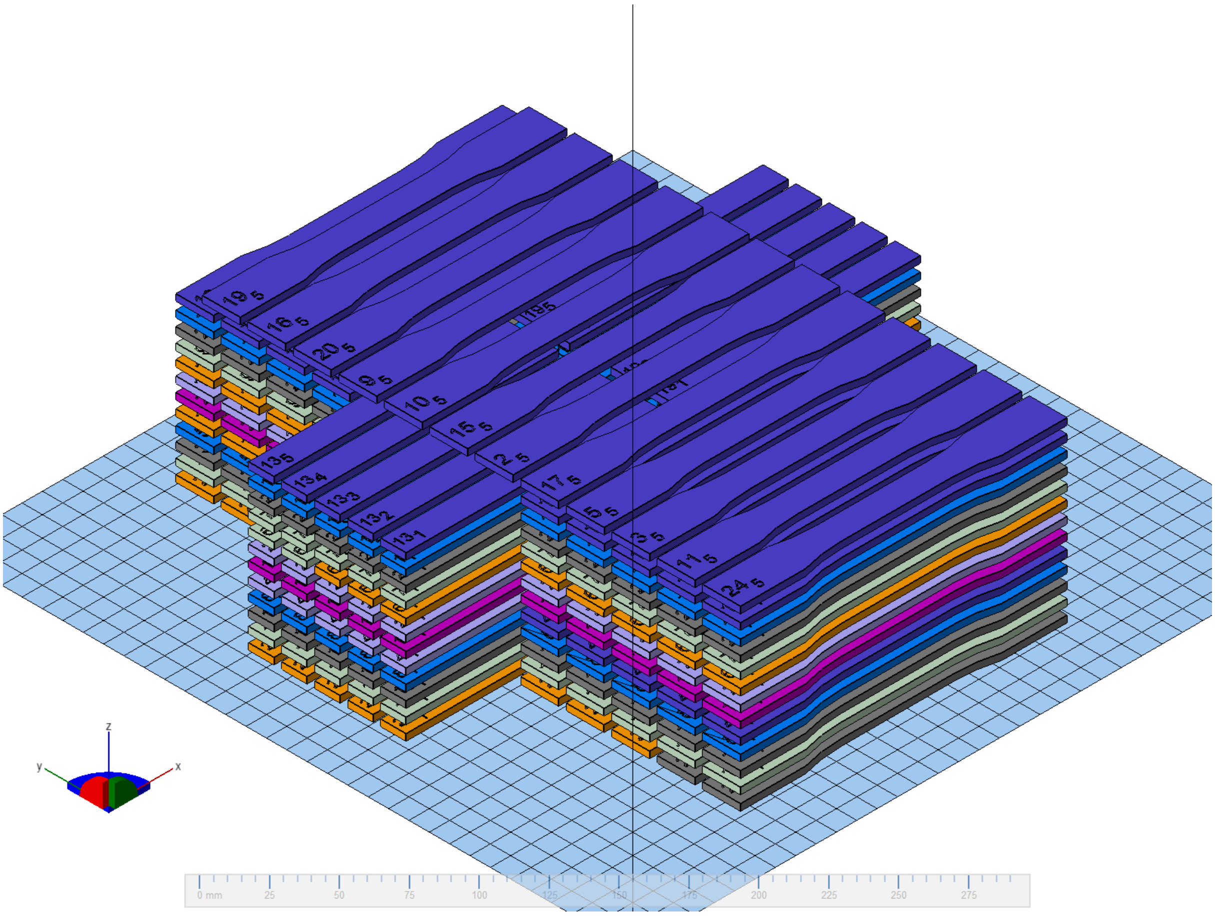

Figure 3.3 – Samples orientation in building platform.

scan speed from 2000-5000 mm/s and scan line spacing from 0.2-0.6 mm. Two layer thickness were evaluated, 120 and 150 μm. Figure 3.4 shows the experiment space covered by Sobol space DOE for PA12 considering the main input variables. The design space has 45 experiments, with each experiment giving a different combination of laser sintering parameter set generated by Sobol sequence.

Figure 3.5 provides the DOE design space coverage for PA12-CF. For PA12-CF laser power was varied from 25-43 W, laser scan speed from 1500-5000 mm/s and scan line spacing from 0.2-0.6 mm. The design space consists of 24 experiments. Main difference between PA12 and PA12-CF DOE relies on the layer thickness parameter which was kept fixed at 150 μm for PA12-CF and the the laser sintering parameters range which applied lower laser power and laser speed range for PA12-CF compared to PA12. Additionally DOE for PA12-CF uses less experiments as it has less input dimensions (3 dimensions) compared to PA12 (4 dimensions). Pre-heating temperature was kept constant at 173 ° for PA12 and at 178 °C for PA12-CF for all DOE trials performed.

For each parameter set 5 repetition points were performed (i.e., 5 samples were manufactured to perform measurements of the response variables). A total of 340 samples for PA12 and 240 samples for PA12-CF were manufactured to perform the DOE measurements.

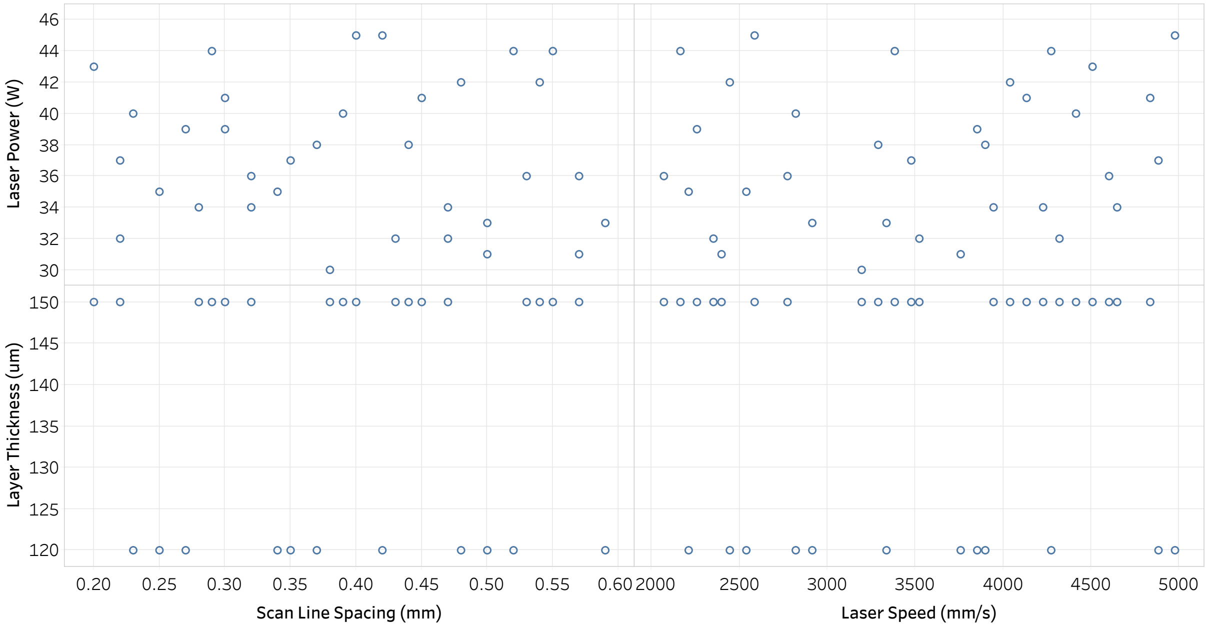

Figure 3.4 – Sobol space filling DOE for PA12.

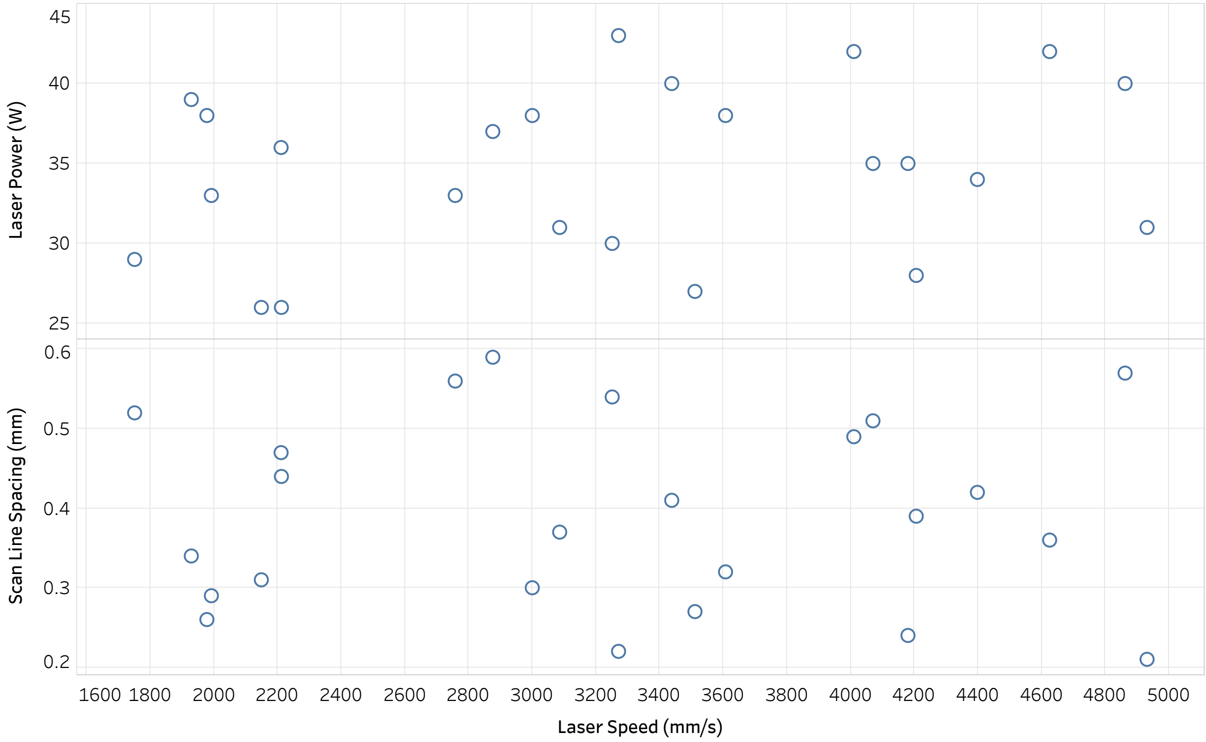

Figure 3.5 – Sobol space filling DOE for PA12-CF.

The main goal of the DOE is to give a robust design space for further modelling of individual laser sintering parameters influence and multi-criteria optimization.

3.4 Energy density influence on output variables

Energy density provides the influence of the main laser sintering parameters combined in one grouped variable. The combination of laser power, laser scan speed, scan line spacing and layer thickness gives an indication of the volumetric energy per unit of single processing track:

$$\psi = \frac{P}{vhw} \tag{3.1}$$

Applying the energy density formula to the DOE variables studied the resulting energy density range for PA12 is 0.091-0.528 J/mm^3 and 0.096-0.493 J/mm^3 for PA12-CF. Important to notice that such high energy density variation is being used for the first time for PA12 and there are no investigations still performed for PA12-CF considering energy density influence, which provides novelty to the study performed using the composite material.

Influence of energy density was evaluated for the following output variables.

- X-direction dimensional accuracy
- Y-direction dimensional accuracy
- Z-direction dimensional accuracy
- Apparent density
- Surface roughness (R_a, R_z, R_y, R_q)
- Tensile strength and nominal strain at Yield
- Tensile strength and nominal strain at Break
- Tensile strength and nominal strain at Proportional limit
- Tensile strength and nominal strain at 0.2 % Offset Yield Strength
- Elastic Modulus
- Flexural strength and nominal strain at Yield
- Flexural strength and nominal strain at Proportional limit
- Flexural strength and nominal strain at 0.2 % Offset Yield Strength
- Flexural modulus

3.5 Gaussian process modelling of laser sintering parameters and outputs

Combined to DOE and to model the influence of the input variables on response variables, Response Surface Modelling (RSM) was adopted. The goal is to use the results from DOE run in order to create an empirical model of the response variables over the design space. In a more general way, this approach concerns supervised learning, which consists of learning the mapping between input and output variables from empirical data (training data). RSM (or supervised learning) can be very useful to predict the behaviour of response variables and provide a set of parameters yielding optimal response.

A training set D is defined as a sequence of n observations, $D = (\boldsymbol{x}_i, y_i) \mid i = 1, ..., n$, where $\boldsymbol{x}_i$ refers to the input vector (covariates) of dimension D and y is the scalar output. The collection of inputs for n cases are aggregated in the D x n design matrix $\boldsymbol{X}$ and the outputs are collected in the vector $\boldsymbol{y}$. In RSM the goal is to find the relationship between inputs and targets by means of a model described by $f(x)$, so that $y = f(x) + \varepsilon$, where f is the function value and ε is the error between observed values y and function values $f(x)$.

Traditional RSM methods include least square method and polynomial fit (linear, quadratic, cubic). Such methods make assumptions about the characteristics of the underlying function $f(x)$.For instance, if the behavior of the output at given inputs is linear, it is reasonable to assume a linear regression model. The main drawback of such approaches is the limited flexibility involved, as the prior assumption of the underlying function can give poor prediction results if the relationship between input and output cannot be reasonably approximated by the given function. Another approach is to give a prior probability to every possible function considered more likely. Although such approach may seem unrealistic due to the fact there are infinite sets of functions to be evaluated, this is precisely what the so called Gaussian Process ($\mathcal{GP}$) aims. Unlike polynomial methods, $\mathcal{GP}$ does not claim specific functions relating to the data, being a less parametric tool (RASMUSSEN; WILLIAMS, 2006). Given a training dataset (collection of inputs and outputs), a Gaussian Process will infer the most likely functions that pass through the observed data. This method uses no descriptive model based on physical processes, instead the model is deduced statistically from measured data only (CAVAZZUTI, 2013). $\mathcal{GP}$ can be described as a distribution over functions and inference taking place directly in the space of functions (RASMUSSEN; WILLIAMS, 2006).

Although less parametric than traditional methods, $\mathcal{GP}$ require some specification of the characteristics of the functions considered for inference. More specifically, Gaussian process is a collection of random variables which is described by its mean function $m(x)$

and covariance function $k(x, x')$. Gaussian process is defined by equation 3.2.

$$\begin{aligned} m(x) &= \mathbb{E}[f(x)] \\ k(x, x') &= \mathbb{E}[f(x) - m(x)(f(x') - m(x')] \\ f(x) &\sim \mathcal{GP}(m(x), k(x, x')) \end{aligned} \tag{3.2}$$

Random variables represent the value of function $f(x)$ at location x. Covariance function specifies the covariance between pairs of random variables. Covariance functions specify important properties of functions such as smoothness and stationarity.

This work proposes for the first time the use of Gaussian process ($\mathcal{GP}$) to perform the RSM of the SLS process variables. $\mathcal{GP}$ method is known to achieve good approximation of response surfaces and improved optimization results, being often used in machine learning tasks (RASMUSSEN; WILLIAMS, 2006). In addition, $\mathcal{GP}$ gives a good prediction of variance, which measures uncertainty of the model. The present work used as covariance function the squared exponential, which is known to give smoother models. The squared exponential covariance function is defined by equation 3.3.

$$cov(f(x), f(x')) = k(x, x') = exp(-\frac{1}{2l_c^2}(x - x')^2) \tag{3.3}$$

Where x and x' and neighbouring input values and $f(x)$ and $f(x')$ are the modelled outputs at the given input values. Parameter l is defined as the characteristic length-scale of the covariance function. This covariance function between outputs is described in terms of their respective inputs. It can be seen that the covariance function is close to unity at variables whose corresponding inputs are very close, decreasing as the distance between the inputs increases.

The response variables evaluated and modelled using $\mathcal{GP}$ are the ones described in subsection 3.4 with the addition of normalized manufacturing time. The $\mathcal{GP}$ modelling for laser sintering parameters used a Matlab implementation of $\mathcal{GP}$ models publicly available (RASMUSSEN, 2020).

The model quality for each response variable was evaluated by means of plots of prediction and measured data and statistical quality criteria such as Root Mean Square Error (RMSE) to check the absolute error measure and the coefficient of determination R^2 to check the relative error of the model and the model quality prediction. RMSE and R^2 are given by equations 3.4 and 3.5 respectively. For both measures the leave one out cross validation was applied, i.e. one point of the training data is left out, the model is trained and the error of the one data point which was not used in the model training is calculated.

This method provides a more robust analysis of the model quality when subjected to an unseen dataset.

$$RMSE = \sqrt{\frac{\sum_{i=1}^{n}(y_{i,pred} - y_{i,meas})^2}{n}} \tag{3.4}$$

$$R^2 = 1 - \frac{\sum_{i=1}^{n}(y_{i,pred} - y_{i,meas})^2}{\sum_{i=1}^{n}(y_{i,meas} - \overline{y})^2} \tag{3.5}$$

3.6 Optimization

The resulting RSM was further used to perform optimization tasks with distinct objectives. To perform the optimization tasks, Evolutionary Algorithm (EA) stochastic optimization was employed. EA aims at simulating the evolution of a population through successive generations of better performing individuals. By applying mutation operators on previous generations, a new generation is created, evaluated for fitness and selected. The steps are repeated until the termination criteria are achieved (STORN; KENNETH, 1997). The main steps in EA optimization are:

1. Initialization: a first population of individuals is randomly created.
2. Mutation: a mutant individual is created for each individual in the population.
3. Cross-over: the mutant individual is combined with its parent to create a trial individual.
4. Evaluation: the fitness of the trial individual is evaluated
5. Selection: the best between trial and parent individual are selected based on the fitness function and survive to the next generation.
6. Repetition: steps 2-5 are repeated until the desired number of iterations is achieved.

To perform the optimization tasks, multi-criteria optimization was employed. Unlike single criteria optimization, where only one objective function is to be minimized or maximized, multi-criteria optimization relies on optimization of two or more objective functions. The results are not a single optimum of the functions. Instead, due to conflicting objectives, the results of a multi-criteria optimization are solution sets representing a compromise (trade-off) between the objectives. These trade-off solutions are called Pareto Solutions.

The multi-criteria optimization considered mechanical properties, surface quality, dimensional accuracy and manufacturing time. Two objectives were optimized at once, while the others were kept at a limit (lower or upper hard limit) to reduce the number of Pareto Solutions. Lower hard limit implies that solutions achieved with values below this threshold are not considered in the optimization, whereas upper hard limit means no consideration of solutions with values above this threshold. The different scenarios considered in the multi-criteria optimization are summarized in Table 3.2 and 3.3.

Table 3.2 – Optimization criteria for PA12.

Criteria	Mechanical Properties	Surface Quality	Manufacturing Time	Dimensional Accuracy
1	Hard lower limit	Hard upper limit	Minimize	Maximize
2	Hard lower limit	Minimize	Minimize	Hard lower limit
3	Maximize	Hard upper limit	Minimize	Hard lower limit
4	Maximize	Hard upper limit	Hard upper limit	Maximize
5	Hard lower limit	Minimize	Hard upper limit	Maximize
6	Maximize	Minimize	Hard upper limit	Hard lower limit

Table 3.3 – Optimization criteria for PA12-CF.

Criteria	Mechanical Properties	Surface Quality	Manufacturing Time	Dimensional Accuracy
1	Hard lower limit	Hard upper limit	Minimize	Maximize
2	Hard lower limit	Minimize	Hard upper limit	Maximize
3	Maximize	Hard upper limit	Hard upper limit	Maximize
4	Hard upper limit	Minimize	Minimize	Hard lower limit
5	Maximize	Minimize	Hard upper limit	Hard lower limit
6	Maximize	Hard upper limit	Minimize	Hard lower limit

A summary of the SLS parameters modelling and optimization framework is described below:

1. Create a design space using a DOE space filling technique (Sobol spaces) to obtain design points uniformly distributed over the design space.
2. Conduct experiments at the design points and collect response data.
3. Develop a Gaussian Process ($\mathcal{GP}$) modelling to obtain a RSM of the output variables.

4. Perform multi-criteria optimization based on stochastic EA to obtain Pareto optimal solutions for different criteria.

3.7 Testing and characterization

3.7.1 Mechanical testing

To evaluate the structural characteristics of the samples manufactured by SLS at different energy densities, a set of destructive mechanical tests was performed. For the samples manufactured in the DOE analysis standard tensile and flexural tests were performed in an EMIC DL500 mechanical testing machine. Tensile tests were conducted according to ASTM Standard D638-02a (2002). Dumb-bell shaped tensile specimens having dimensions of 165 x 19 x 3.2 mm were tested under a displacement rate of 5 mm/min.

ASTM Standard D790-02 (2002) was followed to conduct flexural tests. Specimens with dimensions of 127 x 12.7 x 3.2 mm were measured under three point bending tests procedure, applying a varying cross-head motion and midspan depending on the measured thickness of the sample. For statistical relevance, 5 flexural and 5 tensile specimens were tested for each parameter set tested.

3.7.2 Dimensional, density and surface analysis

Dimensional analysis according to ASTM Standard D5947-11 (2011) was conducted to evaluate the effect of the sintering parameters on dimensional accuracy and distortion of the samples. Width and thickness measurements were performed using a micrometer while a calliper was used to measure specimens length. The resulting data was used to calculate the volume of the flexural samples and to further estimate the apparent density of the samples by measuring their mass with a precision balance.

In addition, surface roughness measurements were performed to evaluate the surface texture of the samples. Surface roughness was measured with a Mahr Perthen Perthometer S8P with a cut-off length of 8 mm. Following roughness parameters were measured: Average surface roughness R_a, Mean roughness depth R_z, Root mean square roughness R_q and Maximum profile height R_y.

3.7.3 Scanning electron microscopy and X-ray diffractometer (XRD)

To evaluate the effect of LS parameters on the microstructure of the samples, SEM images of the fractured area of tensile samples were performed. Additionally SEM images of the samples upper surface were taken to assess the surface morphology of samples manufactured with different LS parameters.

A Tescan Vega 3 scanning electron microscope was used to observe the fractured area of tensile samples and the upper surface morphology of the samples. The specimens were sputtered with gold in a Quorum Q150R ES machine. X-ray diffractometer (XRD) analysis was performed using a Shimadzu XRD 7000 equipment to identify the phases of PA12 and PA12-CF processed at different energy densities. The radiation intensity was detected in the 2θ range of 2-30° with a scan speed of 1 °/min.

3.7.4 Differential scanning calorimeter (DSC) and and Infrared spectroscopy (FTIR)

DSC heating scans were made with a Labsys EVO DTA/DSC Setaram Instrumentation equipment. Sample masses of 20 mg were heated from 20 $°C$ to 200 $°C$ at a rate of 10 °C/min. Crystallinity degree was calculated using equation 3.6 based on the melting area of the DSC measurements and comparing to the melting area of a 100% crystalline PA12 (H_{100}), which is 209.3 J/g based on Gogolewski, Czerniawska & Gasiorek (1980). DSC analysis was performed only for PA12 samples.

$$X_c = \frac{H_c}{H_{100}} \tag{3.6}$$

Infrared spectra (FTIR) of PA12 and PA12-CF samples surface were obtained using a Perkin Elmer LR64912C spectrophotometer in the range of 500-4000 cm^{-}1. Main objective with FTIR was to detect differences in the absoprtion bands of PA12 and PA12-CF processed at different energy densities in order to identify polymer degradation.

3.7.5 Manufacturing time

To evaluate the manufacturing time dependency of laser sintering parameters the calculations of the EOS P396 machine software were used. A reference manufacturing time was used based on the calculation of the manufacturing time of one tensile test sample produced with standard laser sintering parameters (parameter set PA2200 Balance according to manufacturer machine manual (EOS, 2016). The normalized manufacturing time ϑ was calculated based on the ratio between the manufacturing time calculated for the same sample at the same position but with the parameter set resulting from the DOE and the reference manufacturing time. The normalized manufacturing time is given by 3.7.

$$\vartheta = \frac{ManTime_{DOE}}{ManTime_{ref}} \tag{3.7}$$

4 Results and Discussion - PA12

4.1 Influence of energy density - PA12

This section describes the results achieved for PA12 material considering the energy density as main variable, composed by laser power, laser scan speed, scan line spacing and layer thickness (discussed in Chapter 2). Measurement variables evaluated include dimensional accuracy, density, tensile and flexural properties and surface properties, as described in Chapter 3.

4.1.1 Influence of energy density on dimensional accuracy

Figures 4.1, 4.2 and 4.3 depicts box whisker plots of the dimensional accuracy in X, Y and Z direction respectively, expressed in % and at different levels of energy density. X direction accuracy remained high and stable, with all values above 99.5 % at all energy density levels, showing that the laser energy parameters have small influence on X dimension accuracy.

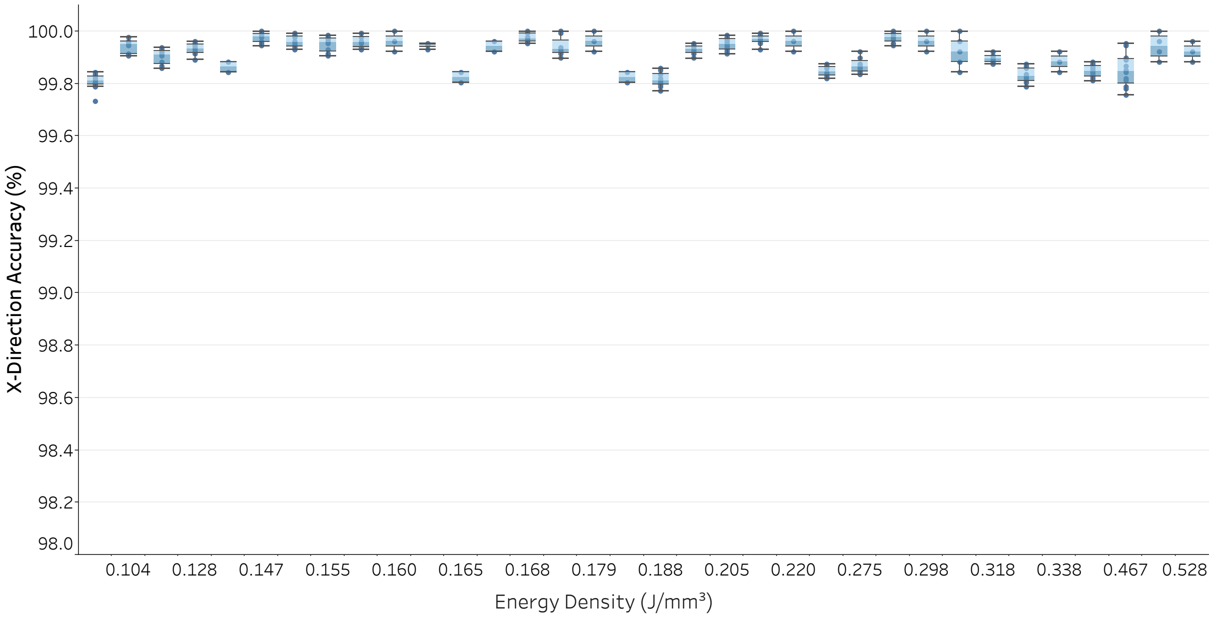

Figure 4.1 – Influence of energy density on X-direction dimensional accuracy of PA12.

Y direction accuracy remains stable at low and mid-range energy levels (up to 0.346 J/mm^3), following a similar tendency than X direction, except that the dimensional accuracy is lower, with average values ranging between 98.4 and 99.3%. With increasing energy density levels, the Y accuracy starts to decrease, reaching 98.18% at 0.220 J/mm^3 and oscillating more at higher energy density but with a clear decrease tendency. Smallest value observed was 93.6% at 0.528 J/mm^3. Also the dispersion of the measurements is higher at increasing energy density levels, showing that the process is more unstable in this area. Measured width values showed a tendency to stay below the desired part width of 12.8 mm for energy density levels up to 0.220 J/mm^3. Above this energy level the opposite trend was observed.

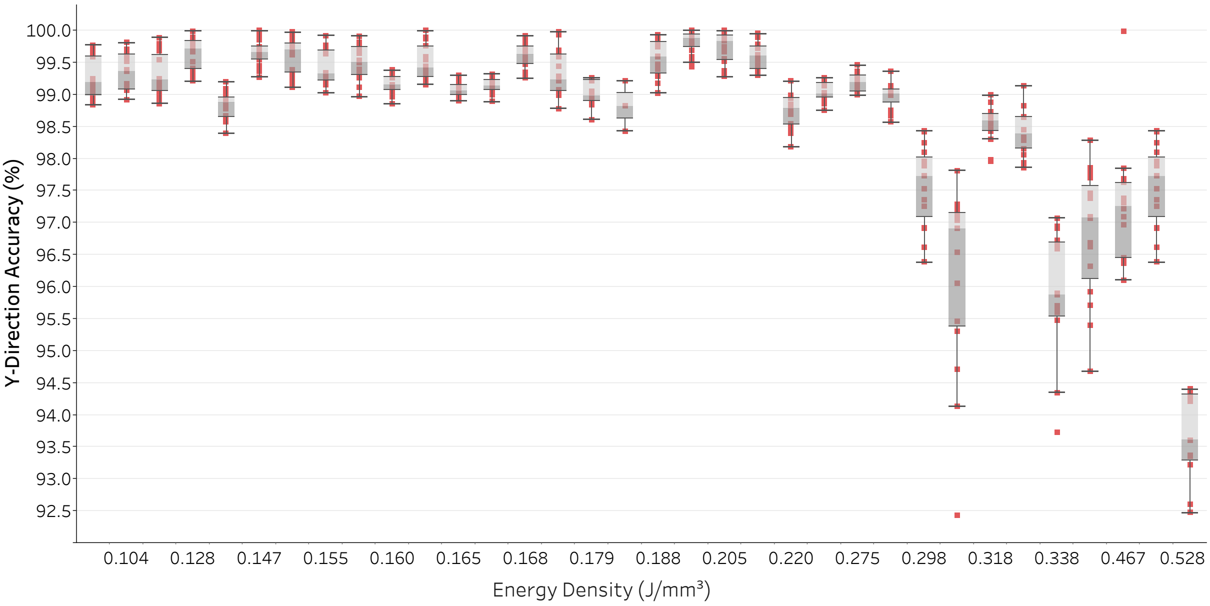

Figure 4.2 – Influence of energy density on Y-direction dimensional accuracy of PA12.

Regarding Z direction accuracy the highest accuracy values are found for low energy density levels (below 0.188 J/mm^3), with values varying between 93% and 99%. Above this energy level Z direction accuracy decreases to 92% at 0.193 J/mm^3 and worsens continuously with increasing energy density, reaching the lowest values of 69% at 0.528 J/mm^3. The dispersion of the values also increases at higher energy levels. Also, the measured thickness values exceeded the desired part thickness of 3.2 mm.

Considering the laser material interaction present during SLS of PA12, the CO_2 laser energy delivered to the powder bed is transferred to the polymer by means of radiation absorption from the powder and multiple transmission to the neighboring particles. PA12 powder shows a high absorptance of radiation at the wavelength of 10.6 μm of the CO_2 laser (LAUMER et al., 2016). The increasing energy delivered by the laser source enhances this heat transfer process and heat is delivered to the surrounding area and underlying powder not targeted by the laser, resulting in an expansion of the heat affected area, decomposition and deformation of the parts and consequently a worse dimensional accuracy. Difference on the shrinkage behavior at X, Y and Z direction during cooling are also reported to have influence on the dimensional accuracy of the parts.

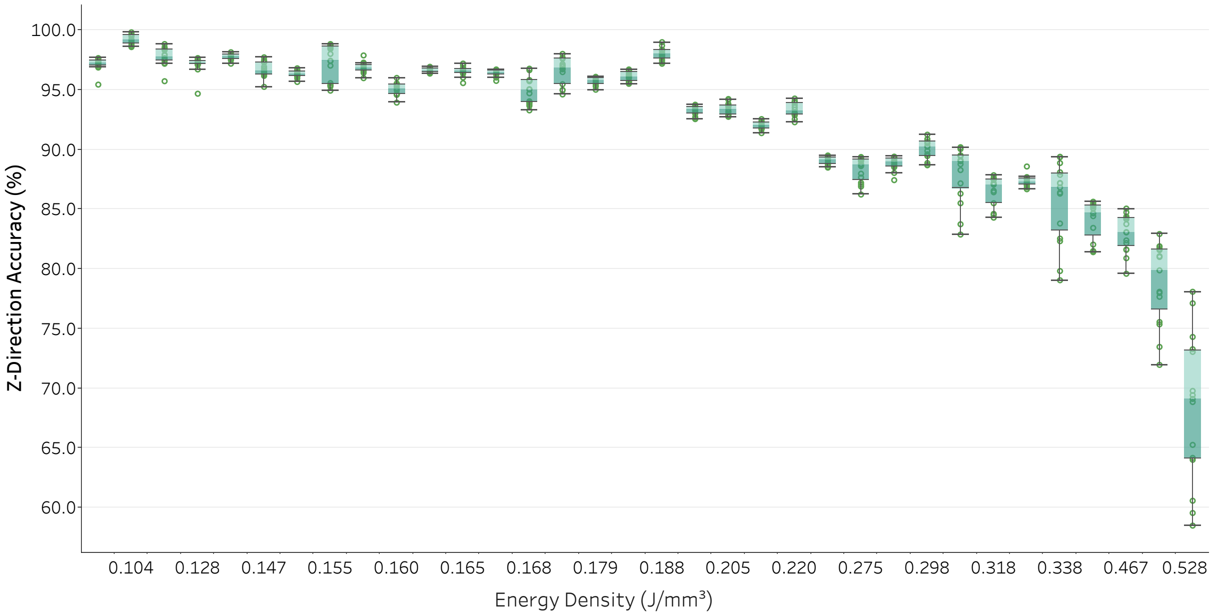

Figure 4.3 – Influence of input energy on Z-direction dimensional accuracy of PA12.

4.1.2 Influence of energy density on density

Figure 4.4 shows a box whisker plot of the measured parts' density as a function of the energy density. At very low energy levels ranging from 0.091 until 0.128 J/mm^3, the parts density is very low, with density values of 0.72 g/cm^3 at 0.091 J/mm^3, but increases in a step-like pattern with increasing energy, reaching 0.87 g/cm^3 at 0.128 J/mm^3. Further increase in energy leads to higher and more stable density values oscillating between 0.91 and 0.97 g/cm^3. Such oscillation can be explained by the influence of the individual process parameters evaluated (laser power, laser speed, scan line spacing and layer thickness) and will be addressed in more detail in the next sections. Highest density values of 0.97 g/cm^3 were found for an energy density of 0.220 J/mm^3.

A further increase on energy density above 0.467 J/mm^3 leads to a decrease on part density, as observed in the graphic at the last energy stages. This is mainly due to the distortion caused by the high energy delivered which increases the part volume and consequently reduces its density.

The densification process and final porosity of LS PA12 parts is directly related to the material properties such as particle shape and distribution, thermal behavior, optical properties, viscosity, molecular weight and surface tension. The "potato" shaped particle of PA12 helps improving the flowability of the powder during powder spreading, which contributes to an effective consolidation of the powder during laser sintering, improving final part density (SCHMID; WEGENER, 2016). Particle size distribution also plays a major role during LS. The PA12 particles studied had an average particle size (d$_{50}$) of 55.1 μm and around 4% particles smaller than 10 μm. Such particle distribution is considered appropriate for LS as discussed in Chapter 2, providing a good powder flowability and

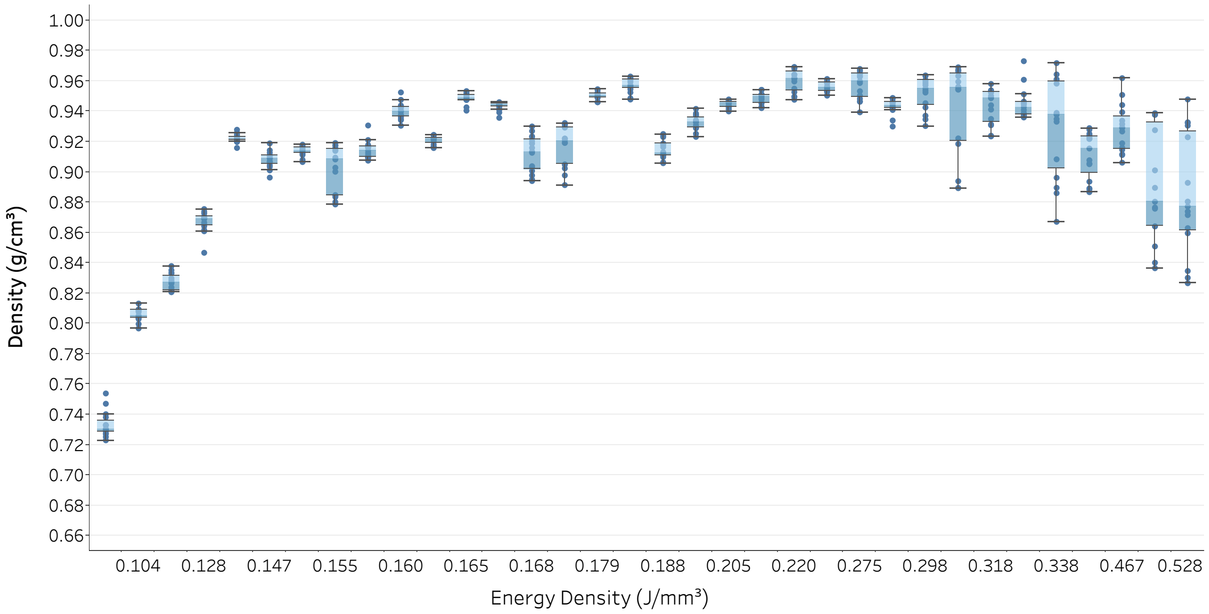

Figure 4.4 – Influence of input energy on parts density for PA12.

minimizing powder sticking during LS (GOODRIDGE; TUCK; HAGUE, 2012).

Besides material characteristics, laser sintering parameters significantly affect density, as could be observed from Fig. 4.4. At low energy densities there is not enough energy for effective melting of the particles (surface and core) and coalescence, resulting in the formation of unsintered particles and pore formation between particles after the laser scanning. In addition, when very low energy is applied the formation of interlayer porosity may also be formed, which enhances the overall porosity of the parts (DUPIN et al., 2012).

Excessive energy values also can promote porosity due to polymer degradation, as also reported in the literature by Athreya, Kalaitzidou & Das (2010) when processing PA12 with carbon black nanocomposites.

The density values obtained differ a little from values reported in the literature. Kruth et al. (2007) reported average values ranging from 0.95-1.00 g/cm^3. Tontowi & Childs (2001) reported maximum values of 0.98 g/cm^3. Wegner & Witt (2012) reported values up to 0.998 g/cm^3.Caulfield, McHugh & Lohfeld (2007) reported even higher values of 1.05 g/cm^3 . On the other hand the density values obtained are in good agreement with the material manufacturer datasheet of 0.93 g/cm^3 using standard laser parameters (EOS, 2020) and also with more recent studies performed with similar machine equipment and material (HOFLAND; BARAN; WISMEIJER, 2017). Different measurement methods as well as machine equipment and type of powder material used can have influence on the values compared.

4.1.3 Influence of energy density on surface roughness

Box whisker plots of average surface roughness and energy density are depicted in Fig. 4.5. Upper (Fig. 4.5a) and lower (Fig.4.5b) surface measurements of the parts were performed. Upper average surface roughness values seem to be higher at low energy density area (up to 0.128 J/mm^3. With increasing energy R_a stabilizes to lower values between 12 and 18 μm. There is a slight tendency for higher R_a values at high energy density range (above 0.384 J/mm^3).

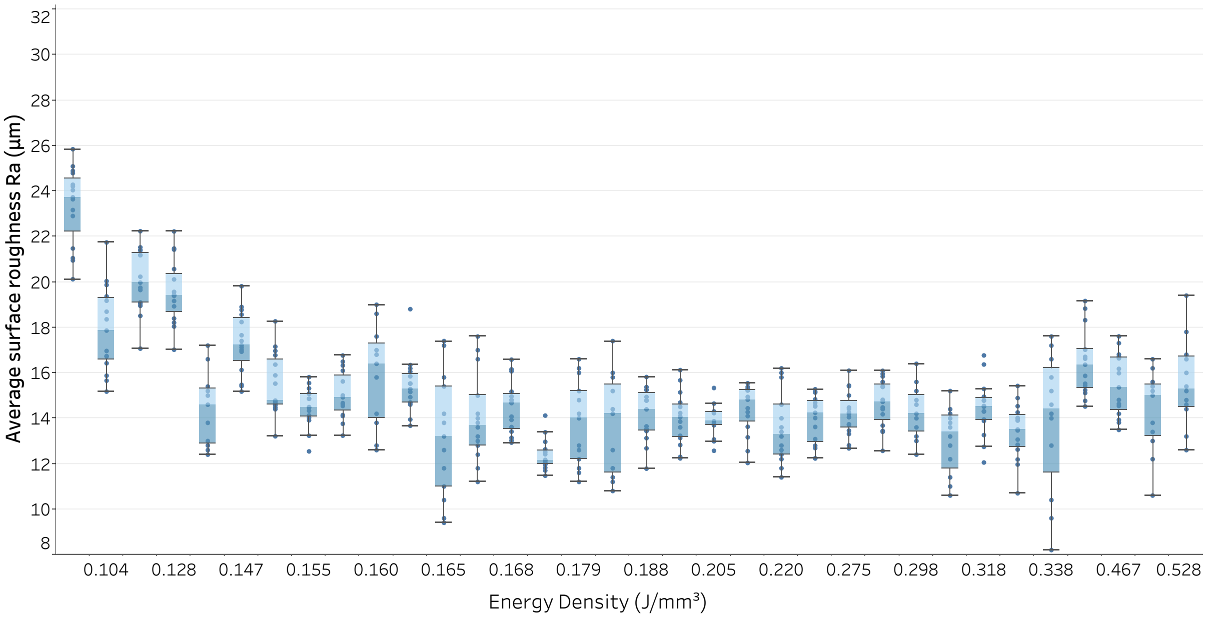

(a)

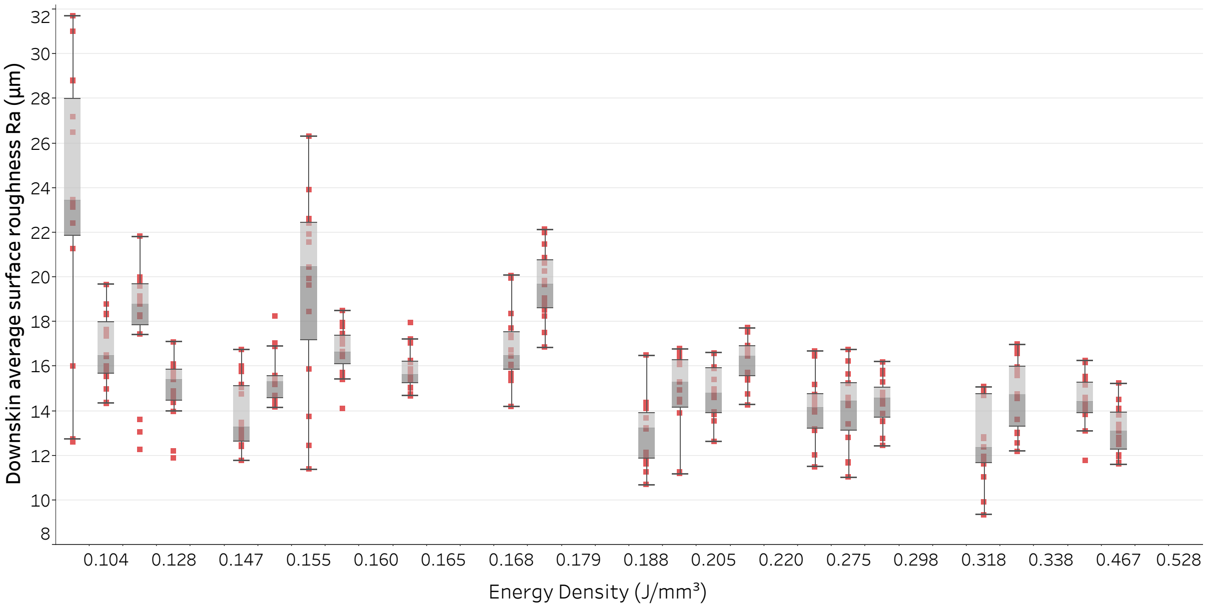

(b)

Figure 4.5 – Influence of input energy on average surface roughness R_a of PA12: (a) Upper surface; (b) Lower surface

Lower surface R_a values follow a similar trend of upper surface measurements, but no clear difference on the values can be defined. Depending on the energy density applied, higher values are observed for lower than upper surface and the other way around.

It can be observed a high variation between the measurements performed. Profile topography measurements are based on scanning a single track of the surface plane and are known for high variation. Besides, as the LS process produces complex and irregular topography profiles, profile measurements are very limited to capture topography information and higher variation can be expected. As observed by other authors, areal topography methods based on optical devices could improve the quality of information from LS surfaces (TOWNSEND et al., 2016).

Besides the high variation of the measurements, R_a values are in general good agreement wiht recently measured values reported in the literature for LS PA12 surfaces, where average R_a values of 16 μm were observed (GUO et al., 2018).

To evaluate the presence of large peaks and valleys along the surface, mean roughness depth R_z measurements were also carried out and are depicted in Fig. 4.6a for upper surface and Fig. 4.6b for lower surface. As can be observed from the graphics, both upper and lower surfaces are characterized by high values of R_z, showing that large peaks and valleys are present in the surface. As observed previously in the R_a measurements, R_z also follows a tendency to decrease with increasing energy density, but increases again at high energy densities (above 0.384 J/mm^3). Such surface profile is typical of powder bed based AM processes, which produces surfaces with sharp peaks and valleys, open and closed porosity on the surface, partially melted and unmelted surfaces.

Laser exposure parameters can influence surface topography. In particular, laser scan spacing is an important parameter which can influence surface roughness. At low scan line spacing values the laser scans parallel lines with some degree of overlap between de lines. The degree of overlap is a measure based on the scan line spacing and the laser beam diameter which shows how strong is the overlapping between two parallel lines. The lower the degree of overlap the less is the interaction between laser lines. As observed from Figure 4.7, at a scan line spacing between 0.2 and 0.4 mm, average surface roughness values remain more or less stable, oscillating between 12-16 μm. The values seem not to depend on the laser power and laser speed. At this scan line spacing range, the overlapping ranges between 20-60 %.

As the scan line spacing increases above 0.42 and the overlapping approaches zero (no overlapping between laser scan lines)and negative values, average surface roughness values R_a increase to 18-23 μm. But here the influence of laser scan speed seems to have an influence on the resulting surface roughness. When no overlap occurs and the laser scan speed is low the surface roughness values remain at level similar to the ones of lower scan line spacing.

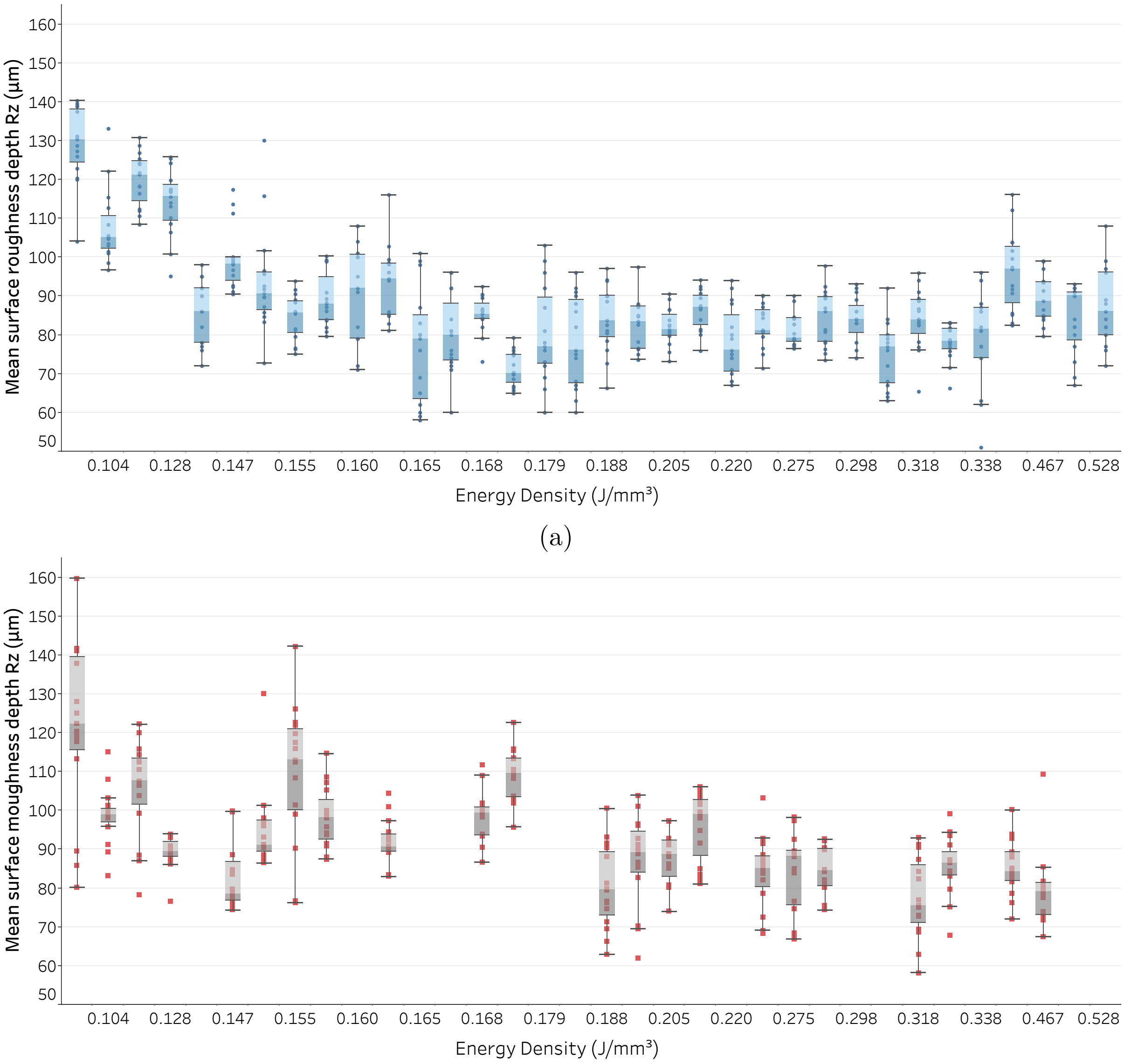

(a)

(b)

Figure 4.6 – Influence of input energy on mean roughness depth R_z of PA12: (a) Upper surface; (b) Lower surface

In order to explain in more detail the observed behavior, Fig. 4.8 shows SEM images of the LS PA12 surface morphology at different energy densities, showing the degree of overlap applied and laser scan speed. At high degree of overlap the surface morphologies are very similar, independently on the laser scan speed applied, with melted areas and some unmelted particles at the surface, as observed in Fig. 4.8a-b.

Increasing the scan line spacing (i.e. reducing the degree of overlap) promotes the formation of a rougher surface with clearly distinguishable laser line marks, as observed in Fig. 4.8c-d. But here the laser scan speed has an influence on the resulting surface morphology. At high laser scan speed (Fig. 4.8c) the surface morphology has more pronounced peaks and valleys derived from the laser passage and many unmolten particles. Reducing the laser scan speed (Fig. 4.8d) allows more time for melting and flowing of the

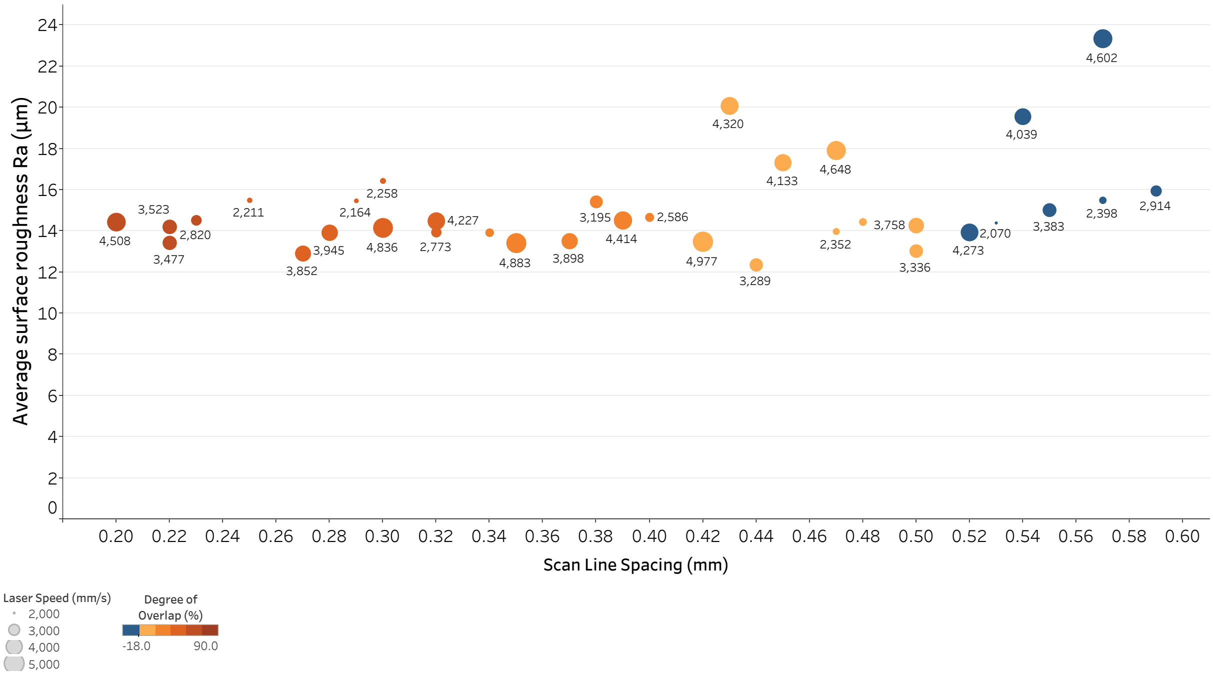

Figure 4.7 – Influence of degree of overlap on surface roughness of LS PA12.

powders during sintering process, improving the densification in the neighbouring areas and producing a smoother surface.

4.1.4 Influence of energy density on tensile properties: Elastic behavior

To evaluate the elastic behavior of LS PA12 samples at different energy densities, standard tensile tests were performed according to (ASTM Standard D638-02a, 2002). Based on the force displacement curve the following characteristics were calculated: proportional limit (MPa), 0.2% offset yield strength (MPa), nominal strain at proportional limit (0.2%), nominal strain at 0.2% offset yield strength and elastic modulus (MPa).

Figure 4.9a depicts proportional limit and 0.2% offset yield strength at different energy density values. Both measures follow a similar trend in respect to the energy density, presenting low values (below 16 MPa for proportional limit and 20 MPa for 0.2% offset yield strength) at energy density levels below 0.128 J/mm^3. Increasing the energy density improves proportional limit and 0.2% offset yield strength, with the values oscillating between 16-22 MPa for proportional limit and 22-28 MPa for 0.2% offset yield strength. Maximum average values of 21.8 MPa for proportional limit and 28.45 MPa for 0.2% offset yield strength were observed at an energy density of 0.298 J/mm^3.

The stress behavior at elastic regime is very similar to density behavior observed above. Again, above a certain energy density level no clear trend can be observed based only on the grouped parameter energy density, suggesting here that the individual laser exposure parameter play an influence on the stresses observed.

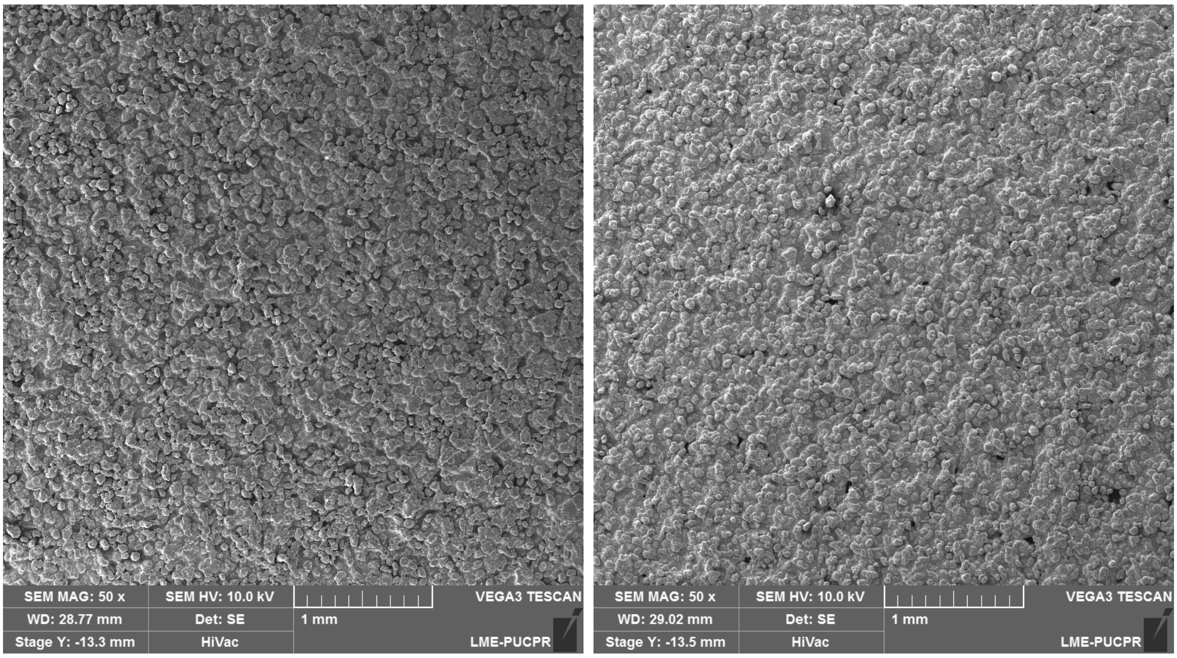

(a) Laser speed: 3,523 mm/s; Degree of overlap: 56 %

(b) Laser speed: 2,773 mm/s; Degree of overlap: 36 %

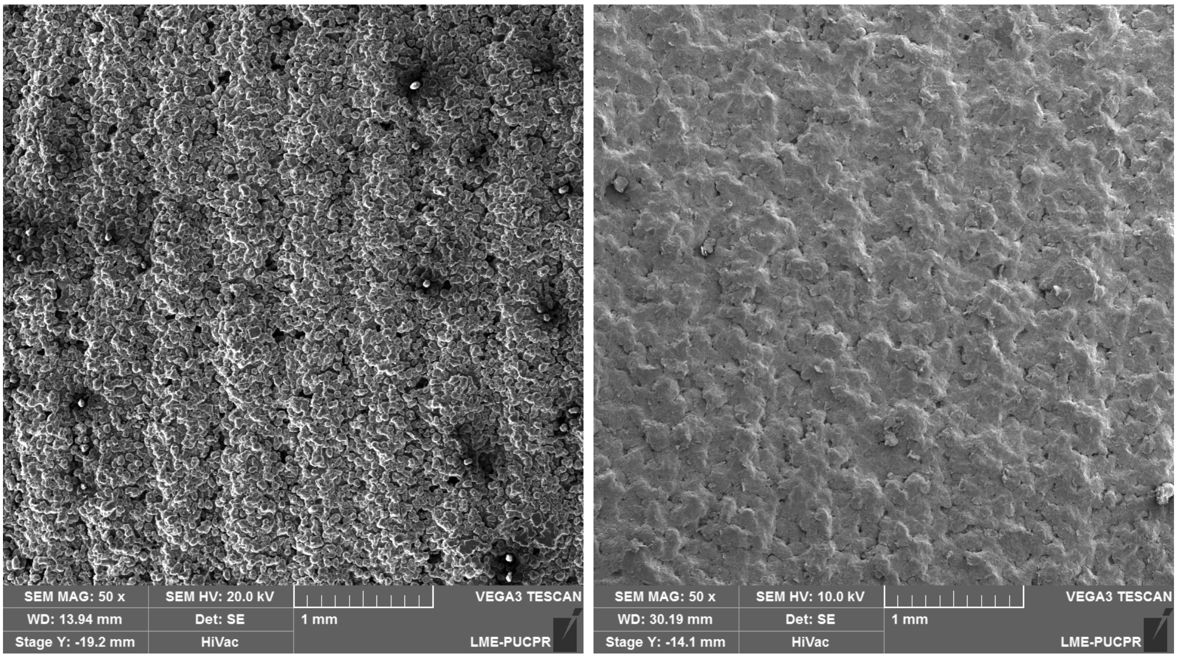

(c) Laser speed: 4,606 mm/s; Degree of overlap: -14 %

(d) Laser speed: 2,914 mm/s; Degree of overlap: -18 %

Figure 4.8 – SEM micrographs of PA12 LS surface morphology.

Nominal strain values (%) at proportional limit and 0.2% offset yield strength are depicted in Fig.4.9b. The nominal strain behavior with energy density is similar to stress behavior observed above, presenting average values below 1.2 % at proportional limit and 1.7 % at 0.2% offset yield values of strain at energy density below 0.128 J/mm^3. Increasing the energy density improves nominal strain at both points evaluated, but the improvement is smoother than with stress values, with values oscillating between 1.2-1.6

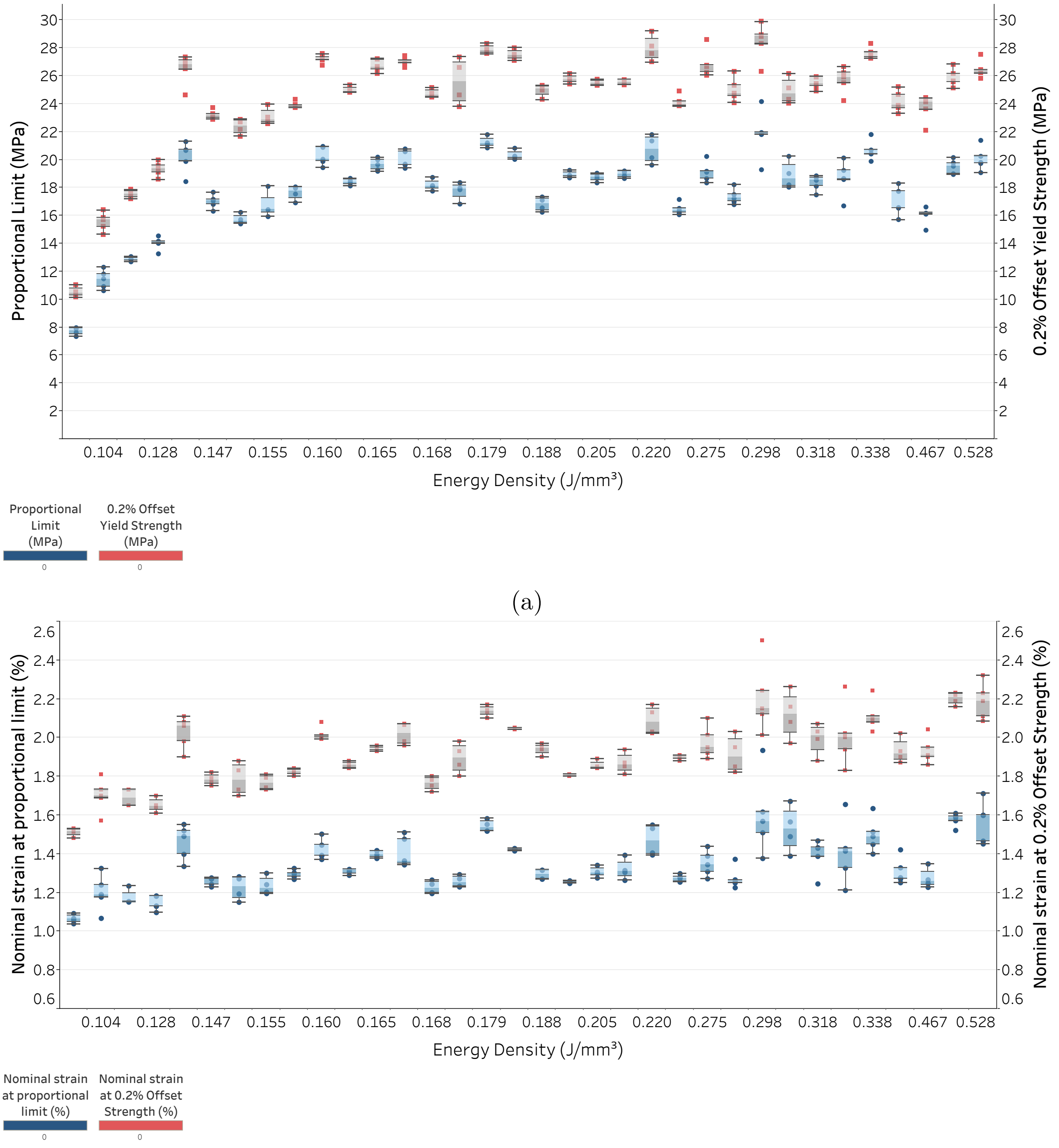

(a)

(b)

Figure 4.9 – Influence of energy density on elastic behavior for PA12.: (a) Stress ; (b) Nominal strain

% at proportional limit and 1.7-2.2 % at 0.2% offset yield. Highest average values of 1.58 % at proportional limit and 2.2 % at 0.2% offset yield were observed at highest energy density (above 0.5 J/mm^3).

Elastic modulus was also calculated based on the stress strain curve and is depicted in Fig. 4.10. As expected, tensile modulus also follows a similar trend of stress and strain with increasing energy density. Very low values of 900 MPa are observed at 0.091 J/mm^3, which start to increase in a step like pattern up to 0.137 J/mm^3, where average values of

1476 MPa are measured. Between an energy density of 0.147-0.290 J/mm^3, elastic modulus oscillates between 1500-1670 MPa, reaching a maximum average value of 1663 MPa at 0.193 J/mm^3. Above 0.290 J/mm^3 there is a slight decrease tendency in elastic modulus and lowest values of 1300 MPa are found for highest energy density area above 0.5 J/mm^3.

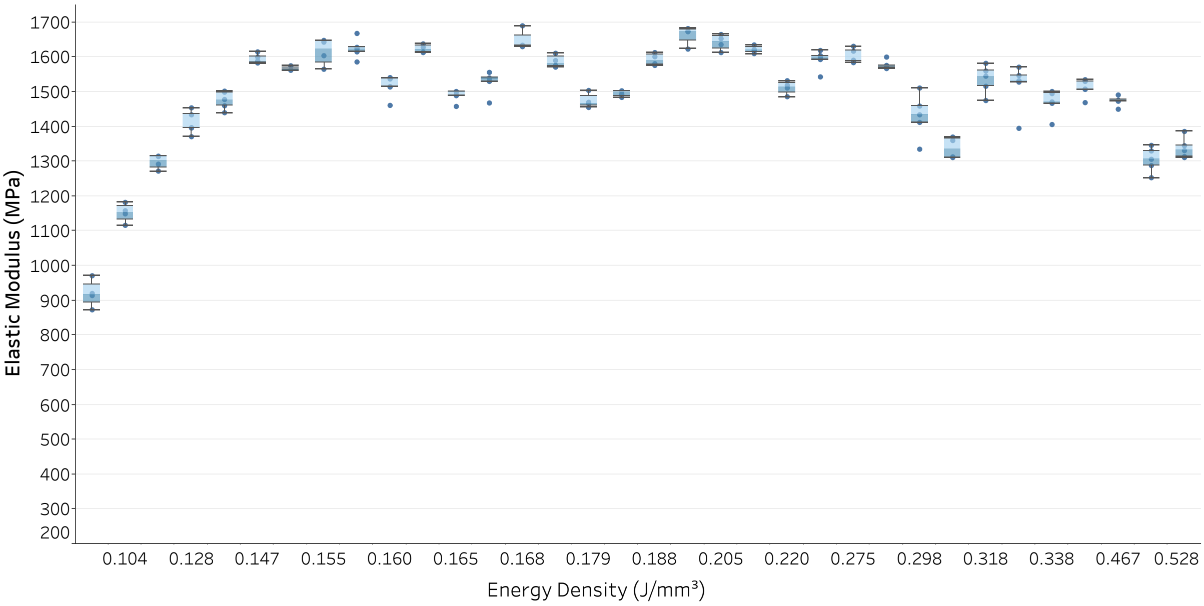

Figure 4.10 – Influence of input energy on elastic modulus for PA12.

Semicrystalline polymers are composed by two phases: crystalline structures consisting of crystal lamellae and disordered amorphous phase present between the lamellae. As observed in DRX measurements (Chapter 3), LS PA12 powder applied has as its crystal form the γ and α phases. This is in agreement with results obtained by other authors (Van Hooreweder et al., 2013).

In LS, as the laser scans the powder melting of the particles occurs, followed by a recrystallization phase. Recrystallization occurs slowly due to the slow cooling conditions of LS process, which is kept at a preheating temperature above 170°C to delay crystalization and part shrinkage. Nevertheless, even if the surface of the particles is molten, the presence of unmolten particle cores remain, as some particle do not recieve enough energy to fully melt (MAJEWSKI; ZARRINGHALAM; HOPKINSON, 2008). Unmolten particles are known to have a higher crystallization degree and contribute to improve elastic modulus, as most of the elastic strain results from the elongation of the interlamellar amorphous phase (JAUFFRÈS et al., 2009).

At very low energy density levels, melting of PA12 particles is poor and there is no effective binding between neighbouring particles as well as interlayer particles, leading to high porosity and low elastic modulus. Therefore, even with a higher crystal degree expected at low energy density due to unmolten particles, the overall high material porosity hinders this effect, as observed by other authors in the literature (DUPIN et al., 2012).

Increasing LS energy density improves the linear properties of LS PA12, as the densification of polymer particles is enhanced and porosity is reduced. On the other hand, higher energy levels induce the melting and recyrstallization of unmolten particles, increasing the melt-recrystallised phase fraction and reducing the crystallinity of LS parts (DUPIN et al., 2012). A reduction in crystal fraction would tend to decrease elastic modulus, but this is not clearly observed in the results for an energy density range of 0.147-0.290 J/mm^3, which shows oscillating values of elastic modulus. This is probably due to the effect of the individual laser exposure parameters which contribute in different manner to the crystal fraction and resulting elastic modulus. Only above a 0.290 J/mm^3 a tendency to decrease elastic modulus is observed and here the effect of crystal fraction reduction may be more pronounced.

4.1.5 Influence of energy density on tensile properties: Plastic behavior

Measured plastic properties of LS PA12 along energy density were also evaluated and are depicted in Fig. 4.11. In the low energy density area (below 0.128 J/mm^3), strength at yield and break (Fig. 4.11a) present very low values of 15-30 MPa, with the values increasing step wisely with increasing energy. Both strength at yield and break present similar values, suggesting that LS PA12 presented little plastic deformation and no necking and fractured in a more brittle manner when achieved the maximum stress.

Increasing the energy density between 0.137 and 0.193 improves strength at yield and break from 37.5 MPa at 0.147 J/mm^3 to 43.4 MPa at 0.193 J/mm^3, with similar yield and break stresses. A further increase in energy density between 0.205-0.275 J/mm^3 enhances yield strength from 44 to 46 MPa and a reduction in break strength from 42.6 to 39.1 MPa, indicating a more pronounced plastic deformation with necking formation. At higher levels of energy density yield and break strength seems to stabilize to slightly lower values around 44 MPa and 41 MPa respectively. At very high energy density there is a reduction in yield and break strength. Maximum average yield strength of 46 MPa is achieved at 0.275 J/mm^3.

Compared to literature, tensile yield strength found in the present work are a little lower.Wegner & Witt (2012) reported maximum values of 51.3 MPa. The obtained maximum values are also below material manufacturer datasheet of 48 MPa using standard laser parameters (EOS, 2020) and also Hofland, Baran & Wismeijer (2017), who reported 50.1 MPa. On the other hand, Caulfield, McHugh & Lohfeld (2007) reported lower values below 40 MPa and Stichel et al. (2018) reported lower values ranging from 41-45 MPa. Again the differences in processing conditions, machine equipment and measuring method may be the cause of divergence on values obtained.

Figure 4.11b shows the nominal strain at yield and break with increasing energy density. Yield and break strain start with values below 6% at energy densities below 0.128

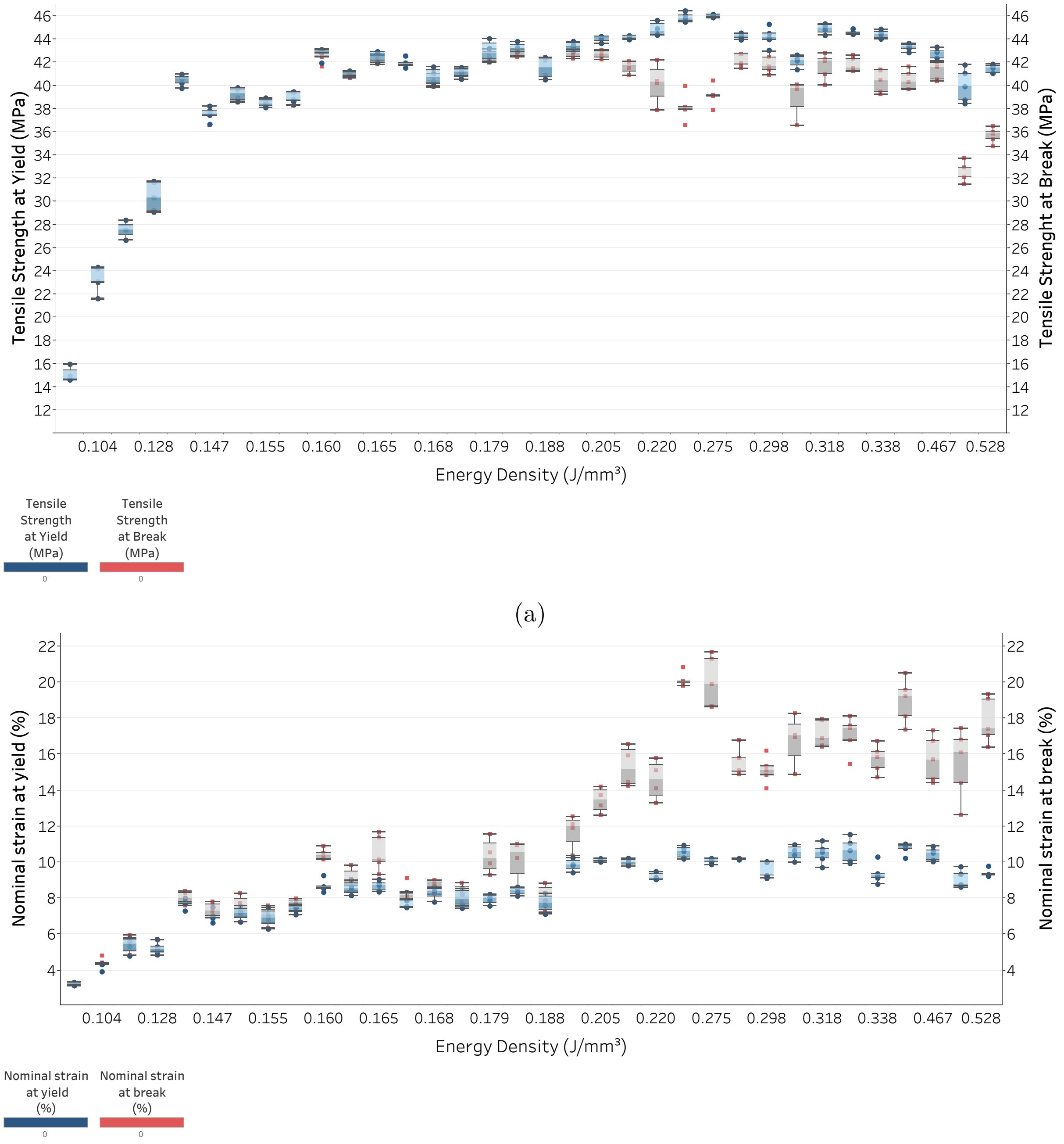

(a)

(b)

Figure 4.11 – Influence of energy density on plastic behavior for PA12.: (a) Stress ; (b) Nominal strain

J/mm^3, with similar values of yield and break strain, reinforcing the more brittle behavior at this energy area. Applying more energy promotes more plastic strain, with values below 10% for yield and break strain. Yield and break strain start to diverge in this energy range but still with no clear tendency. Only at energy density above 0.193 J/mm^3 yield and break strain diverge more strongly, with the yield strain presenting stable values between 10-11% and strain at break increasing from 8% at 0.188 J/mm^3 to 20% J/mm^3 at 0.27-0.275 J/mm^3, where maximum strain at break is found. Further increase on the energy density promotes a reduction in strain at break, with values oscilating between

15 and 19%.Strain at yield shows stable values along the higher energy density range, decreasing to 9% only at the highest energy densities applied.

Compared to the literature, maximum strain at break values found are in good agreement with material manufacturer datasheet, which reports 18% (EOS, 2020). Griessbach, Lach & Grellmann (2010) reported maximum values around 18%, whereas Wegner & Witt (2012) who reported 21.2%. Stichel et al. (2018) found strain at break values between 14-32%.

In order to further investigate the plastic behavior, SEM micrographs of fractured surfaces at different energy densities were performed and are shown in Fig. 4.12. Pictures reveal a high interparticle and interlayer porosity formation in LS samples produced with 0.091 and 0.115 J/mm^3, as shown in Fig. 4.12a-d. Higher magnification shown in the overlapped micrograph shows large presence of unmolten particles.

Increasing the energy to 0.115 J/mm^3 (Fig. 4.12c-d) improves interlayer bonding, but a porous and brittle interlayer structure can still be observed with unmolten particles present also between the layers. Some plastic deformation is visible from the micrographs which also correlates with an increase in nominal strain.

With a further increase on energy density to 0.160 J/mm^3 (Fig. 4.12e-f) the interlayer structure is no more evident and the porosity is mainly formed by closed pores surrounded by molten particles. At 0.179 J/mm^3 (Fig. 4.12g-h) the structure seems slightly more dense than at 0.160 J/mm^3 but both structures present similar levels of plastic deformation, indicating that fracture mechanism is not only governed by overall porosity.

At 0.219 J/mm^3 (Fig. 4.12i-j) there is no visible improvement in porosity but a significant improvement on plastic strain, with the sample presenting a more ductile failure, as can be observed by the elongated fibrils present in the overlapped micrograph. Figure 4.12k-l shows the fractured surface of PA12 where the highest plastic strain occurred. Indeed the micro structure reveals significant plastic strain, with highly stretched and thicker fibrils. At the highest energy density of 0.528 J/mm^3 (Fig. 4.12m-n) the fractured surface reveals less stretched fibrils.

As stated above, at very low energy densities PA12 particles do not melt completely, showing a high porosity degree between particles and also between layers. From fracture mechanics studied by Stichel et al. (2018), a critical crack size of 3.5 mm would be necessary for crack growth initiation. As observed from the SEM micrographs, at low energy density large pore sizes exists and they are connected within each layer, which is clearly larger than the critical crack size calculated. Thus at an energy level below 0.158 J/mm^3 the fracture is induced by crack nucleation at interlayer region. This is in agreement with SEM micrographs, where a brittle fracture occurred where interlayer porosity was visible.

Plastic deformation in semi-crystalline polymers is caused by elongation of amor-

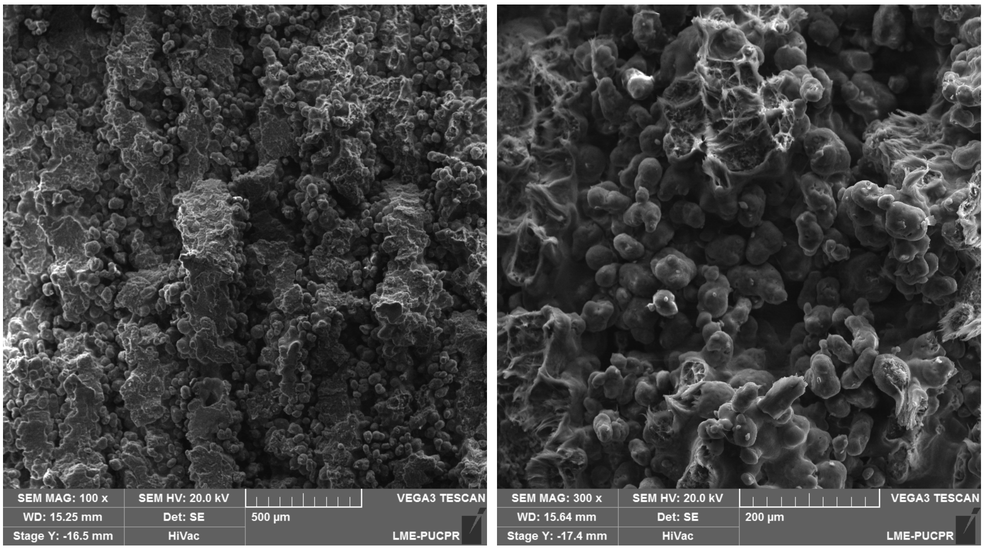

(a) Energy Density: 0.091 J/mm^3 (b) Energy Density: 0.091 J/mm^3

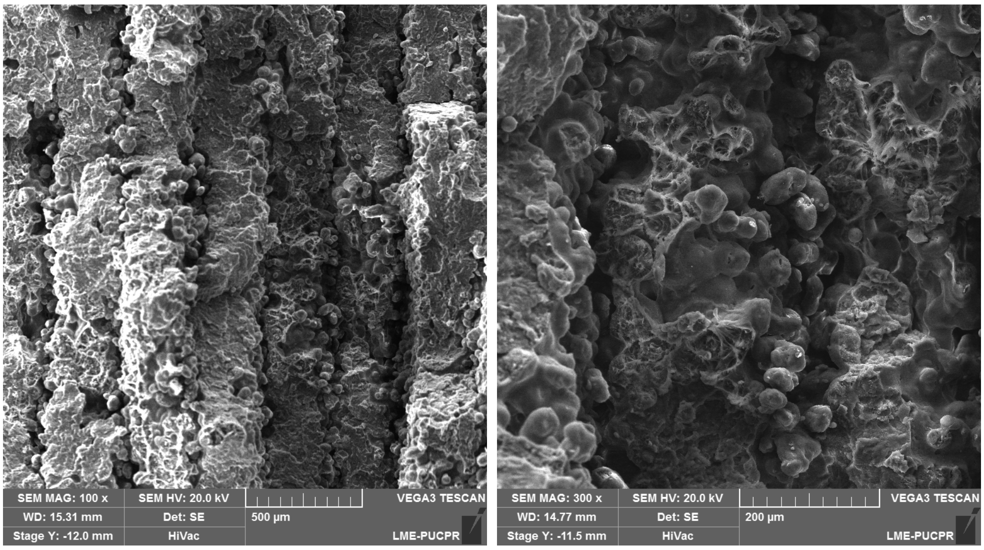

(c) Energy Density: 0.115 J/mm^3 (d) Energy Density: 0.115 J/mm^3

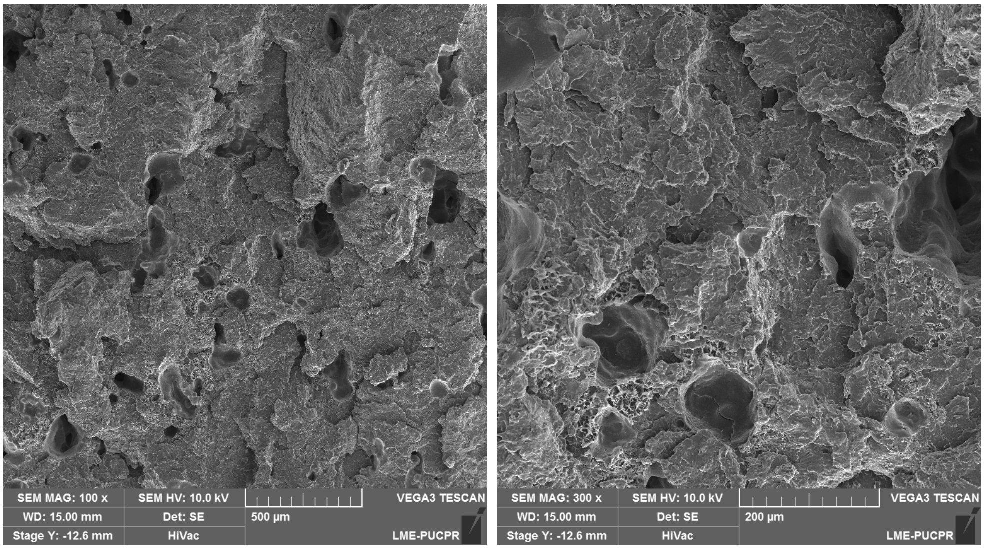

(e) Energy Density: 0.160 J/mm^3 (f) Energy Density: 0.160 J/mm^3

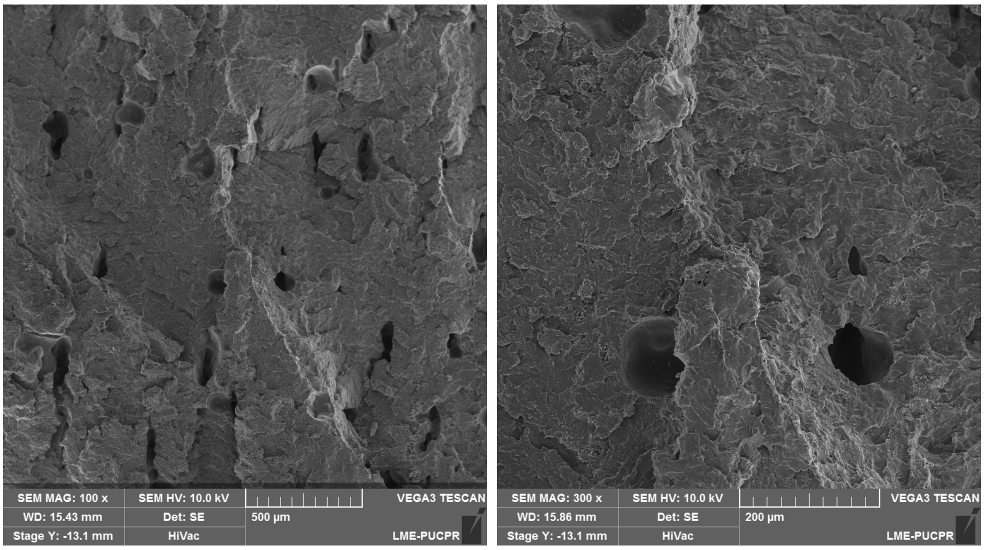

(g) Energy Density: 0.179 J/mm^3 (h) Energy Density: 0.179 J/mm^3

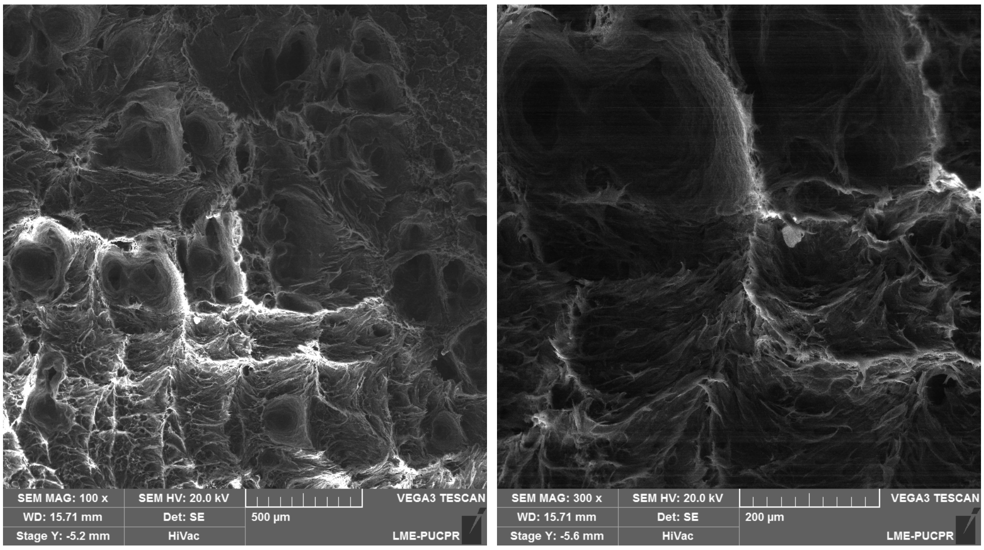

(i) Energy Density: 0.219 J/mm^3 (j) Energy Density: 0.219 J/mm^3

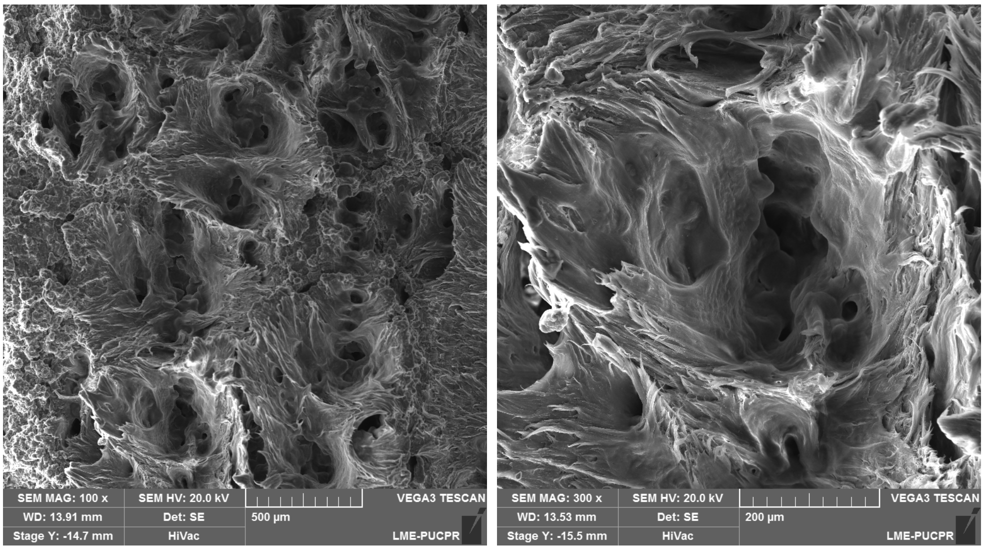

(k) Energy Density: 0.27 J/mm^3 (l) Energy Density: 0.27 J/mm^3

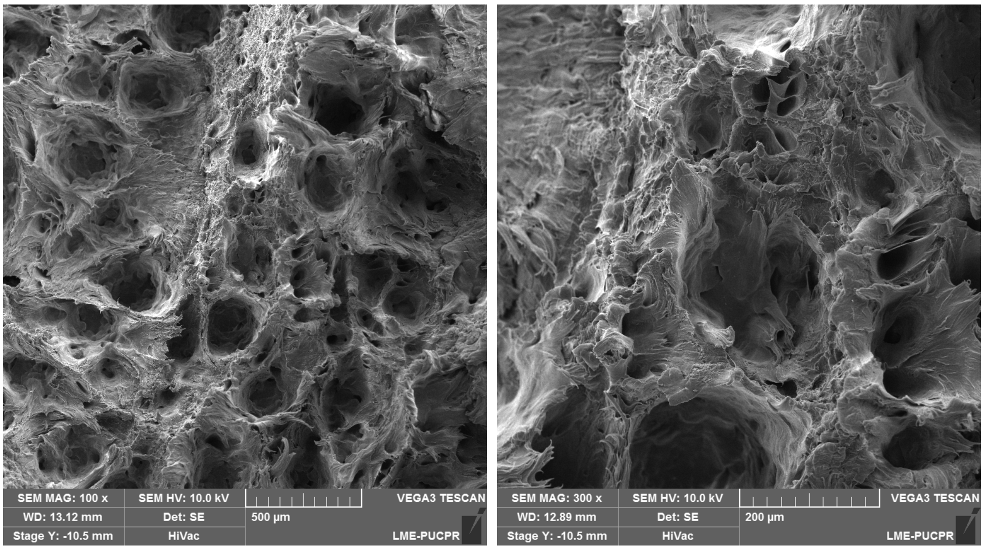

(m) Energy Density: 0.528 J/mm^3 (n) Energy Density: 0.528 J/mm^3

Figure 4.12 – SEM micrographs of fractured PA12 LS surfaces.

phous tie chains and alignment of lamellar crystalline phase along the tensile axis. SEM micrographs revealed the presence of unmolten particles throughout the fractured surface and between layers. As discussed previously, such unmolten particles present a higher degree of crystallinity than molten-recrystalized particles. Therefore a more brittle fracture behavior can be expected as the final degree of crystallinity of the samples is greater at low energy density (DUPIN et al., 2012).

Increasing the energy density promotes a better densification of the particles and interlayer porosity structure evolves to a more dense structure formed by molten-recrystallized phases,a smaller content of unmolten particles surrounded by smaller residual pores. Ductility is improved by the smaller pores which favours slow crack propagation. As the molten-recrystallized phase content increases, overall crystal fraction is reduced, leading to an increase in the plastic strain (MAJEWSKI; ZARRINGHALAM; HOPKINSON, 2008).

4.1.6 Influence of energy density on flexural properties

Figures 4.13a-b show box-whisker plots of flexural modulus and strength as a function of energy densities, respectively. Flexural modulus follows a similar behaviour as tensile modulus, with low modulus values of 800 MPa at very low energy densities and increasing step wisely to 1517 MPa at 0.151 J/mm^3. Flexural modulus oscillates more than tensile modulus within increasing energy density, with values ranging from 1300 and 1600 MPa at energy densities between 0.151 and 0.467 J/mm^3. This might indicate more sensitivity of flexural modulus to the individual SLS parameters. Maximum flexural modulus observed was 1600 MPa at an energy density of 0.2 J/mm^3. For energy densities above 0.5 J/mm^3 there is a pronounced drop in flexural modulus.

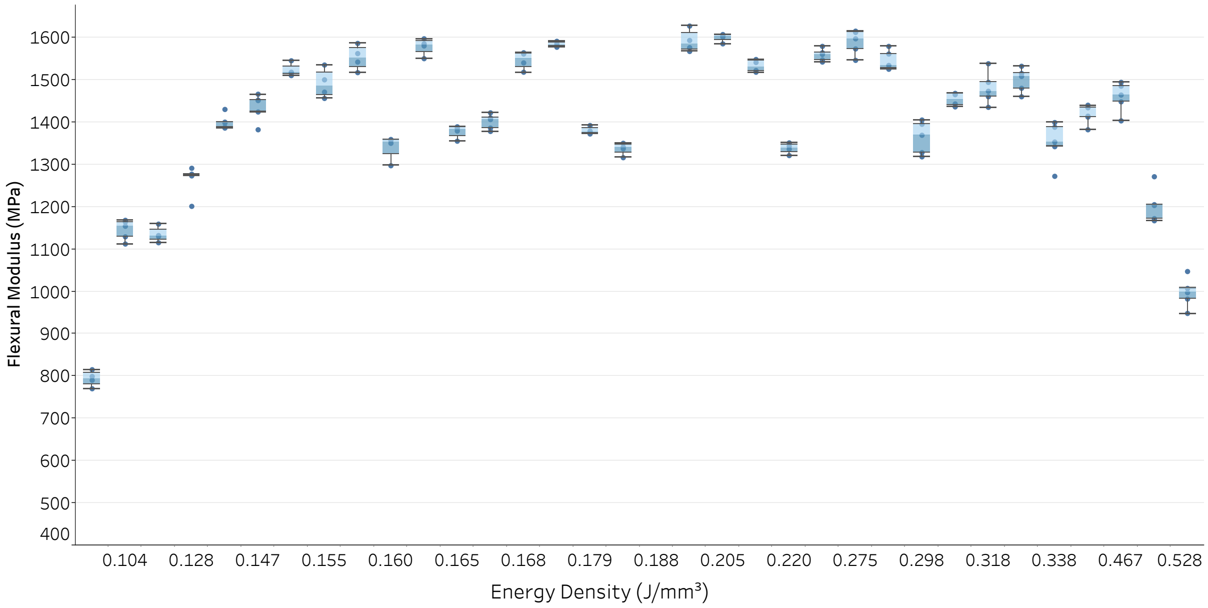

(a)

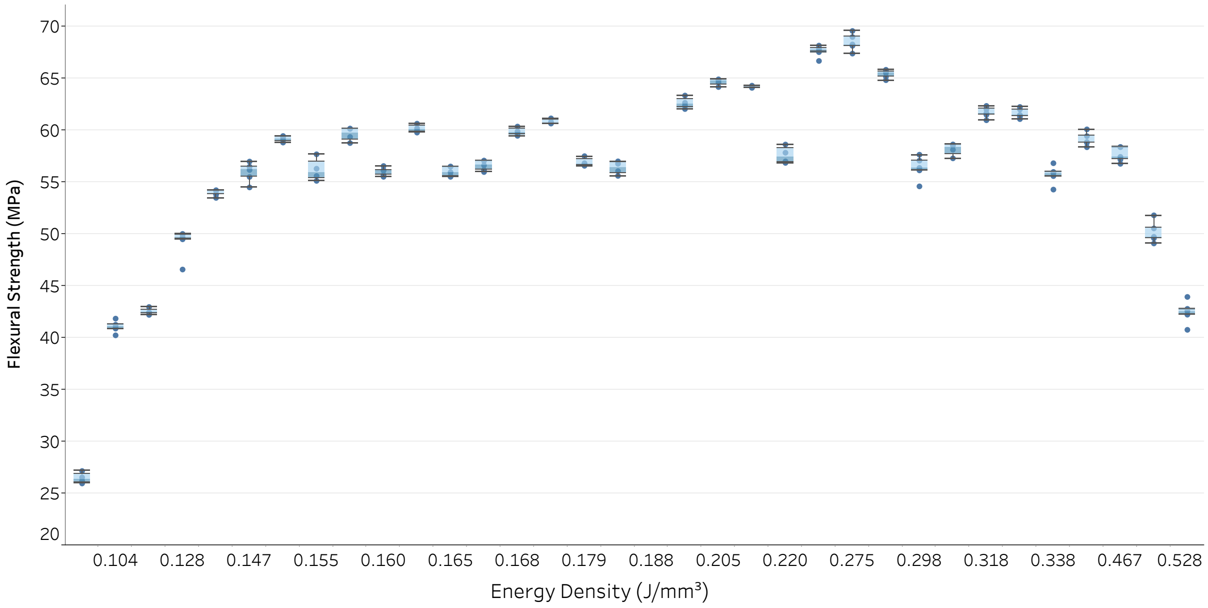

(b)

Figure 4.13 – Influence of energy density on flexural properties for PA12.: (a) Flexural modulus ; (b) Flexural strength.

Flexural strength showed in 4.13b follows a similar behaviour of flexural modulus, with values as low as 26 MPa at 0.091 J/mm^3 and step-wisely increasing to 59 MPa at 0.151 J/mm^3. Between 0.151 and 0.18 J/mm^3 flexural strength oscillated between 55 and 60 MPa. Between 0.19 and 0.29 J/mm^3 there is a tendency to increase flexural strength values , which oscillate between 62 and 68 MPa, achieving an average maximum of 68.24 MPa at 0.275 J/mm^3. Above this energy level up to 0.5 J/mm^3 there is a decrease of the values back to 55-60 MPa area. Above 0.5 J/mm^3 flexural strength sharply decreases to values between 50 and 42 MPa. Compared to tensile strength, flexural strength shows higher oscillation to energy density, suggesting a higher sensibility of flexural properties to individual LS parameters.

4.1.7 Influence of energy density on crystallization behavior

The effects of energy density on crystallization behaviour of LS PA12 were evaluated by XRD and DSC analysis. XRD patterns of PA12 powder and LS PA12 samples processed at different energy densities are shown in Fig. 4.14. PA12 powder XRD reveals the existence of two separate peaks occurring between a 2θ of 20-24°. The first peak at 2θ of 20.92° is associated with the γ crystal form and the second peak at 2θ of 21.9° is associated with the α crystal form.

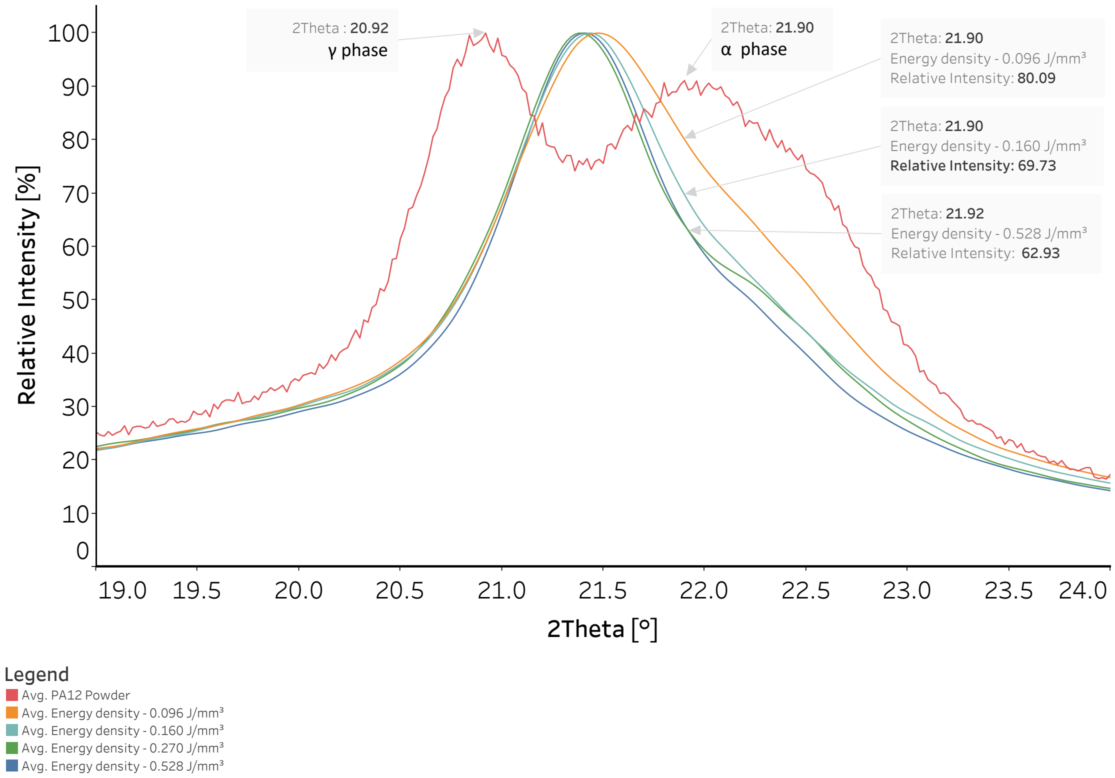

Figure 4.14 – XRD patterns of PA12 powder and LS PA12 samples processed at different energy densities.

LS samples processed at 0.096 J/mm^3 shows a change on crystal structure, with γ form more pronounced but the α form still present as indicated by a higher intensity at the 2θ location of α. It is known that the α form transforms to γ form when heated to melting point (ATKINS; HILL; VELURAJA, 1995). The α form structure reveals that the presence of unmolten particles is more pronounced at this very low energy level, which has corroborates the results observed in SEM images. Furthermore, the presence of two crystal structures after LS has been reported in the literature (DUPIN et al., 2012), (Van

Hooreweder et al., 2013) and is associated with the slow cooling conditions of LS process, which is kept at higher temperature during LS to avoid part warpage which promotes more time for recrystallization to occur.

Increasing the energy density results in XRD narrower peaks at corresponding 2θ positions with a decrease in the relative intensity related to the α crystal form. The reduction in the α crystal form at higher LS energy densities reveals a more effective melting of PA12 particles, increasing the molten-recrystallized fraction of PA12 present in γ form.

DSC measurements of PA12 powder and LS PA12 samples at different energy densities are depicted in Fig.4.15. PA12 powder exhibits a single high melting endotherm with melting peak at 183 °C. The crystallinity degree can be calculated based on the melting area of the DSC and compared to the melting area of a 100% crystalline PA12, which is 209.3 J/g based on Gogolewski, Czerniawska & Gasiorek (1980). Based on the integral of the heat flow curve the calculated crystallinity degree X_C is 30.8%.

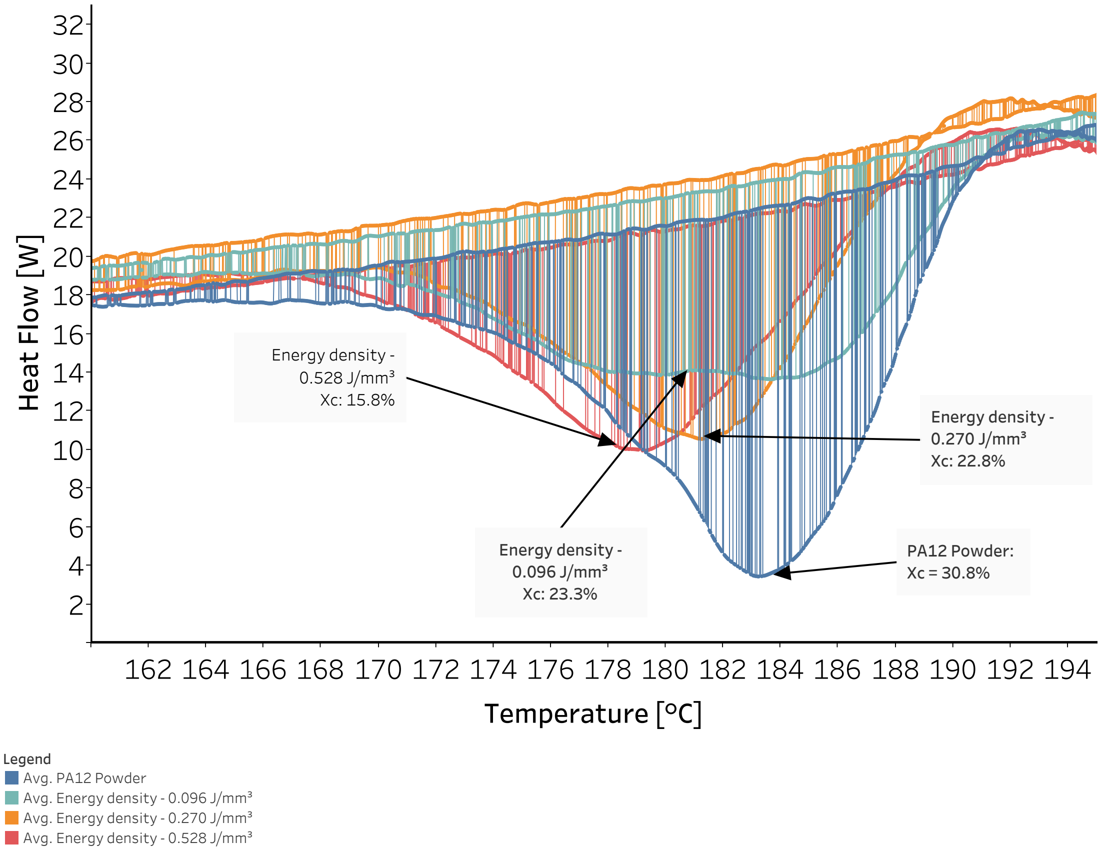

Figure 4.15 – DSC measurements of PA12 powder and LS PA12 samples processed at different energy densities.

DSC endotherm of laser sintered samples processed with 0.096 J/mm^3 reveals the presence of two melting peaks, one at 183 °C and other at 179 °C. The two melting peaks are associated with the presence of both unmolten and melt-recrystallized phases (DUPIN et al., 2012), indicating that the LS energy density applied was not enough to fully melt particles and further confirming the XRD results. The estimated crystallinity degree X_C is 23.3%. At an energy density of 0.270 J/mm^3 there is a single melting peak with melting temperature at 181.5 °C, showing an improvement on the melting of the powder particles and a further decrease on the crystallinity degree to 22.8%. Increasing the LS energy density to 0.528 J/mm^3 shifts the melting temperature to 179 °C and significantly reduces the crystallinity degree X_C to 15.8%.

The reduction in crystal fraction at increasingly LS energy densities is associated with the improvement of melting and consolidation of PA12 powder particles. Improvement of melting conditions results in higher melt-recrystallized phase fraction, which is less crystalline than the unmolten particles, decreasing the overall crystallinity of the material.

XRD and DSC measurements corroborate the observed mechanical behaviour of SLS samples processed at different energy densities. The lower crystal fraction (i.e. higher amorphous fraction) observed for samples produced with higher energy density leads to improved nominal strain at break, as the plastic strain involved in semi-crystalline polymers is governed by the elongation of amorphous tie chains. Nevertheless such behaviour is observed only until a certain energy density, above which the elongation at break is reduced, as observed for the samples produced with 0.528 J/mm^3. At this energy level the polymer degradation may be more pronounced.

To investigate further the observed mechanical behavior at higher energy densities Fig. 4.16 illustrates FTIR spectra of PA12 powder and LS samples processed at different energy levels. Infrared band assignments are shown in Table 4.1 (RHEE; WHITE, 2002). The spectra for PA12 powder and LS samples produced with 0.091 J/mm^3 and 0.270 J/mm^3 remain very similar regarding absorption intensity at different wavenumbers.

For an energy density of 0.528 J/mm^3 the overall absorption at the assigned wavenumbers is increased compared to the FTIR spectra at lower energy densities. The higher absorption may be associated with a higher chain mobility caused by chain scission of PA12 (ZHANG; ADAMS, 2016), indicating that some level of polymer degradation might occur at this LS energy density. Other authors observed this behaviour by measuring viscosity of PA12 samples processed at different energy levels, showing a decrease in viscosity with increased energy densities applied. The decrease in viscosity is associated with a lower polymer molecular weight caused by chain scission (DRUMMER; WUDY; DREXLER, 2014). The higher chain mobility can also be associated with a decrease of crystallinity degree at this energy level.

Additionally no modifications were observed in the region of 1700-1750 cm$^-1$, which is related to carbonyl groups formed during polyamide oxidation (CELINA et al.,

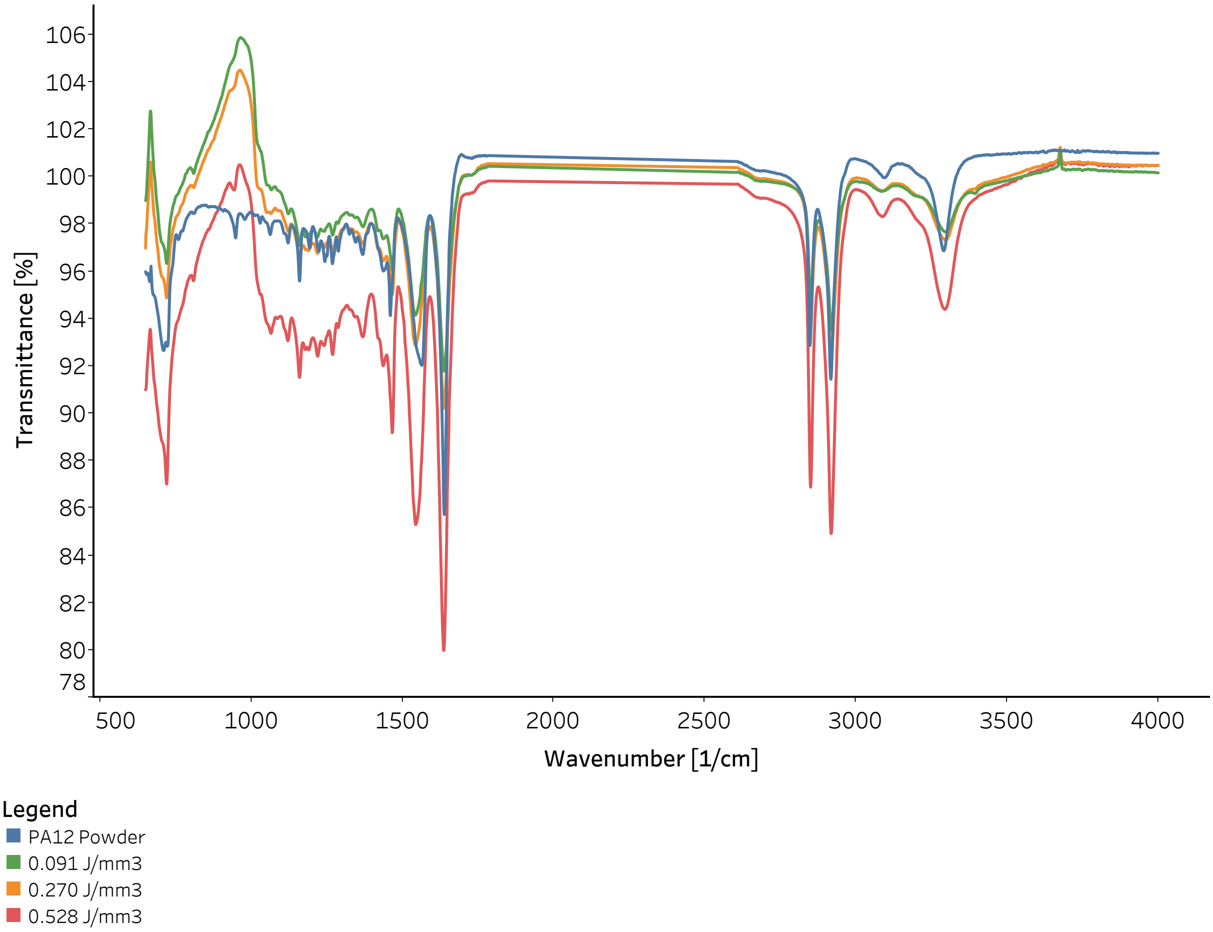

Figure 4.16 – FTIR spectra of PA12 powder and LS PA12 samples processed at different energy densities.

1997). This suggests that the nitrogen atmosphere during LS process protected PA12 from oxidation even at higher energy density levels.

4.2 Gaussian process response surface modelling - PA12

This section presents the results after model training of the dataset using the Gaussian process ($\mathcal{GP}$) described in section 3.5.

4.2.1 Model quality

In order to quantify the proposed model in respect to the input variables, two statistical measures were taken for each desired response variable: root mean square error ($RMSE$), which measures the absolute difference between the modelled and measured values; and the coefficient of determination (R^2), which is derived from the comparison of the variance after model training with the variance of the mean of all measured data.

As a quality criteria of the model the following was considered: for $0.6<R^2<0.9$ the model was considered good for qualitative predictions; for $R^2>0.9$ the model was considered

Table 4.1 – FTIR spectra assignment of PA12 (RHEE; WHITE, 2002).

Wavenumber (cm$^-1$)	Assignment
3294	N—H stretching
3086	Fermi-resonance of N—H stretching
2918	CH2 asymmetric stretching
2850	CH2 symmetric stretching
1636	Amide I (C═O stretching)
1543	Amide II (C—N stretching)
1466	CH2 bend
1436	C═O bend
1419	C═O bend
1368	CH bend, CH2 twisting
1288	CH2 wagging or CH2 twisting
1269	Amide III (C—N stretching + C═O inplane bending)
1242	Gauche carboxyl-methylene group
1219	Gauche nitrogen-methylene group
1190	Splitting of amide II
1159	Skeletal motion involving CONH
1122	C—C stretching
1065	Skeletal motion involving CONH
1028	CONH inplane
980	C—CO stretching
946	CONH inplane
720	CH2 rocking
680	Amide V (α) (C═O out of plane bending)

good for quantitative predictions. For R^2 below 0.6 the model was not considered reliable.

Table 4.2 presents a summary of RMSE and R^2 for each response function. RMSE of accuracy responses are low whereas R^2 for X and Y-direction accuracy are only suitable for qualitative predictions with R^2 of 0.79 and 0.88 respectively. Only Z-direction accuracy model presented a high R^2 of 0.95 which can be used for quantitative predictions.

The $\mathcal{GP}$ trained model for density shows good results for RMSE (close to the RMSE of the training data) and a good R^2 of 0.91. Compared to the literature, polynomial models used presented better R^2 values (HOFLAND; BARAN; WISMEIJER, 2017; WEGNER; WITT, 2012). Surface roughness model showed a higher RMSE, which is in agreement with the results showed in previous sections, where a high variance of the the measured variable was observed, with the model following a similar trend. R^2 of 0.65 was also low

Table 4.2 – Response functions model quality: RMSE and R^2.

Response variable	RMSE	R^2
X-Direction accuracy [%]	0.0267	0.7939
Y-Direction accuracy [%]	0.4815	0.8813
Z-Direction accuracy [%]	1.3864	0.9504
Density [g/cm^3]	0.0149	0.9079
Surface roughness R_a [μm]	1.5703	0.6520
Tensile strength at yield [MPa]	0.59	0.9917
Tensile strength at break [MPa]	0.7746	0.9830
Proportional limit [MPa]	0.6833	0.9443
0.2% offset yield strength [MPa]	0.6593	0.9674
Nominal strain at yield [%]	0.3479	0.9662
Nominal strain at break [%]	0.8424	0.9700
Nominal strain at proportional limit [%]	0.0710	0.7626
Nominal strain at 0.2% offset yield strength [%]	0.0686	0.8458
Elastic modulus [MPa]	29.4507	0.9620
Flexural proportional limit [MPa]	1.3336	0.9417
Flexural offset yield strength [MPa]	0.8188	0.9841
Flexural strength [MPa]	0.6558	0.9937
Flexural modulus [MPa]	25.8510	0.9796
Flexural strain at proportional limit [%]	0.1032	0.7911
Flexural strain at offset yield [%]	0.0881	0.8404
Flexural strain at yield [%]	0.2498	0.6367

and not reliable for quantitative predictions, but qualitative assessment might be inferred.

Considering mechanical properties, both tensile strength at yield and break showed very good RMSE and R^2 of 0.99 and 0.98 respectively, which shows that the $\mathcal{GP}$ trained model is very good for quantitative predictions. Also the results are slightly better than polynomial models which reached R^2 values of 0.97. Proportional limit and and 0.2% offset yield strength also presented good model quality for quantitative assessment, but lower than yield and break strength. The higher variation of the measured variable might play an influence. Model for elastic modulus also showed good quality for quantitative assessment, with R^2 of 0.96. The results are marginally better than polynomial models derived for elastic modulus, where R^2 of of 0.95 were achieved.

Nominal strain at yield and break followed a similar trend of strength, showing very good predictive quality of 0.97. These results are much better than the ones found using polynomial methods, where R^2 of 0.86 were achieved (HOFLAND; BARAN; WISMEIJER, 2017; WEGNER; WITT, 2012). Nominal strain at proportional limit and 0.2% offset yield strength were lower than their corresponding models for strength and only reliable for qualitative assessment.

Flexural properties followed a similar trend than tensile properties. $\mathcal{GP}$ models for strength achieved high R^2 values. Flexural modulus R^2 of 0.98 was higher than tensile modulus. For flexural strain the $\mathcal{GP}$ models also achieved lower R^2 values. $\mathcal{GP}$ model for flexural strain at yield achieved very low correlation factor R^2 of 0.63. This is mainly due to the low sensitivity of this response variable to the input laser sintering variables.

4.2.2 Response surfaces

This subsection presents response surfaces obtained after $\mathcal{GP}$ model training for PA12. A given response variable is a function of the four input variables: laser power, laser scan speed, scan line spacing and layer thickness. This results in a hyperplane in a 5 dimensional space that cannot be graphically presented with all variables. To be able to graphically represent the response surfaces of the output variables, three-dimensional intersection plots of this hyperplane are given, with two input variables in x and y axis and one output variable in the z axis. The remaining two input variables remain constant at the given hyperplane. For each output variable evaluated two three-dimensional graphs are presented: response surface as a function of laser power and laser scan speed at constant scan line spacing and layer thickness; response surface as a function of scan line spacing and layer thickness at constant laser power and laser scan speed.

4.2.2.1 Dimensional accuracy

Figure 4.17a shows the Y-direction accuracy response surface as a function of laser power and laser scan speed at a scan line spacing of 0.4 mm and layer thickness of 120 μm. It can be observed that Y-direction accuracy varies significantly with laser speed, with positive gradient in direction of higher laser speeds. Laser power also influences Y-direction accuracy, although the gradient is smaller and positive towards increasing laser power. Lowest values for Y-direction accuracy were found at a combination of low laser power and low laser speed, increasing with higher laser power and speed but only until laser power reaches around 37 W, above which Y-direction accuracy decreases.

Figure 4.17b shows the Y-direction accuracy response surface as a function of scan line spacing and layer thickness at constant laser power and laser speed of 38 W and 3500 mm/s. Layer thickness is treated as a discrete variable as it was only measured at 120 and 150 μm. Lowest values of Y-direction accuracy are found for a combination of 120 μm and 0.2 mm, with increasing gradient in direction of higher scan line spacing and layer thickness. The gradient effect is more pronounced at low scan line spacing values, being smoothed for higher scan line spacing and layer thickness, meaning that the influence

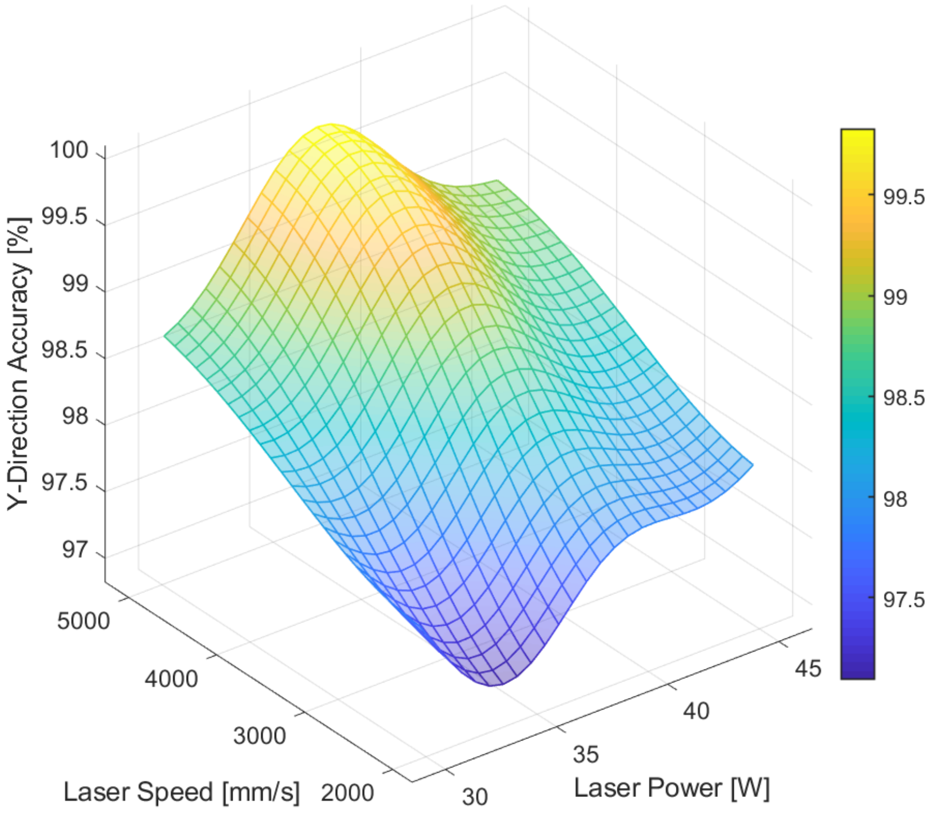

(a) Y-direction accuracy over laser power and laser speed

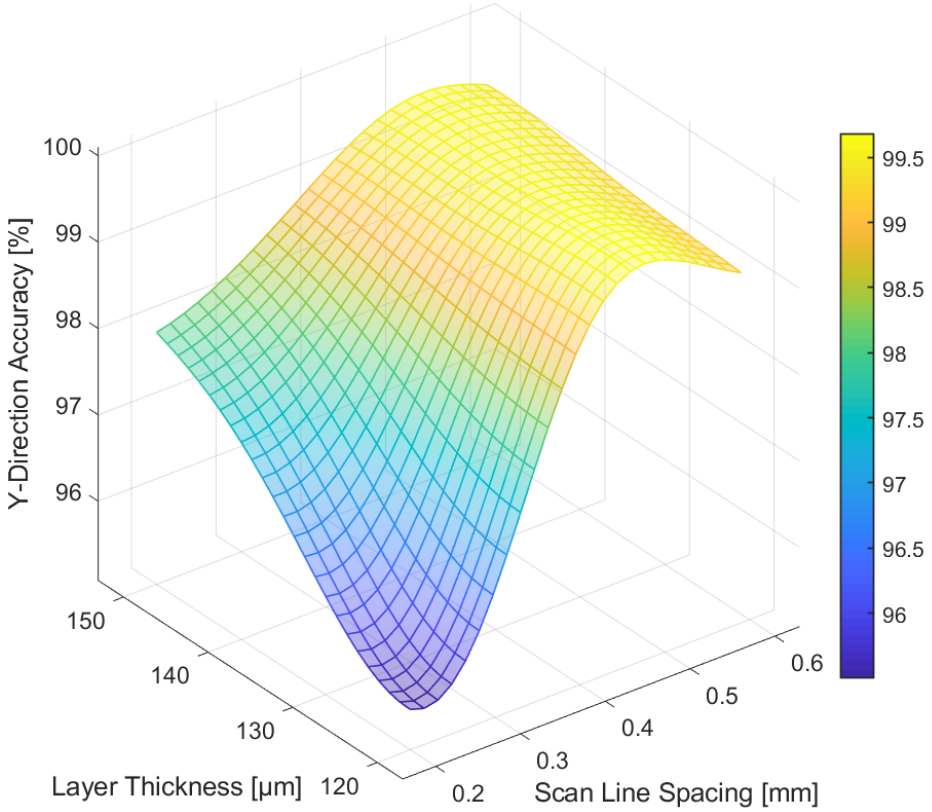

(b) Y-direction accuracy over scan line spacing and layer thickness

Figure 4.17 – Response surfaces for Y-direction accuracy.

of scan line spacing is lower for higher layer thickness values. Also the influence of layer thickness is lower at increasing scan line spacing values, being almost neutral between 0.5 and 0.6 mm.

The results obtained with $\mathcal{GP}$ training for Y-direction accuracy shows that the individual input variables play an important role to describe the response variable. Regarding layer thickness and scan line spacing the tendency is clearly to improve accuracy towards lower energy density values (i.e. higher scan line spacing and layer thickness). Laser power and laser scan speed present a more non-linear effect. This is in agreement with the results found for Y-direction accuracy as a function of energy density (Fig. 4.2), where higher accuracy was found at low energy density values, low accuracy at high energy density, and oscillating between.

The relative relevance of each input parameter on Y-direction accuracy is presented in Fig. 4.18. High relevance values mean that small changes on the input parameters cause significant changes on the response variable whereas low relevance values indicate that changes in the response variable occur only over large input length-scale. The graphic shows all parameters play a relevant role on Y-direction accuracy, with laser power as the most relevant parameter, followed by layer thickness. Scan line spacing is the third most influencing parameter and laser speed the least relevant.

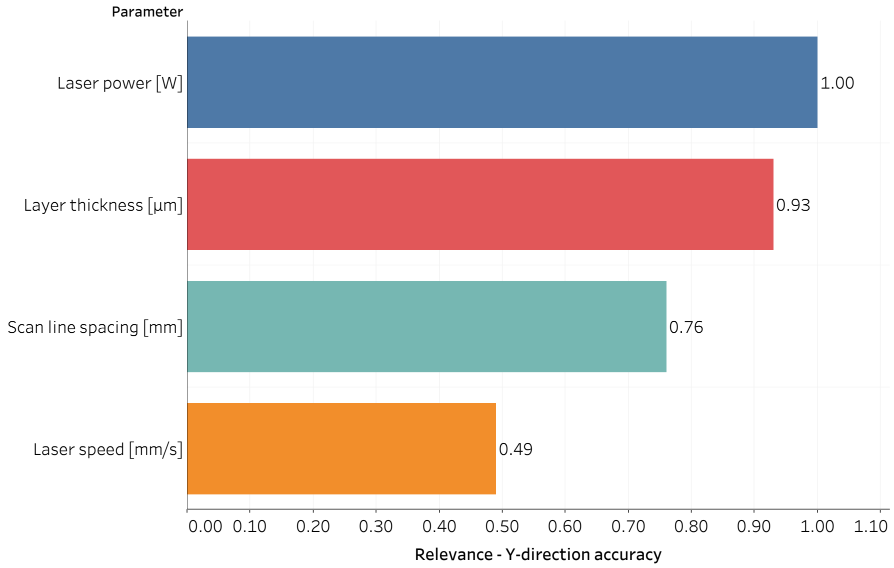

Figure 4.18 – Sensitivity of LS process parameters on Y-direction accuracy.

Figure 4.19a depicts response surface for Z-direction accuracy as a function of laser power and laser speed at a scan line spacing of 0.4 mm and layer thickness of 120 μm. The surface shows low dimensional accuracy (around 86 %) at high laser power and low laser scan speed, increasing in direction to higher laser speed and low laser power, but only until laser power is below 35 W, below this value there is a tendency for decreasing

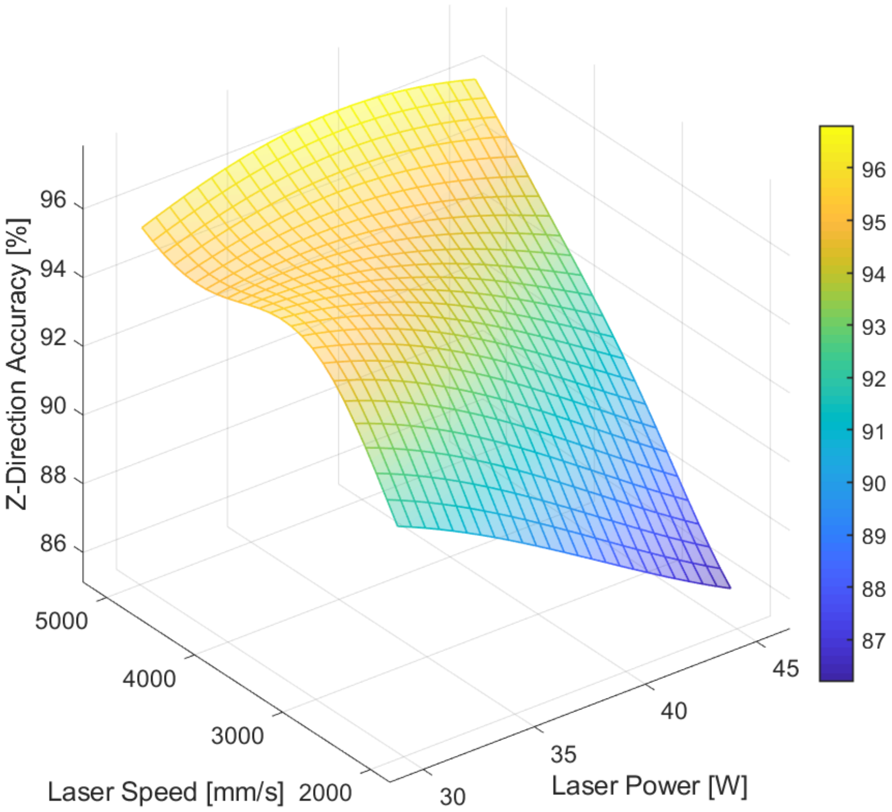

(a) Z-direction accuracy over laser power and laser speed

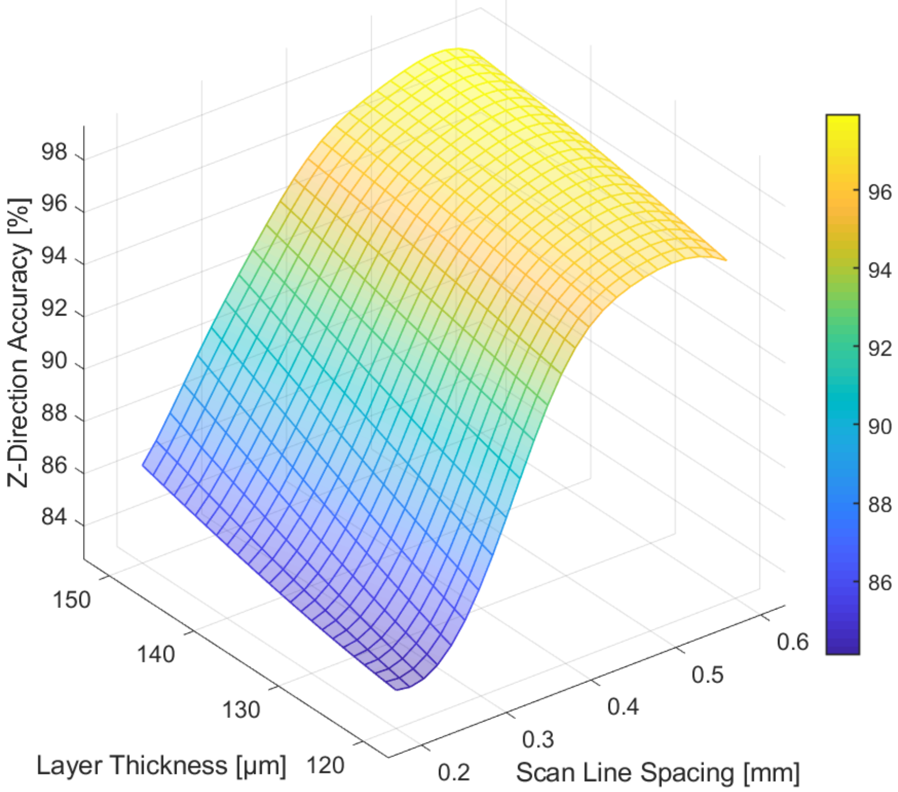

(b) Z-direction accuracy over scan line spacing and layer thickness

Figure 4.19 – Response surfaces for Z-direction accuracy.

Z-direction accuracy. Highest accuracy achieved is 96 % at a laser power between 37-40 W and laser speed of 5000 mm/s. In addition, laser scan speed shows higher influence on Z-direction accuracy compared to laser power.

Response surface for Z-direction accuracy as a function of scan line spacing and layer thickness are shown in Fig. 4.19b at constant laser power and laser speed of 38 W and 3500 mm/s. Lowest values of 84 % are found for low scan line spacing of 0.2 mm and layer thickness of 120 μm. Accuracy increases in direction of increasing layer thickness and scan line spacing reaching maximum values at the highest scan line spacing of 0.6 mm and layer thickness of 150 μm. The influence of layer thickness is less pronounced than scan line spacing, which contributes strongly to Z-direction accuracy.

Both graphics presented show an increase in Z-direction accuracy towards low energy densities. Indeed this was observed in Fig 4.3 and can be explained based on the idea that higher energy densities perform adequate consolidation of powders but also consolidate particles in the heating zone of the laser beam, therefore increasing the amount of material joined together at each layer and consequently worsening accuracy.

Most relevant parameter on Z-direction accuracy is scan line spacing as presented in Fig 4.20. Second parameter is laser scan speed, with much less relevance. Laser power and layer thickness are the least relevant parameters with around 0.2 relevance.

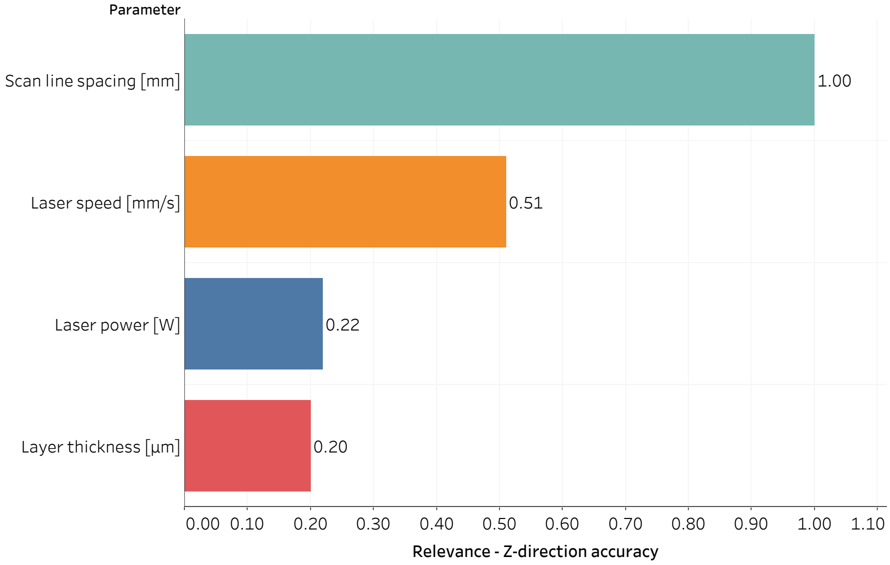

Figure 4.20 – Sensitivity of LS process parameters on Z-direction accuracy.

4.2.2.2 Surface roughness

Figure 4.21a shows the $\mathcal{GP}$ trained surface response for average surface roughness R_a as a function of laser power and laser speed for constant layer thickness of 150 μm and

0.6 *mm* scan line spacing. At low scan speeds surface roughness has more or less stable values around 14 μm independently of the laser power applied. Increasing the laser speed above 3500 mm/s leads to rougher surfaces of R_a above 18 μm, reaching a maximum of 24 μm at 37 W and 4500 mm/s.

The surface is generated for a scan line spacing of 0.6 *mm*, implying that the distance between laser lines is higher than the laser beam radius, therefore no overlapping between laser lines is present. The model captures the behavior observed previously in Figure 4.7, showing the contribution of low laser speed to reduce the influence of no overlapping on surface roughness.

Figure 4.21b depicts the surface for average surface roughness R_a as a function of scan line spacing and layer thickness at constant laser power of 38 W and laser speed of 3500 mm/s. Lowest surface roughness values of 13 μm are found at 0.3 *mm* scan line spacing, increasing with higher scan line spacing. Layer thickness plays a minor role on surface roughness, although its influence increases towards higher scan line spacing values.

The relative influence of the individual parameters on surface roughness is depicted in Fig. 4.22. Laser speed presents the highest sensitivity overall, followed by scan line spacing. Layer thickness and laser power present lowest relevance, although not neglectful.

It is important to remark that the model quality achieved for surface roughness was intermediate (R^2 of 0.65) and only good for qualitative assessment, therefore the response

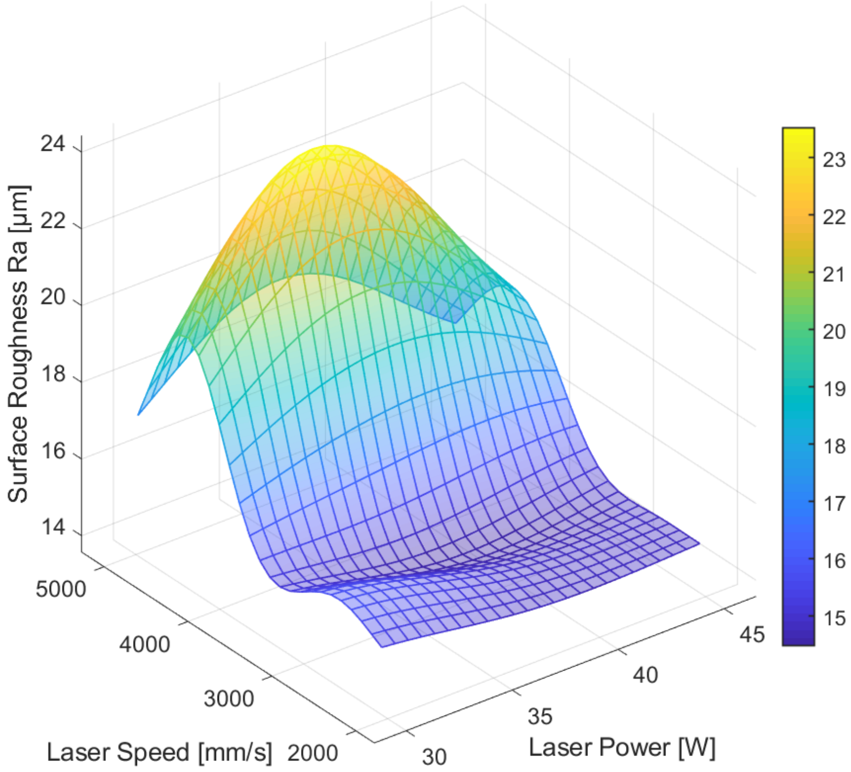

(a) Surface roughness R_a over laser power and laser speed

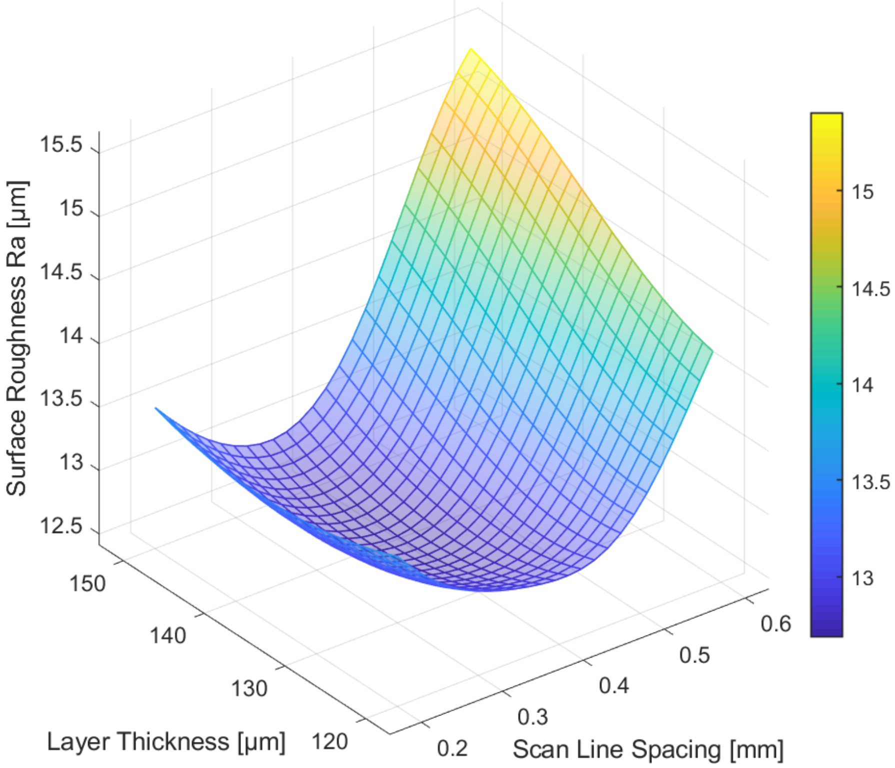

(b) Surface roughness R_a over scan line spacing and layer thickness

Figure 4.21 – Response surfaces for surface roughness R_a.

surfaces obtained can only be evaluated in this light.

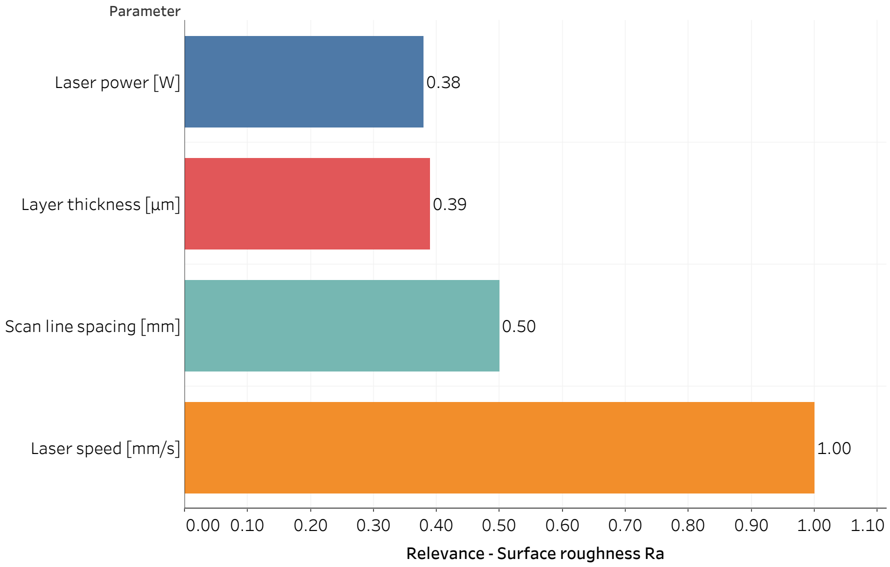

Figure 4.22 – Sensitivity of LS process parameters on surface roughness.

4.2.2.3 Density

Figure 4.23a shows the $\mathcal{GP}$ trained surface response for density as a function of laser power and laser speed for constant layer thickness of 150 μm and 0.4 mm scan line spacing.

Density starts with low values of 0.84 g/cm^3 at high laser speed and low laser power, increasing sharply with a gradient in direction to lower laser speeds and higher laser power, decreasing again at laser speed below 2500 mm/s. At laser speed between 3500-400 mm/s and maximum laser power of 45 W highest density of 0.96 g/cm^3 is found. At very low laser speeds the contribution of laser power to density is small whereas laser speed plays a major influence over the whole response surface evaluated.

Density over scan line spacing and layer thickness at 2000 mm/s laser speed and 45 W laser power are shown in Figure 4.23b. The response surface plotted was chosen due to illustrate the inverse effect the variables have when high energy density parameter values (i.e. laser power and speed) are used. The lowest density values are found at low scan line spacing and layer thickness. The use of these values in combination to the other parameters generates a negative effect on density as too much energy is applied over the powder bed, contributing to increase the consolidation of powder particles nearby the heating zone of the laser and leading to a volume increase of the part and reduction in density. At this

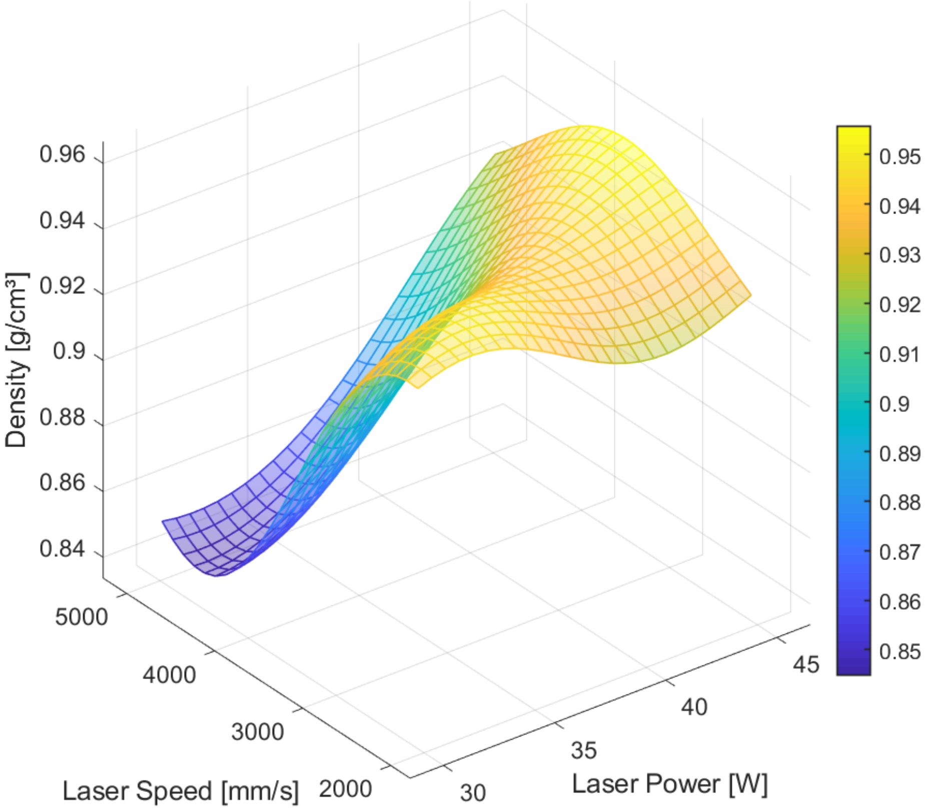

(a) Density over laser power and laser speed

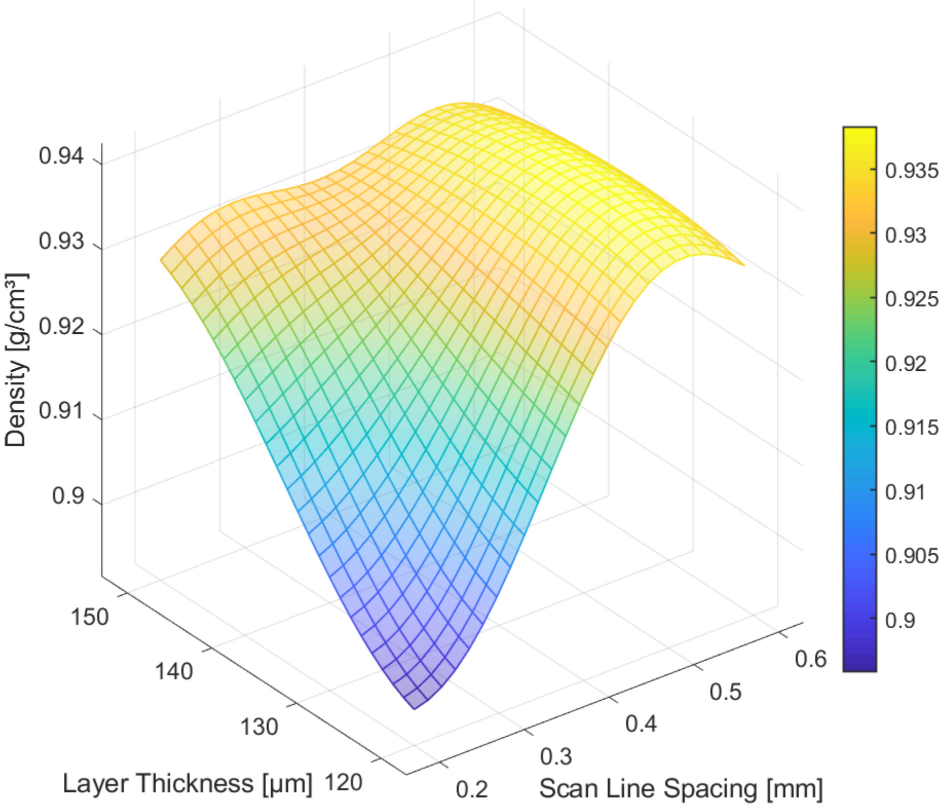

(b) Density over scan line spacing and layer thickness

Figure 4.23 – Response surfaces for density.

already high energy level, density is improved towards higher layer thickness's and scan line spacing, as they help reducing energy density level and parts volume increase.

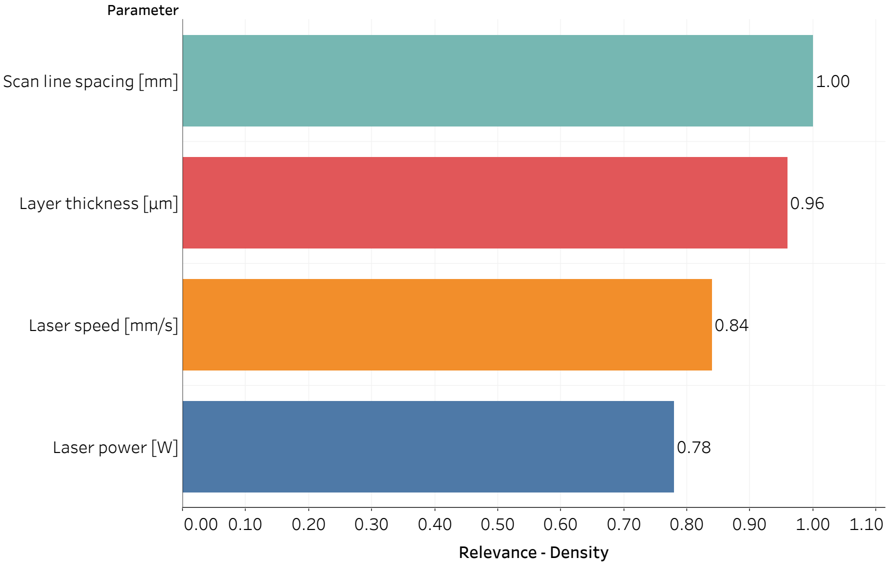

Figure 4.24 – Sensitivity of LS process parameters on density.

Considering the sensitivity of process parameters on density, all parameters present a high influence on the response of this variable as presented in Fig. 4.24. Scan line spacing and layer thickness are the most relevant followed by laser speed and laser power.

4.2.2.4 Proportional limit

Figure 4.25a shows the response surface for proportional limit over laser power and laser speed for constant layer thickness of 150 μm and 0.4 mm scan line spacing.

Lowest values for proportional limit are found at low laser power and high laser speed, gradually increasing in direction to higher laser power and laser speed. The gradient in direction of laser speed is higher than laser power gradient, showing that laser speed might influence more significantly this response variable. Interestingly the highest proportional limit of 20 MPa is found for low laser speed and low laser power.

Proportional limit over scan line spacing and layer thickness are depicted in Fig. 4.25b. Laser power and laser speed are fixed at 38 W and 5000 mm/s. The combination of high scan line spacing and layer thickness leads to very low proportional limit values of 8 MPa, which gradually increase in direction of lower scan line spacing. Layer thickness influences proportional limit more significantly at high scan line spacing, decreasing its relevance at lower scan line spacing. The response surface reveals a plateau starting at 0.35 mm, above which proportional limit varies little with the input parameters.

The relevance of the individual parameters on proportional limit is presented in Fig. 4.26. Overall layer thickness has the highest influence over proportional limit, followed by scan line spacing, laser speed and laser power.

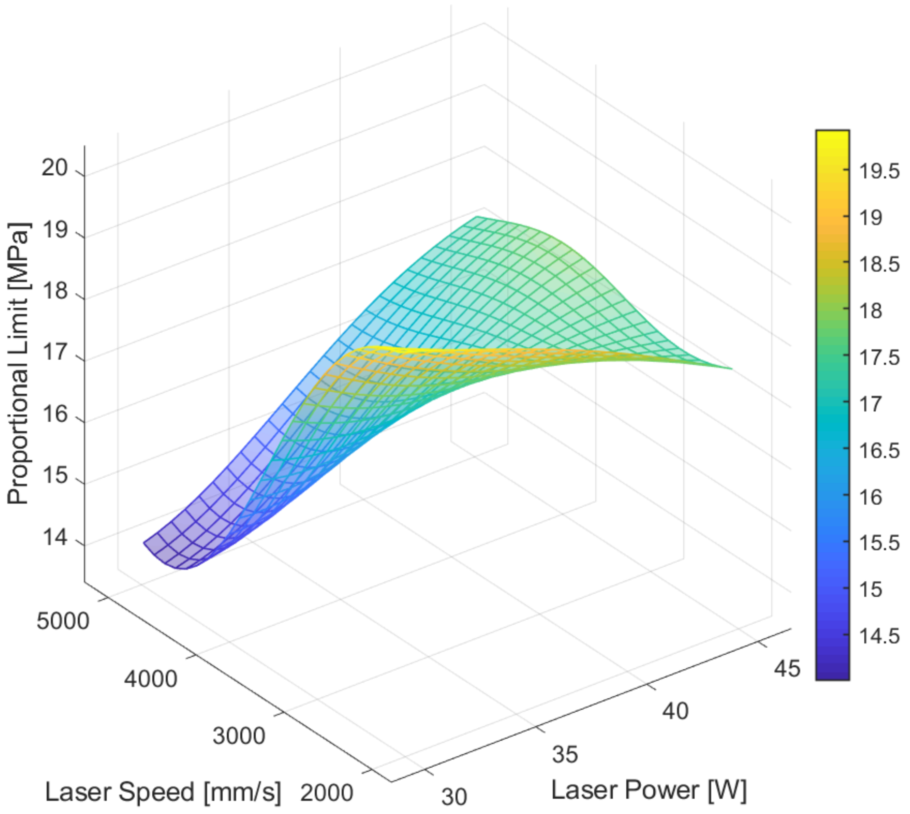

(a) Proportional limit over laser power and laser speed

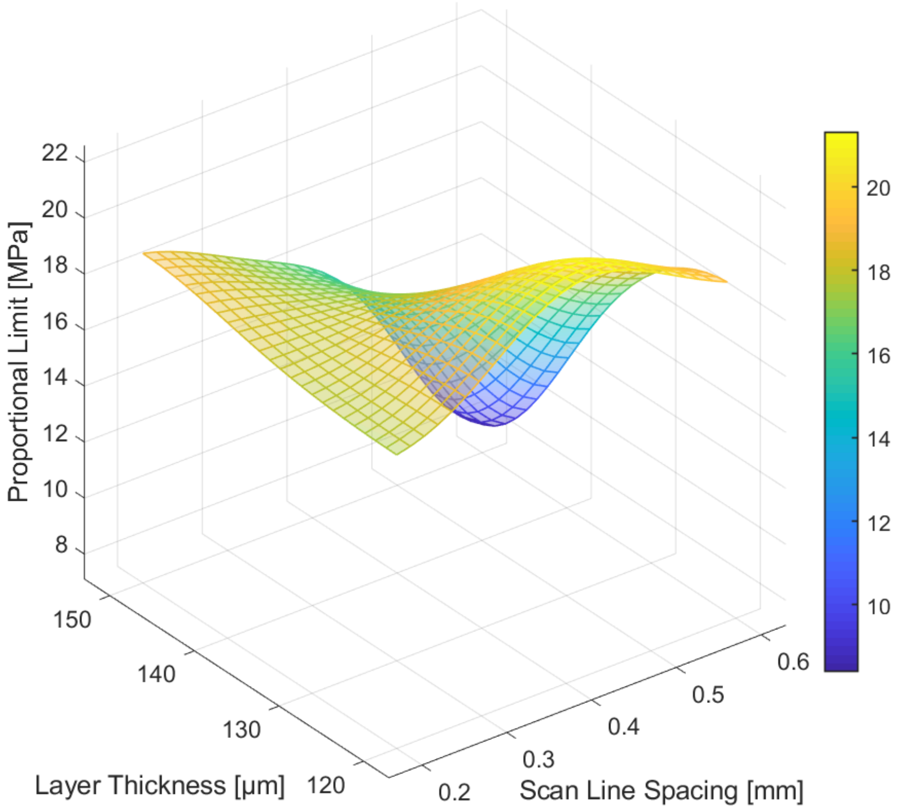

(b) Proportional limit scan line spacing and layer thickness

Figure 4.25 – Response surfaces for proportional limit.

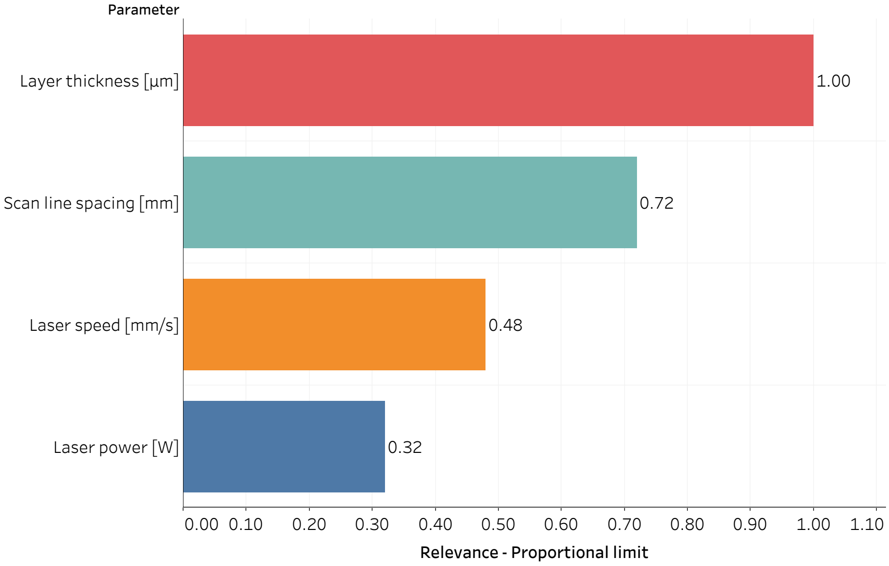

Figure 4.26 – Sensitivity of LS process parameters on proportional limit.

4.2.2.5 Elastic modulus

Figure 4.27a shows the response surface for elastic modulus over laser power and laser speed for constant layer thickness of 150 μm and 0.4 mm scan line spacing. Lowest values for elastic modulus (1350 MPa) are found at low laser power and high laser speed, increasing sharply in both direction towards higher laser power and lower laser speed. Highest elastic modulus of 1750 MPa are found at maximum laser power and laser speed between 4500-4000 mm/s.

There is also one local maximum at very low laser speed of 2000 mms and low laser power of 30 W. Further increase in laser power and reduction in laser speed leads to a reduction on elastic modulus.

Fixing laser power at 38 W and laser speed at 3500 mm/s, the generated response surfaces of elastic modulus over scan line spacing and layer thickness are shown in Fig. 4.27b. The surface has a typical horse cell shape, with lowest values at the two extremes of the surface located at 120 μm and 0.2 mm and 150 μm and 0.6 mm. Between the low extreme points elastic modulus increases reaching a maximum of 1650 MPa at a layer thickness of 150 μm and scan line spacing between 0.3 and 0.4 mm. Scan line spacing provides the characteristic non-linear shape of the surface. Layer thickness has major influence on elastic modulus as well, but its behaviour depends strongly on the scan line spacing level. At scan line spacing between 02 and 0.45 mm higher layer thickness leads to higher elastic modulus, whereas at higher scan line spacing values the opposite trend is observed.

As discussed in subsection 4.9, the linear properties of polymers depends strongly

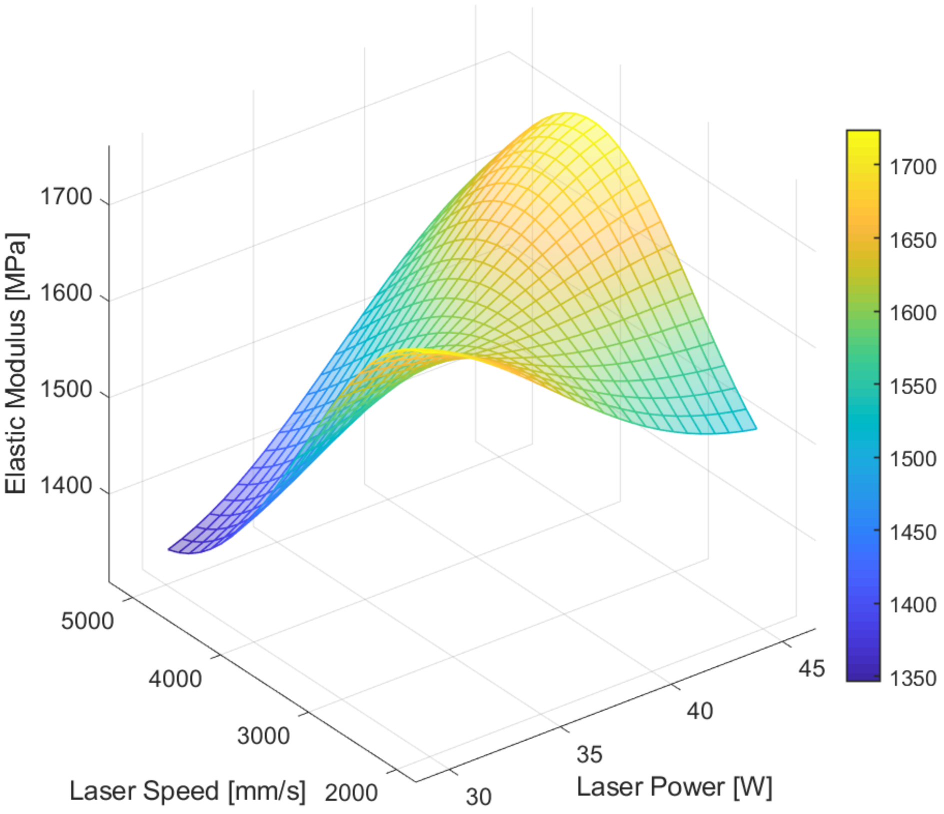

(a) Elastic modulus over laser power and laser speed

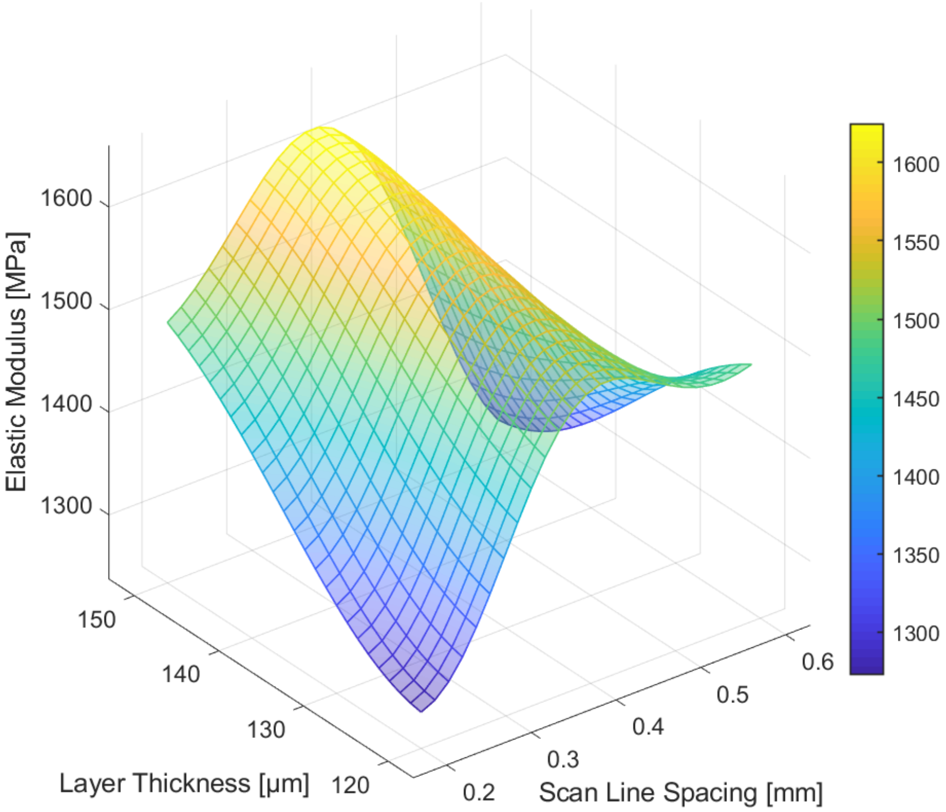

(b) Elastic modulus scan line spacing and layer thickness

Figure 4.27 – Response surfaces for elastic modulus.

on the balance between porosity and crystal fraction present after LS. It was observed that such crystal fraction reduction could provide a decrease in elastic modulus for energy densities above 0.29 J/mm^3. The $\mathcal{GP}$ trained model successfully described this behaviour by showing a reduction in elastic modulus in direction to higher energy densities, exemplified here as an increase in laser power and decrease in laser speed as depicted in Fig. 4.27a. This region corresponds to an energy density above 0.29 J/mm^3. Also a reduction in elastic modulus due to high porosity could be described by the model as observed in region of very low laser power and high laser speed.

Elastic modulus is influenced by all parameters studied as shown in Fig. 4.28. Similar to proportional limit, scan line spacing and layer thickness have the highest relevance, followed by laser speed and laser power. It seems logical to attribute the highest influence on linear properties to layer thickness and scan line spacing, as they influence the amount of layers and laser lines necessary to build a part. On the other hand the response surface shown in Fig. 4.27b shows that this behaviour is of high non-linear nature. For instance, at 0.2 mm scan line spacing and 120 μm layer thickness (energy density of 0.45 J/mm^3) it would be expected to have higher elastic modulus due to the higher concentration of laser lines and layers in the part, but the opposite is found. Again this is due to the balance between porosity and crystal fraction described before, with the reduction in crystal fraction playing a major role in decreasing elastic modulus, as described in 4.1.7.

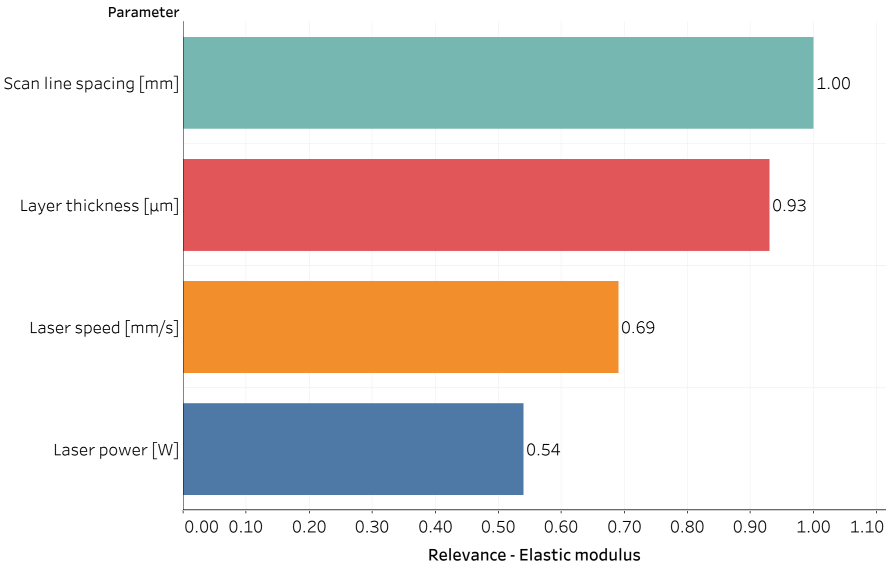

Figure 4.28 – Sensitivity of LS process parameters on elastic modulus.

4.2.2.6 Tensile yield strength

Figure 4.29a shows the gaussian process trained response surface for tensile yield strength over laser power and laser speed at a scan line spacing of 0.4 mm and layer thickness of 150 μm. The model reveals low values of tensile strength (30 MPa) at low laser power and high laser speed, increasing in direction of higher laser power and lower laser speed. Laser speed improves yield strength for a laser power below 35 W, above this level a reduction in yield strength is started for a given laser power. A similar, yet smoother, behavior can be observed for laser power, which contributes to higher yield strength values but only until laser speed is above 2500 mms. Local maximum is found for laser power of 45 W and laser speed between 3000-3500 mm/s.

Keeping a constant laser power of 38 W and laser speed of 3500 mm/s, the Gaussian process trained response surface of yield strength over scan line spacing and layer thickness is depicted in 4.29b. The surface shape shows low yield strength values at high scan line spacing and layer thickness and increasing with a gradient in direction towards lower layer thickness's and scan line spacing, reaching maximum values of 45 MPa at a scan line spacing of 0.3 mm where a small plateau is reached. Following the gradient to smaller layer thickness and scan line spacing reduces yield strength. Scan line spacing seems to influence more strongly the response variable at this point in the hyperplane, specially for higher layer thickness. Yield strength also responds to layer thickness variations, mainly at scan line spacing values at the extremes of the surface, i.e, between 0.5-0.6 mm and below 0.3 mm.

Yield strength is basically governed by the energy density delivered to the power bed. At very low energy densities (e.g. high laser speed and low laser power), there is not enough consolidation of the polymer powders, leading to high porosity and consequently low yield strength. At adequate levels of energy density stable yield strength values of 45 MPa can be reached, mainly due to the low porosity achieved and adequate crystal fraction. When too high energy density is applied (e.g. low layer thickness and scan line spacing combined to already high laser power) there is a reduction in yield strength which can be caused by parts distortion in volume, polymer degradation and reduction in overall crystal fraction as already discussed in subheading 4.1.5.

Relative relevance of input variables to yield strength are shown in Fig. 4.30. Layer thickness and scan line spacing are the most relevant variables derived from the $\mathcal{GP}$ training. Although lower, yield strength also shows sensitivity to laser speed and to laser power in a lower extent.

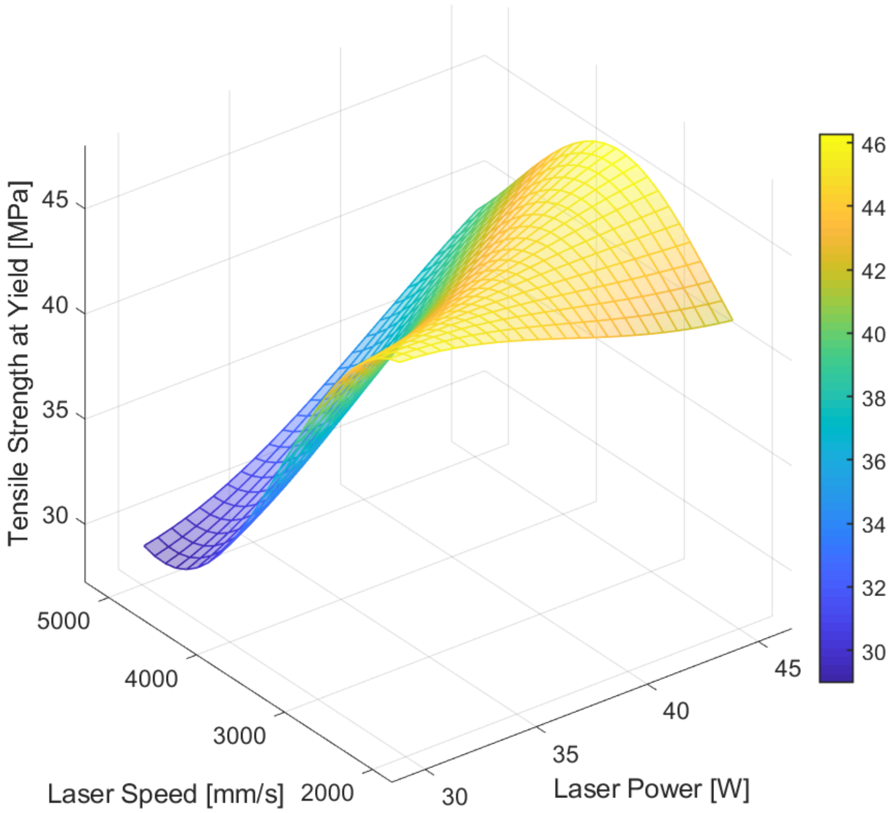

(a) Tensile yield strength over laser power and laser speed

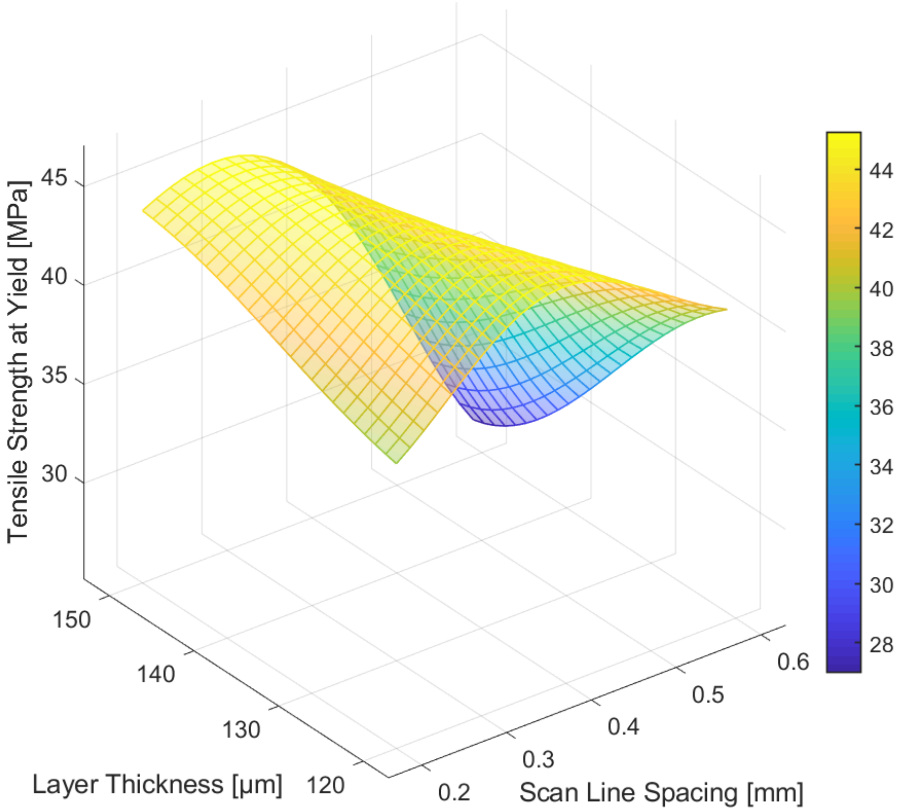

(b) Tensile yield strength scan line spacing and layer thickness

Figure 4.29 – Response surfaces for tensile strength.

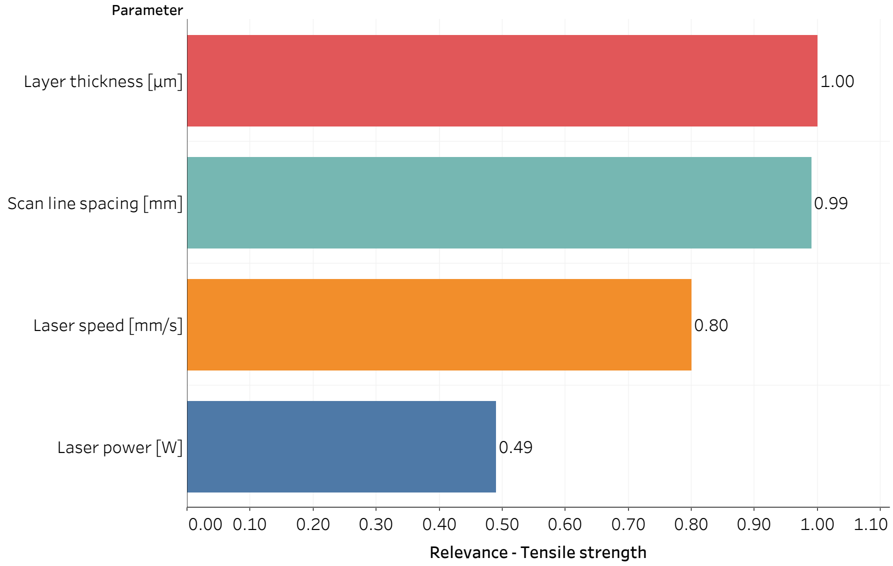

Figure 4.30 – Sensitivity of LS process parameters on tensile yield strength.

4.2.2.7 Nominal strain at break

Figure 4.31a depicts nominal strain at break over laser speed and laser power at 0.4 *mm* scan line spacing and 150 *µm*. Lowest values of 5 % are found at the lowest laser power and highest laser speed applied. A first smooth gradient in direction to higher laser power and laser speed is observed, which gradually sharpens as laser power and speed increases. Maximum nominal strain of 20 % is achieved at 37 *W* and 2000 *mm/s*. Further advance in direction towards lower laser speed and high laser power results in a decrease on nominal strain.

Keeping constant laser power at 38 *W* and laser speed at 2000 *mm/s* the response surface of nominal strain at break over scan line spacing and layer thickness are shown in Fig. 4.31b. Lowest values are observed at the extremities of the surface, located 120 *µm* layer thickness and 0.2 *mm* scan line spacing and 150 *µm* and 0.6 *mm*. At 150 *µm* layer thickness, decreasing scan line spacing sharply increases strain at break, reaching a maximum of 21 % at 0.3 *mm* and decreasing at lower scan line spacing values. At 120 *µm* layer thickness a similar behavior is observed, except that a maximum strain at break of 18 % is reached at a higher scan line spacing of 0.5 *mm*, decreasing with lower scan line spacing values.

As discussed in subsection 4.1.5, applying laser sintering parameters to increase energy density promotes better densification of the part, reducing porosity and improving ductility. Additionally crystal fraction of the samples are decreased also improving plastic strain behavior. The Gaussian process model for nominal strain at break describes this behavior in detail and also captures regions where energy density is excessively high to

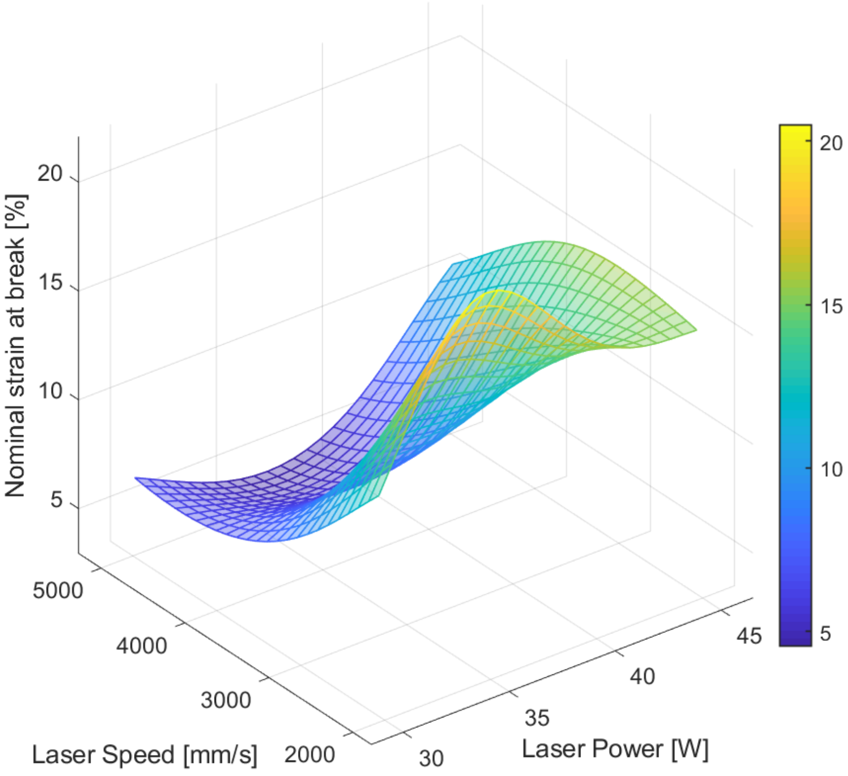

(a) Nominal strain at break over laser power and laser speed

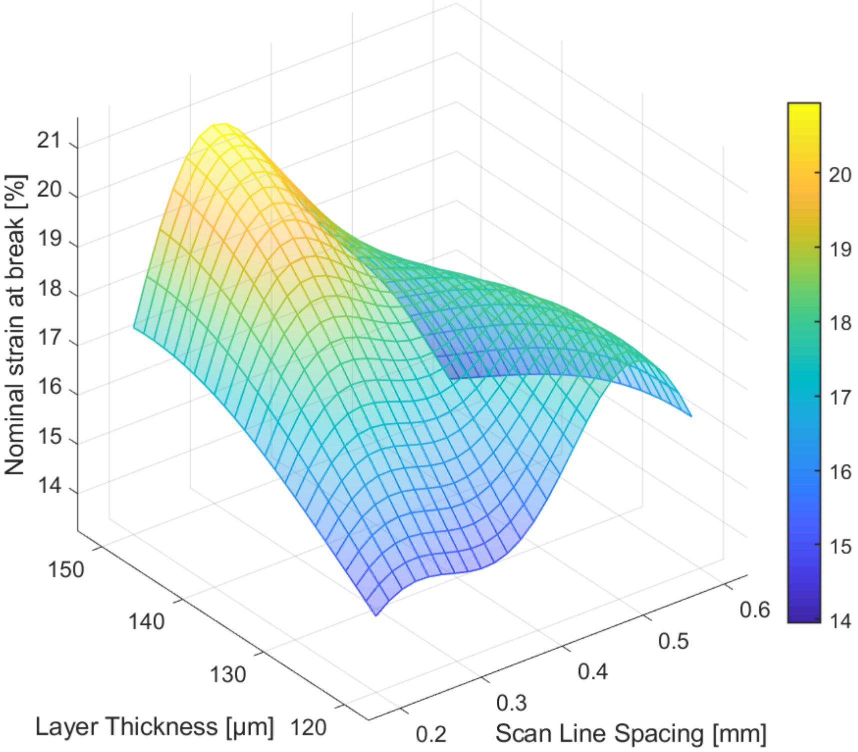

(b) Nominal strain at break over scan line spacing and layer thickness

Figure 4.31 – Response surfaces for nominal strain at break.

cause a negative impact on nominal strain. This is observed in both surfaces presented at regions of high energy density. For instance at 120 μm layer thickness and 0.2 mm scan line spacing in Fig. 4.31b and at 45 W laser power and 2000 mm/s laser speed in Fig. 4.31a. Also the model described the effect of low energy density LS parameters where high porosity is present, leading to poor consolidation of polymer particles and fragile fracture in samples. This is illustrated in Fig. 4.31a at low laser power and high laser speed area.

Relative relevance of input parameters on nominal strain at break are given in Fig. 4.32. Scan line spacing has the highest relevance followed by laser power, laser speed and layer thickness with a smaller relevance.

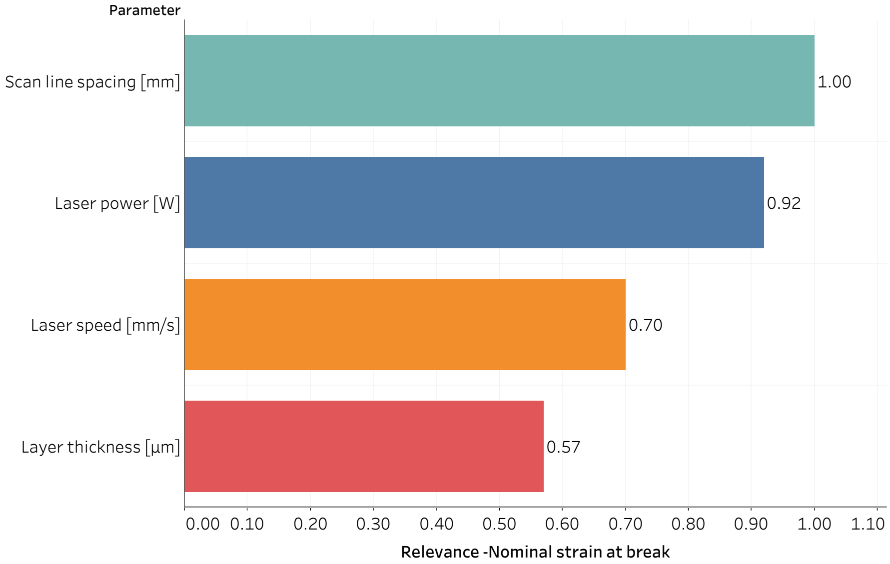

Figure 4.32 – Sensitivity of LS process parameters on nominal strain at break.

4.2.2.8 Flexural modulus

Flexural modulus over laser power and laser speed at 0.2 mm scan line spacing and 150 μm are given in Fig. 4.33a. Lowest values for flexural modulus are found for low laser speed and laser power. Flexural modulus is improved with a gradient towards low laser power and high laser speed, reaching a maximum of 1600 MPa at 30 W laser power and between 4000-4500 mm/s laser speed. Increasing laser power while keeping laser speed constant improves flexural modulus only at low laser speed region.

The response surface for flexural modulus over scan line spacing and layer thickness at 3500 mm/s laser speed and 45 W is depicted in Fig. 4.33b. The surface has a bell shape with local minimum of 1400 MPa at the extremities of the map located at: layer thickness of 120 μm layer thickness and 0.6 mm and 0.2 mm scan line spacing; 150 μm layer thickness and 0.2 mm. At 120 μm layer thickness there is a depression at 0.4 mm scan line spacing giving flexural modulus value of 1350 MPa. Local maximum flexural

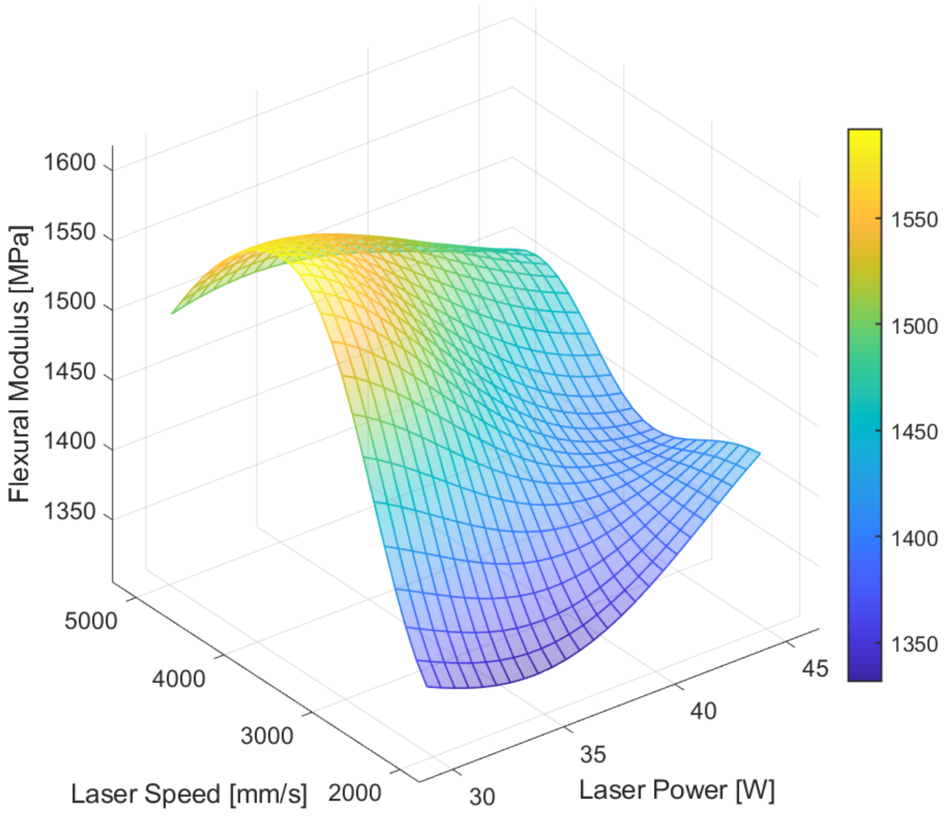

(a) Flexural modulus over laser power and laser scan speed

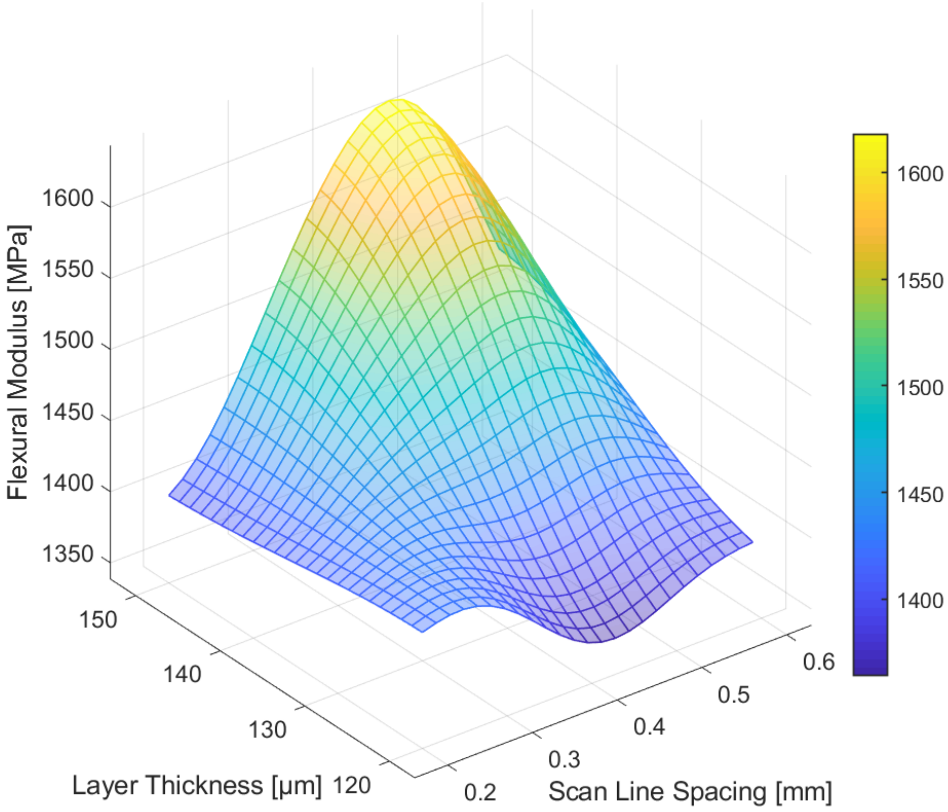

(b) Flexural modulus over scan line spacing and layer thickness

Figure 4.33 – Response surfaces for flexural modulus.

modulus of 1600 MPa is found at 150 μm layer thickness and between 0.4-0.5 mm scan line spacing.

Both graphics illustrate how conflicting and non-linear the LS parameters choice can be depending on the energy region in the hyperplane. For instance at a low scan line spacing region (high energy density delivered from laser beam) the choice of higher laser speed and low laser power leads to better flexural modulus. In a similar manner at a high laser power it might be appropriate to choose for higher scan line spacing and higher layer thickness.

Figure 4.34 depicts the relative relevance of the individual LS parameters on flexural modulus. Laser speed and scan line spacing have the highest relevance followed by laser power and to a lower extent layer thickness. Flexural modulus is sensitive to all parameters on some degree and none of them should be neglected in the model.

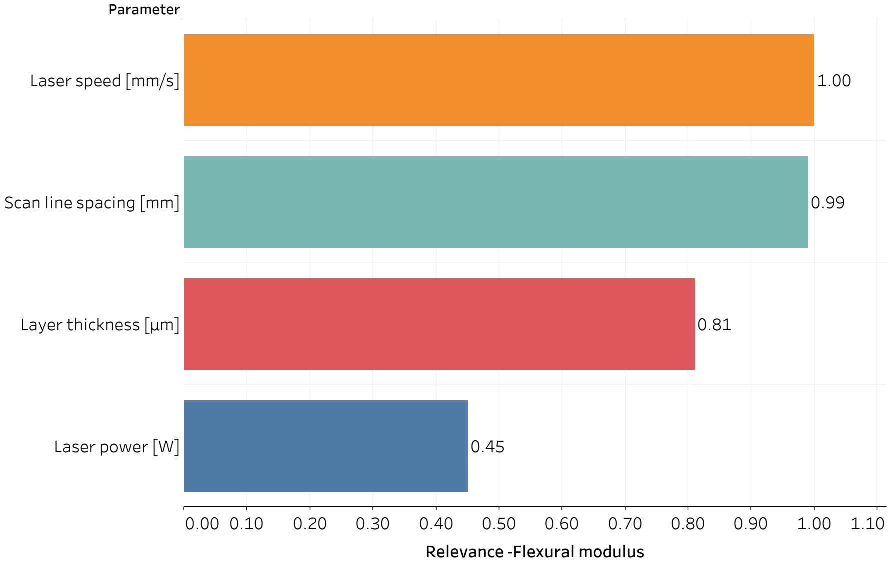

Figure 4.34 – Sensitivity of LS process parameters on flexural modulus.

4.2.2.9 Flexural strength

Flexural strength over laser power and laser speed at 0.4 mm scan line spacing and 150 μm are given in Fig. 4.35a. The surface shows a valley of 45 MPa at 4000 mm/s and 30 W. Between 30-40 W the model captures an opposite effect on laser speed, increasing flexural strength at higher laser speeds. This effect is stronger at lower laser power. Flexural strength increases in direction of higher laser power and lower laser speed. A plateau is reached around 3000 mm/s and laser power above 35 W with a local maximum of 65 MPa. Further decrease in laser speed worse flexural strength. Laser power has a stronger effect at lower laser speed and laser speed has a stronger effect at lower laser power.

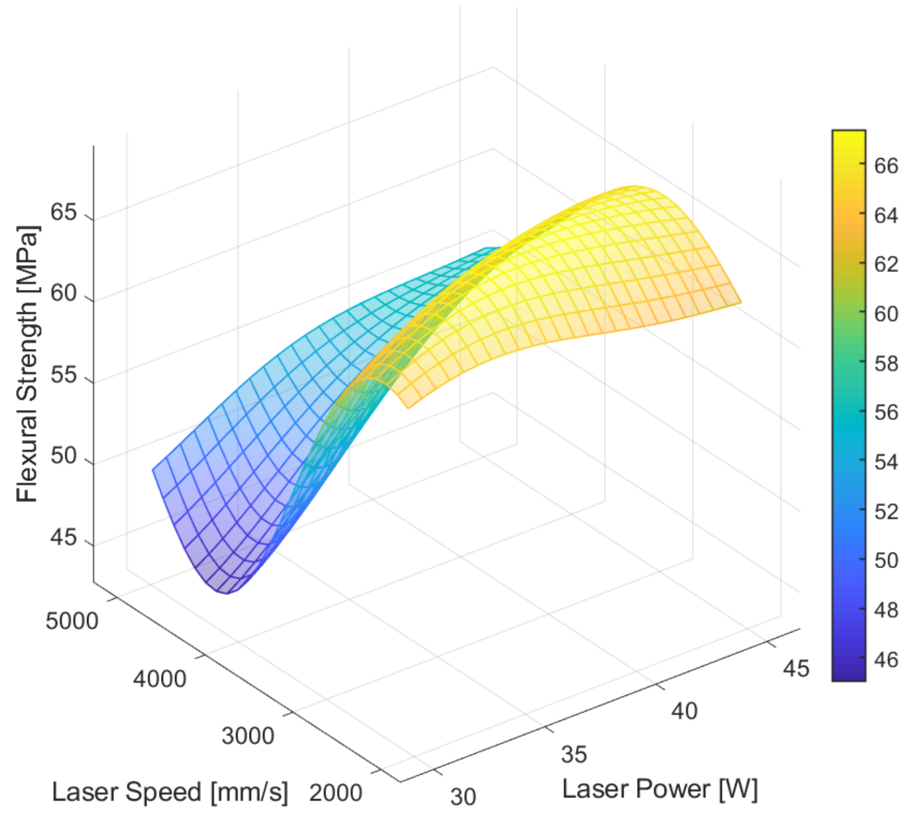

(a) Flexural strength over laser power and laser scan speed

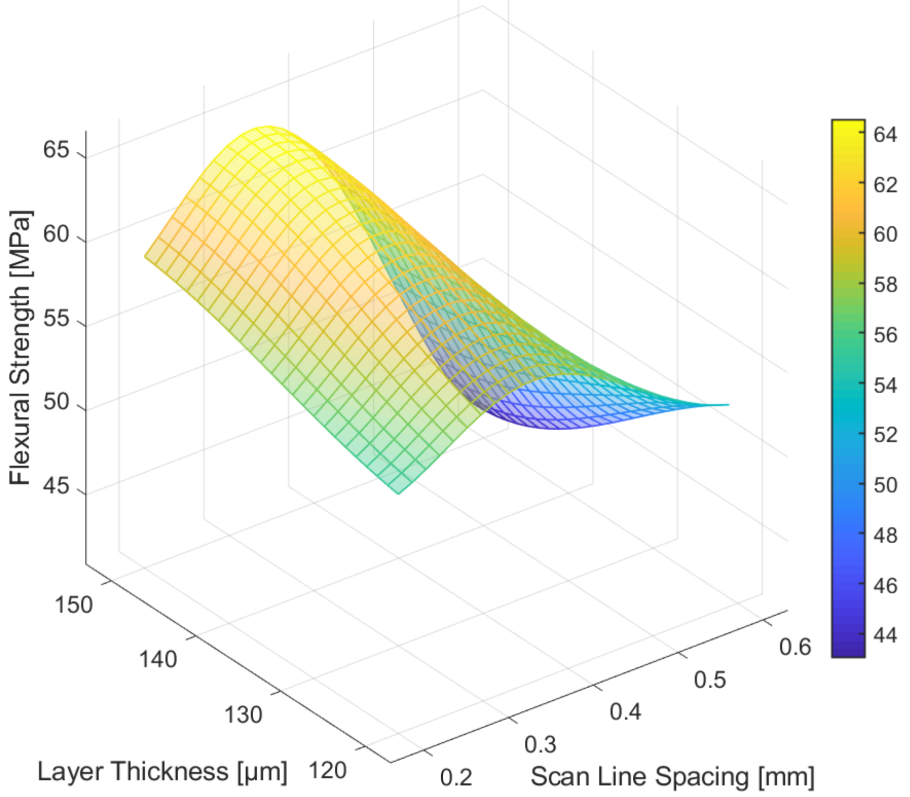

(b) Flexural strength over scan line spacing and layer thickness

Figure 4.35 – Response surfaces for flexural strength.

Response surface generated for flexural strength over scan line spacing and layer thickness at 3500 mm/s laser speed and 38 W laser power are depicted in Fig. 4.35b. Flexural strength starts with low values of 45 MPa at highest scan line spacing and layer thickness, increasing sharply in direction towards lower scan line spacing and 150 μm layer thickness. At 120 μm the increase is smoother. Flexural strength is increased until 0.32 mm scan line spacing, reaching a maximum at 150 μm, afterwards decreasing at lower scan line spacing values. Same effect is observed at 120 μm layer thickness but in a smoother shape.

Relative relevance of each LS parameter on flexural strength is given in Fig. 4.36. Scan line spacing has the highest relevance, which in accordance to the response surfaces obtained and also due to the influence scan line spacing has on the number of total exposures the surface has, which has a high influence on flexural properties. Laser speed and layer thickness are the second and third most influencing parameters. Laser power is the least relevant parameter.

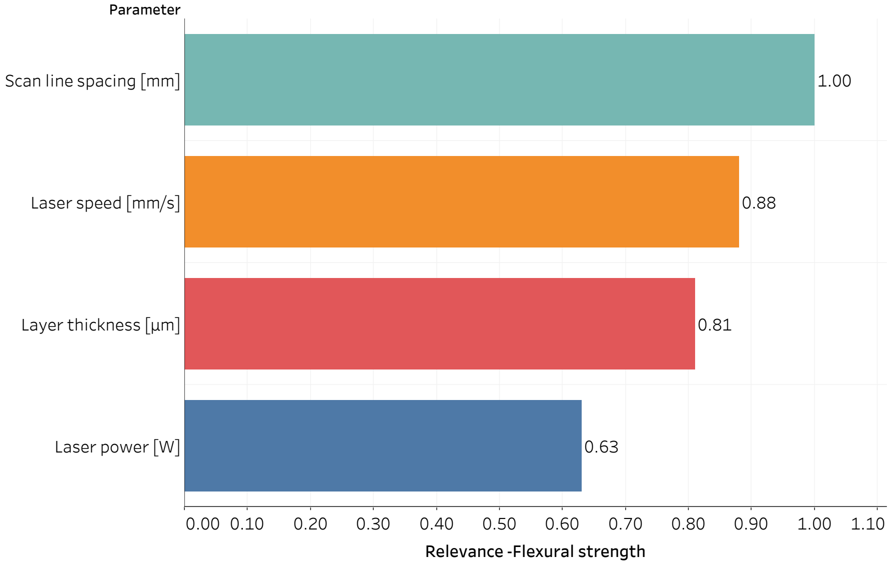

Figure 4.36 – Sensitivity of LS process parameters on flexural strength.

4.2.2.10 Normalized manufacturing time

Gaussian process model for normalized manufacturing time over laser speed and laser power at 0.4 mm scan line spacing and 120 μm layer thickness is depicted in Fig. 4.37a. Normalized manufacturing time varies almost linearly with laser speed, with lowest values at high laser speed and increasing in direction of lower laser speed. This is in agreement with the LS process behavior, as the laser speed influences the time required to scan the powder bed, with higher laser speed requiring less time than lower laser speed

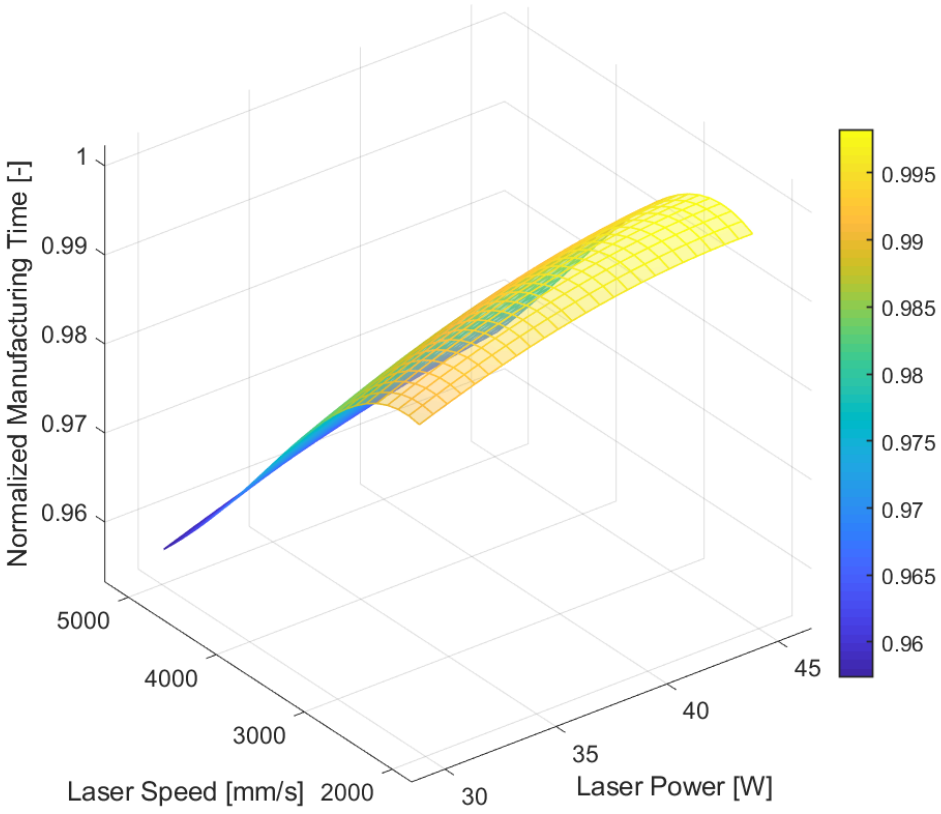

(a) Manufacturing time over laser power and laser speed

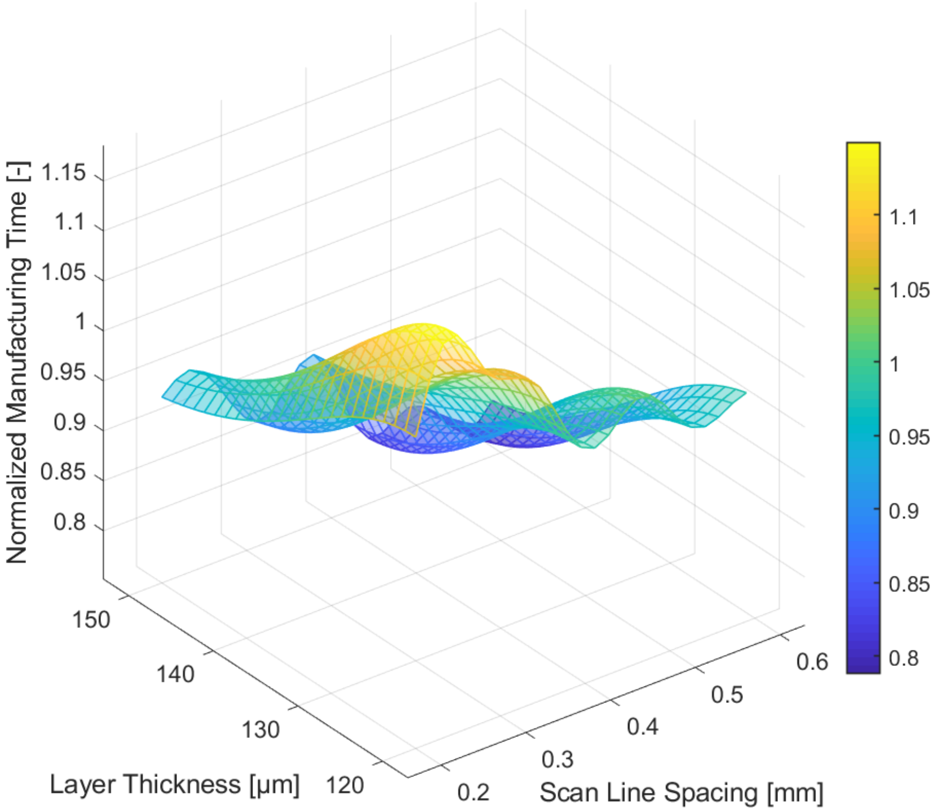

(b) Manufacturing over scan line spacing and layer thickness

Figure 4.37 – Response surfaces for normalized manufacturing time.

to scan over the same powder bed surface. Laser power does not influence significantly normalized manufacturing time.

Normalized manufacturing time over scan line spacing and layer thickness at laser power of 38 W and laser speed of 3500 mm/s is shown in Fig. 4.37b. The surface modelled shows lowest values of 0.8 at higher layer thickness and scan line spacing and increases in an oscillating manner in direction towards lower layer thickness and scan line spacing. This is in agreement with laser sintering process, as the lower scan line spacing results in higher amount of total laser exposures that need to be scanned to fill the powder bed. Lower layer thickness also results in higher number of layers needed to build the same part. The oscillating behavior observed in the $\mathcal{GP}$ model is probably due to differences in manufacturing time calculations at near scan line spacing points and due to different amount of total laser lines exposures calculated by the machine software at different scan line spacing values, which lead to some discrepancy in the calculation of the manufacturing time.

Sensitivity of normalized manufacturing time to the input parameters is given in Fig. 4.38. Scan line spacing is by far the most relevant parameter, followed by layer thickness with 0.41 relative relevance. This is an interesting result considering that layer thickness is supposed to play a major role in manufacturing time. Indeed scan line spacing parameter results in the number of total laser exposures over the powder bed and the range scan line spacing was varied during modelling is much broader than layer thickness, which helps understand why scan line spacing has such strong influence on manufacturing time. Laser speed comes as third most influencing parameter but with a much lower relevance

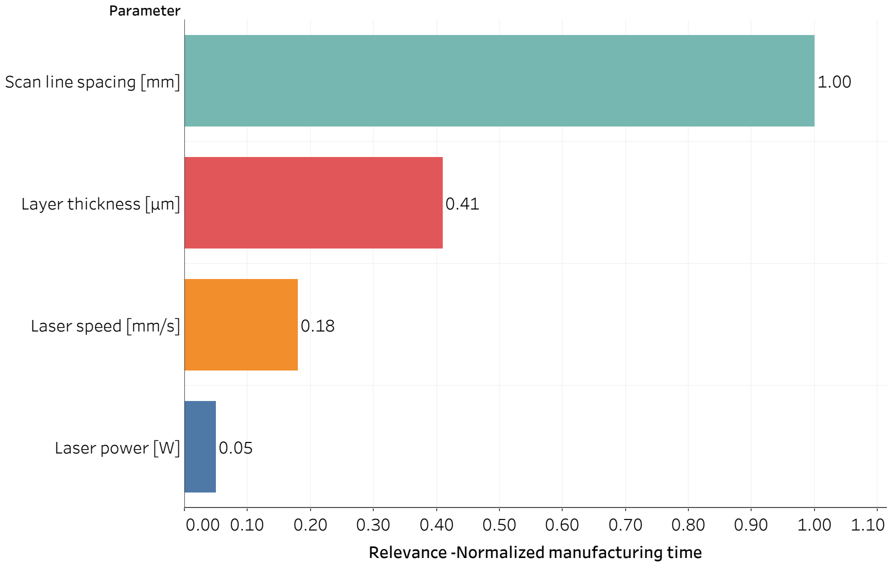

Figure 4.38 – Sensitivity of LS process parameters on normalized manufacturing time.

than scan line spacing and layer thickness. Laser power has the lowest relevance and can even be considered not relevant to the model.

4.3 Optimization via evolutionary algorithm

This section describes the multi-objective optimization tasks performed after supervised learning via Gaussian Process was conducted. As described in chapter 3, multi-criteria optimization relies on optimization of two or more objective functions. The results are not a single optimum of the functions. Instead, due to conflicting objectives, the results of a multi-criteria optimization are solution sets representing a compromise (trade-off) between the objectives. These trade-off solutions are called Pareto solutions.

Stochastic optimization via Evolutionary Algorithm (EA) was employed to perform the optimization tasks. The multi-objective optimization considered optimization of mechanical properties, surface quality, dimensional accuracy and manufacturing time. Two objectives were optimized at once, while the others were kept at a limit (lower or higher hard limit) to reduce the number of Pareto solutions.

4.3.1 Criteria 1 - Optimization of manufacturing time and dimensional accuracy

Criteria 1 aims optimization of dimensional accuracy and manufacturing time while keeping mechanical properties and surface quality within adequate values. To perform this task, all accuracy output parameters were maximized as well as normalized manufacturing time. Tensile strength, elastic modulus and strain at break were kept as hard lower bounds of 40 MPa, 1490 MPa and 11 %. Surface roughness was used as a weak lower bound at 15 μm.

Figure 4.39 shows the Pareto solutions found after the optimization task is completed. The results are shown for Z-direction accuracy over normalized manufacturing time, which were the main objective variables used to perform the optimization. The pareto solutions represent a set of possible solutions and the trade-off curve between dimensional accuracy and manufacturing time can be observed. Two areas were selected for evaluation: one area with Z-accuracy between 94 and 96 % and normalized manufacturing time below 0.9; second area with Z-direction above 96 % and normalized manufacturing time also below 0.9.

Resulting laser sintering optimal parameters for the areas selected are given in Fig. 4.40.The areas chosen as optimal give a different set of parameters. The combination of low laser power and low laser speed is a feasible choice for this optimization task as well as high laser power and high laser speed. The selection considered only layer thickness of 150

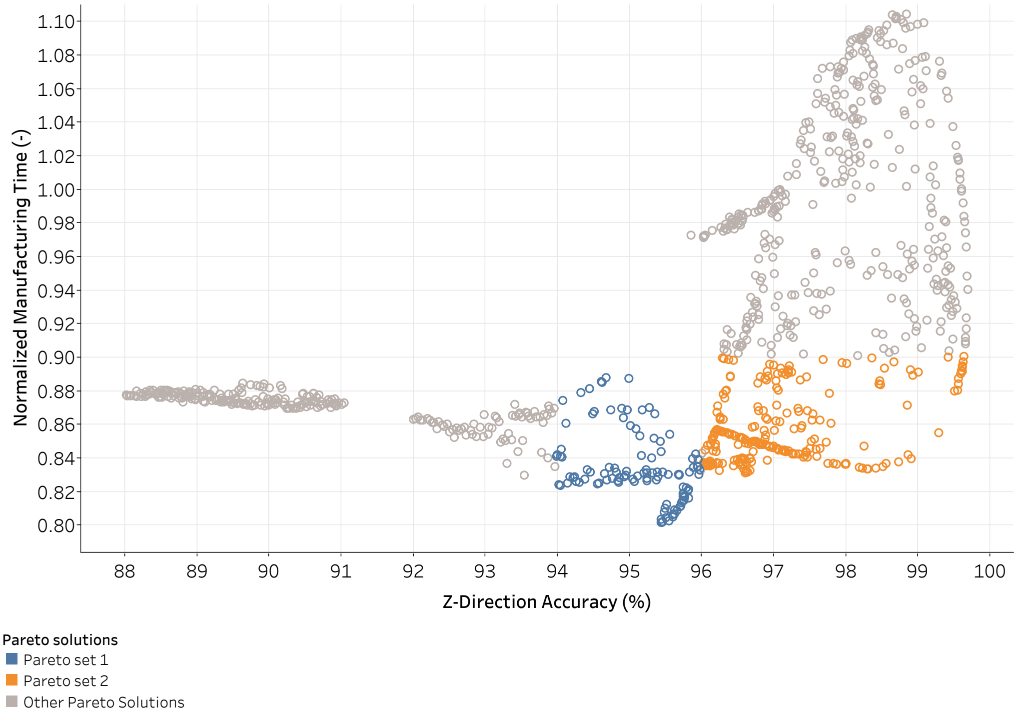

Figure 4.39 – Pareto solutions after optimization task with criteria 1.

μm as this parameter choice maximize manufacturing time. All range of scan line spacing available was covered as well. It is clear that the choice of lower laser speed is conditioned to higher scan line spacing as can be observed in Fig. 4.40a-b.

Other output variables kept as hard or weak limits are depicted in the graphics of Fig. 4.41a-b. In the selected optimal areas, elastic modulus, tensile strength and nominal strain at break (shown in upper left and right graphics) were kept at desired levels set during the optimization task and vary depending on the specific choice of the laser sintering parameters. For instance, in the group set 1 with lower z-direction accuracy there is a wide range of values for tensile strength and elastic modulus, covering all hard limit area specified during optimization. The same analysis can be drawn to nominal strain at break.

Y-direction accuracy was kept at high levels above 99 % for both selected sets as observed in middle graphics. Surface roughness values on chosen area were all below 16.5 μm, slightly above the lower limit specified during optimization, which is acceptable considering the parameter was set as a weak bound limit in order not to constrain too much the Pareto solutions. Values for density vary in a wide range depending on the parameter set chosen.

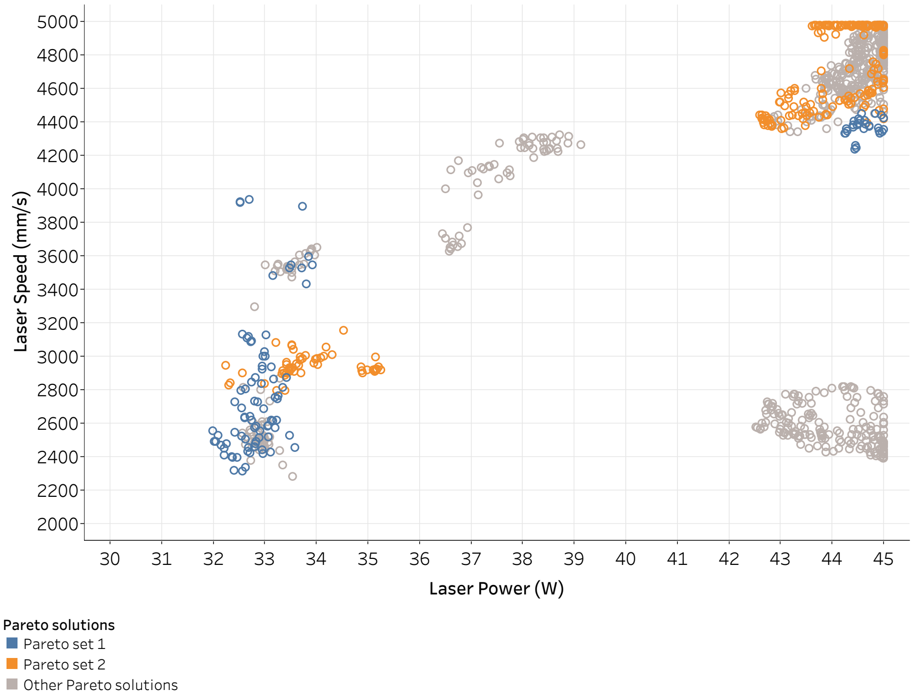

(a) Pareto solutions for laser power and laser speed.

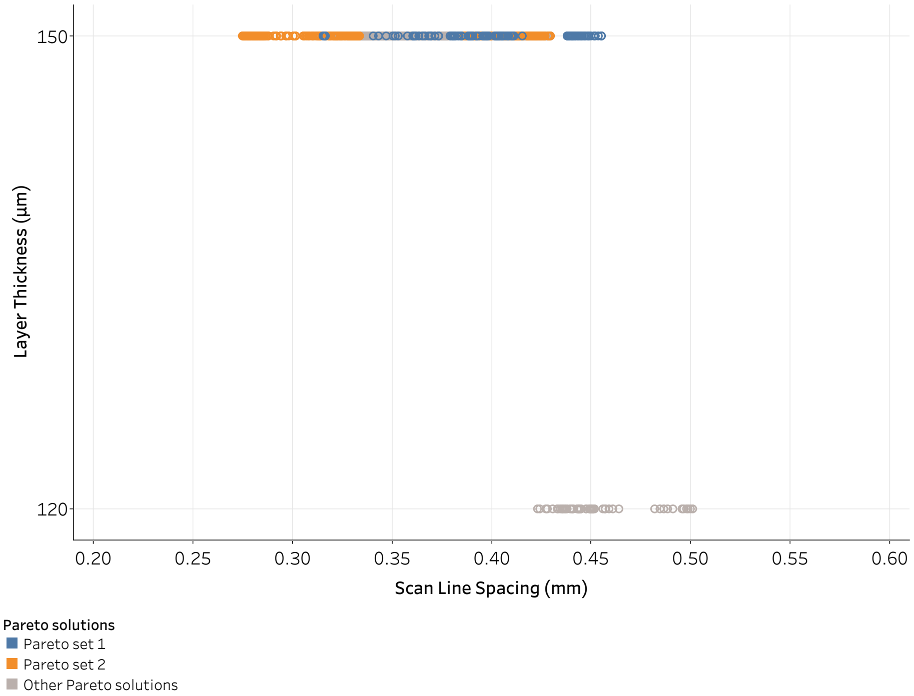

(b) Pareto solutions for scan line spacing and layer thickness.

Figure 4.40 – Pareto solutions for laser sintering parameters.

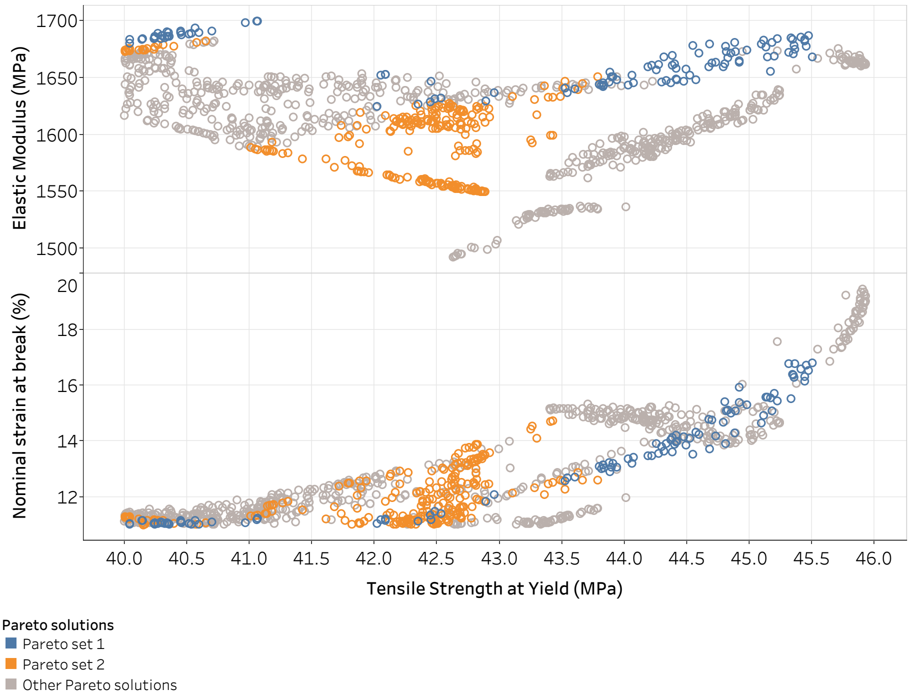

(a) Pareto solutions for elastic modulus, tensile strength at yield and nominal strength.

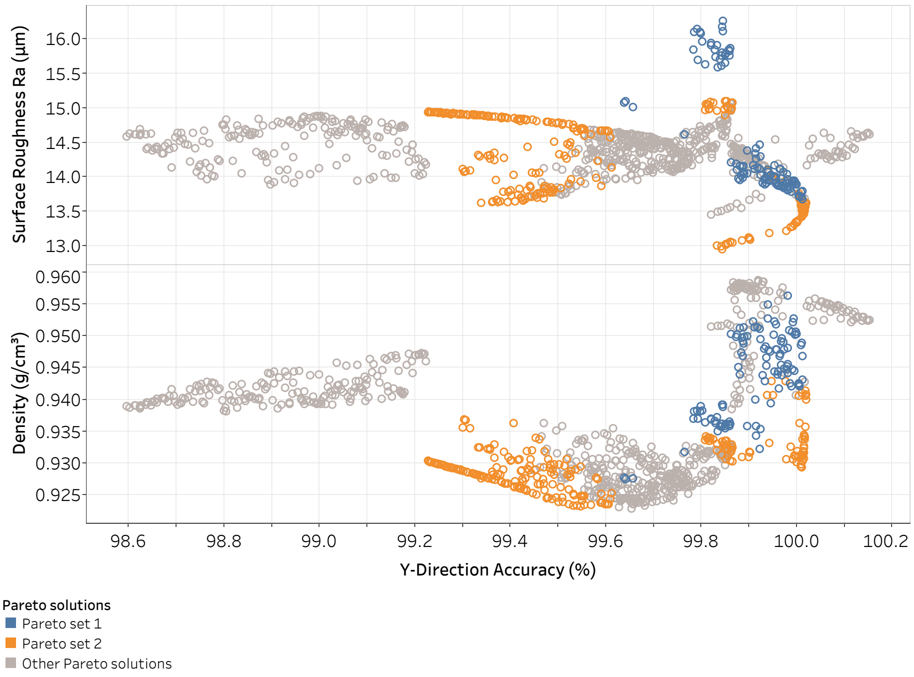

(b) Pareto solutions for surface roughness, density and Y-direction accuracy.

Figure 4.41 – Output variables Pareto solutions for criteria 1.

4.3.2 Criteria 2 - Optimization of manufacturing time and surface roughness

Goal of criteria 2 is to minimize both manufacturing time and surface roughness. Tensile strength, elastic modulus and nominal strain at break were kept as hard lower bounds of 40 MPa, 1490 MPa and 11 %. Dimensional accuracy at x, y and z direction were also kept as hard lower bonds at 99, 98 and 90 % respectively.

Pareto solutions derived from EA optimization are given in Fig. 4.42. The graphic shows a typical shape of Pareto frontier with the trade-off solution clearly defined. Two regions of interest were defined: first region defines lower normalized manufacturing time between 0.81-0.83 at a cost of slightly higher surface roughness; second regions allows normalized manufacturing time between 0.83-0.85 and lower surface roughness between 12.5-13.5 μm.

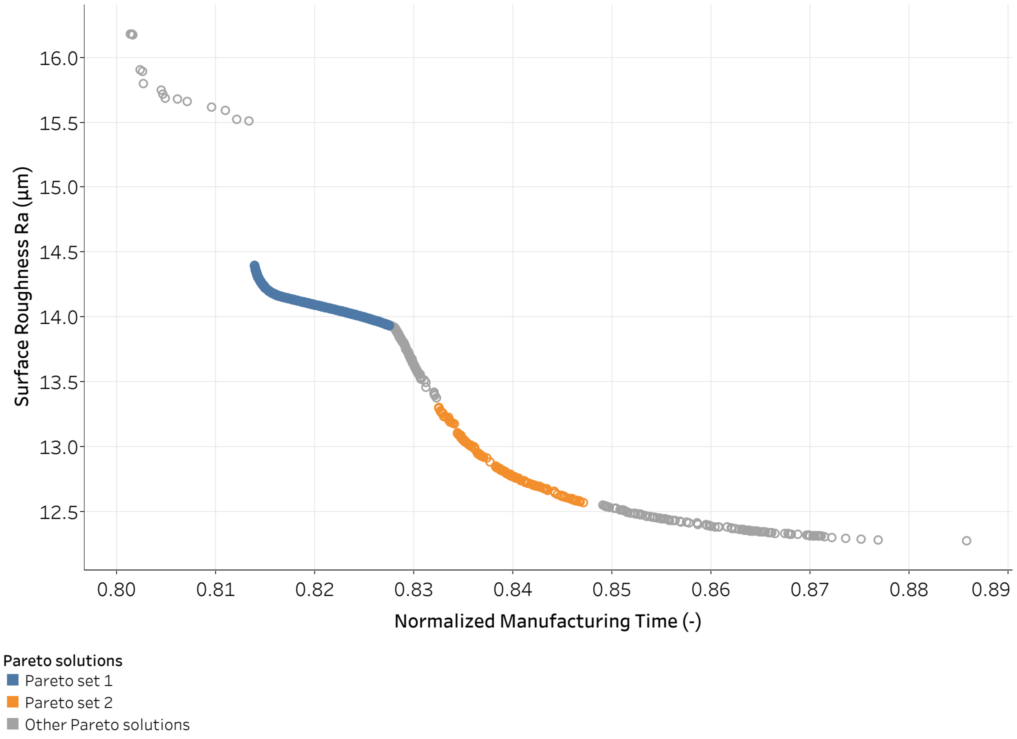

Figure 4.42 – Pareto solutions after optimization task with criteria 2.

Laser sintering parameters at optimum conditions for criteria 2 are given in Fig. 4.43a-b. At Pareto solution set 1 the parameter set is described by low laser speed and laser power and scan line spacing around 0.4 mm whereas at Pareto set 2 the optimal parameter set is represented by medium laser speed and laser power with slightly higher scan line spacing at 0.45 mm. Layer thickness is kept at 150 μm.

Figure 4.44a-b shows the output variables at the Pareto solutions for optimization criteria 2. Elastic modulus was kept always above 1600 MPa for both pareto sets chosen, with higher values (around 1700 MPa) for Pareto set 1 and 1600 MPa for Pareto set 2.

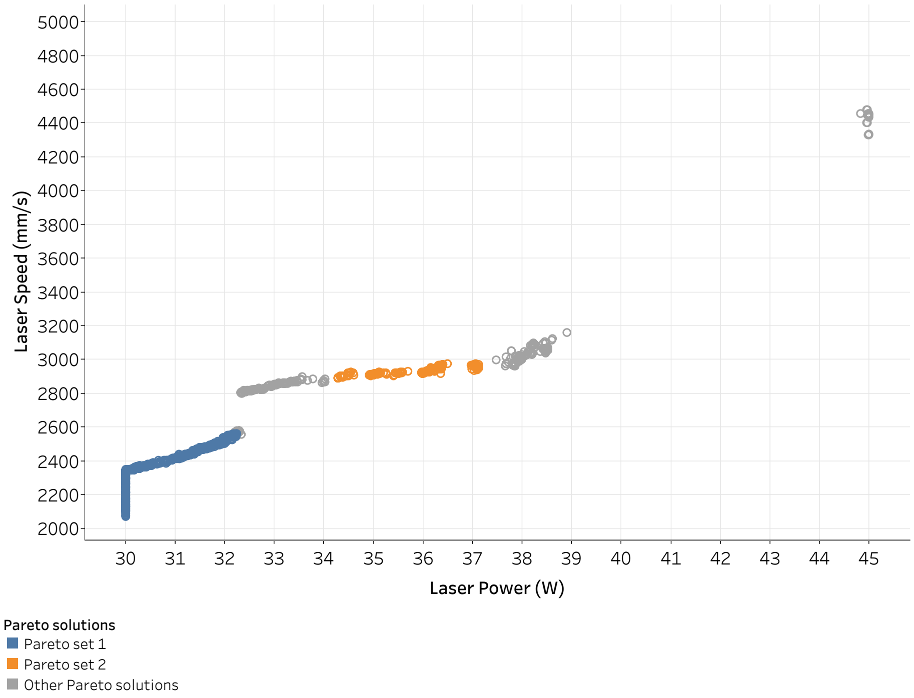

(a) Pareto solutions for laser power and laser speed.

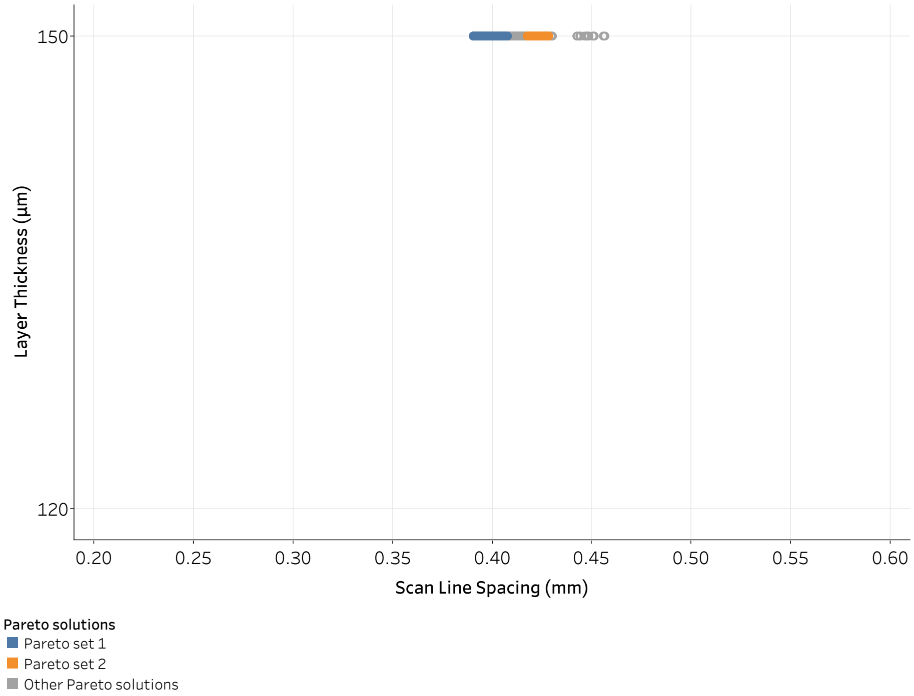

(b) Pareto solutions for scan line spacing and layer thickness.

Figure 4.43 – Pareto solutions for laser sintering parameters for criteria 2.

Similar analysis can be made for tensile strength and nominal strain at break, with higher values for these output parameter at Pareto set 1.

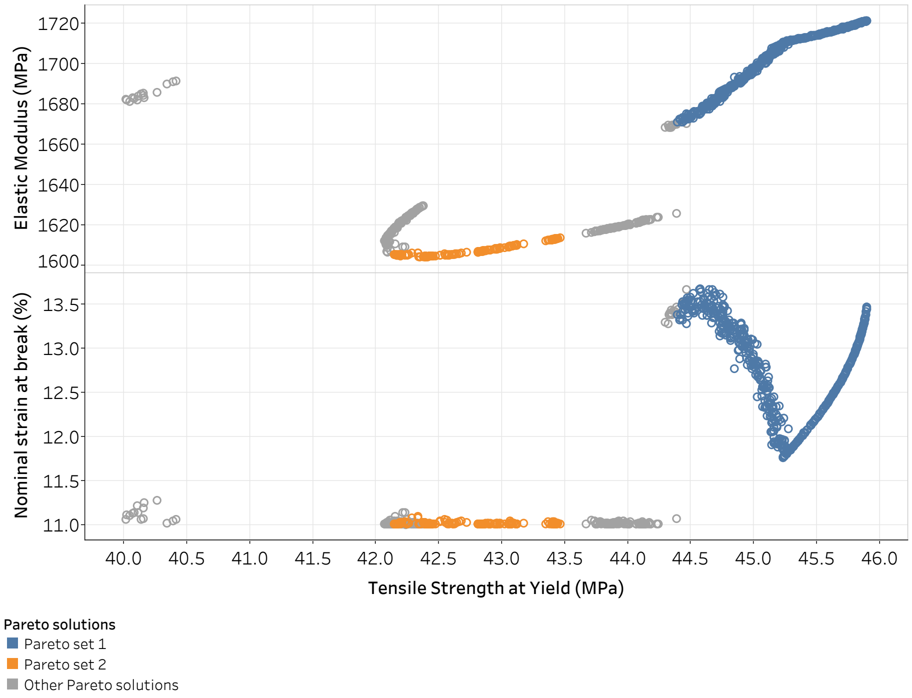

(a) Pareto solutions for elastic modulus, tensile strength at yield and nominal strength

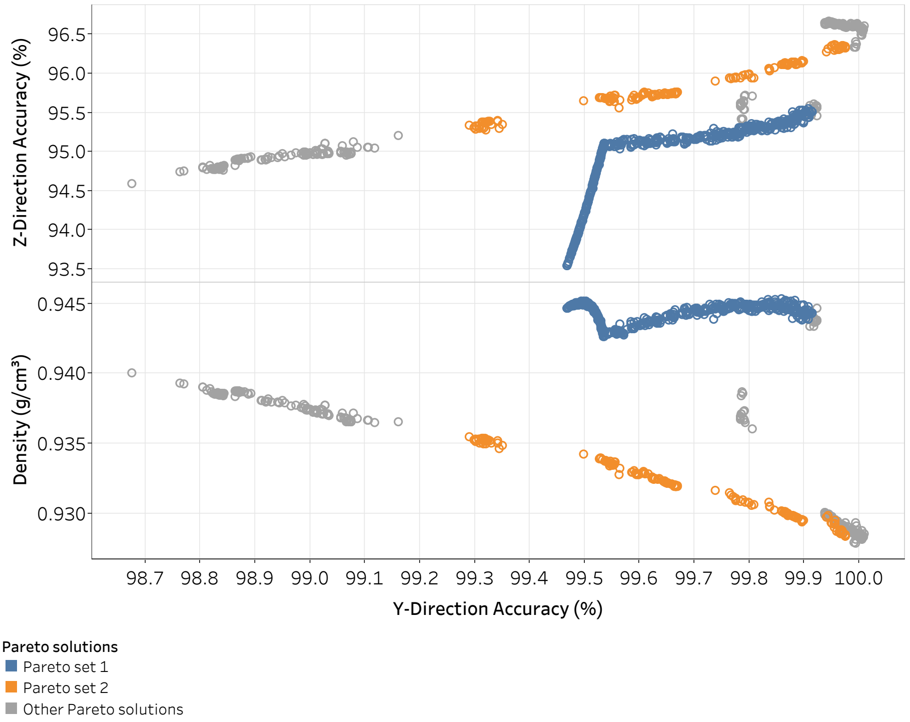

(b) Pareto solutions for Z-direction accuracy, density and Y-direction accuracy

Figure 4.44 – Output variables Pareto solutions for criteria 2.

It can be observed from Fig. 4.44b Z-direction accuracy was kept between 93-95 % for Pareto set 1 and between 95-96.5 % for Pareto solutions set 2. Y-direction was always above 99 % for both Pareto sets chosen. Density at Pareto set 1 was at 0.945 g/cm^3, slightly above density values at Pareto set 2 where values between 0.93-0.935 g/cm^3 were achieved.

4.3.3 Criteria 3 - Optimization of manufacturing time and mechanical properties

The goal of optimization task with criteria tree is minimizing manufacturing time and maximizing mechanical properties. Maximization of mechanical properties was performed for elastic modulus, tensile strength and nominal strain at break. To perform the task and have a solution set with coherent values, dimensional accuracy was set as hard lower bond for X, Y and Z direction at 99, 98 and 90 % whereas surface roughness was set as hard upper bond at 16 μm. Figure 4.45 shows all Pareto solutions after optimization task with criteria 3.

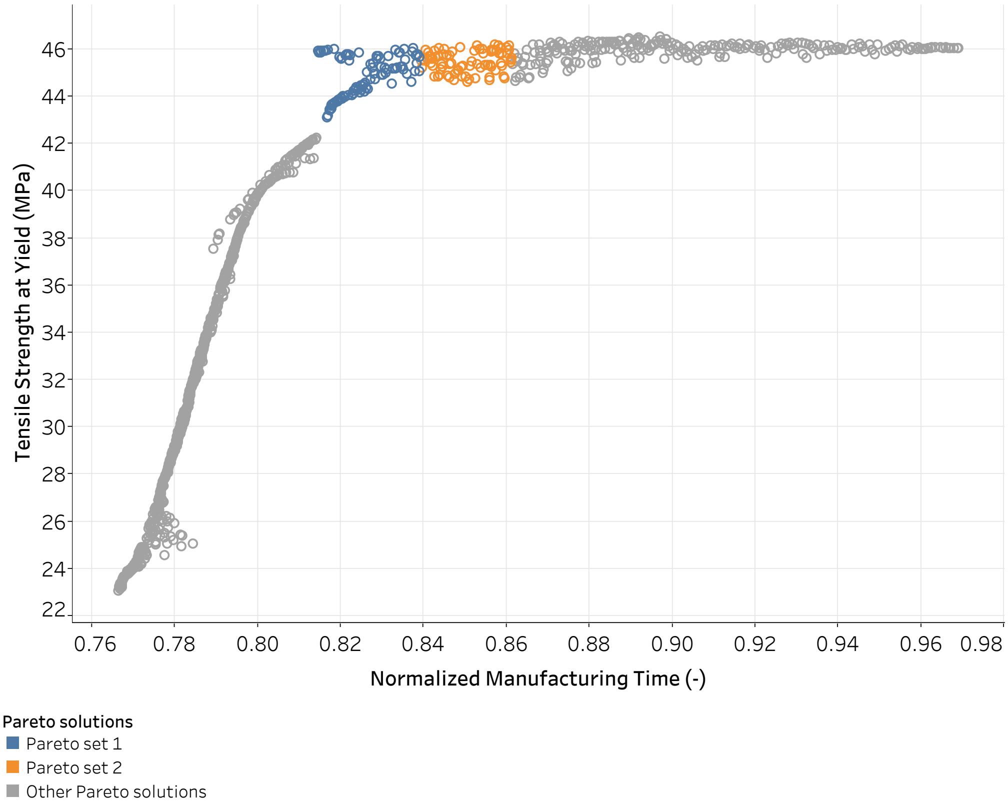

Figure 4.45 – Pareto solutions after optimization task with criteria 3.

The Pareto frontier is well defined showing all possible combinations of normalized manufacturing time and tensile strength for criteria 3. Two typical trade-off solution were chosen for evaluation: first area combining lower manufacturing time (between 0.81-0.84) and yield strength above 43 MPa; second Pareto set with normalized manufacturing time between 0.84-0.86 and yield strength above 44 MPa.

Optimized laser sintering parameters for criteria 3 are depicted in Fig. 4.46a-b. The chosen Pareto sets concentrate laser speed and laser power in two regions: laser scan speed below 2500 mm/s and laser power varying from 30-35 W; laser power at maximum evaluated value of 45 W and laser speed varying from 3300-3900 mm/s. From Fig. 4.46b only 150 μm layer thickness was considered in Pareto frontier while scan line spacing at the Pareto sets chosen varied from 0.35-0.45 mm. The higher laser power settings is associated with a higher laser speed and scan line spacing in order to compensate the energy delivered to the powder bed.

Figure 4.47a-b shows the resulting output parameters after optimization with EA. For both Pareto sets chosen density was at levels above 0.943 g/cm^3, elastic modulus also was located at maximum area between 1630-1750 MPa. Nominal strain at break presented higher variation at the Pareto solution sets, ranging from 11.5-23 %.

Z-direction accuracy presented in Fig. 4.47b achieved lower values at Pareto set 2 compared to Pareto set 1, ranging between 92-95 % at both solution sets. This effect was a result of the higher energy density applied at this optimization task, which led to penalty in dimensional accuracy in order to maximize mechanical properties. Y-direction

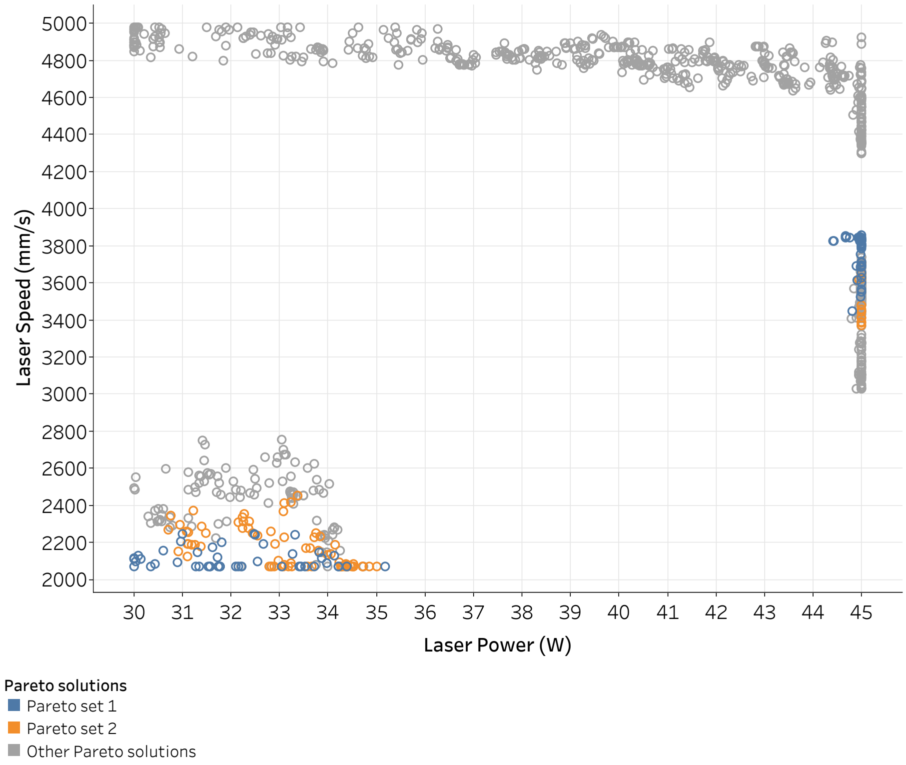

(a) Pareto solutions for laser power and laser speed.

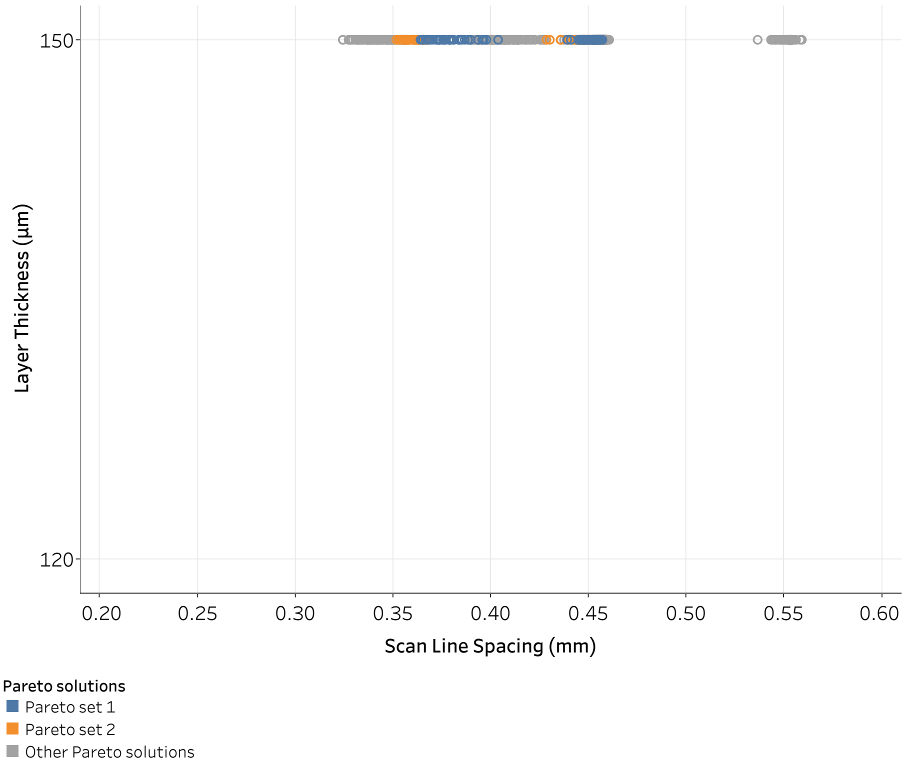

(b) Pareto solutions for scan line spacing and layer thickness.

Figure 4.46 – Pareto solutions for laser sintering parameters for criteria 3.

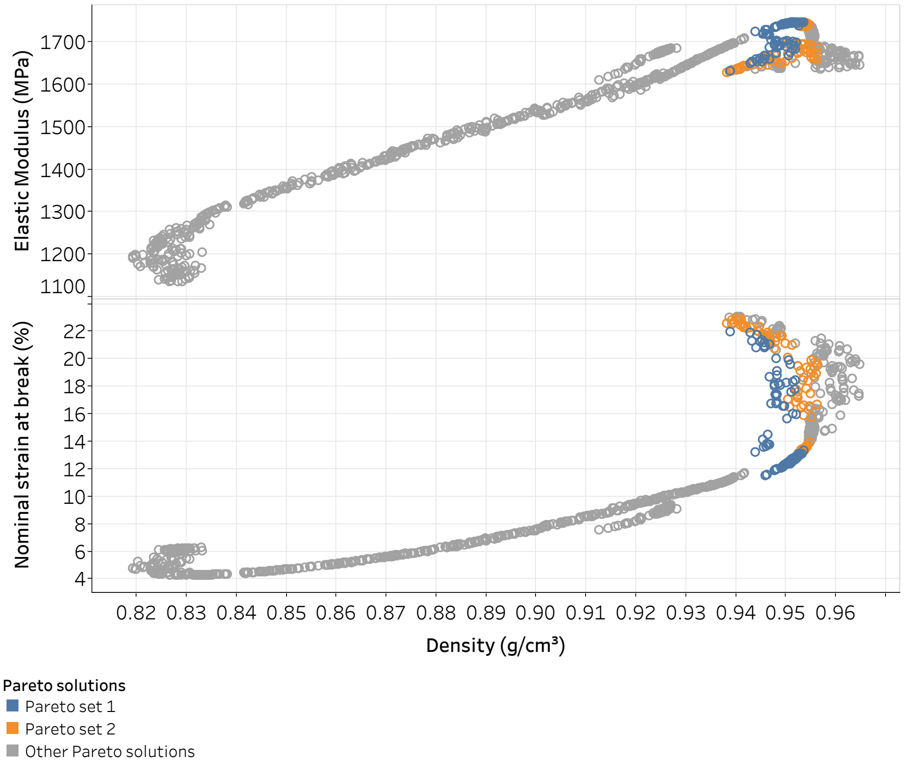

(a) Pareto solutions for elastic modulus, density and nominal strain at break.

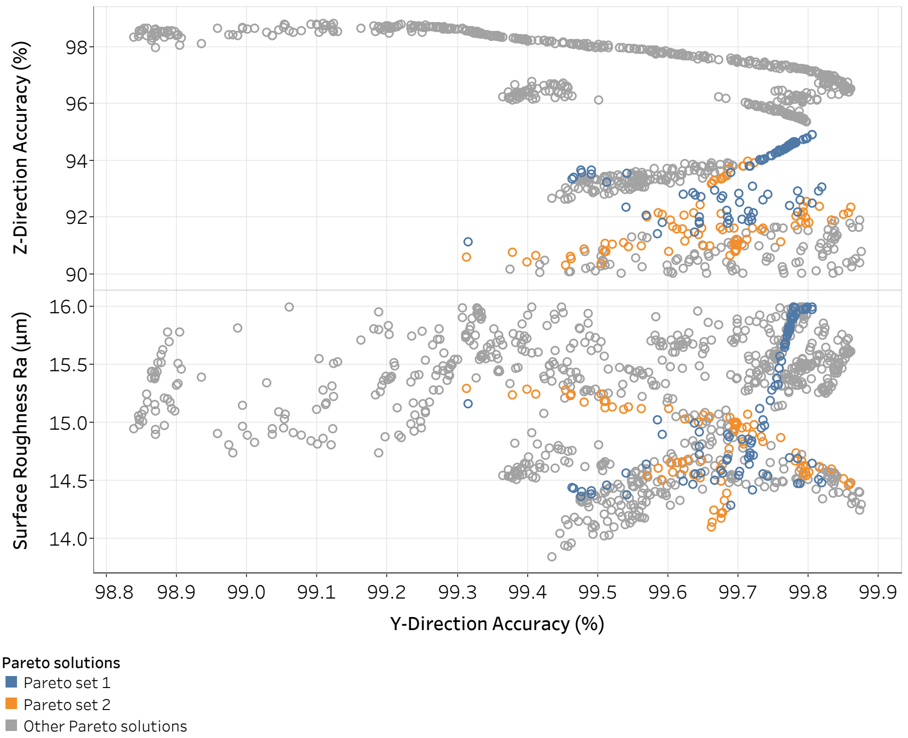

(b) Pareto solutions for Z-direction accuracy, Y-direction accuracy and surface roughness R_a.

Figure 4.47 – Output variables Pareto solutions for criteria 3.

accuracy was also kept at high levels, above 99 % independently of the Pareto solution set chosen. Average surface roughness varied between 14-16 μm, as specified by the hard upper bound during the optimization task.

4.3.4 Criteria 4 - Optimization of dimensional accuracy and mechanical properties

Criteria 4 objective is to optimize dimensional accuracy and mechanical properties. To perform the task, maximization of mechanical properties was performed for elastic modulus, tensile strength and nominal strain at break while maximization of dimensional accuracy in all directions was set. Normalized manufacturing time was kept as hard upper bound of 1 and surface roughness as a hard upper bound of 16 μm.

Pareto solutions after EA optimization with criteria 4 are depicted in Fig. 4.48. Pareto frontier can be easy distinguishable with trade-off solutions for both optimized variables visible. Two regions of interest were selected: first Pareto set with Z-direction accuracy between 92-95 % and tensile yield strength above 44 MPa; second Pareto set with Z-direction accuracy above 95 % and yield strength above 42 MPa.

Laser sintering optimized parameters for criteria 4 are depicted in 4.49a-b. There is

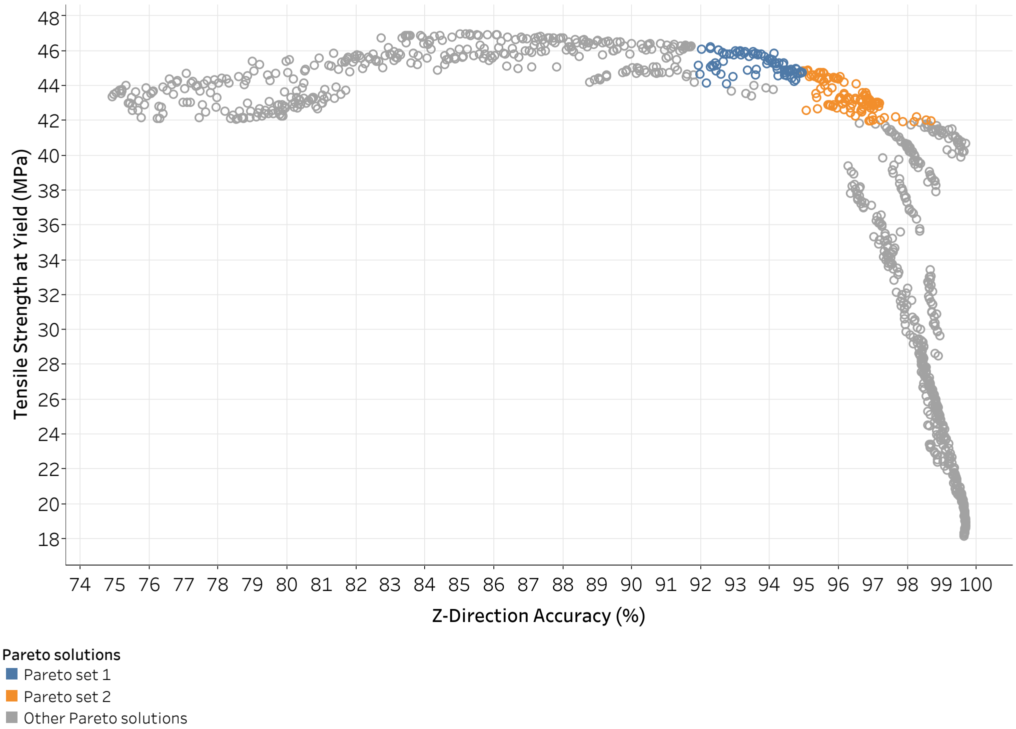

Figure 4.48 – Pareto solutions after optimization task with criteria 4.

a wide range of laser parameter combinations available. For Pareto set 1 (more focused on higher mechanical properties at a cost of lower dimensional accuracy) four main regions can be observed: low laser speed and low laser power, intermediate laser speed and laser power between 32-35 W. laser speed between 2000-3500 mm/s and laser power between 35-39 W. Laser speed between 3400 mm/s and higher laser power between 41-45 W.

For Pareto set 2 three main areas can be distinguished: intermediate laser speed between 3000-3500 mm/s and laser low laser power below 35 W; high laser speed above 4400 mm/s and laser power between 36-39 W; very high laser power above 4700 mm/s and high laser power above 42 W.

Pareto solutions were found for both layer thickness's evaluated. Pareto set 1 is more concentrated on 150 μm while Pareto set 2 on 120 μm. Scan line spacing for Pareto set 1 at 120 μm is concentrated at 0.4 mm while a wider range between 0.35-0.45 mm is found for a layer thickness of 150 μm. Pareto set two also has a wide range of scan line spacing values available at 150 μm, ranging from 0.31-0.48 mm.

Pareto solutions for other output parameters are shown in Fig. 4.50a-b. Elastic modulus for Pareto set 1 was kept at higher levels (between 1600-1700 MPa) than Pareto set 2 (between 1400-1600 MPa). Nominal strain at break for Pareto set 1 was between 11-19 %.

Lower values are found for Pareto set 2, ranging from 8-14 %. Density is similar for

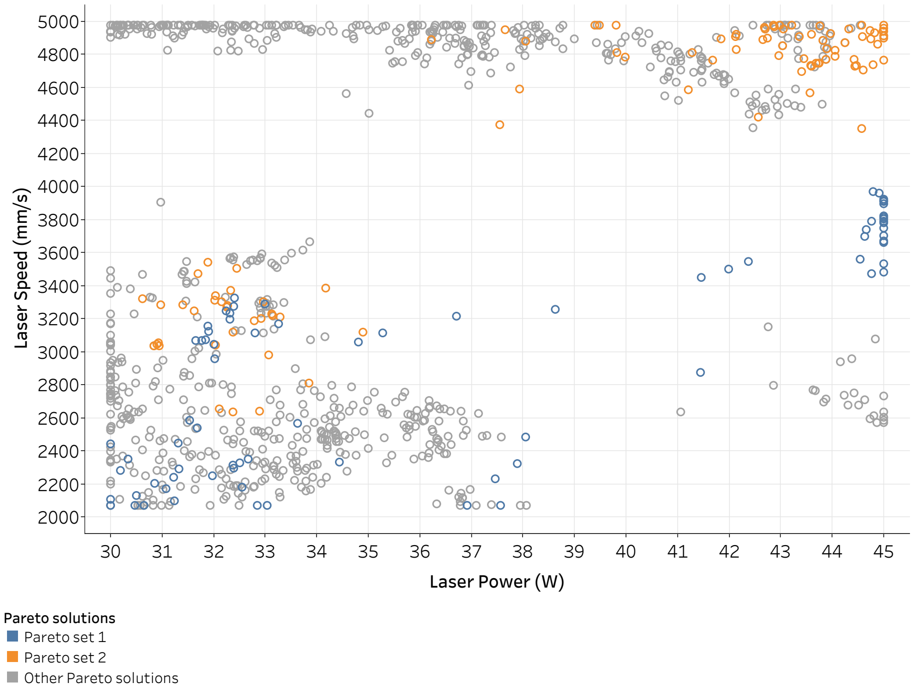

(a) Pareto solutions for laser power and laser speed.

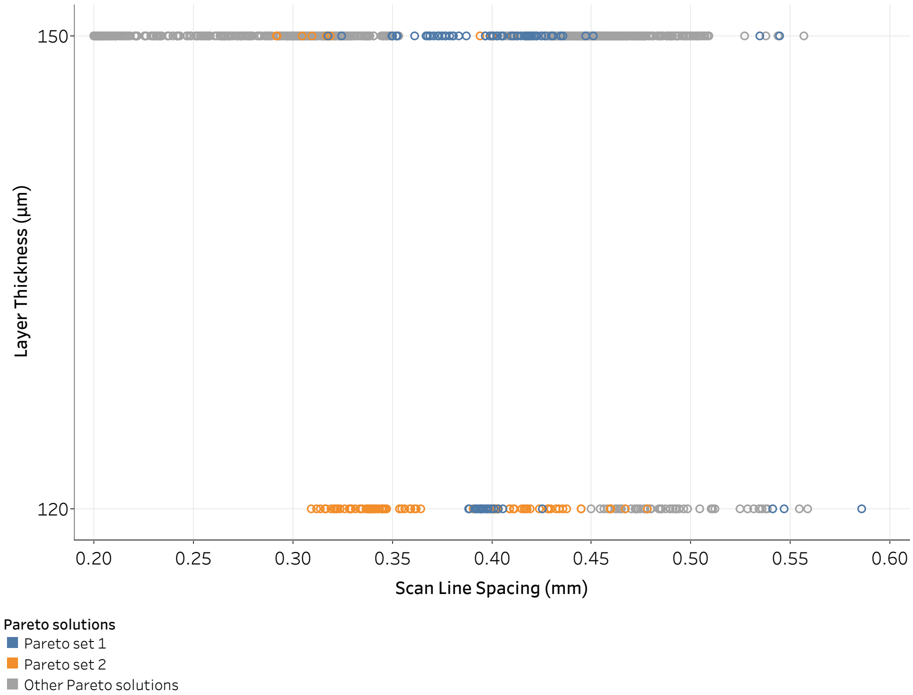

(b) Pareto solutions for scan line spacing and layer thickness.

Figure 4.49 – Pareto solutions for laser sintering parameters for criteria 4.

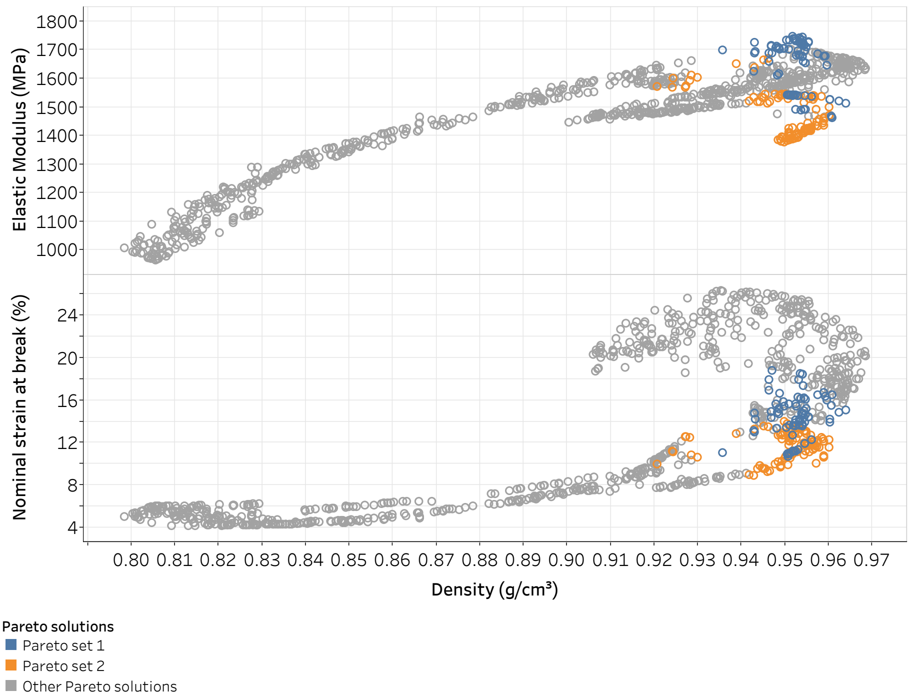

(a) Pareto solutions for elastic modulus, density and nominal strain at break

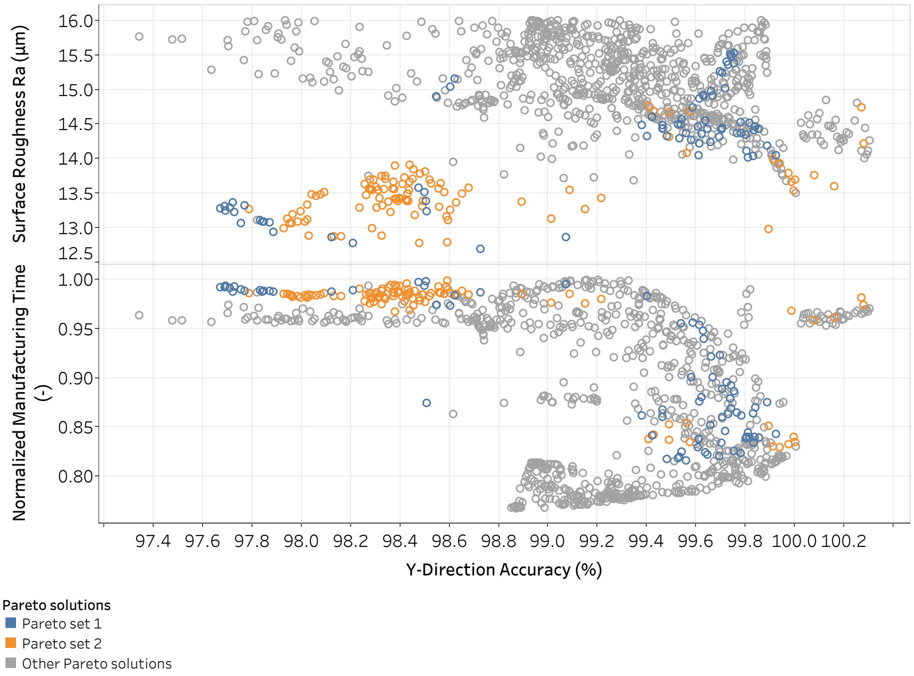

(b) Pareto solutions for normalized manufacturing time, Y-direction accuracy and surface roughness R_a

Figure 4.50 – Output variables Pareto solutions for criteria 4

both Pareto sets varying between 0.94-0.964 g/cm^3. These results illustrate how conflicting the choice of parameters can be when dimensional accuracy and mechanical properties are involved in the multi-objective optimization task.

Surface roughness R_a data shown in Fig. 4.50b reveal slightly higher values (around 14.5 μm) for Pareto set 1 compared to to Pareto set 2 (around 13.5 μm). Normalized manufacturing time was near unity for majority of solutions in Pareto set 2 whereas the main solutions for Pareto set 1 were found to be between 0.82-0.9. Y-direction accuracy for Pareto set 1 reached higher levels (mainly above 99 %) compared to Pareto set 2 where most solutions were concentrated below 99 %).

4.3.5 Criteria 5 - Optimization of dimensional accuracy and surface roughness

Optimization task wit criteria 5 aims maximization of dimensional accuracy and minimization of surface roughness. Tensile strength, elastic modulus and strain at break were kept as hard lower bounds of 40 MPa, 1490 MPa and 11 %. Normalized manufacturing time was set as a hard upper bound at 1.

Figure 4.51 shows the EA optimized results for surface roughness over Z-direction accuracy. Pareto frontier is also well defined with trade-off solutions clearly visible. Of specific interest are two regions: region one (Pareto set one) with minimum surface roughness values achieved and intermediate Z-direction accuracy between 94-96 %; second

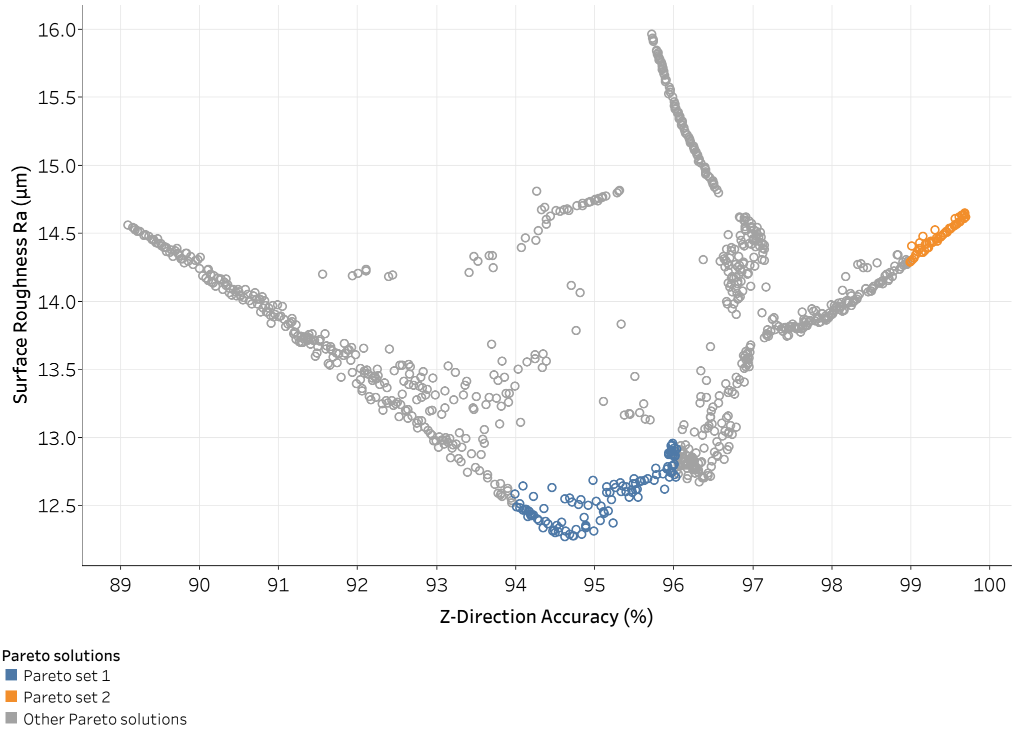

Figure 4.51 – Pareto solutions after optimization task with criteria 5.

region (Pareto set 2) maximizes Z-direction accuracy at the cost of a slightly higher surface roughness of 14.5 μm.

Laser sintering parameters at optimal conditions for criteria 5 are depicted in 4.52a-b. Pareto set 1 solutions concentrate laser speed between 2900-3400 mm/s, spreading laser power between 33-41 W. Pareto solution set 2 concentrates both laser speed at the highest values applied (above 4800 mm/s) and laser power above 44 W. Scan line spacing values for Pareto set 1 are located in a narrow area between 0.39-0.42 mm at 150 μm layer thickness and between 0.41-0.43 mm at 120 μm layer thickness. For Pareto set 2 scan line spacing values are located in an even narrower region between 0.33-0.35 mm and only for a layer thickness of 150 μm. The results are in good agreement with the response surfaces generated from Gaussian process learning, where surface roughness reached minimum values (Figure 4.21) at the regions indicated by Pareto set 1, while Pareto set 2 solutions gave good Z-accuracy results at high laser speed and laser power settings (Figure 4.19).

Figure 4.53a-b shows the output values after optimization task with criteria 5. From Fig. 4.53a elastic modulus at Pareto set 1 varied between 1540-1650 MPa and remained stable at 1600 MPa at Pareto set 2. Highly stable values for nominal strain at break were achieved for both Pareto sets, remaining at 11 %. A higher variation for yield strength was found , specially at Pareto set 1, spreading over between 43-45 MPa.

Two clusters were found for density at Pareto 1 set as shown in Fig. 4.53b, one with higher density values near 0.96 g/cm^3 and the other with lower values around 0.94 g/cm^3. For Pareto set 2 density values achieved stable values around 0.923 g/cm^3. Normalized manufacturing time for Pareto set 1 also presented two cluster of solutions, one with lower relative time at 0.89 and below and the other cluster with normalized manufacturing time near unity. For Pareto set 2 normalized manufacturing time presented a high variation between 0.91 and 1. Y-direction accuracy did not vary significantly at Pareto set 1, ranging from 98-99.5 %, whereas at Pareto set 2 uniform values near 99.6 % were found.

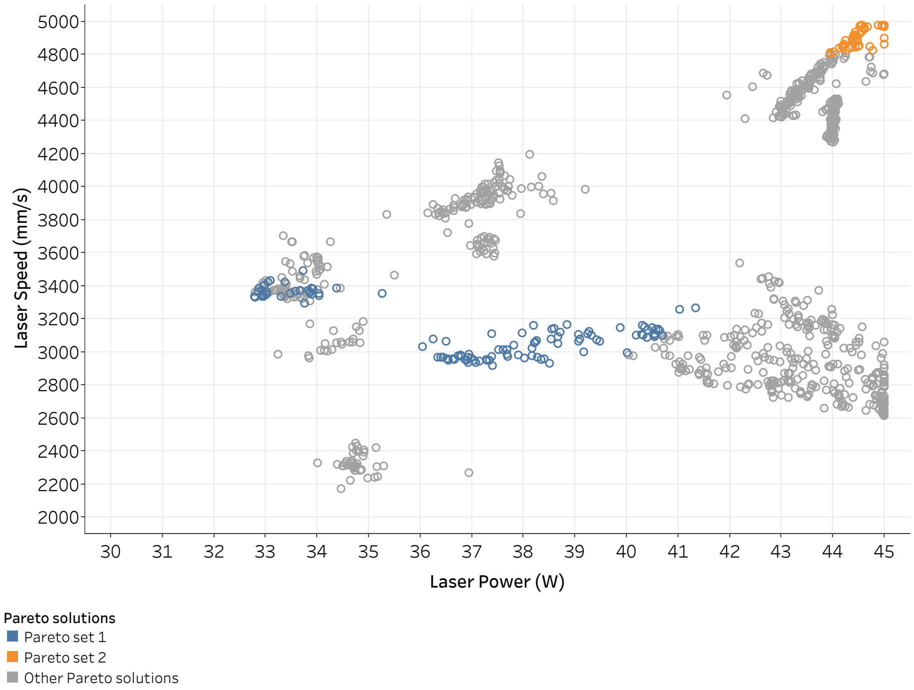

(a) Pareto solutions for laser power and laser speed.

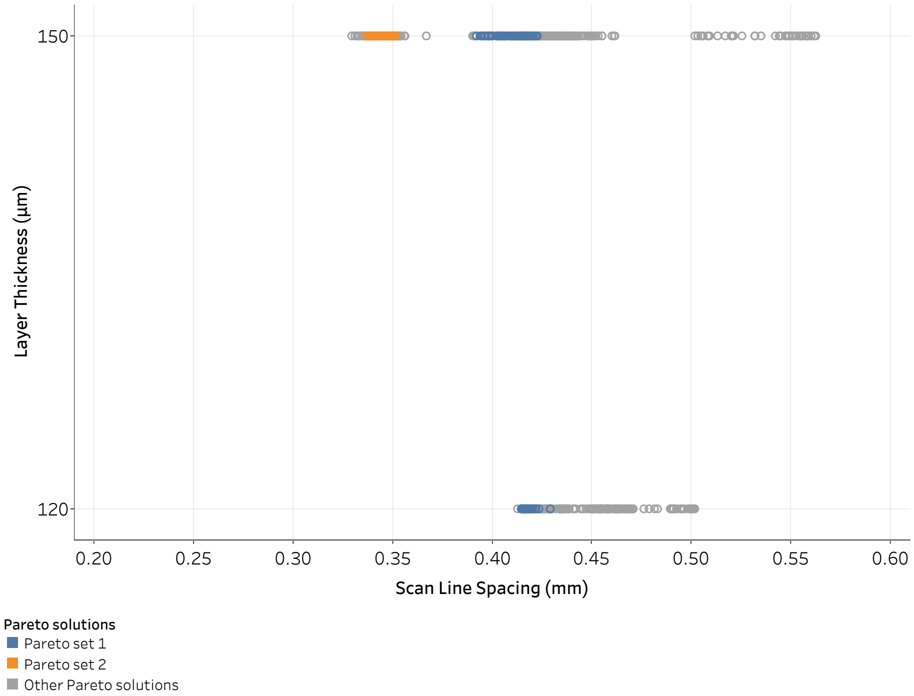

(b) Pareto solutions for scan line spacing and layer thickness.

Figure 4.52 – Pareto solutions for laser sintering parameters for criteria 5.

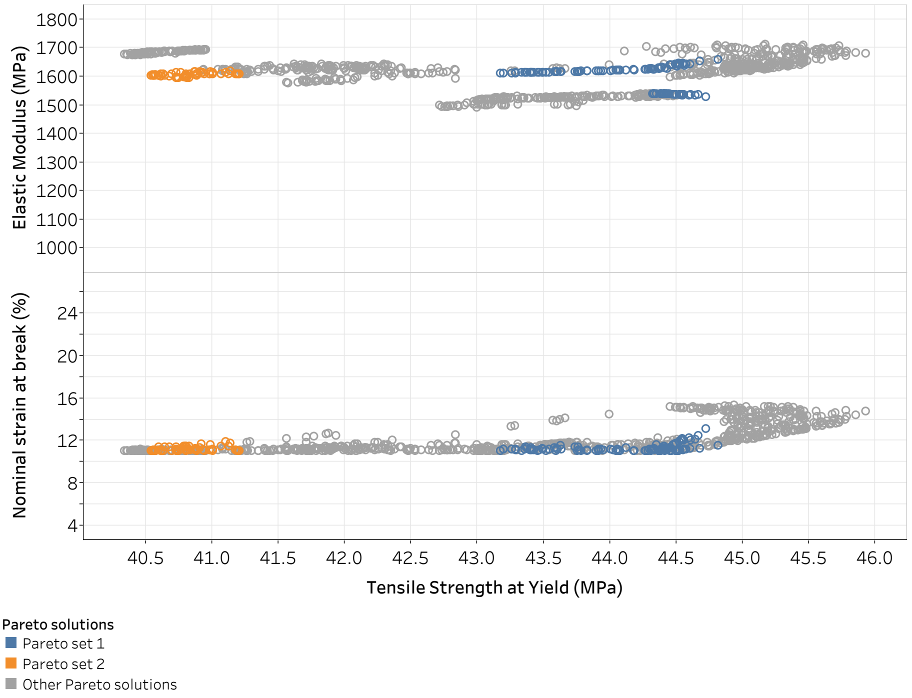

(a) Pareto solutions for elastic modulus, yield strength and nominal strain at break.

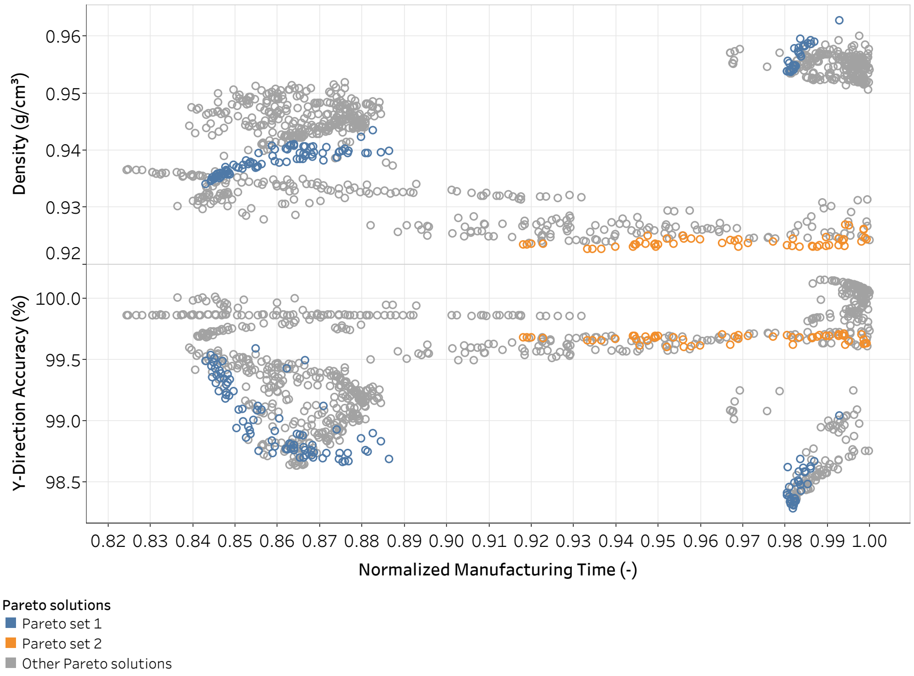

(b) Pareto solutions for normalized manufacturing time, Y-direction accuracy and density.

Figure 4.53 – Output variables Pareto solutions for criteria 5.

4.3.6 Criteria 6 - Optimization of mechanical properties and surface roughness

Optimization task with criteria 6 seeks maximization of mechanical properties and minimization of surface roughness R_a. To perform the optimization task, X, Y and Z direction accuracy were set as hard lower bound at 99, 98 and 90 respectively while normalized manufacturing time was kept as hard upper bound at 1.

Figure 4.54 shows the EA optimization results for yield strength over surface roughness R_a. Typical trade-off solutions can be observed at the Pareto frontier. Two Pareto solution sets were chosen for evaluation: Pareto set 1 was chosen near at the start of the Pareto trade-off curve, lightly penalizing surface roughness (values between 12.5-12.8 μm) at the benefit of higher tensile strength (yield strength between 45-45.6 MPa); Pareto set 2 focus on maximum yield strength values (above 46 MPa) at penalty of higher surface roughness (between 13.5-14.8 μm).

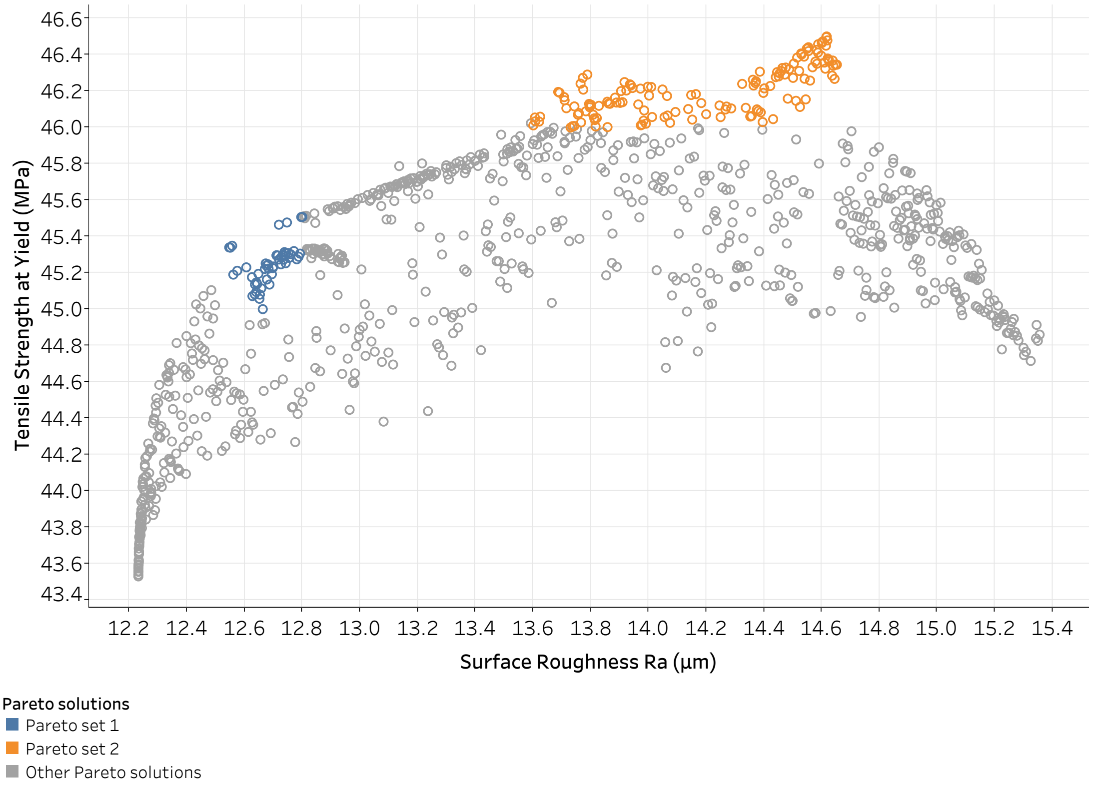

Figure 4.54 – Pareto solutions after optimization task with criteria 6.

Laser sintering parameter at optimized objective functions for criteria 6 are shown in Fig. 4.55a-b. For Pareto solutions set 1 one well distinguishable area is observed with a narrow range of laser speeds between 3000-3400 mm/s and wider laser power area between 35-42 W. Optimized solutions at Pareto set 2 are clustered in two regions: low laser speed (below 2800 mm/s mainly) and low laser power (below 35 W); intermediate laser speed between 3200-3600 mm/s and maximum laser power at 45 W.

A wide range of scan line spacing is available in Pareto set 1,from 0.3-0.4 mm at

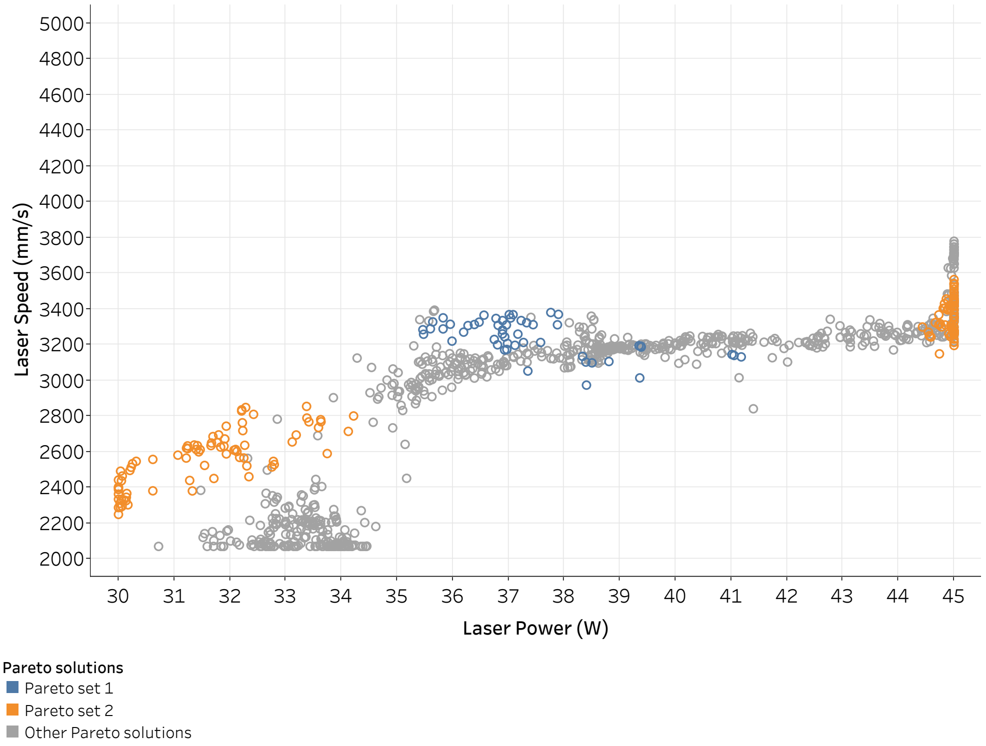

(a) Pareto solutions for laser power and laser speed.

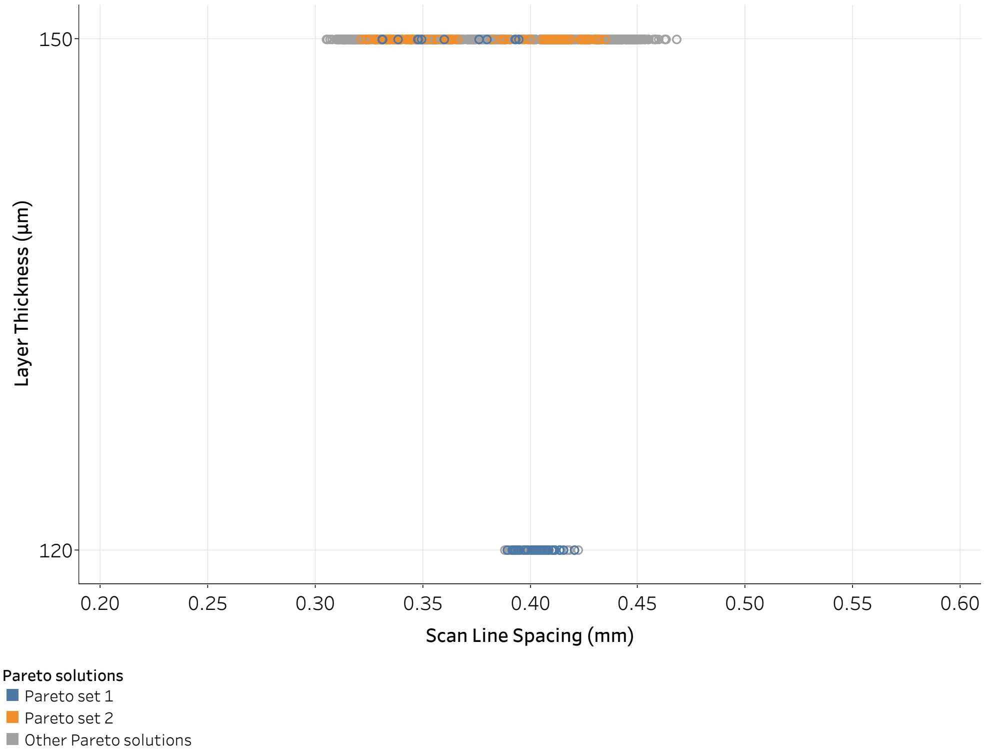

(b) Pareto solutions for scan line spacing and layer thickness.

Figure 4.55 – Pareto solutions for laser sintering parameters for criteria 6.

a layer thickness of 150 μm. For 120 μm layer thickness the scan line spacing range is narrowed to values between 0.39-0.41 mm. Scan line spacing options at Pareto set 2 range from 0.31-0.43 mm only for 150 μm layer thickness.

Figure 4.56a-b depicts the output parameter calculations at Pareto frontier for criteria 6. Elastic modulus at Pareto region 1 ranges from 1500-1600 MPa, while higher values are found for Pareto set 2 (from 1600-1700 MPa). Nominal strain at break remains at intermediate levels between 12-16 % at Pareto set 1 whereas Pareto set 2 gives better nominal strain ranging from 14-21 %. The better output parameters for Pareto set 2 are a consequence of the trade-off region chosen, focusing more on mechanical properties rather than surface roughness. Density at Pareto set 1 presented higher variation (from 0.94-0.963 g/cm^3) and lower values than set 2 (from 0.95-0.966 g/cm^3), which can also be considered a consequence of the focus on mechanical properties given for Pareto set 2, which is correlated to density of the specimens.

Z-direction accuracy ranged from 90-95 % at Pareto set 1 and from 90-93 % for Pareto set 2, therefore lower accuracy in Z-direction may be expected for Pareto set 2. An opposite effect was observed Y-direction accuracy, with Pareto set 1 resulting in lower accuracy (from 98-99 %) than Pareto set 2 (above 99 %). Normalized manufacturing time was clustered in two narrow regions for Pareto set 1: first region with values of 0.89-0.9 and a second region with higher normalized times near unity. A wide spread was observed for normalized manufacturing time in Pareto set 2, ranging from 0.86-0.96.

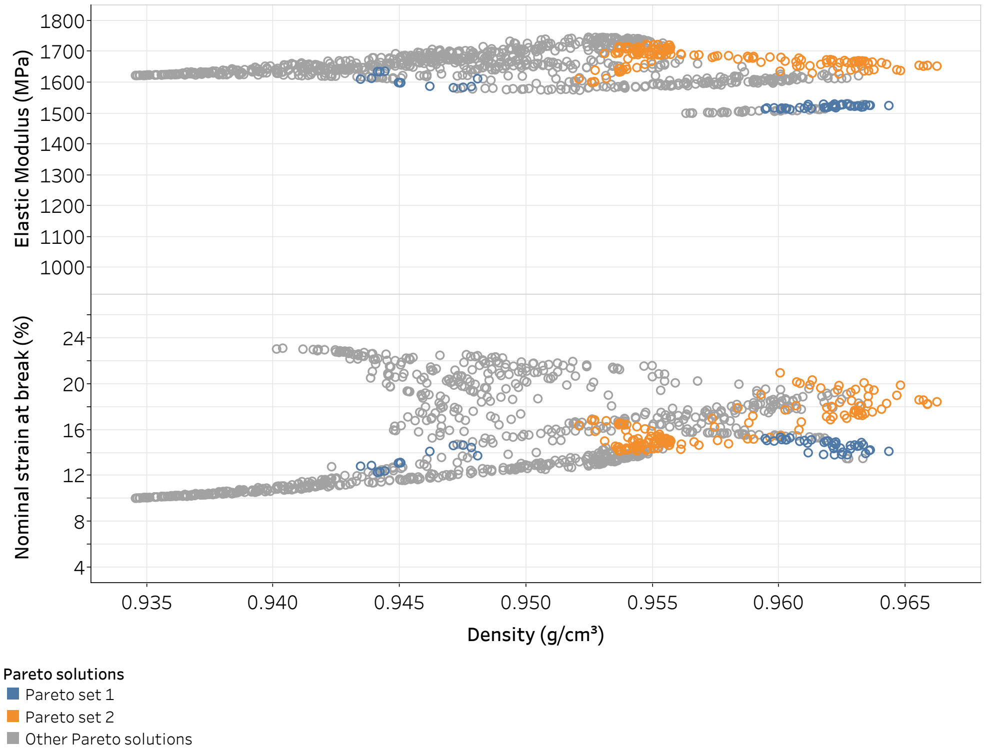

(a) Pareto solutions for elastic modulus, density and nominal strain at break.

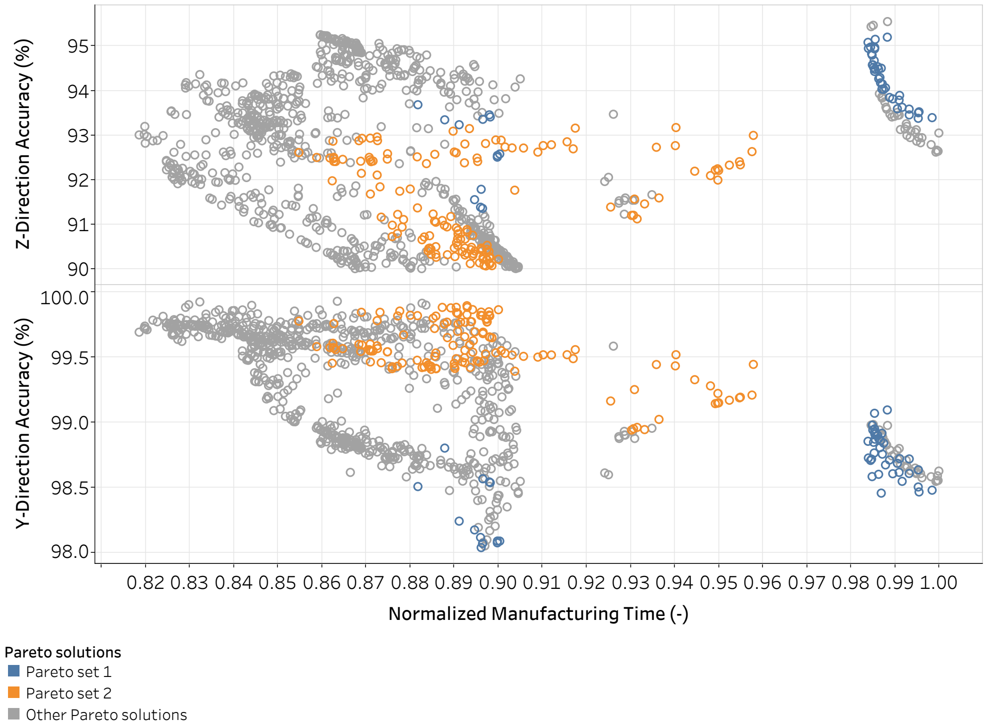

(b) Pareto solutions for normalized manufacturing time, Y-direction accuracy and Z-direction accuracy

Figure 4.56 – Output variables Pareto solutions for criteria 6.

5 Results and Discussion - PA12-CF

5.1 Influence of energy density - PA12-CF

This section describes the results achieved for PA12-CF composite material considering the energy density as main variable, composed by laser power, laser scan speed, scan line spacing and layer thickness (discussed in Chapter 2). Measurement variables evaluated include dimensional accuracy, density, surface roughness and tensile properties, as described in Chapter 3.

5.1.1 Influence of energy density on dimensional accuracy

Box whisker plots of dimensional accuracy in X, Y and Z direction over energy density are depicted in Figs. 5.1, 5.2 and 5.3. High values are observed for X-direction accuracy over all energy density area covered, remaining above 99.6 % up to 0.381 J/mm^3. At higher energy levels a higher dispersion can be observed as well as a slight decrease in accuracy.

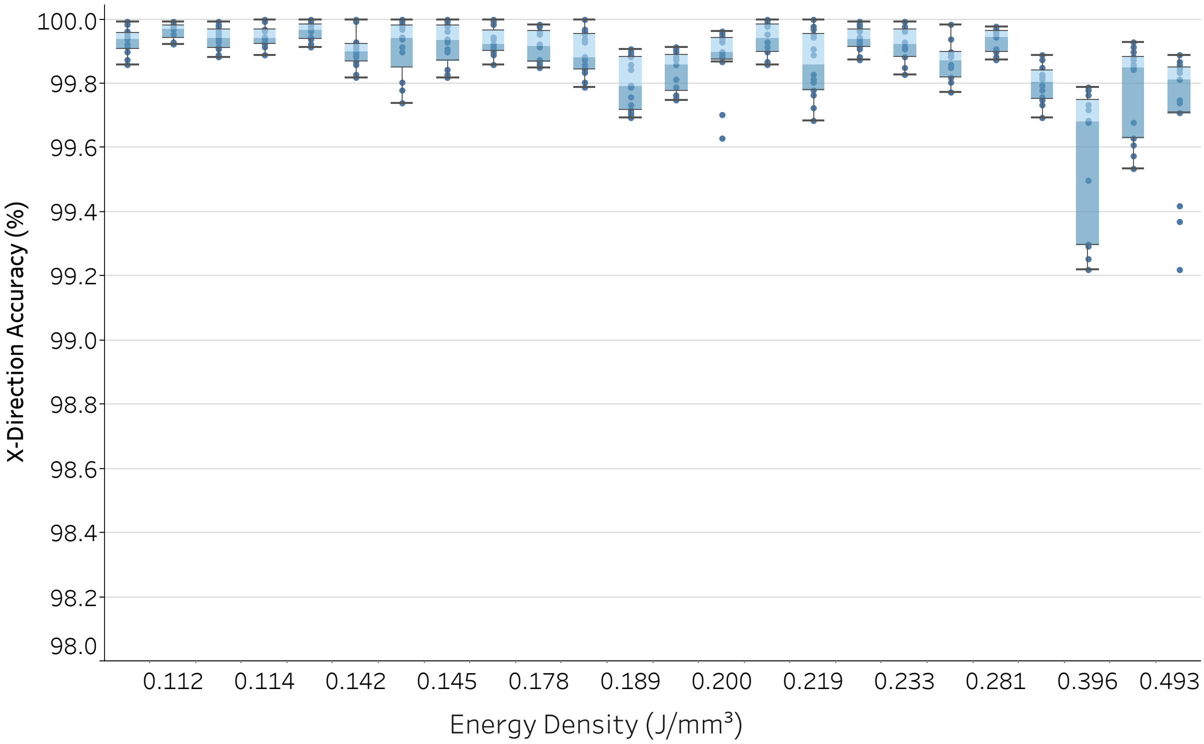

Figure 5.1 – Influence of energy density on X-direction dimensional accuracy of PA12-CF.

Y-direction accuracy remains above 98 % and stable up to 0.212 J/mm^3 energy density. Between 0.219-0.281 J/mm^3 higher dispersion in measured values are observed although mean values remain at adequate levels (above 98 % on average). An abrupt change occurs at energy densities equal or above 0.381 J/mm^3, showing much higher dispersion of the measured values and significant reduction in average accuracy to levels below 96 %.

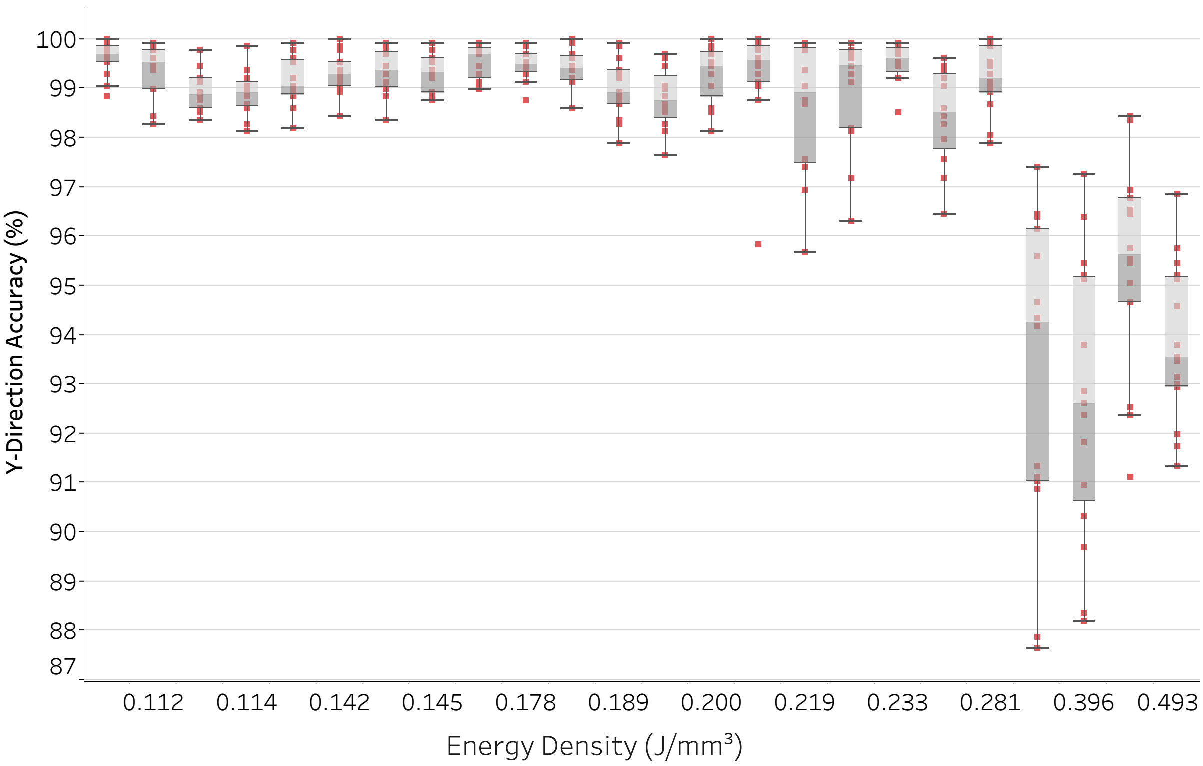

Figure 5.2 – Influence of energy density on Y-direction dimensional accuracy of PA12-CF.

Z-direction accuracy measurements are depicted in Fig. 5.3. A clear behavior can be observed from the graphic: between 0.096 and 0.123 J/mm^3 accuracy values are above 95 % on average. Further increase in energy density leads to a step wise decrease in Z-direction accuracy from 94 % at 0.142 J/mm^3 to 88.25 % at 0.178 J/mm^3. Between 0.178 and 0.281 J/mm^3 measurement values remain more or less stable, with upper and lower hinge oscillating between 85 and 90 %. At an energy densities of 0.381 J/mm^3 and above Z-direction accuracy sharply decreases to average values between 75-80 % and a higher dispersion between measurements can be observed.

As described in in section 4.1.1, the laser energy delivered to the powder bed undergoes radiation absorption by the PA12-CF particles and multiple transmission to neighbouring particles. Both PA12 and CF in the form of anthracite have good absorption at the CO_2 laser wavelength of 10.2 μm (LAUMER et al., 2016; RIBEIRO et al., 2018). Addition of carbon fiber in anthracite form to PA12 improves thermal conductivity of the powder bed (HERRIN; DEMING, 1996), leading to more heat transferred to the surrounding and underlying unsintered powder, worsening dimensional accuracy of the parts. It has been observed by simulation modelling with PA12 and carbon nanotubes (CNTs) that the laser heat affected area is wider and deeper when laser sintering PA12-CNT than PA12 (BAI et al., 2015). At higher energy densities this effect is more pronounced

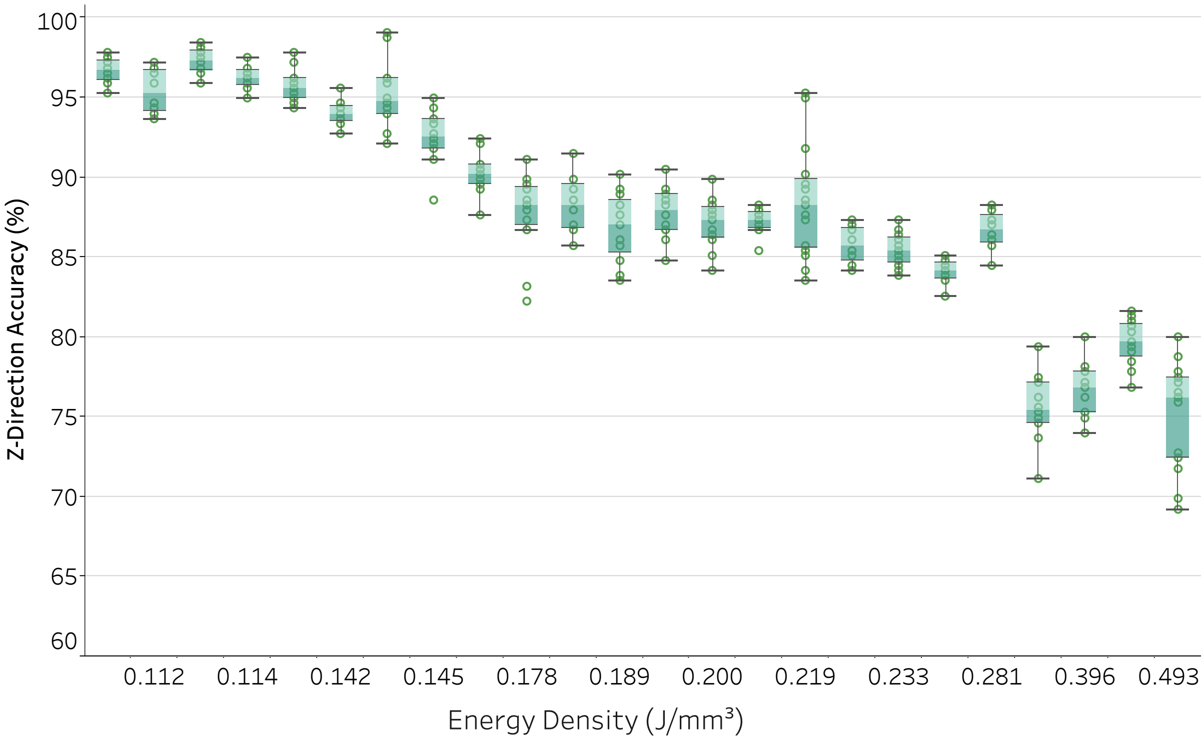

Figure 5.3 – Influence of input energy on Z-direction dimensional accuracy of PA12-CF.

due to the higher heat affected area. This may explain the lower accuracy of PA12-CF samples in X and Y direction compared to pure PA12.

5.1.2 Influence of energy density on surface roughness

Box whisker plots of average surface roughness R_a over energy density are shown in Fig. 5.4. No clear tendency can be observed on surface roughness and energy density, with the values oscillating between 11 and 20 μm regardless of the energy density applied. A high variation between measurements at the same energy density can be observed. This is typical from laser sintered surfaces which produced highly irregular and complex surface topographies which cannot be totally captured by profile measurement techniques such as the one used in this study. The presence of carbon short fibers adds another factor which contributes to the high variation observed.

In section 4.1.3 it was observed the influence that laser sintering parameters play surface topography of PA12, more specifically by evaluating the effect degree of overlap via scan line spacing calculations and laser speed have on surface roughness. A similar analysis was carried out for PA12-CF material. Figure 5.5 shows the effect of overlap degree on average surface roughness R_a as well as the intensity of the laser speed applied highlighted as a size dimension on the graphic. Contrary to what was observed for PA12, overlap degree seems to have no influence on the average values of R_a for LS surfaces of PA12-CF. Average surface roughness values oscillate between 12 and 16 μm independently on the scan line spacing and laser speed applied.

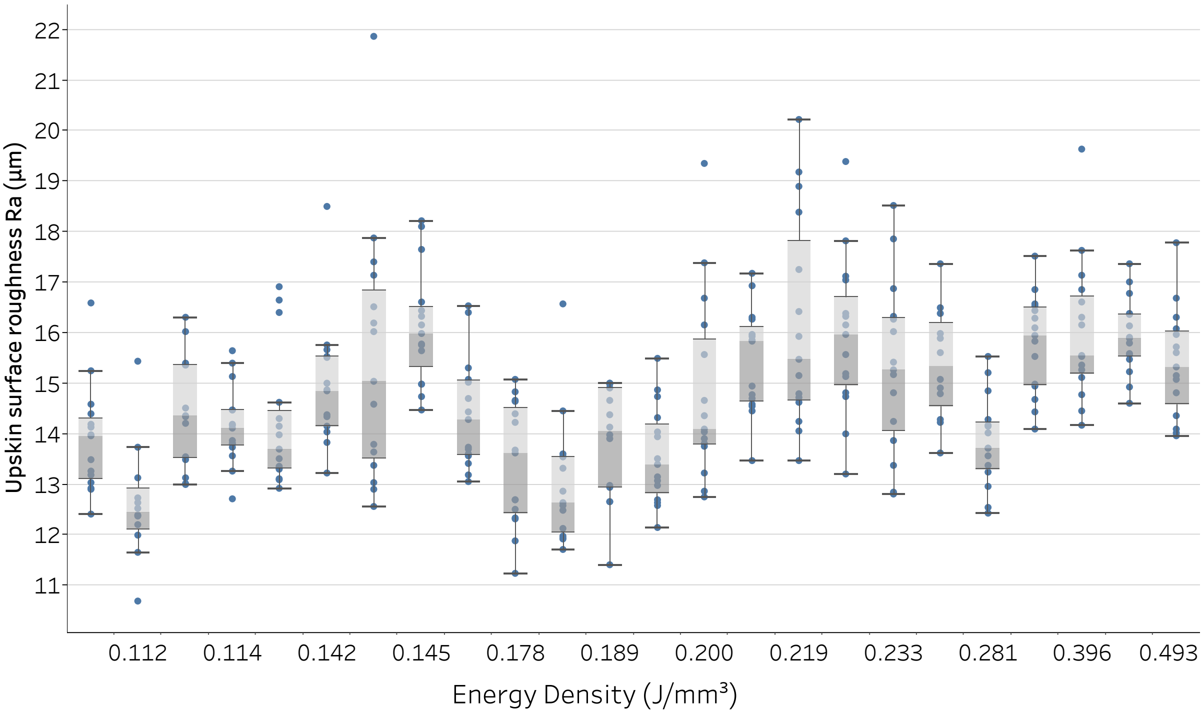

Figure 5.4 – Influence of energy density on average surface roughness R_a of PA12-CF.

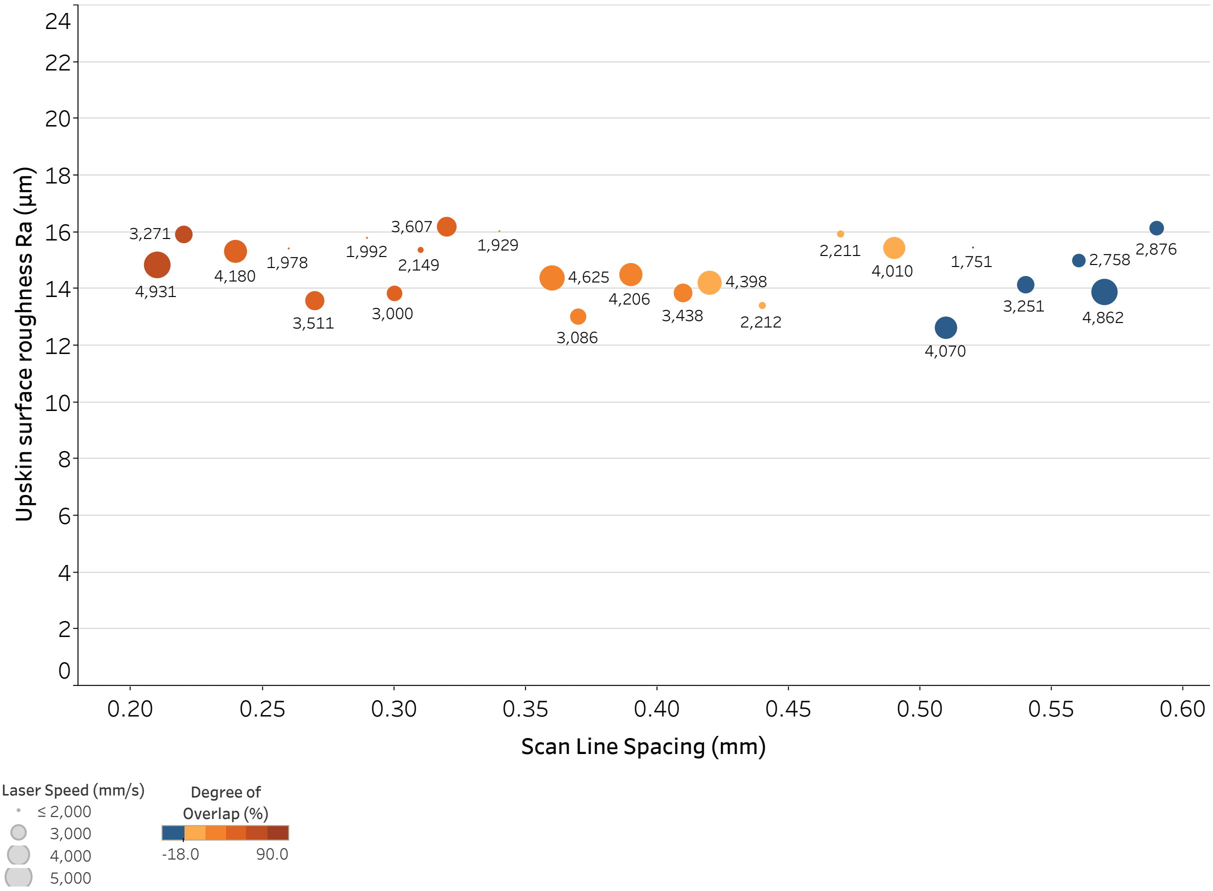

Figure 5.5 – Influence of degree of overlap on surface roughness of LS PA12-CF.

To further evaluate if changes on surface topography could be observed, Fig. 5.6

shows LS surface morphology of PA12-CF samples captured with SEM at different energy densities and overlap degrees. From the micrographs no differences can be observed on

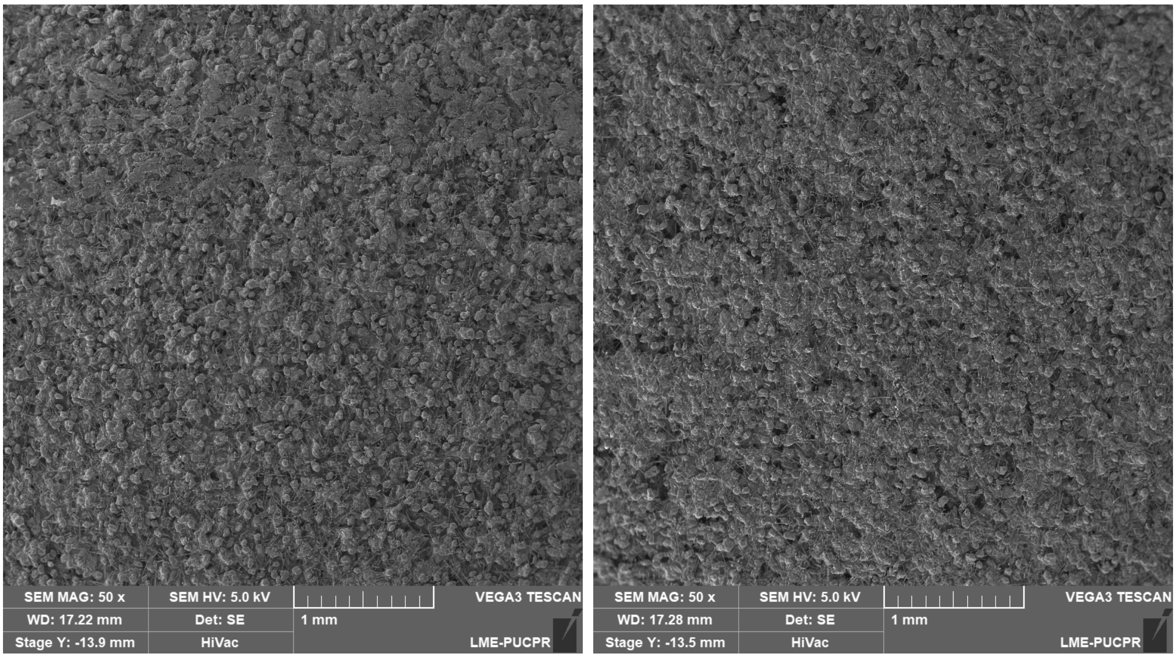

(a) Laser speed: 3,000 mm/s; Degree of overlap: 40 %

(b) Laser speed: 4,206 mm/s; Degree of overlap: 22 %

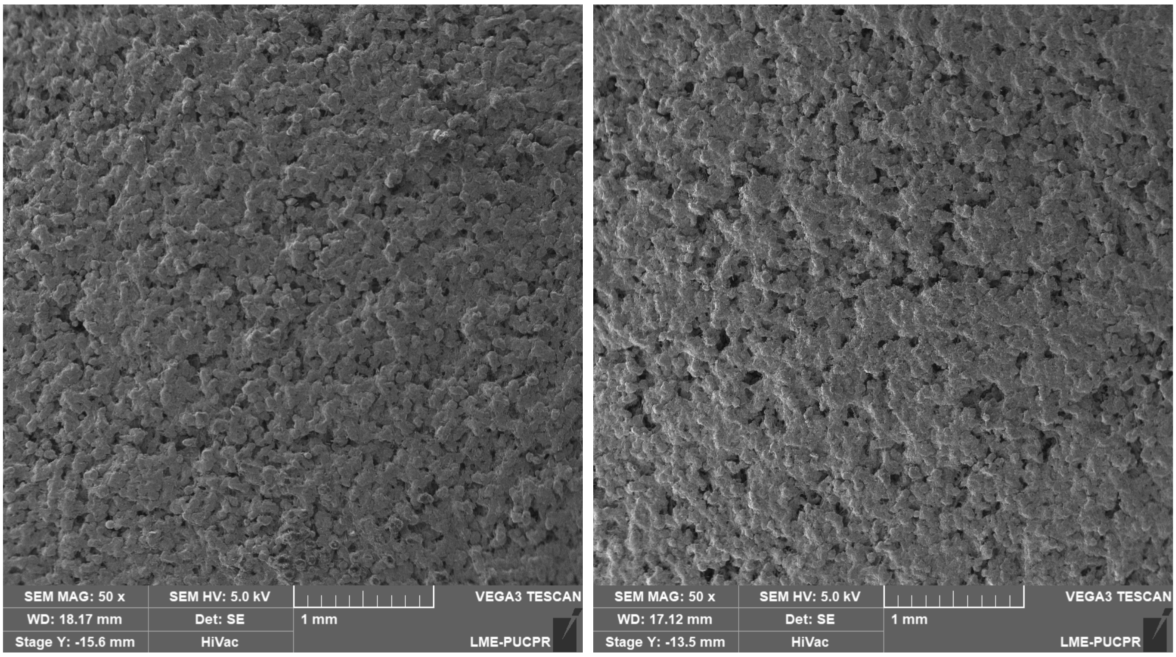

(c) Laser speed: 2,758 mm/s; Degree of overlap: -12 %

(d) Laser speed: 4,862 mm/s; Degree of overlap: -14 %

Figure 5.6 – SEM micrographs of PA12-CF LS surface morphology.

surface morphology of samples processed at different overlap degrees, even for negative overlap degrees from Fig. 5.6c-d (no overlap present) the surface morphologies are very similar. Scan line spacing seems to play a small or even not significant role on surface morphology. Also the combination of negative overlap degree and high laser speed (observed to be a major factor to change surfaces on PA12) did not contribute to modifications in surface morphology of PA12-CF samples.

A possible explanation for the surface results observed can be attributed to the increase on laser heat affected area caused by the presence of carbon fibers on PA12. Due to its higher thermal conductivity, carbon fibers enhance the heat transferred to surrounding particles during SLS, increasing the heat affected area of the laser. A higher heat affected area increases the real overlap degree, promoting a smoothing of the LS surfaces. Experiments with higher overlap degrees could be performed to confirm this hypothesis.

5.1.3 Influence of energy density on density

Box whisker plot of the measured parts' density over energy density are depicted in Fig. 5.7. Low density values around 0.84 g/cm^3 are found at energy density of 0.096 J/mm^3. Slight increase in energy density to 0.112 J/mm^3 improves considerably parts density to 0.92 g/cm^3. From 0.114-0.123 J/mm^3 there is a plateau between with density values between 0.95-0.97 g/cm^3. Further energy density increase improves density in a step like pattern from 0.98 to 1.03 g/cm^3, after which another plateau is reached until 0.181 J/mm^3. Maximum average density is found at at this plateau with an average of 1.03 g/cm^3. From 0.189-0.26 J/mm^3 density values oscillate between 1.00 and 1.02 g/cm^3 on average. Above 0.26 J/mm^3 density starts to decrease to values below 1.00 g/cm^3 on average.

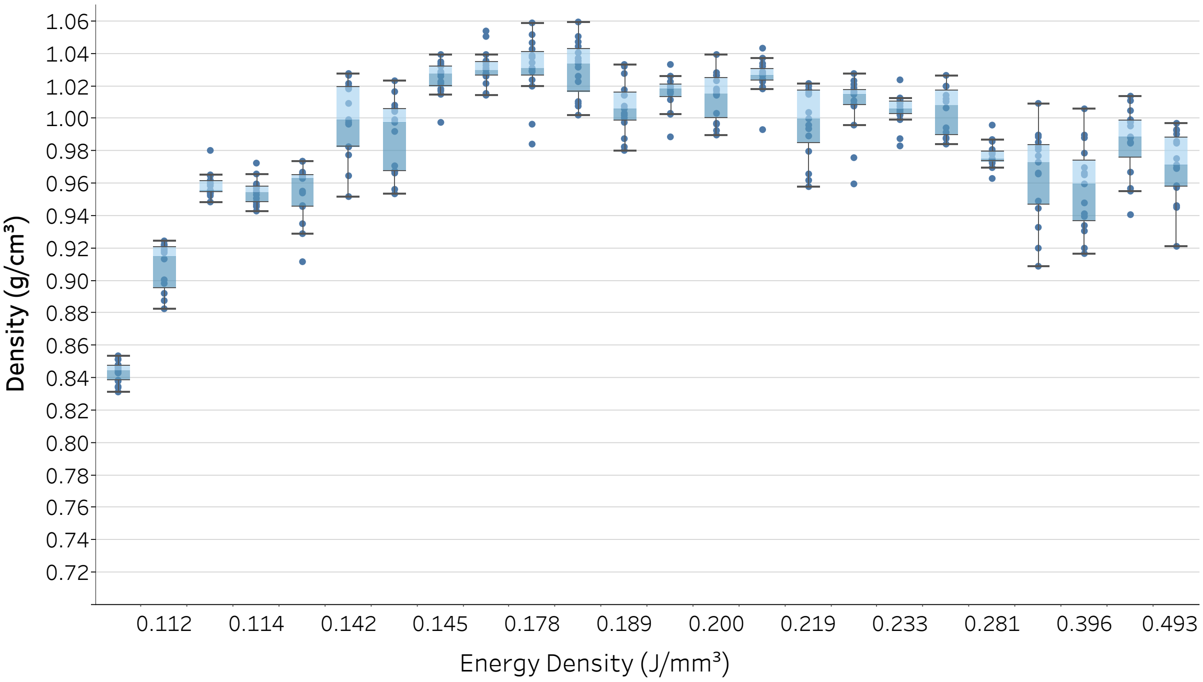

Figure 5.7 – Influence of energy density on parts density for PA12-CF.

SLS is a highly complex process where a combination of factors may influence porosity formation and density. Material characteristics such as particle shape and distribution play an important role on packing density of the powder bed. PA12 particles have "potatoe" shape morphology and an adequate particle size distribution which favours powder spreading and flowability during LS process. Carbon fibers present in the studied material can influence negatively powder spreading over the platform due to their high aspect ratio, causing voids in the packed powder which can lead to porosity after LS consolidation (JANSSON; PEJRYD, 2016).

From laser sintering perspective of composite materials, the very short laser material interaction during LS leads to main consolidation mechanism of PA12-CF powders via particle rearrangement phase during liquid phase sintering (LPS), where the liquid phase (PA12) surrounds the solid particles (CF) via capillary forces (ANESTIEV; FROYEN, 1999). Molten pool morphology and intensity of capillary forces are directly related to the magnitude of Marangoni flow generated during laser sintering, which depends on materials aspects such as viscosity of molten phase and surface tension gradient.

Laser sintering parameters can significantly affect Marangoni flow, rearrangement phase during LPS and resulting density as observed in Fig. 5.7. At very low energy levels the powder particles do not melt effectively and in sufficient amount so that PA12 liquid phase can flow through the solid carbon fiber particles, leading to a higher fraction of unsintered particles in the part and also to interlayer porosity. Additionally Marangoni flow magnitude is low due to the lower temperature gradient between the center and edge of the molten pool, concentrating the heat near the center of the laser spot and leading to a narrow molten pool. All these aspects result in a poor rearrangement phase during LPS, resulting in poor consolidation of the composite powder and higher porosity.

Increasing energy density reduces porosity due to higher amount of liquid present, improving spreading kinetics during liquid phase sintering rearrangement phase. Marangoni flow is increased due to higher temperature gradients existing, effectively transferring heat from center to the edge of the molten pool, generating a wider molten pool and leading to improved LPS particle rearrangement phase. But an optimum level of energy exists, above which a negative effect on density is observed, which is caused by the increased molten pool area generated by higher magnitude Marangoni flow, increasing the resulting part volume and consequently reducing density. Polymer degradation can also lead to lower density.

5.1.4 Influence of energy density on tensile properties - Elastic behavior

Elastic behavior of PA12-CF was evaluated based on force displacement measurements with following properties obtained: proportional limit (MPa), 0.2% offset yield strength (MPa), nominal strain at proportional limit (0.2%), nominal strain at 0.2% offset yield strength and elastic modulus (MPa).

Figure 5.8a shows proportional limit and 0.2 % offset yield strength. Lowest values of proportional limit (16 MPa) and 0.2 % offset yield strength (22 MPa) are found at the lowest energy density level J/mm^3. Mechanical properties linearly increase with higher energy densities up to 0.145J/mm^3, reaching 31 MPa for proportional limit and 40 MPa for 0.2 % offset yield strength. From 0.145 until 0.2 J/mm^3 the values oscillate between 31-35 MPa on average for proportional limit and between 41-43 MPa on average for 0.2 % offset yield strength, reaching maximum values at 0.19 J/mm^3.

Further increase in energy density reduces linear tensile properties of the composite material and the values oscillate between 25-30 MPa and 35-40 MPa for proportional limit and 0.2 % offset yield strength respectively. A slight tendency to decrease mechanical properties for energy densities above 0.281 J/mm^3 is observed. Compared to PA12 linear strength properties described in 4.1.4, PA12-CF outperforms PA12 in 60 % depending on the energy density used to process the sample.

Nominal strain values at proportional limit and 0.2 % offset yield strength are shown in Fig. 5.8b. Nominal strain behavior at elastic regime varies little. Except for the lowest energy density value applied, nominal strain at proportional limit oscilates in a narrow region between 1-1.12 % on average. Strain at 0.2 % offset yield strength follows a similar behavior, with values oscillating between 1.4-1.55 % on average. Lower values are also found at the highest energy density applied (0.493 J/mm^3). Compared to PA12, nominal strain values for PA12-CF are lower (45 % lower depending on the energy density), which is expected for polymer composites considering the more brittle nature of the material.

Elastic modulus calculated values over energy density are shown in Fig. 5.9. At the lowest energy density of 0.096 J/mm^3 elastic modulus was 2400 MPa, increasing step-wisely at higher energy values, reaching 3566 MPa at 0.145 J/mm^3. From 0.168-0.189 J/mm^3 there is a slight decrease on elastic modulus, with a plateau around 3450 MPa. At 0.19 J/mm^3 the highest elastic modulus of 3669 MPa is reached, significantly higher than elastic modulus at a slightly lower energy level, demonstrating the importance individual laser exposure parameters play on mechanical properties. From 0.212-0.281 J/mm^3 elastic modulus decreases again to values between 3200-3500 MPa on average. Further increase on energy density above 0.281 J/mm^3 leads to an overall elastic modulus reduction, except for the measuring point at 0.398 J/mm^3, which exhibited elastic modulus of 3445 MPa.

Compared to PA12, PA12-CF elastic modulus was increased by 120 %, which demonstrates the benefit carbon fibers provide on reinforcement of PA12 matrix. Compared to material datasheet provided by material manufacturer (EOS, 2020) and the work conducted by Jansson & Pejryd (2016), elastic modulus values found for samples manufactured in x direction in the present work are significantly lower. Jansson & Pejryd (2016) reported average elastic modulus of 6300 MPa, and the material datasheet from

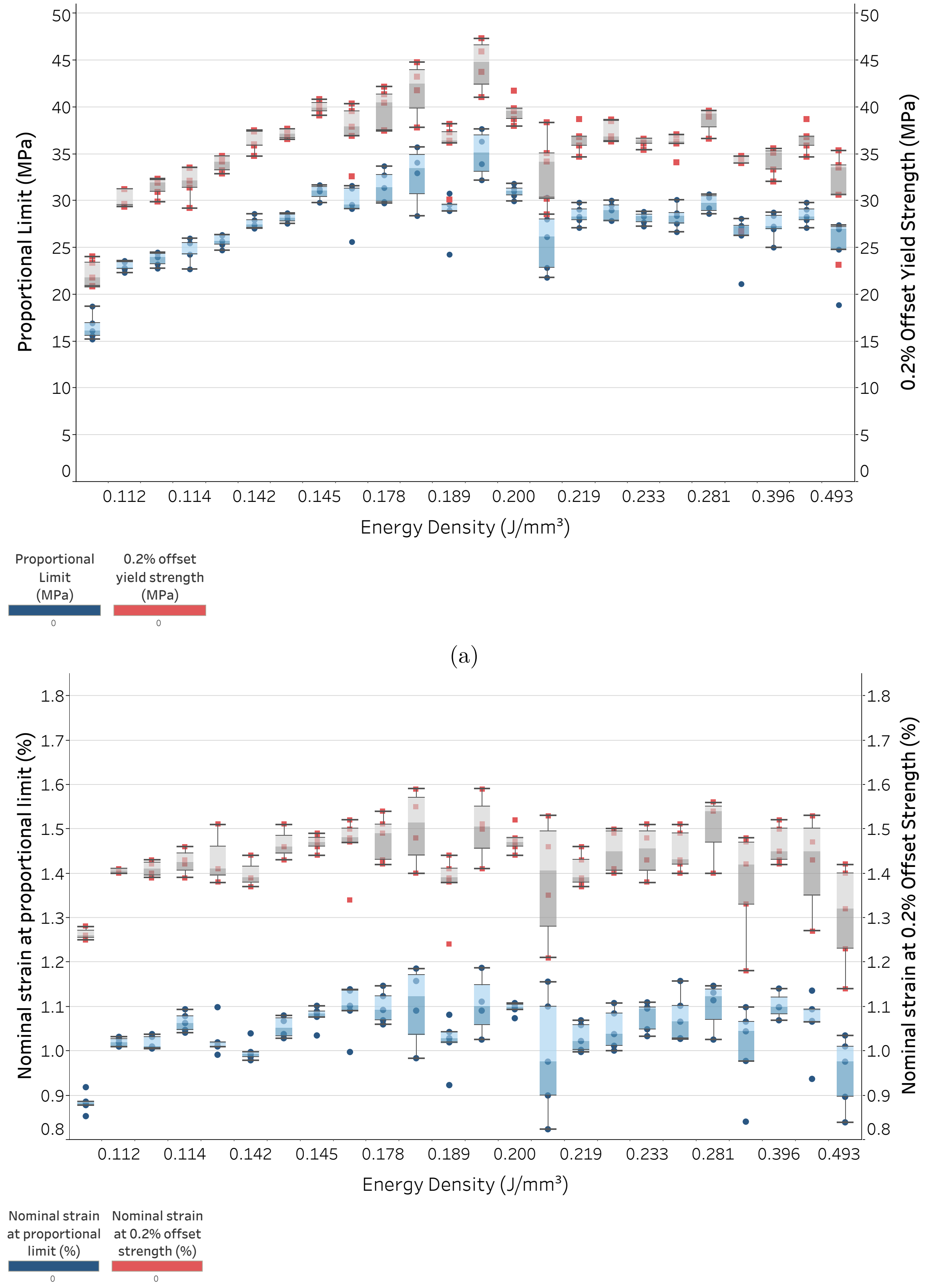

(a)

(b)

Figure 5.8 – Influence of energy density on elastic behavior for PA12-CF: (a) Stress ; (b) Nominal strain

material manufacturer reports similar values for x direction. The reason for the lower values found remain unknown.

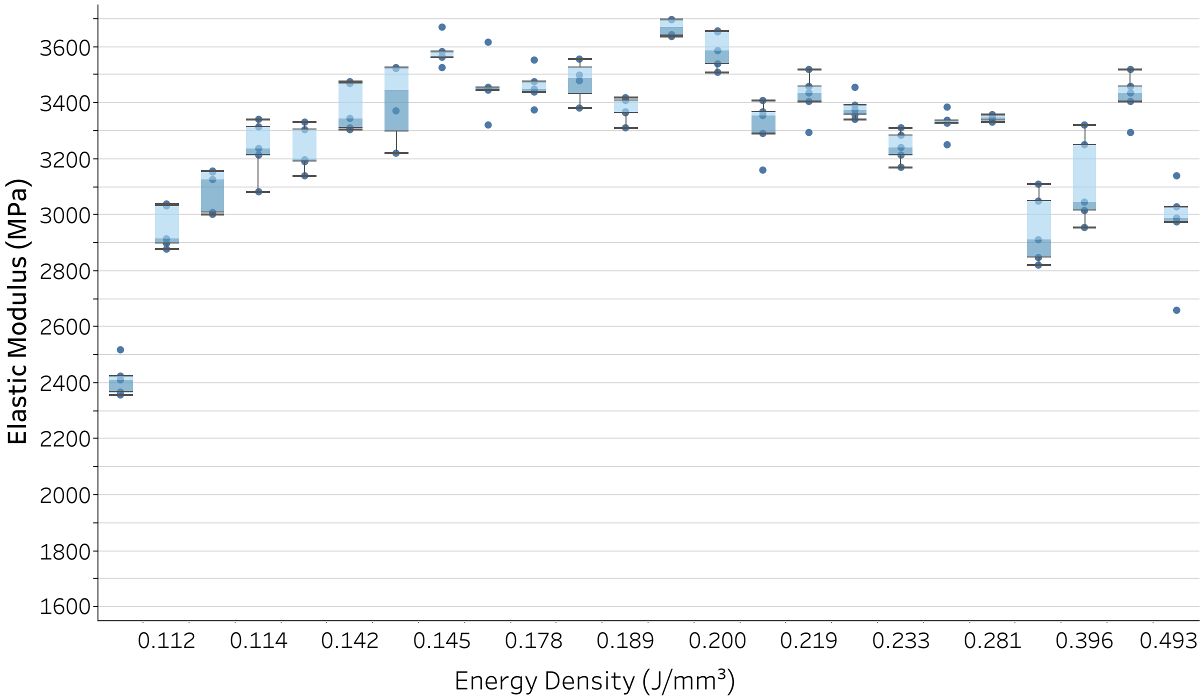

Figure 5.9 – Influence of energy density on elastic modulus for PA12-CF.

Elastic behaviour of polymer composites depends on the homogeneity of filler dispersion on the matrix and the adhesion between filler and polymer matrix. dispersion of the filler. PA12-CF composites proved to have superior elastic properties compared to pure PA12, even at the lowest energy density applied elastic modulus was much higher than pure PA12. This is mainly due to a good dispersion and adhesion of carbon fibers on PA12 matrix (QI; CHEN; WANG, 2017). For polymer composites this comes at the cost of lower strain as the filler present causes local fragility to the matrix.

Additionally, consolidation mechanism by liquid phase sintering mechanism and recrystallization phase play an important role on the homogeneity of filler dispersion and adhesion at matrix-filler interface (KRUTH et al., 2007). At low energy densities liquid phase sintering is poor due to low liquid content flowing through the filler solid particles. Marangoni flow magnitude is also low due to the lower thermal gradient occurring at the molten pool, leading to a poor rearrangement phase during LPS and weak adhesion between filler and matrix and lower elastic properties.

At higher energy density levels liquid phase sintering mechanism is enhanced by the higher liquid content, reducing the viscosity of the molten pool and promoting an increase on the capillary forces acting during rearrangement phase. Rearrangement phase is therefore improved, contributing to a better densification process and better dispersion of filler in the polymer matrix.

Increasing energy density further decreases linear tensile properties of PA12-CF. At higher energy densities where adequate consolidation was achieved and porosity diminished, recrystallization behavior may play a major role. As discussed in section 4.1.4 increased energy levels decrease overall crystal fraction of the PA12 samples due to increased molten-recrystallized phase present in the LS sample. The reduced crystal fraction could lead to a reduction in linear properties as higher crystallization degree is associated with improved linear properties (JAUFFRÈS et al., 2009; DUPIN et al., 2012).

5.1.5 Influence of energy density on tensile properties - Plastic behavior

Figure 5.10a shows tensile strength at yield and break point over energy density. At lowest energy densities of 0.096 J/mm^3, both measured strengths present low values of 31.87 MPa on average. The similar values of yield and break strength suggest no little or no plastic deformation at all, resulting in brittle fracture.

Strength values increase step-wisely with increasing energy density values, reaching 65 MPa on average at 0.168 J/mm^3. Between 0.168-0.231 J/mm^3 the values oscillate between 63-66.5 MPa, reaching maximum values at 0.2 J/mm^3 energy density.Further increase on energy density leads to a reduction in both yield and break strength to values below 63 MPa, except for energy density of 0.398 J/mm^3 which reached 64 MPa on average.

Compared to PA12, PA12-CF improves yield strength in 44 %. Compared to the literature, tensile yield strength is in good agreement with the results found by Jansson & Pejryd (2016) and Liu et al. (2019), where average values of 66.7 MPa and 65.6 MPa were found respectively. Compared to the material manufacturer datasheet (72 MPa declared by (EOS, 2020)) yield strength values are slightly lower.

Nominal strain at yield and break points over energy density are depicted in Fig. 5.10b. Both yield and break strain start with very similar levels of 2.5 % at the lowest energy density level, indicating the brittle fracture behavior in this are. Strain values increase step-wisely towards higher energy densities, reaching 4.2 % at 0.114 J/mm^3. At higher energy densities strain values oscillate with a clear increase gradient. Additionally yield and break strain start to achieve different values at 0.142 J/mm^3, suggesting that more plastic deformation is present. Highest strain values are found at 0.168 J/mm^3. Between 0.168 and 0.493 J/mm^3 both strain at yield and break oscillate between 4.7-5.75 %, with strain at break values slightly above strain at yield.

Compared to the literature nominal strain at break values are considerably higher than average values of 3 % reported by Jansson & Pejryd (2016). Material manufacturer also reports lower values of 4.1 % (EOS, 2020).

SEM micrographs of fractured surfaces of PA12-CF processed by LS at different

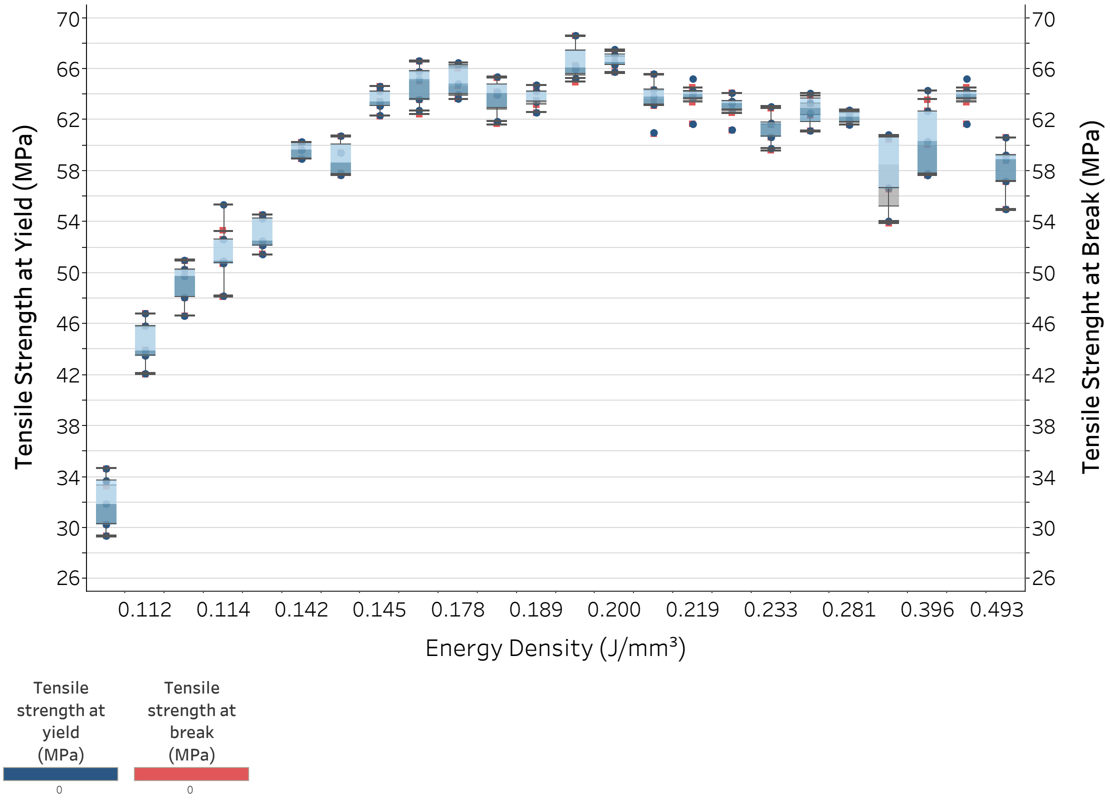

(a)

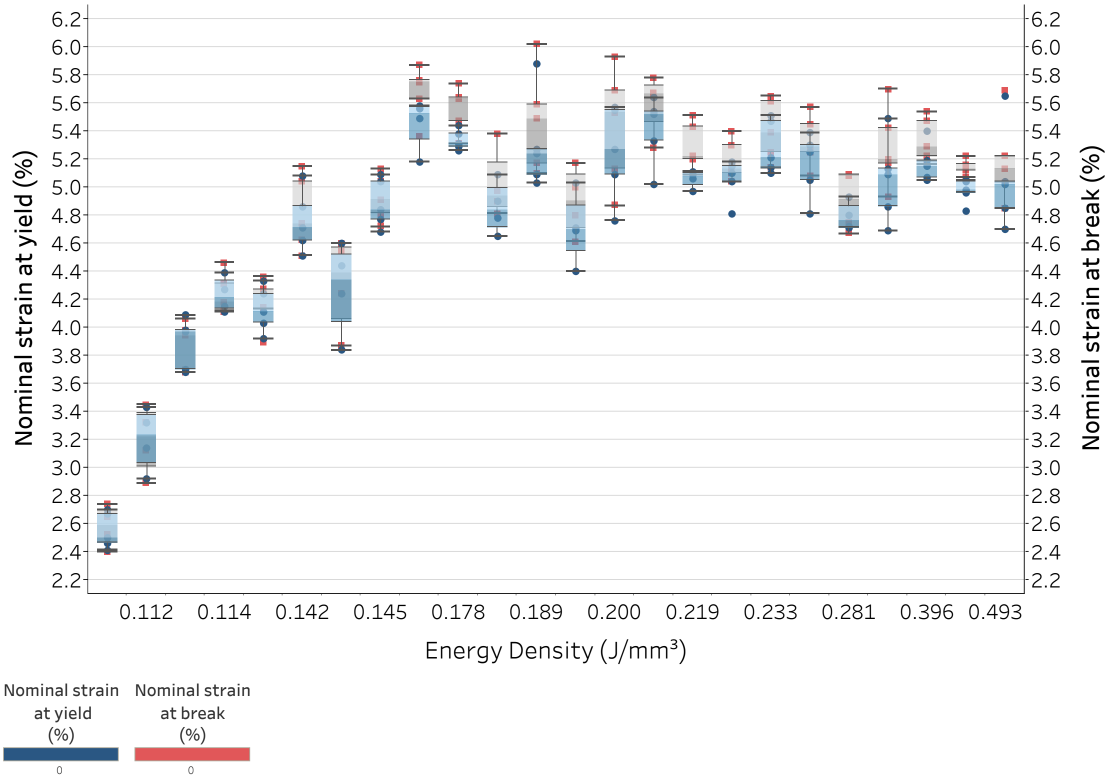

(b)

Figure 5.10 – Influence of energy density on plastic behavior for PA12-CF: (a) Stress ; (b) Nominal strain.

energy densities are depicted in Fig. 5.11. At 0.096 and 0.114 J/mm^3 SEM images (Fig. 5.11a-d) reveal the presence of interparticle and interlayer porosity, with well distinguishable layers. Higher magnification images show a high content of unmolten PA12 particles and carbon fibers which are not surrounded by PA12 matrix, indicating a poor level of consolidation.

At a higher energy level of 0.142 J/mm^3 fractured surfaces show a denser structure with PA12 matrix embedding carbon fibers, indicating better adhesion between the two phases. Carbon fibers are uniformly dispersed in the polymer matrix. Porosity can be observed and also some fibers pullout from the matrix.

Further increase on energy density to 0.168 J/mm^3 (strain at break was the highest at this energy level) leads to higher plastic deformation as observed in Fig. 5.11e, with elongated fibrils visible in direction of the stress applied. The plastic deformation occurs in PA12 matrix and the cracks originate at the interface between PA12 and carbon fibers as can be observed in more detail in Fig. 5.11f. This fracture mechanism is well known to composite materials as the interface between adjoining and different materials results in stress concentration. Additionally carbon fibers seem preferentially oriented in direction of tensile force applied, which is in agreement with the results found by Jansson & Pejryd (2016).

Figure Fig. 5.11g-h shows the fractured surfaces of LS samples processed with the highest energy level of 0.493 J/mm^3. No significant changes in the microstructure can be seen, with plastic deformation also occurring. In Fig. 5.11h carbon fiber pullout from PA12 matrix can be observed, reinforcing that the fracture mechanism occurs at the interface between the carbon fiber and matrix.

As described before, SLS is a process with very short laser material interaction time where liquid phase sintering rearrangement phase is the predominant consolidation mechanism occurring. At very low energies, there is no effective consolidation of the particles, resulting in high number of pores present, interlayer porosity and large quantity of unmolten particles. Additionally the adhesion of carbon fiber to PA12 matrix is poor as there is not enough liquid content to promote proper liquid phase sintering. Crack nucleation is induced in both interlayer region and interface between carbon fiber and PA12, leading to low yield strength values and very low elongation at break measured.

Energy increase improves capillary forces during LPS rearrangement phase as the liquid content in molten pool is higher, and PA12 matrix can effectively surround carbon fiber particles, forming a coherent structure with good adhesion between fiber and matrix and low porosity as observed in SEM micrographs. The resulting microstructure is formed by molten-recrystallized PA12 phase, smaller content of unmolten particles and carbon fibers. As the plastic deformation occurring in the composite material results from PA12 deformation, the lower content of unmolten particles results in lower crystallinity of PA12

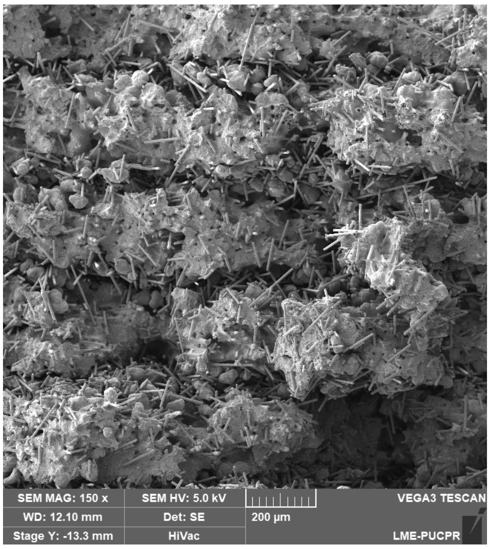

(a) Energy Density: 0.096 J/mm^3

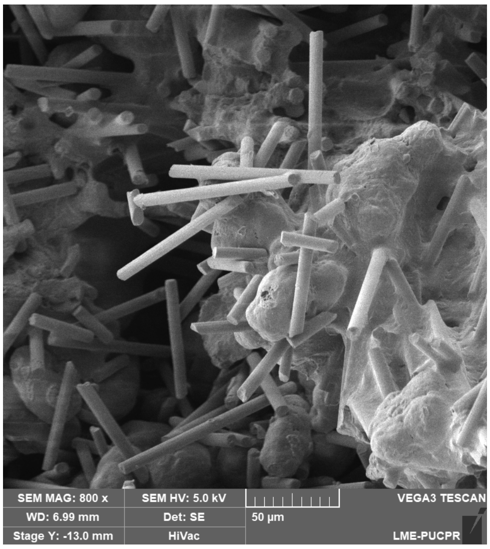

(b) Energy Density: 0.096 J/mm^3

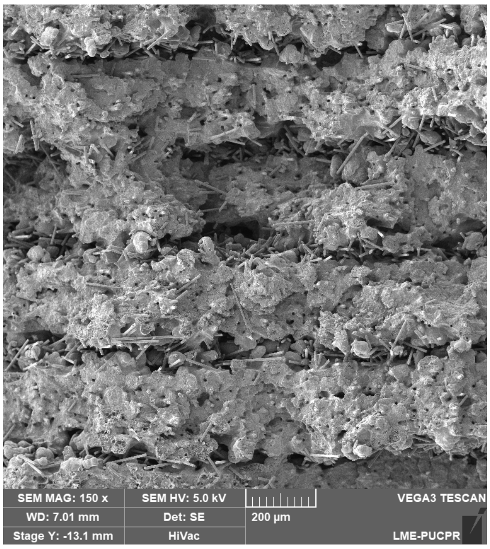

(c) Energy Density: 0.114 J/mm^3

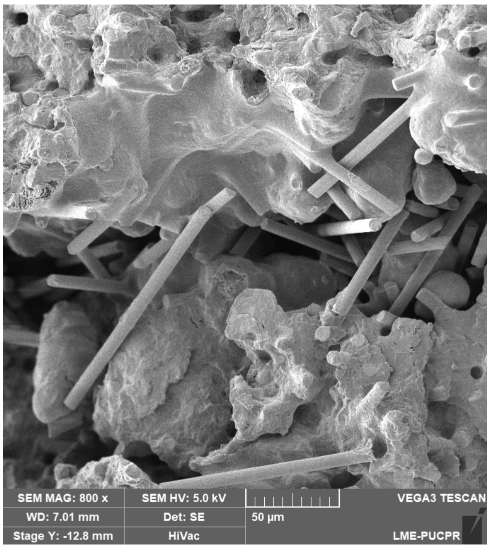

(d) Energy Density: 0.114 J/mm^3

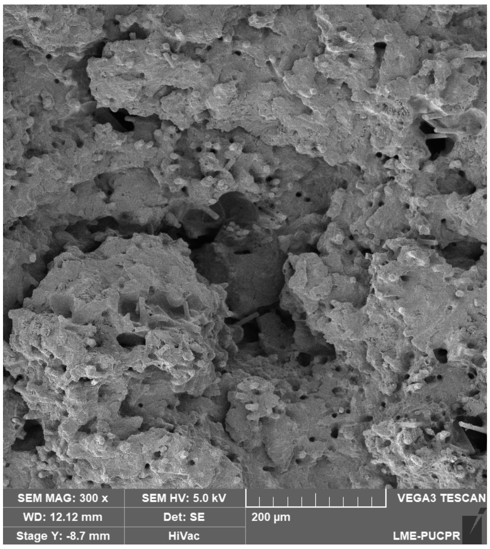

(e) Energy Density: 0.142 J/mm^3

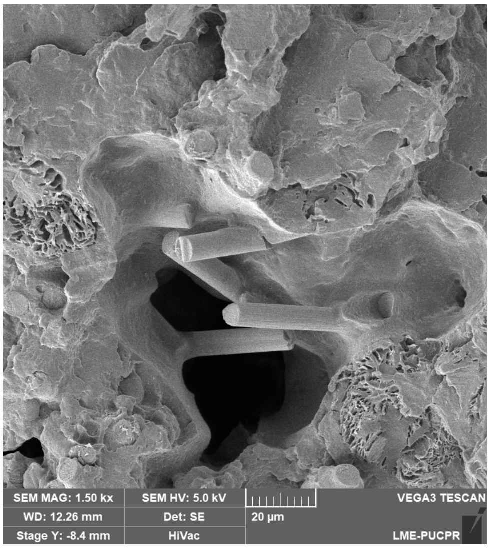

(f) Energy Density: 0.142 J/mm^3

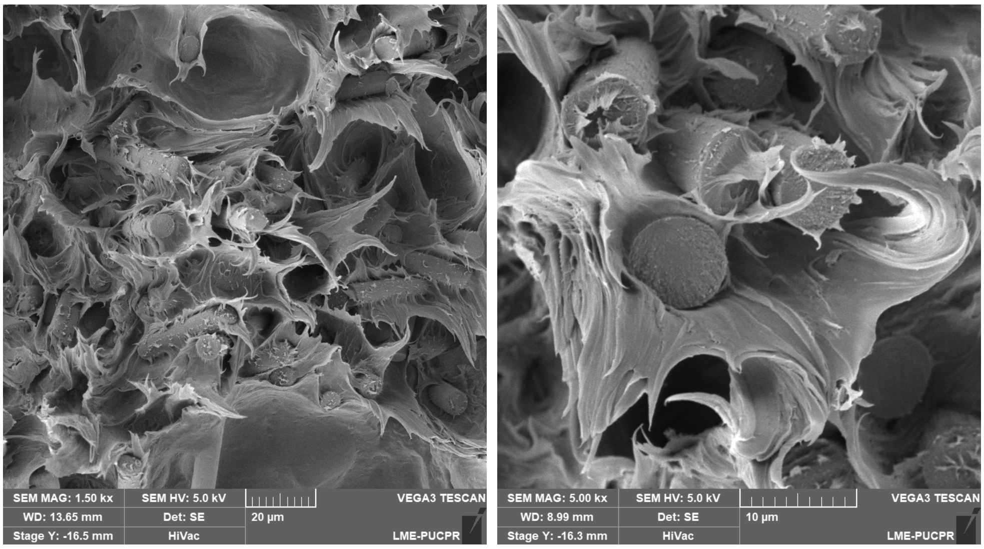

(g) Energy Density: 0.168 J/mm^3 (h) Energy Density: 0.168 J/mm^3

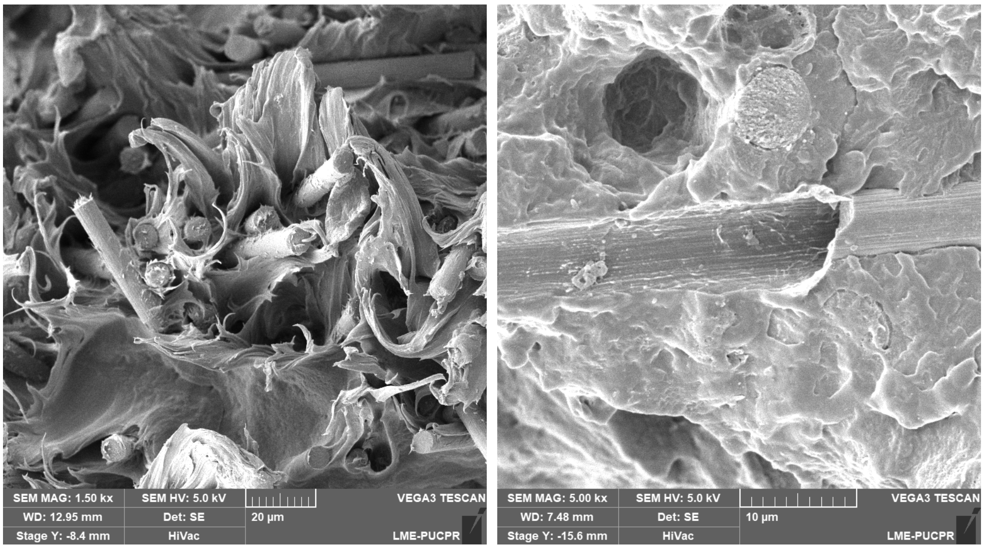

(i) Energy Density: 0.493 J/mm^3 (j) Energy Density: 0.493 J/mm^3

Figure 5.11 – SEM micrographs of fractured PA12-CF LS surfaces.

(i.e. amorphous content of PA12 is increased) improving plastic strain. Compared to PA12, plastic strain of PA12-CF is much lower even improving energy density, but such trend is common for composites as the fracture mechanism occurs at the interface between filler and matrix material and stress concentrations are induced.

5.1.6 Influence of energy density on crystallization behavior

XRD patterns of PA12-CF and PA12 powder and SLS PA12-CF samples processed at different energy densities are shown in Fig. 5.12. PA12-CF powder XRD reveals the existence of two separate peaks occurring between a 2θ of 20-24°. The first peak at 2θ of 20.92° is associated with the γ crystal form and the second peak at 2θ of 21.9° is associated with the α crystal form. Compared to PA12 XRD, PA12-CF shows broader reflection spectrum in the range between 20-25°, this is mainly due to the amorphous structure of anthracite present in the carbon fibers (RIBEIRO et al., 2018).

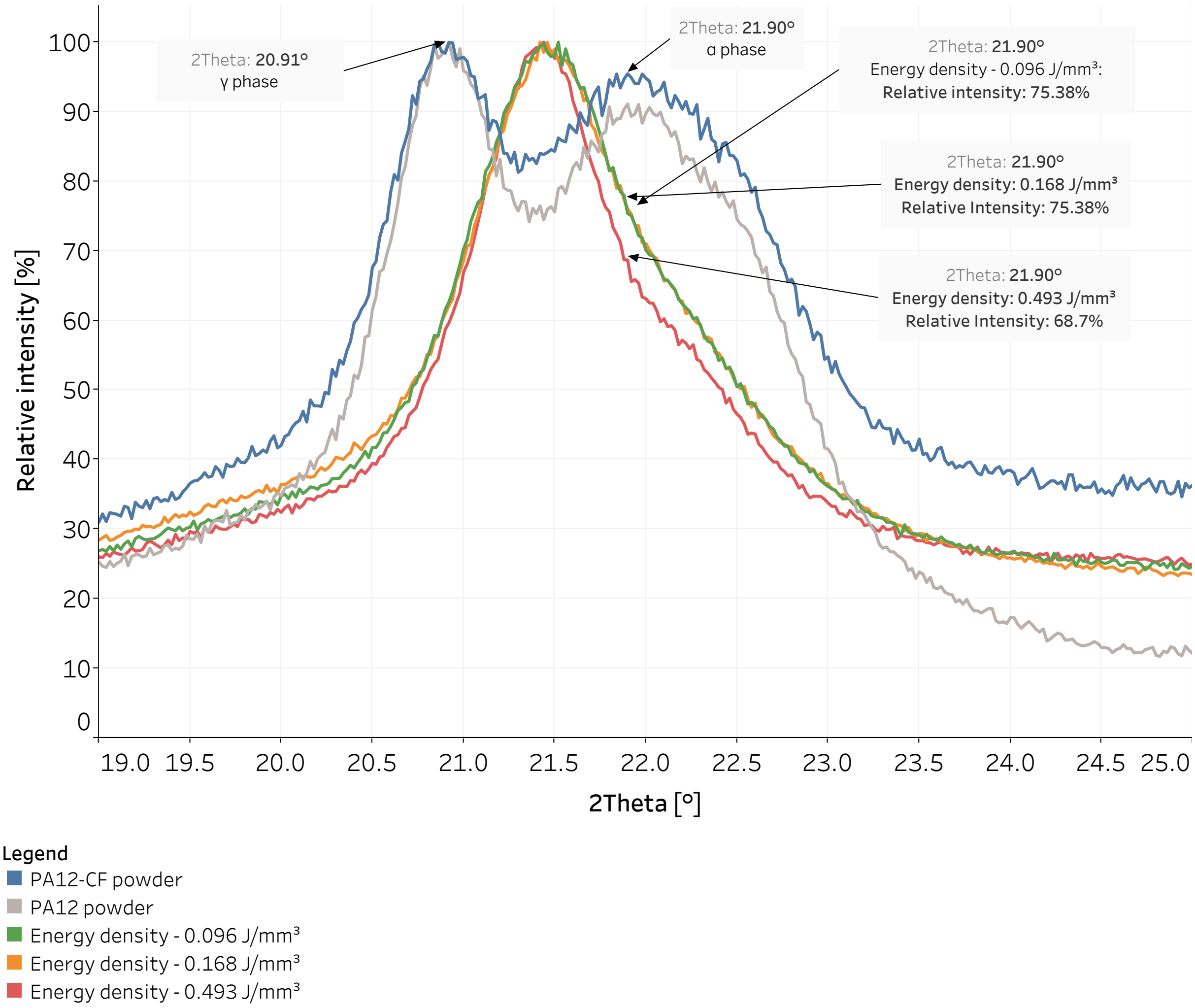

Figure 5.12 – XRD patterns of PA12-CF and PA12 powder and LS PA12-CF samples processed at different energy densities.

Laser sintered samples processed at 0.096 J/mm^3 show a change on crystal structure, with γ form as main phase present and α form still present as indicated by a higher intensity at the 2θ location of α. As discussed in subsection 4.1.7, α form transforms to γ form when heated to melting point (ATKINS; HILL; VELURAJA, 1995) and is associated to reduction of unmolten particles during LS and improved consolidation of the material during SLS process.

Increasing the energy density to 0.168 J/mm^3 does not show any significant change on crystalline structure compared to 0.096 J/mm^3. Reason for this can be associated to the surface position XRD was captured, which could not detect differences between the surfaces processed at different energy levels. Only at the highest energy level of 0.493 J/mm^3 there is a significant decrease in the relative intensity related to the α crystal form. As observed in SEM micrographs and from nominal strain measurements performed there was no improvement on nominal strain at break at this energy level, on the contrary, a trend to slight reduce strain was observed. This may be associated to polymer degradation.

In order to investigate the degradation behavior Fig. 5.13 shows the FTIR spectra of PA12-CF LS samples processed at different energy densities. Infrared band assignments are shown in Table 5.1 (RHEE; WHITE, 2002). The band assignments for carbon fiber are superposed with band assignments of PA12 so no significant differences can be observed specifically regarding carbon fiber spectra.

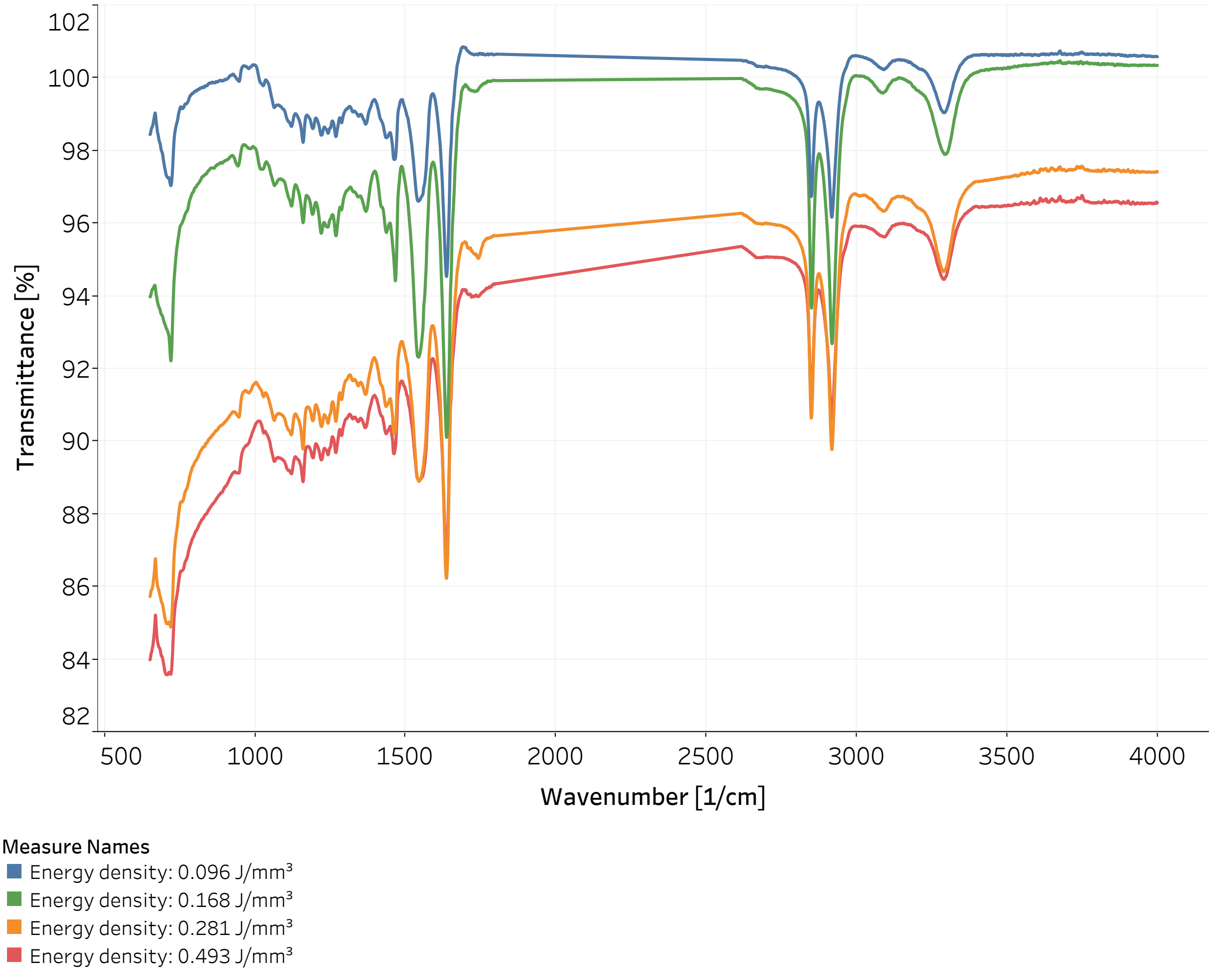

Figure 5.13 – FTIR spectra of LS PA12-CF samples processed at different energy densities.

There is an overall absorption increase at the assigned wavenumbers towards increasing energy densities, which can be associated with higher chain mobility caused by chain scission (ZHANG; ADAMS, 2016).

Additionally some modifications were observed for samples produced with 0.281 and 0.493 J/mm^3 in the region of 1700-1750 cm^{-}1, which is related to carbonyl groups formed during polyamide oxidation (CELINA et al., 1997). Such changes in absorption at this region might suggest some level of oxidation of the samples processed at higher energy densities. Such changes in absorption at this region suggest some level of oxidation of the samples processed at higher energy densities, which could lead to lower mechanical properties as observed. Another possible explanation for the effect observed is based on the decomposition of oxygen groups on the surface of carbon fiber released in the form of CO and CO_2 during laser sintering. Upon laser exposure, oxygen groups released in the form of gas could promote the formation of pores, creating stress concentration areas in the materials and reducing mechanical properties. This behavior has been observed in previous studies (JING et al., 2017) and the present work shows that it is intensified with increasing energy density. The porosity increase is corroborated by density measurements performed, showing a density reduction for samples processed at higher energy levels.

Table 5.1 – FTIR spectra assignment of PA12-CF.

Wavenumber ($\mathrm{cm}^{-}1$)	Assignment
3294	N — H stretching
3086	Fermi-resonance of N — H stretching
2918	CH2 asymmetric stretching
2850	CH2 symmetric stretching
1750	C ═ O stretching
1636	Amide I (C ═ O stretching)
1543	Amide II (C — N stretching)
1466	CH2 bend
1436	C ═ O bend
1419	C ═ O bend
1368	CH bend, CH2 twisting
1288	CH2 wagging or CH2 twisting
1269	Amide III (C — N stretching + C ═ O inplane bending)
1242	Gauche carboxyl-methylene group
1219	Gauche nitrogen-methylene group
1190	Splitting of amide II
1159	Skeletal motion involving CONH
1122	C — C stretching
1065	Skeletal motion involving CONH
1028	CONH inplane
980	C — CO stretching
946	CONH inplane
720	CH2 rocking
680	Amide V (α) (C ═ O out of plane bending)

5.2 Gaussian process response surface modelling - PA12-CF

This section presents the results after model training of the dataset using supervised learning Gaussian process ($\mathcal{GP}$) described in section 3.5.

5.2.1 Model quality

As described in section 4.2.1, two criteria were adopted to evaluate model quality:root mean square error (RMSE) and the coefficient of determination (R^2).

Same approach as used for PA12 model is used for PA12-CF, models with $0.6<R^2<0.9$ are considered good for qualitative predictions; models with $R^2>0.9$ are considered good for quantitative predictions. Models with R^2 below 0.6 are considered reliable. Only models with $R^2>0.6$ are considered for further analysis of response functions as qualitative analysis can be performed and interesting information can be derived even from models with intermediate quality.

Table 5.2 presents a summary of RMSE and R^2 for each response function. X-direction accuracy shows very low values of R^2 and are not reliable. Reason for the low model quality may be a small sensitivity of the output variable to the input variables trained, as it was observed from the measurements done for X-direction accuracy over energy density depicted in Fig. 5.1. Y- direction accuracy has better model quality ($R^2=0.74$) and qualitative assessment can be made. Z- direction accuracy model training resulted in a very good R^2 of 0.93 and can be used for quantitative assessment.

Density model quality is intermediate, with an R^2 of 0.85, which can be used for qualitative predictions. Surface roughness model quality is very poor ($R^2=0.3$) and cannot be considered reliable. Main reason for low model quality is the high variance of measurements performed (very noisy results) due to the nature of laser sintered samples and also the measurement method applied, which used profile measurement. Also there is little or no influence of the parameters evaluated on surface roughness as observed from Fig. 5.4.

Mechanical properties reached very good model quality. Tensile strength at yield and at break reached low RMSE and high R^2 of 0.96. Elastic modulus also achieved very good correlation and is good for quantitative assessment. Proportional limit and 0.2% offset yield strength achieved intermediate results with $R^2=0.81$, nevertheless the model quality is good for qualitative assessment. Regarding strain, $\mathcal{GP}$ model training for nominal strain at yield and break resulted in good model quality, with low RMSE and high R^2 of 0.92. Model quality was poor for nominal strain at proportional limit and 0.2% offset yield strength, being not reliable for evaluation.

Overall $\mathcal{GP}$ model training resulted in good model quality. Considering this is

Table 5.2 – Response functions model quality: RMSE and R^2.

Response variable	RMSE	R^2
X-Direction accuracy [%]	0.000875	0.4789
Y-Direction accuracy [%]	0.0128	0.7375
Z-Direction accuracy [%]	0.0172	0.9343
Density [g/cm^3]	0.01776	0.8472
Surface roughness R_a [μm]	1.3807	0.2960
Elastic modulus [MPa]	86.7118	0.9645
Tensile strength at yield [MPa]	1.5953	0.9615
Tensile strength at break [MPa]	1.5303	0.9644
Proportional limit [MPa]	1.7198	0.8094
0.2% offset yield strength [MPa]	2.0922	0.8084
Nominal strain at yield [%]	0.2053	0.9222
Nominal strain at break [%]	0.2212	0.9237
Nominal strain at proportional limit [%]	0.054	0.4616
Nominal strain at 0.2% offset yield strength [%]	0.064	0.4306

the first time supervised learning with $\mathcal{GP}$ is applied to polymer composite materials manufactured by SLS, the results are important to provide a deeper mapping on the influence of the main laser sintering variables over important output parameters. The model results are discussed in next sections.

5.2.2 Response surfaces

Response surfaces obtained after $\mathcal{GP}$ model training for PA12-CF. A given response variable is a function of the three input variables: laser power, laser scan speed, scan line spacing. Layer thickness was fixed at 150 μm. This results in a hyperplane in a 4 dimensional space that cannot be graphically presented with all variables. To be able to graphically represent the response surfaces of the output variables, three-dimensional intersection plots of this hyperplane are given, with two input variables in x and y axis and one output variable in the z axis. The remaining input variable is fixed at the given hyperplane. For each output variable evaluated two three-dimensional graphs are presented: response surface as a function of laser power and laser scan speed at constant scan line spacing; response surface as a function of scan line spacing and laser scan speed at constant laser power and laser scan speed.

5.2.2.1 Dimensional accuracy

Figure 5.14a shows the Y-direction accuracy response surface over laser power and laser scan speed at a scan line spacing of 0.4 mm.

Y-direction accuracy varies significantly with laser speed, with positive gradient in direction of higher laser speeds. Laser power influences with lower relevance Y-direction accuracy. Maximum values are reached at 3000 mm/s and 35 W laser power. Above 3000 mm/s a plateau is formed with high values of Y-direction accuracy (above 0.99). Lowest values for Y-direction accuracy were found at a combination of intermediate laser power and low laser speed.

Response surface for Y-direction accuracy over laser speed and scan line spacing at 35 W laser power are depicted in Fig. 5.14b. Values as low as 0.92 are found at low scan speed and scan line spacing, steeply increasing in direction of higher laser speed and scan line spacing. Both variables have a strong influence on Y-direction accuracy. There is a large plateau area at high Y-direction accuracy area where stable Y-direction accuracy values (above 0.99) are observed. At this plateau scan line spacing and laser speed have very small influence.

Sensitivity of Y-accuracy over the evaluated parameters are shown in Fig. 5.15. Laser speed presents the highest influence over Y-direction accuracy, followed by scan line

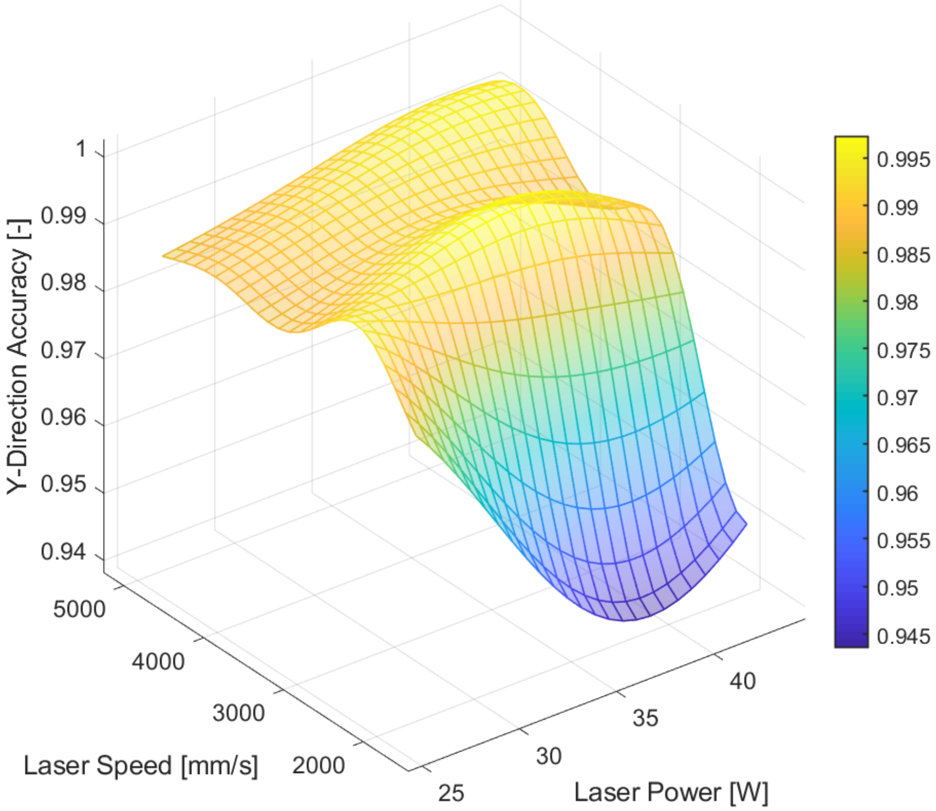

(a) Y-direction accuracy over laser power and laser scan speed.

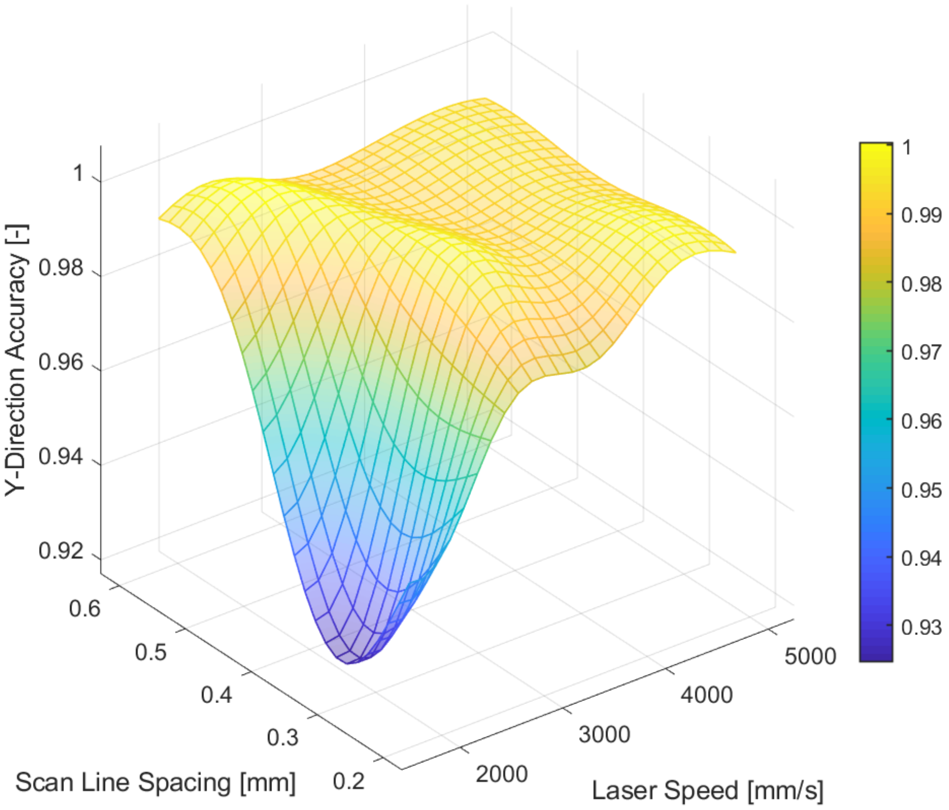

(b) Y-direction accuracy over scan line spacing and layer thickness.

Figure 5.14 – Response surfaces for Y-direction accuracy.

spacing and at last laser power with lowest relevance.

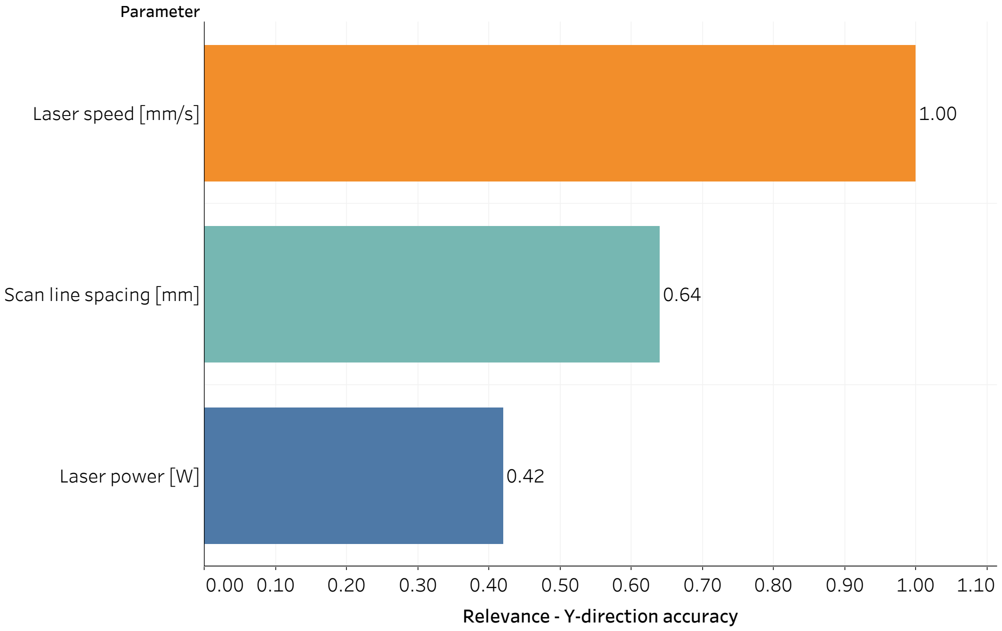

Figure 5.15 – Sensitivity of Y-direction accuracy on LS process parameters.

Figure 5.16a shows the response surface of Z-direction accuracy over laser power and laser speed at 0.4 *mm* scan line spacing. Map topology follows a linear behavior with both laser power and laser speed, with lowest values found at low laser speed and high laser power. Z-direction accuracy improves in direction towards high laser speed and low laser power, reaching a maximum of 0.95 at 25 *W* laser power and 5000 *mm*/*s* laser speed.

Z-direction accuracy map over laser speed and scan line spacing is depicted in Fig. 5.16b. The behavior is not linear as observed in Fig. 5.16a but a clear tendency of low accuracy at low laser speed and low scan line spacing can be observed, improving in direction towards higher scan line spacing and higher laser speed.

Relevance of individual laser sintering parameters over Z-direction accuracy is shown in 5.17. As expected from the response surfaces, scan line spacing and laser speed play the major relevance, whereas Z-direction accuracy is less sensible to laser power.

Both accuracy values in Y and Z direction shows a similar behavior of improved values at lower energy density range. For instance lower laser speed increases the exposure time the powder bed is subjected to the laser, increasing the laser beam heat affected area in both Y and Z directions, decreasing accuracy as surrounding particles may be consolidated together with the target particles scanned by the laser. Scan line spacing acts in a similar way but increasing the number of exposures and the overlap degree between laser lines, also contributing to a higher heat affected area and worsening dimensional

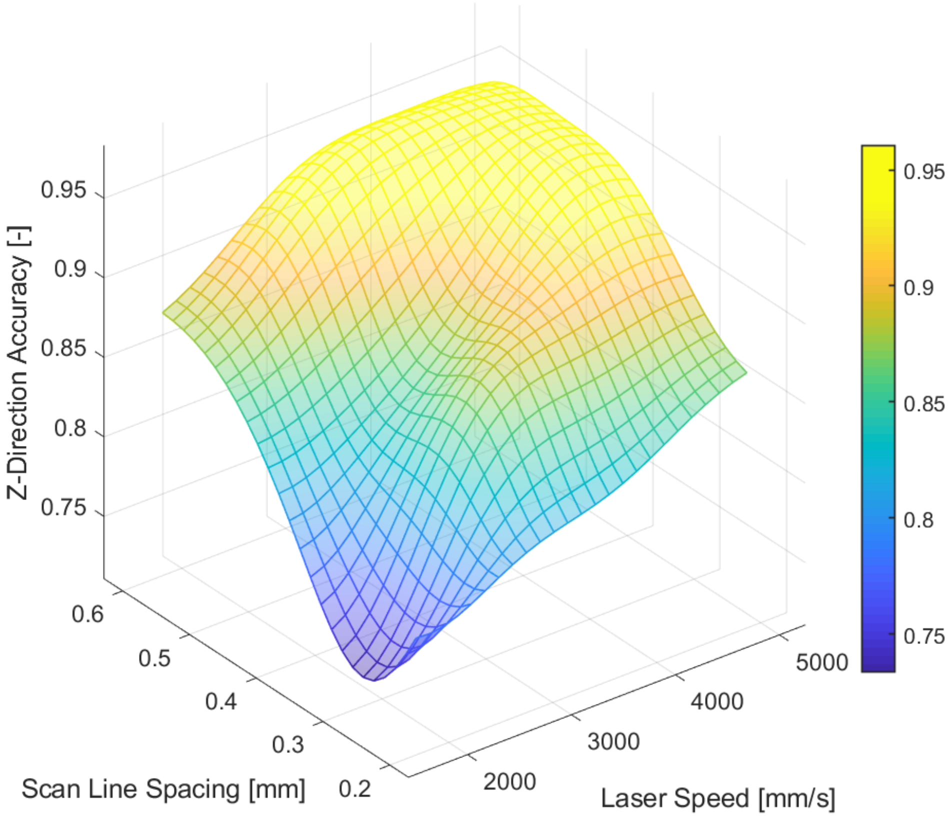

(a) Z-direction accuracy over laser power and laser scan speed.

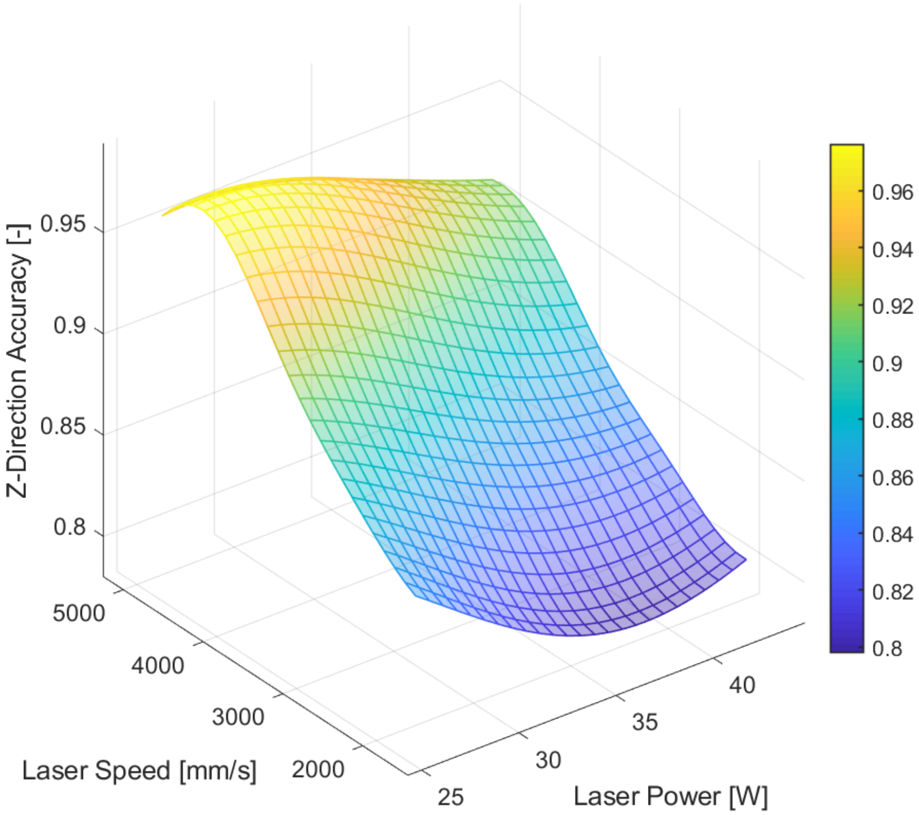

(b) Z-direction accuracy over laser speed and scan line spacing.

Figure 5.16 – Response surfaces for Z-direction accuracy.

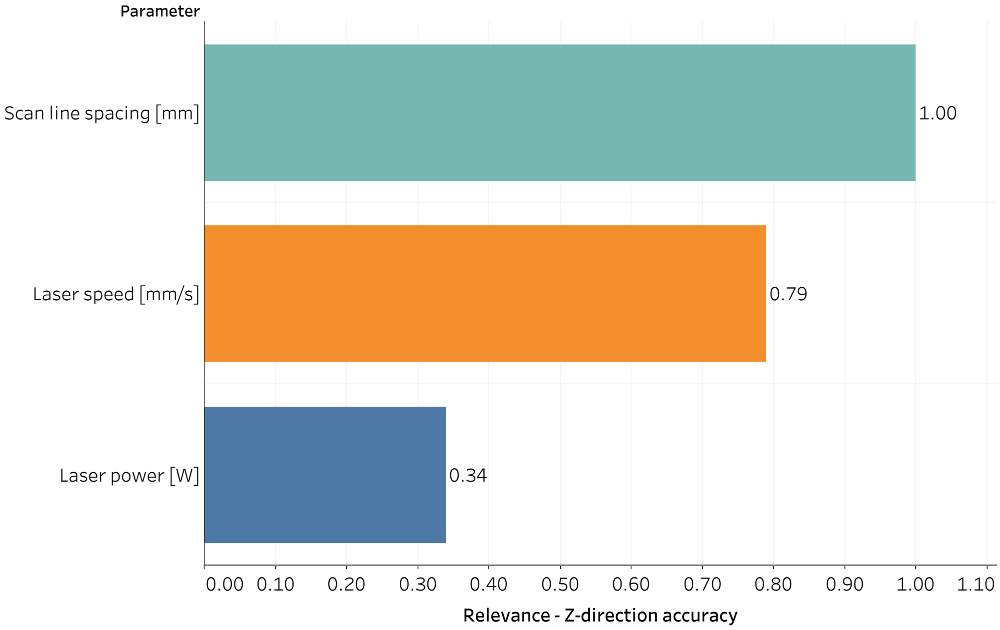

Figure 5.17 – Sensitivity of Z-direction accuracy on LS process parameters.

accuracy. Higher laser power affects the molten pool width and depth during laser sintering, also impacting heat affected area and accuracy.

5.2.2.2 Density

Density response surface over laser power and laser speed at 0.4 mm scan line spacing are depicted in Fig. 5.18a. Surface topology shows very low density values of 0.92 g/cm^3 at highest laser speed and lowest laser power, increasing in direction of lower laser scan speed and higher laser power. The gradient in laser speed direction is higher than laser power indicating higher relevance of laser speed. The surface shows local maximum of 1.04 g/cm^3 at near 3000 mm/s and 25 W laser power. At constant laser power, there is a decrease on density for lower values than 3000 mm/s. There is another high density of area 1.02 g/cm^3 at highest laser speed of 5000 mm/s and highest laser power. Keeping the gradient in direction of higher laser power and lower laser speed decrease density

Density over laser speed and scan line spacing at 35 W laser power are shown in Fig. 5.18b. The maps shows lowest density values of 0.82 g/cm^3 located at high laser speed and scan line spacing, steeply increasing in direction of lower scan line spacing and laser speed. A maximum large area with density values over 1.03 g/cm^3 is observed at different combinations of low laser speed and high scan line spacing and high laser speed and low scan line spacing. After this maximum area is reached and further decreasing laser speed and scan line spacing leads to a reduction in density values.

Relevance analysis ranks scan line spacing as most influencing parameter on density as depicted in 5.19 followed closely by laser speed. Density is less sensible to laser power but cannot be neglected by the model.

As observed in subsection 5.1.3, density shows high variation with the laser energy delivered to the powder bed, and a non-linear response to energy density was observed. Energy density influences directly on the liquid phase sintering dynamics occurring during SLS and therefore impacting densification behavior of the material. The Gaussian process model trained could capture the behavior observed over the individual laser sintering parameters. For instance higher laser speed decreases the laser material interaction time, reducing the time liquid molten PA12 has to surround CF particles, decreasing the rearrangement phase kinetic force and leading to lower density. At the same time this can be compensated with lower scan line spacing and higher overlap degree so that the number of total exposures the same area has is increased, improving sintering dynamics. Another approach could be to increase laser power to keep same energy level delivered to the powder bed, but such approach may not be the most effective due to the lower sensibility density has over laser power. The model also shows the complexity of the individual parameters to achieve optimal response. The simple decrease of laser speed and scan line spacing or increase in laser power leads to a reduction in density as more energy delivered to the powder bed may lead to volume increase due to consolidation of neighbouring particles not scanned by the laser beam.

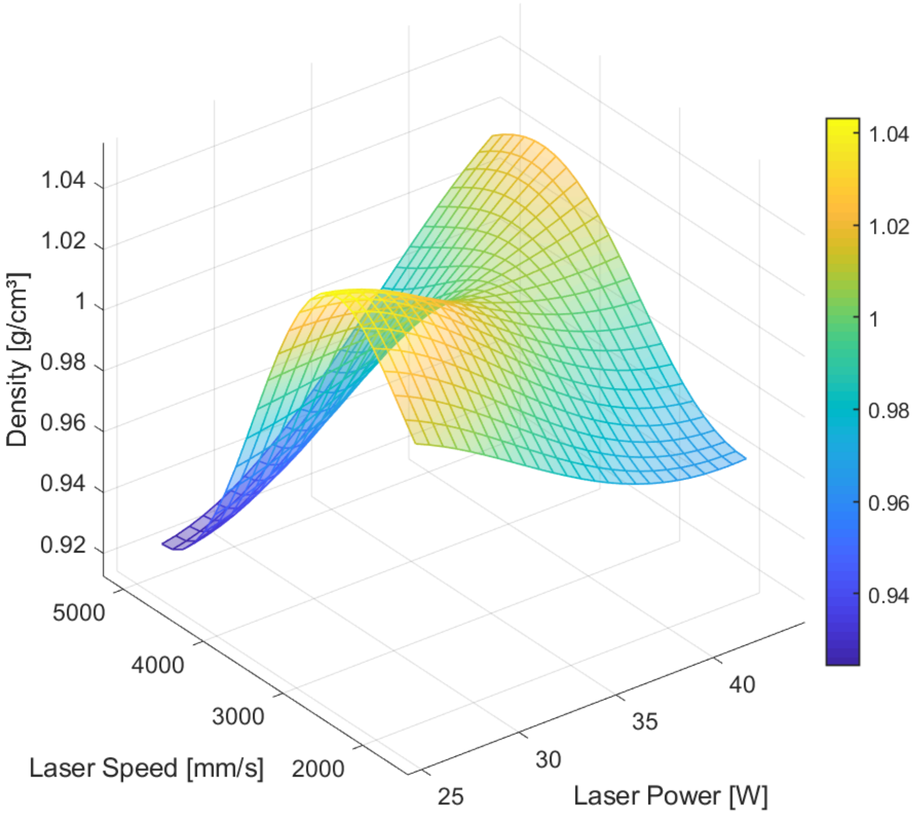

(a) Density over laser power and laser scan speed

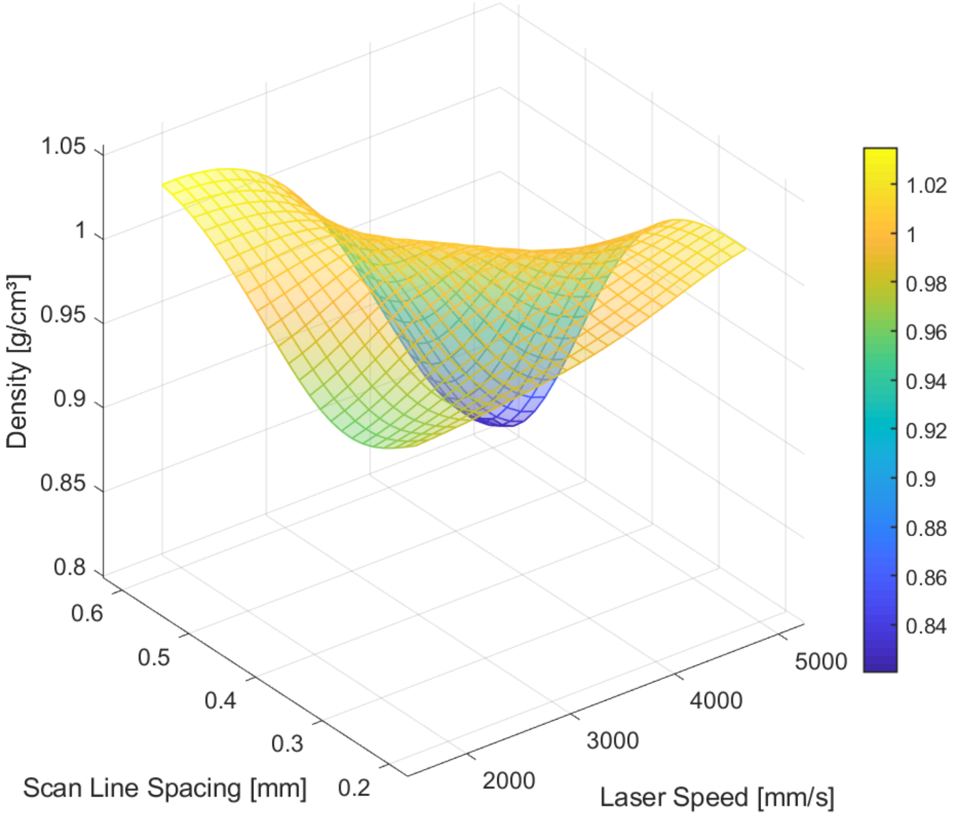

(b) Density over laser speed and scan line spacing

Figure 5.18 – Response surfaces for density.

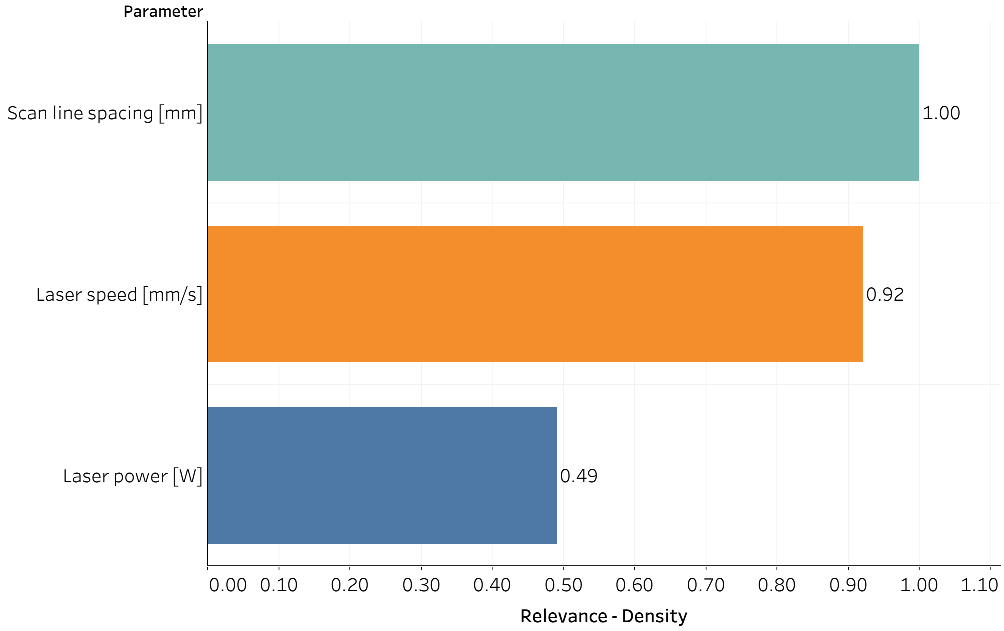

Figure 5.19 – Sensitivity of density on LS process parameters.

5.2.2.3 Proportional limit

Proportional limit over laser power and laser speed at 0.4 mm scan line spacing are depicted in Fig. 5.20a. The map is highly non-linear and shows two clear gradients in direction of higher proportional limit: first gradient in direction towards higher laser power when laser speed is fixed at higher area. Very low values (24 MPa) of proportional limit are found at high laser speed and 25 W, increasing in direction towards high laser power. The second gradient starts with low values at high laser power and low laser speed, increasing in direction lower laser power while keeping the laser speed constant. This region concentrates the highest values for proportional limit, reaching near 34 MPa. The combination of low laser power and low laser speed results in a proportional limit decrease.

Figure 5.20b shows proportional limit response surface over laser speed and scan line spacing at constant laser power of 42 W. The map also shows a highly non-linear behavior over both input variables. Lowest values of less than 20 MPa are found for a combination of high laser speed and scan line spacing. There is first a steep increase in direction of lower scan line spacing and laser speed, reaching more stable values at both combination of low scan line spacing and high laser speed and high scan line spacing and low laser speed. Maximum values of near 34 MPa are found at 3000 mm/s and 0.6 mm scan line spacing. Going further in direction of lower scan line spacing and low laser speed decreases proportional limit to values near 25 MPa.

Relevance of laser sintering parameters on proportional limit are depicted in Fig. 5.21. Laser speed plays the major relevance followed by scan line spacing. Proportional

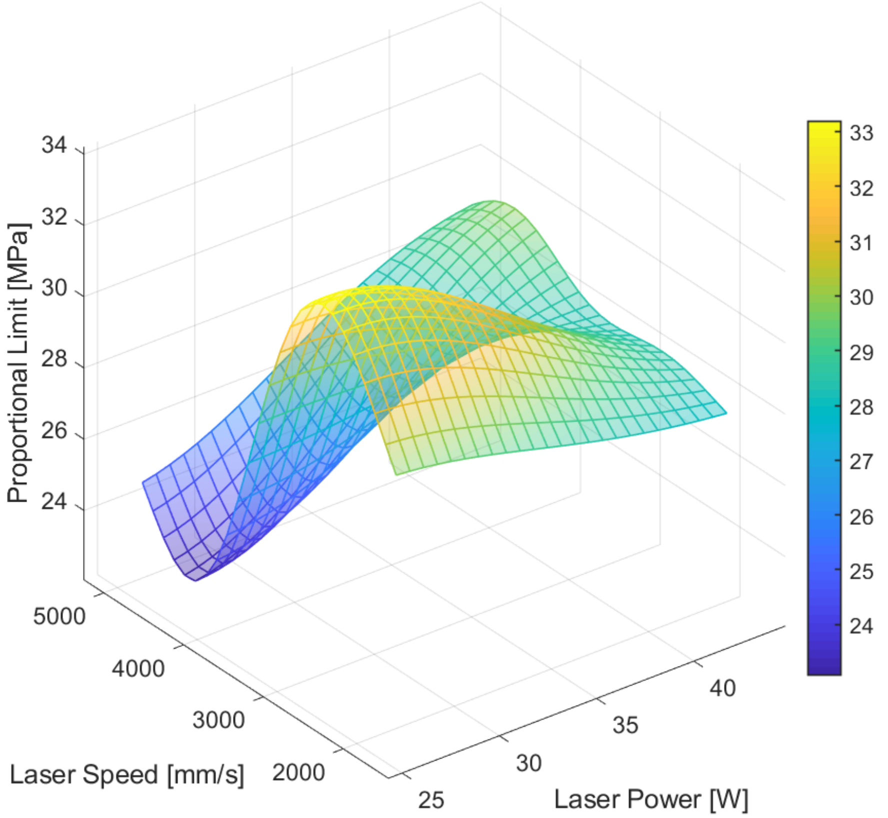

(a) Proportional limit over laser power and laser scan speed

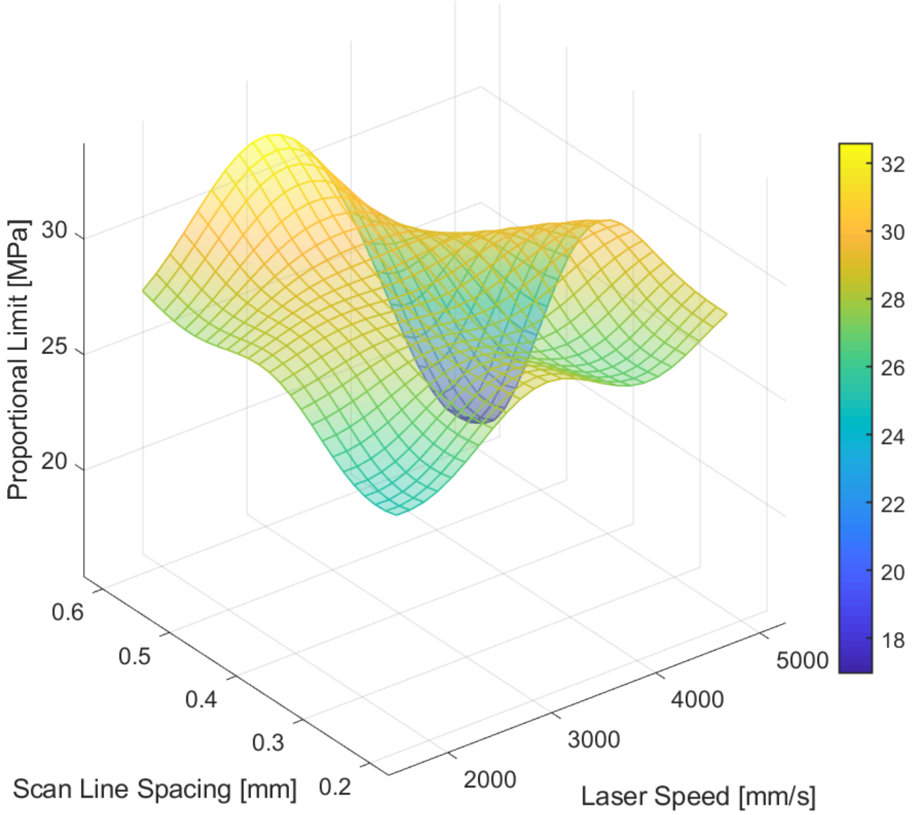

(b) Proportional limit over laser speed and scan line spacing

Figure 5.20 – Response surfaces for proportional limit.

limit is less sensitive to laser power, although the model shows a significant relevance.

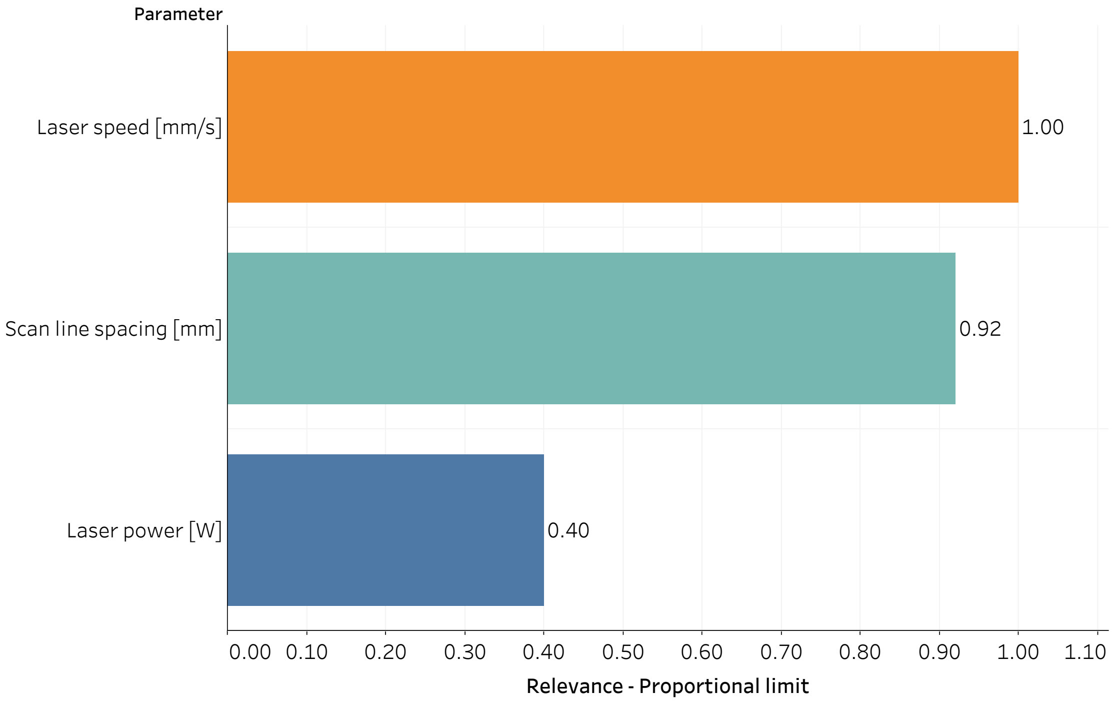

Figure 5.21 – Sensitivity of proportional limit on LS process parameters.

5.2.2.4 Elastic modulus

Response surface of elastic modulus over laser speed and laser power at 0.4 mm scan line spacing are shown in Fig. 5.22a. Elastic modulus follow a similar map topology as proportional limit, with lowest modulus values of near 3000 MPa concentrated at 4000 mm/s and 25 W laser power and increasing in direction of both lower laser scan speed and high laser power. Two distinct maximum areas of elastic modulus near 3600 MPa can be observed, one located at intermediate speed of 3000 mm/s and lowest laser power and the other maximum region located at maximum laser power of 43 W and 4200 mm/s laser speed. Further increase in laser power combined with lower laser speed results in lower elastic modulus (3300 MPa). Similar behavior is found at the lowest laser speed evaluated, regardless of the laser power.

Elastic modulus response surface over laser speed and scan line spacing at 35 W laser power is depicted in Fig. 5.22b. Lowest elastic modulus of 2400 MPa is found at high scan line spacing and high laser speed values, steeply increasing with a gradient in direction towards lower scan line spacing and laser speed, but only until a certain extent where elastic modulus values are more stable. Maximum values near 3600 MPa can be found at different sites in the map: scan speed close to 3500 mm/s and scan line spacing near 0.3 mm; scan speed close to 3000 mm/s and scan line spacing of 0.6 mm; scan speed

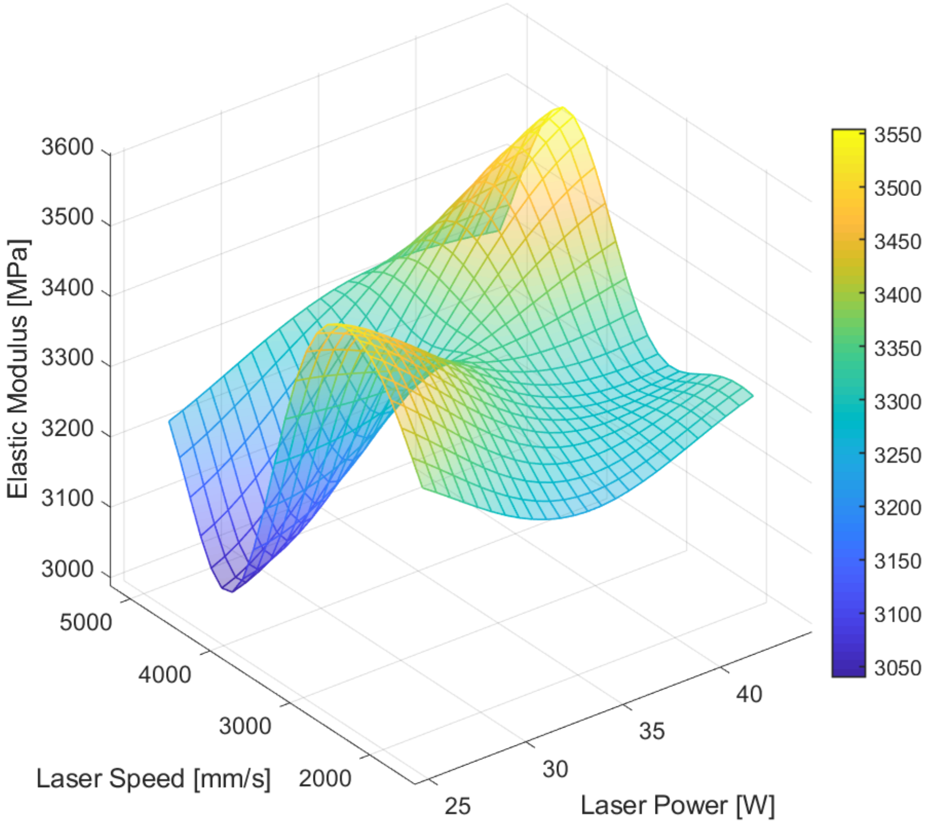

(a) Proportional limit over laser power and laser scan speed

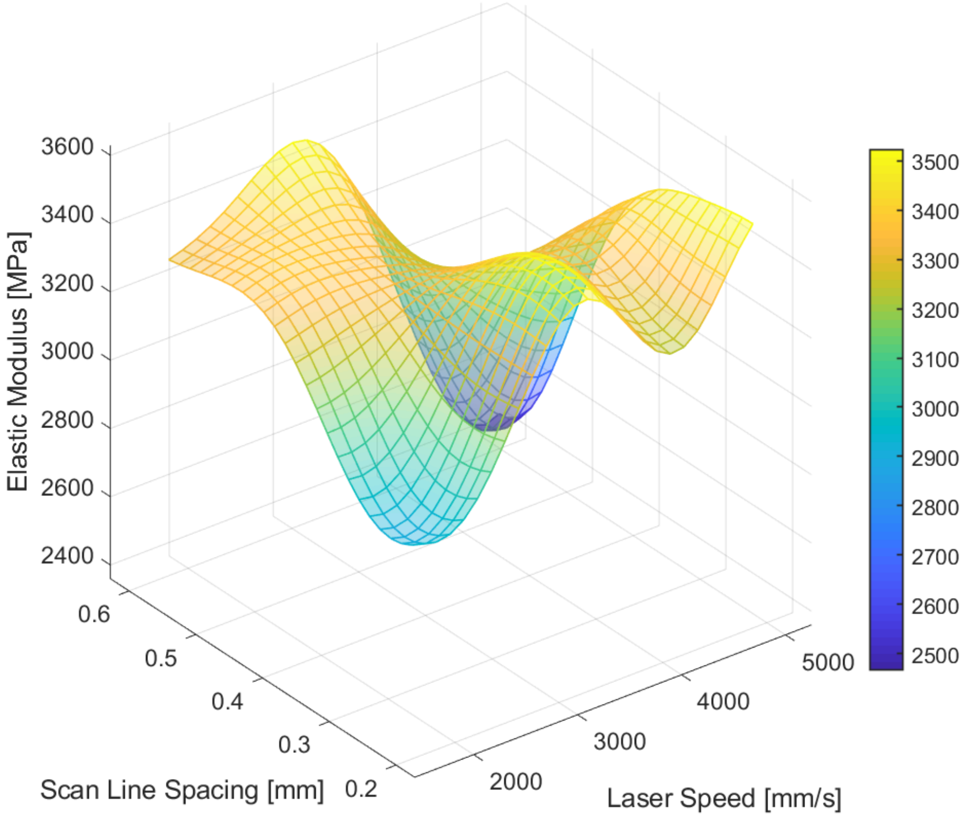

(b) Elastic modulus over laser speed and scan line spacing

Figure 5.22 – Response surfaces for elastic modulus.

of 5000 mm/s and scan line spacing of 0.2 mm. Combination of very low laser power and scan line spacing results in low elastic modulus.

Relevance of laser sintering parameters on proportional limit are depicted in Fig. 5.23. Similar to proportional limit response sensitivity, laser speed plays the major relevance followed by scan line spacing. Laser power has the lowest relevance among studied parameters.

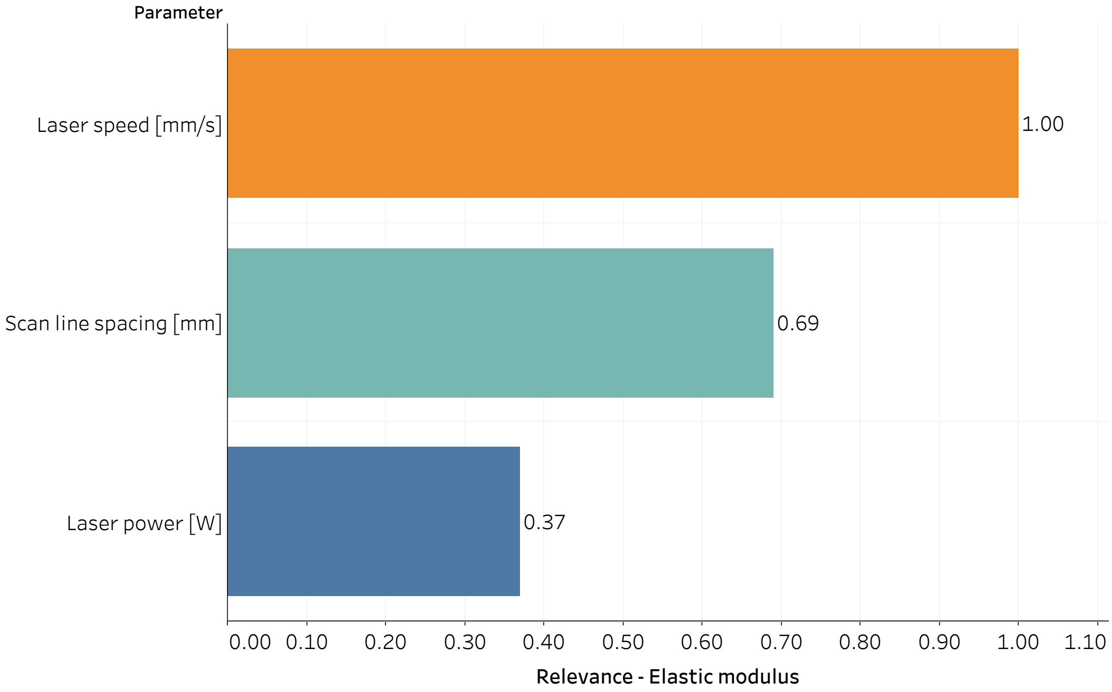

Figure 5.23 – Sensitivity of elastic modulus on LS process parameters.

The results from Gaussian process learning of the measured data shows a highly non-linear dependence on the individual laser sintering variables. This is reflected in the maps shape found, where different regions of maximum outputs were observed screening the variables range. The model did capture well the trade-off between low laser speed and high scan line spacing for instance as well as the compromise between low scan line spacing and high laser speed necessary to achieved maximum elastic properties. The specific laser sintering parameters necessary to achieve this goal can cover a wide area of the design space considered. Such trade-off exemplifies the results at optimal liquid phase sintering conditions to achieve a combination of low porosity and adequate adhesion between carbon fiber filler and PA12 matrix. For instance, the individual use of high laser speed may promote poor sintering conditions as there is no time for effective liquid formation and presence for prolonged time. But its combination with low scan line spacing results in short exposure time but with higher number of exposures due to the higher overlapping between laser lines, providing more time for rearrangement phase during liquid phase sintering to occur.

Additionally the $\mathcal{GP}$ model described well the decrease of elastic properties towards higher energy density parameters usage, exemplified here as combination of very low laser speed ans scan line spacing, or high laser power and low laser speed. At this parameter set region, polymer degradation may occur resulting in lower elastic properties.

5.2.2.5 Tensile yield strength

Figure 5.24a shows the response surface after $\mathcal{GP}$ training for yield strength over laser power and laser speed at 0.4 mm. Surface topology is similar to elastic properties modelled, presenting lowest yield strength of 45 MPa at 4000 mm/s laser speed and 25 W laser power. At constant laser power, there is a steep increase in yield strength towards lower laser speed values, reaching a maximum of 65 MPa near 3000 mm/s, decreasing at lower laser speeds. Keeping laser speed constant at nearly 4000 mm/s, increasing laser power improves yield strength significantly reaching 65 MPa at maximum laser power of 43 W. At the lower speed area (below 2500 mm/s) a plateau is formed with slightly lower yield strength values at 62 MPa.

Yield strength over laser speed and scan line spacing at 35 Wlaser power are depicted in Fig. 5.24b. Lowest yield strength values (30 MPa) are found at high laser speed and high scan line spacing, steeply increasing in direction to lower laser speed and scan line spacing. A stable plateau with yield strength near 65 MPa is reached in two areas: scan line spacing between 0.4-0.6 mm and laser speed below 3000 mm/s; scan line spacing between 0.2-0.3 mm and laser speed above 4000 mm/s. Further decrease in both laser speed and scan line spacing reduces yield strength values to 60 MPa.

Relevance of individual laser sintering parameters on yield strength is depicted in Fig 5.25. Similar to elastic properties, laser speed has the major relative relevance overall, followed by scan line spacing and to a less extent laser power.

Gaussian process model described with good accuracy the measured data for yield strength. The response surfaces for laser power and laser speed shows the correlation between different parameters. For instance, there is a shift of optimal laser speed depending on laser power applied. High laser power results in a shift towards higher laser speed to get highest local values of yield strength. In a similar way, highest mechanical properties are found for lower laser speed when low laser power is applied. The results also show the compensation is not linear, i.e. compensating one parameter do not necessarily leads to optimum mechanical properties. This is shown when in the same surface response when using even lower laser speed at the minimum laser power applied. As the effect of laser speed is more pronounced than laser power, reducing laser speed may lead to a reduction in mechanical properties due to reasons addressed in subsection 5.1.5.

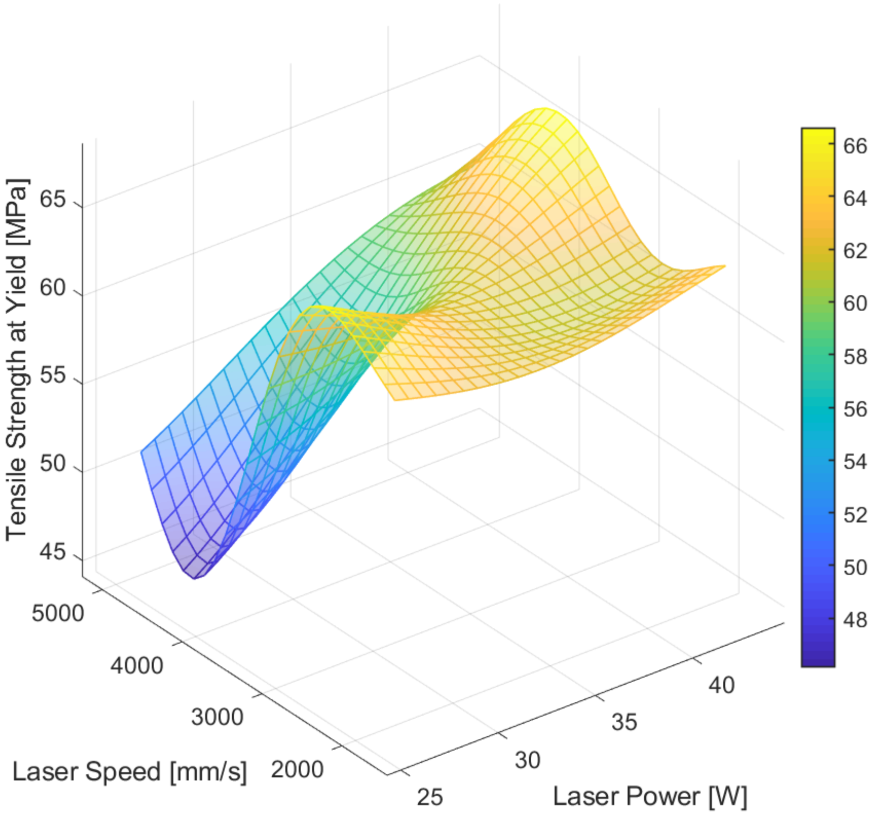

(a) Yield strength over laser power and laser scan speed

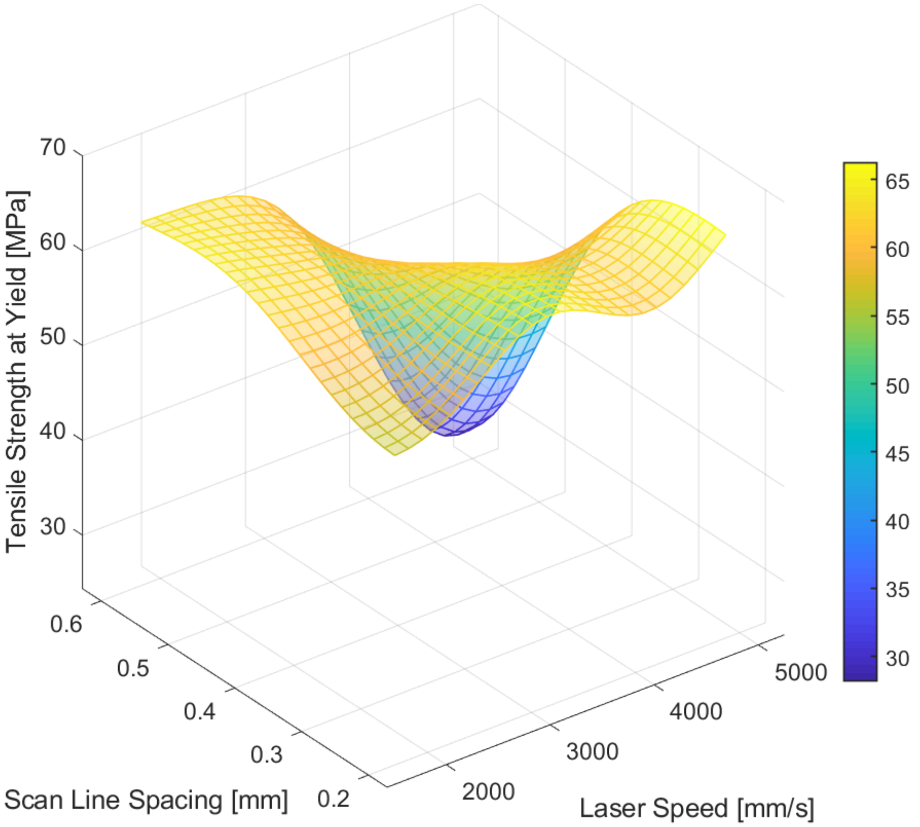

(b) Yield strength over laser speed and scan line spacing

Figure 5.24 – Response surfaces for yield strength.

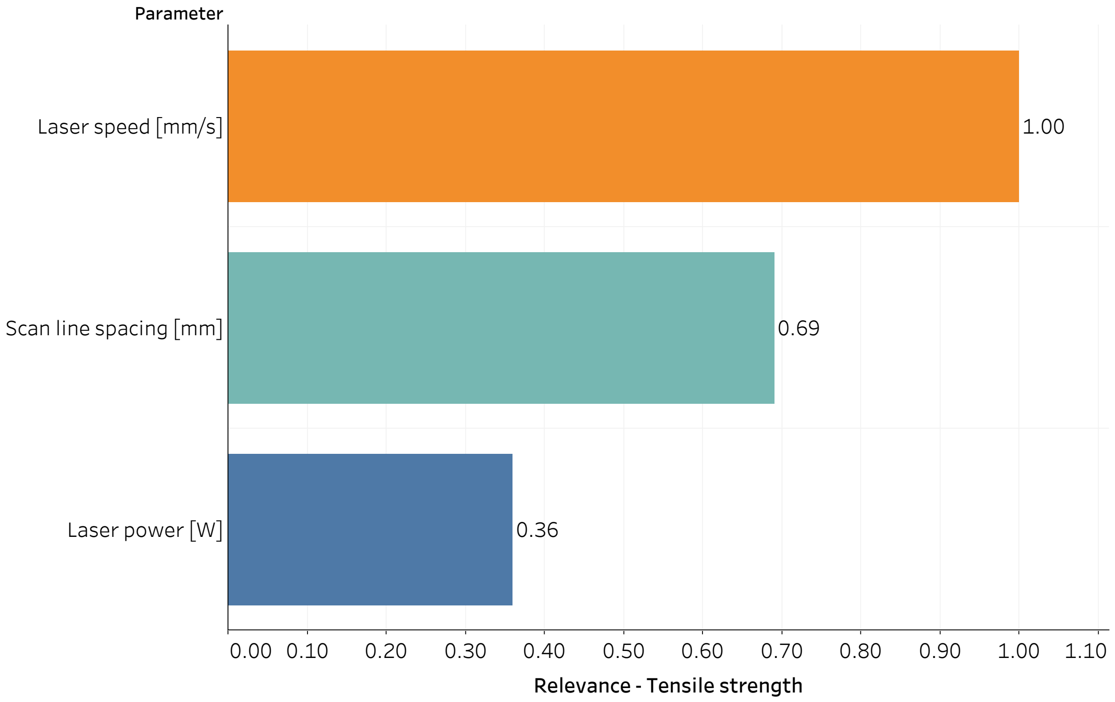

Figure 5.25 – Sensitivity of yield strength on LS process parameters.

5.2.2.6 Nominal strain at break

Nominal strain at break modelled surface over laser power and laser speed at 0.4 *mm* scan line spacing is depicted in Fig. 5.26a. The model predicts very low strain at break (3.5 %) at low laser power and high laser speed. A gradual transition to increased strain at break values in direction towards lower laser speed and higher laser power is observed. Maximum values of nominal strain near 5.7 % are observed in two regions in the map: laser speed around 4500 mm/s and laser power at 43 W; laser speed at 2000 mm/s and laser power at 25 W. Apart from these two regions there is a plateau in the high laser power low laser speed area with slightly lower nominal strain at break values (near 5.3 %).

Figure 5.26b shows the response surface of nominal strain at break over laser speed and scan line spacing at 35 W laser power. Surface topology is similar to that found for yield strength, exhibiting lower values of nominal strain at high laser speed and scan line spacing and steeply increasing in direction to lower laser speed and scan line spacing. A plateau is reached in the areas of low laser speed and high scan line spacing and high laser speed and low scan line spacing. Continuous decrease of laser speed below 3000 mm/s and scan line spacing below 0.35 mm slightly reduces nominal strain to values near 5 %.

Sensitivity of nominal strain at break over each laser sintering parameter evaluated is shown in Fig. 5.27. Contrary to strength properties, scan line has the highest relevance amount the parameters, followed by laser speed and laser power in a lower degree.

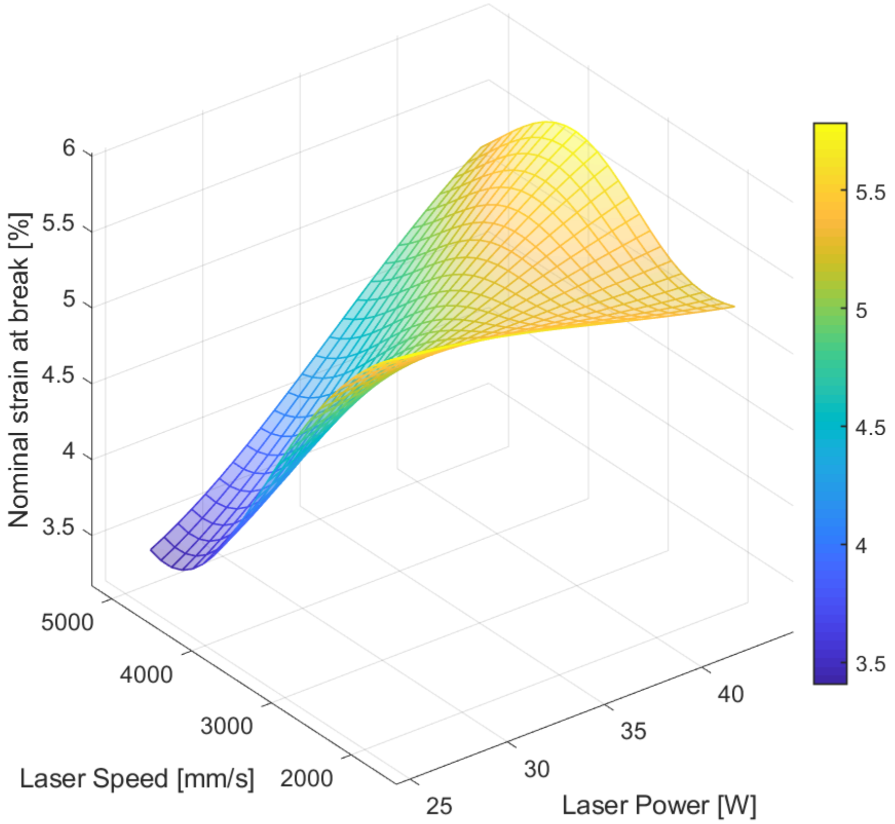

(a) Nominal strain at break over laser power and laser scan speed

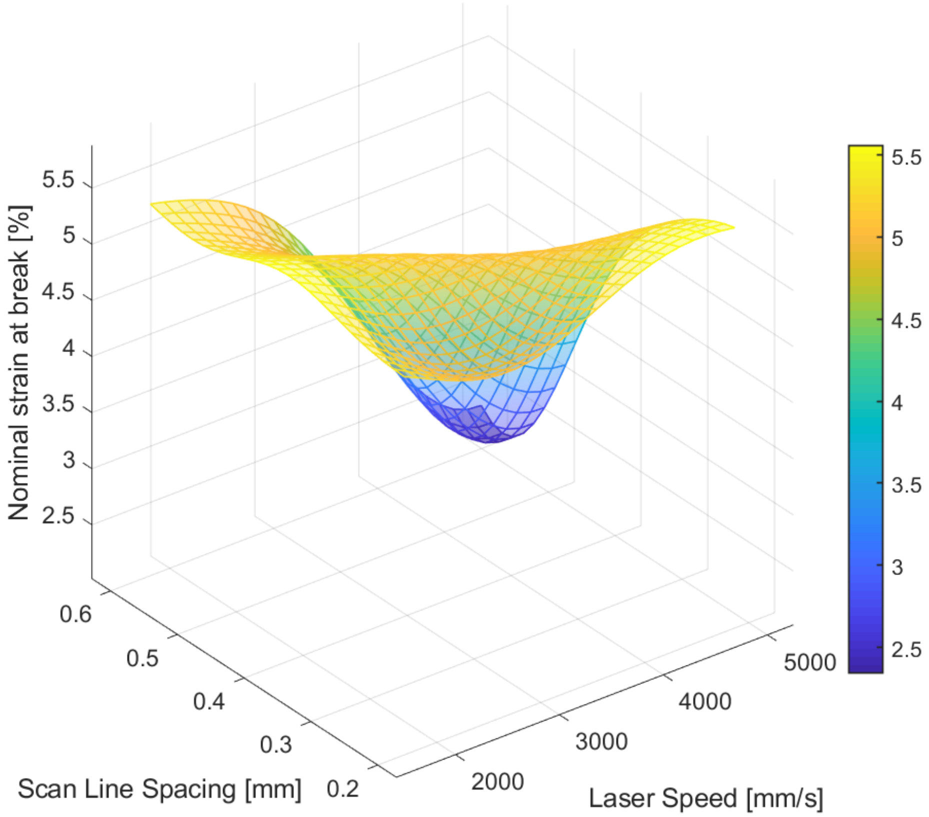

(b) Nominal strain at break over laser speed and scan line spacing

Figure 5.26 – Response surfaces for nominal strain at break.

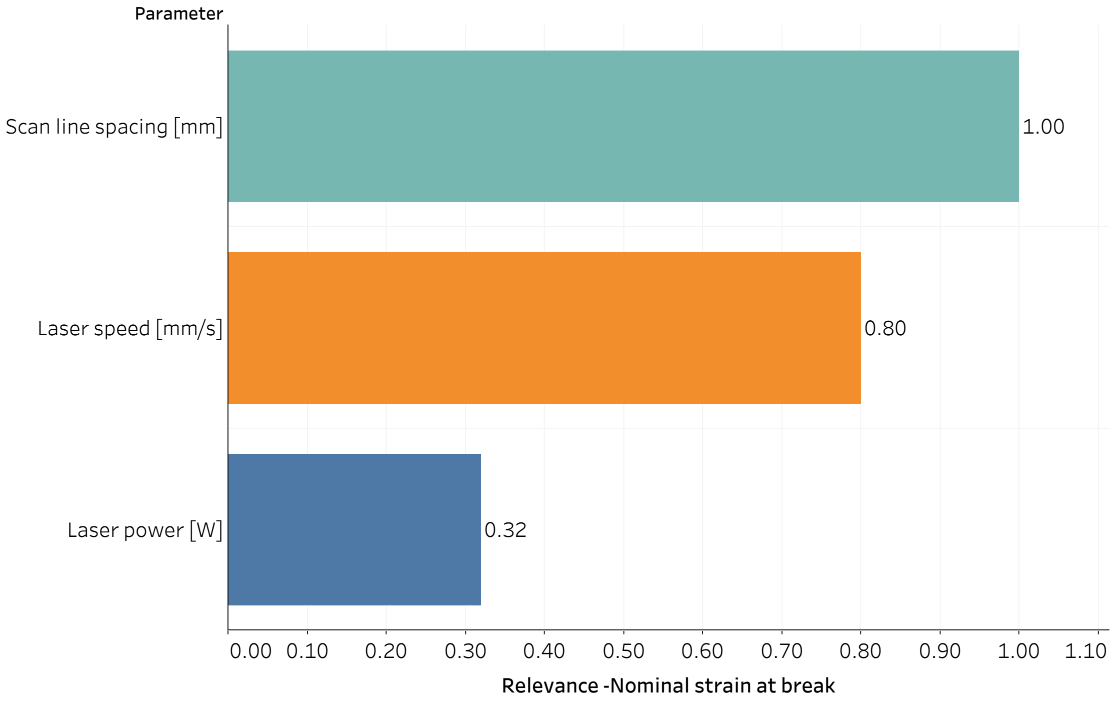

Figure 5.27 – Sensitivity of nominal strain at break on LS process parameters.

The proposed Gaussian process model for strain at break reveals individual parameters and their interactions play an important role on plastic behavior. At very low laser power and high laser speed there is no sufficient laser material interaction present during SLS to promote adequate sintering conditions as there is not enough liquid phase present in the molten pool, leading to poor capillary forces to induce proper rearrangement of the carbon fiber particles within polymer matrix. Similar behavior can be expected at high laser speed and scan line spacing parameter setting. Increase in laser power and decrease in laser speed improves molten pool liquid content due to the slower laser passage and higher laser energy, enhancing capillary forces induced by Marangoni flow generated by the temperature gradient present. Additionally the presence of higher liquid content reduces friction forces, contributing to better flow of molten PA12 around carbon fiber particles. All these aspects results in better rearrangement phase during liquid phase sintering, promoting better densification of the parts ad improved nominal strain, as the plastic strain on PA12-CF results from deformation of amorphous chains located in PA12 matrix. Similar analysis can be derived for scan line spacing, but here the major influence is on the number of total laser exposures the same powder bed surface will receive.

The model also shows there is a limit above which plastic deformation starts to decrease. This limit is associated with laser parameters interaction, which could be observed using a combination of high laser power and low laser speed and low laser speed and scan line spacing. At this parameter set configuration some polymer degradation could be present and may be responsible for the reduction in plastic strain at break.

5.2.2.7 Normalized manufacturing time

Figure 5.28a shows normalized manufacturing response surface over laser power and laser speed at 0.4 *mm* scan line spacing. Normalized manufacturing time varies almost linearly with laser speed, with lowest values at high laser speed and increasing in direction of lower laser speed. This is in agreement with the LS process behavior, as the laser speed influences the time required to scan the powder bed, with higher laser speed requiring less time than lower laser speed to scan over the same powder bed surface. The reduction in time is not of great scale however, maximum reduction in 3 % is observed at highest laser speed applied. Laser power does not influence significantly normalized manufacturing time.

Normalized manufacturing time over laser speed and scan line spacing at 35 *W* laser power are depicted in Fig.5.28b. The model shows a smooth surface with lowest manufacturing time of 0.965 at highest laser speed and scan line spacing, increasing in direction towards low laser speed and scan line spacing. Maximum values of 1.04 are found at lowest laser speed and scan line spacing evaluated.

As shown in Fig. 5.29, scan line spacing has the highest influence on normalized manufacturing time, closely followed by laser speed. As expected, normalized manufacturing

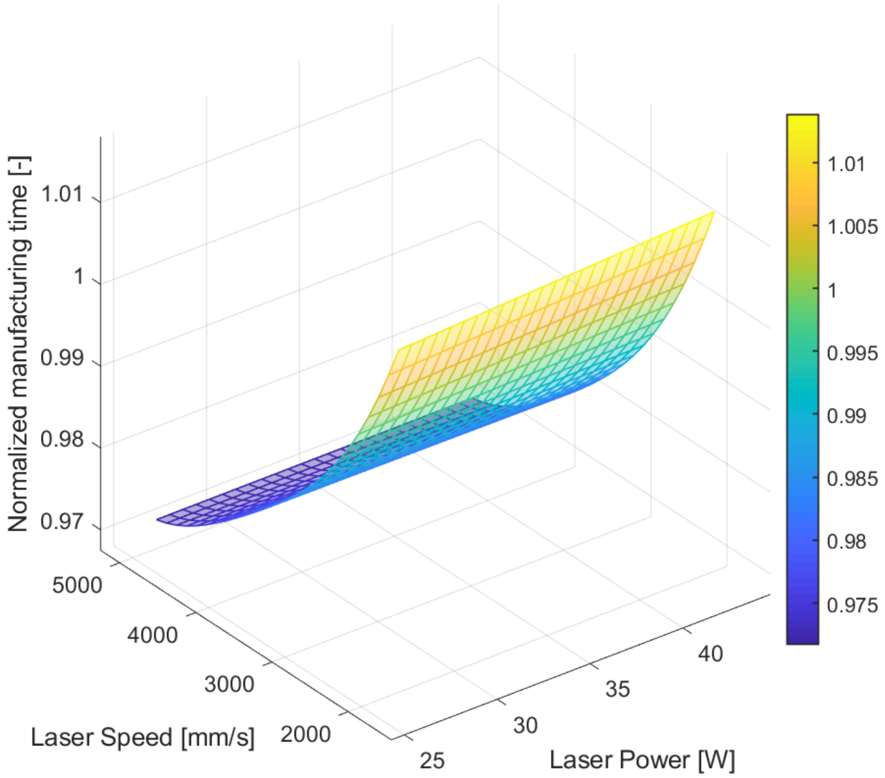

(a) Normalized manufacturing time over laser power and laser scan speed

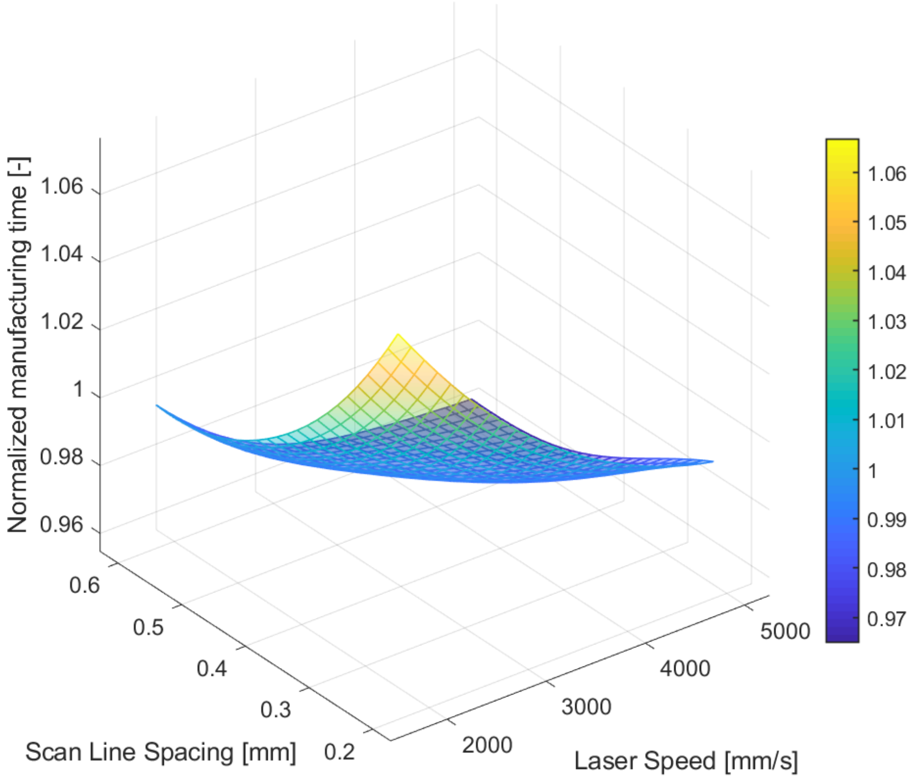

(b) Normalized manufacturing time over laser speed and scan line spacing

Figure 5.28 – Response surfaces for normalized manufacturing time.

time is not influenced by laser power.

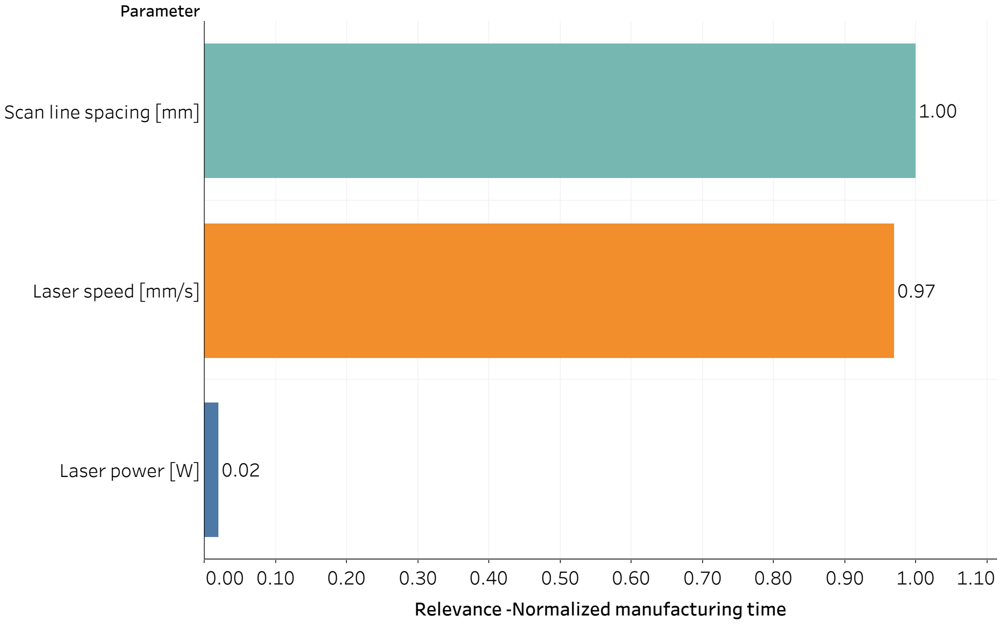

Figure 5.29 – Sensitivity of normalized manufacturing time on LS process parameters.

5.3 Optimization via evolutionary algorithm

This section describes the multi-objective optimization tasks performed via Evolutionary Algorithm (EA) after supervised learning via Gaussian Process was conducted. The multi-objective optimization results in solutions sets representing a trade-off between objectives, which are known as Pareto solutions.

The multi-objective optimization considered optimization of mechanical properties, surface quality, dimensional accuracy and manufacturing time. Although surface roughness model quality was poor, it was subjected to optimization. Two objectives were optimized at once, while the others were kept at a limit (lower or higher hard limit) to reduce the number of Pareto solutions.

5.3.1 Criteria 1 - Optimization of manufacturing time and dimensional accuracy

Criteria 1 seeks the optimization of manufacturing time and dimensional accuracy while keeping mechanical properties and surface roughness within adequate values. In order to perform this task, mechanical properties were set as hard upper limits, meaning that optimization solutions which results in mechanical properties lower than the thresholds set as hard upper limits will de discarded. Yield strength was set as hard upper bound t 59 MPa, elastic modulus at 3276 MPa and nominal strain at break at 4.87 %. Surface roughness was set as a weak lower bound, which is a softer form of hard bound, meaning that values above the limit set are not optimized further. Surface roughness was set at 14.77 μm.

Figure 5.30 depicts the Pareto solutions for Z-direction accuracy and normalized manufacturing time after optimization task with criteria 1. Maximum accuracy achieved is 0.94 while minimum normalized manufacturing time is 0.97. Two Pareto sets were chosen from all solutions at Pareto frontier: Pareto set 1 shows lowest values for normalized manufacturing time (0.97) and good Z-direction accuracy around 0.937; Pareto set 2 has slightly better values for Z-direction accuracy (near 0.94) at a cost of higher normalized manufacturing time (0.976-0.977). It is clear that the first Pareto set chosen provides a better solution set for the optimization task, nevertheless Solution set 2 was chosen for comparison as well.

Laser sintering parameters at Pareto frontier can be observed in Fig. 5.31. Pareto set 1 laser sintering parameters are clustered at higher laser power are between 42-43 W, high laser speed area between 4300-4500 mm/s and scan line spacing between 0.43-0.44 mm. Pareto solution set 2 gives a completely different scenario of lower laser power at 33 W, lower laser speed near 2800 mm/s and very high scan line spacing at 0.57 mm. The solutions sets chosen show how distant parameter combination can be to achieve similar

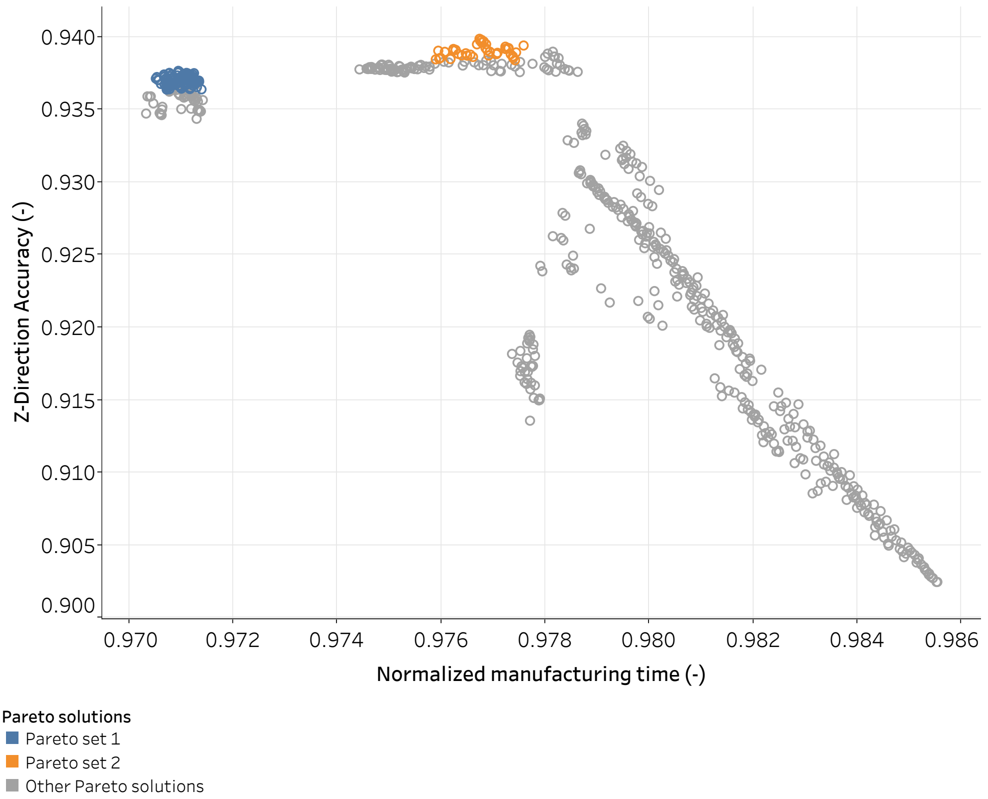

Figure 5.30 – Pareto solutions after optimization task with criteria 1.

targets. Pareto set one gives better results in terms of normalized manufacturing time as the laser speed applied is much higher than Pareto set 2.

Output parameters for Pareto solutions optimization task with criteria 1 are depicted in Fig. 5.32. Values for elastic modulus yield strength and nominal strain at break for Pareto set 1 and 2 were all near the hard upper limit defined for the optimization task. Slightly better mechanical properties are found for Pareto set 1. This is due to the conflicting objectives defined between accuracy, manufacturing time and mechanical properties. The parameters which give best accuracy and manufacturing time come at a cost of lower mechanical properties. Nevertheless as the optimization was hard bounded with limit thresholds for mechanical properties, the parameter set solution should give adequate mechanical properties for PA12-CF.

Y-direction accuracy, surface roughness R_a and density are depicted in Fig. 5.33. Surface roughness values are slightly lower at Pareto set 1 compared to Pareto set 2. Density values are very similar to both Pareto sets and the values are within adequate range (1.00 g/cm^3) for the material (material manufacturer reports standard values of 1.04 g/cm^3). Y-direction accuracy gives very good values between 0.995-0.996 for Pareto set 1 and 0.991-0.993 for Pareto set 2.

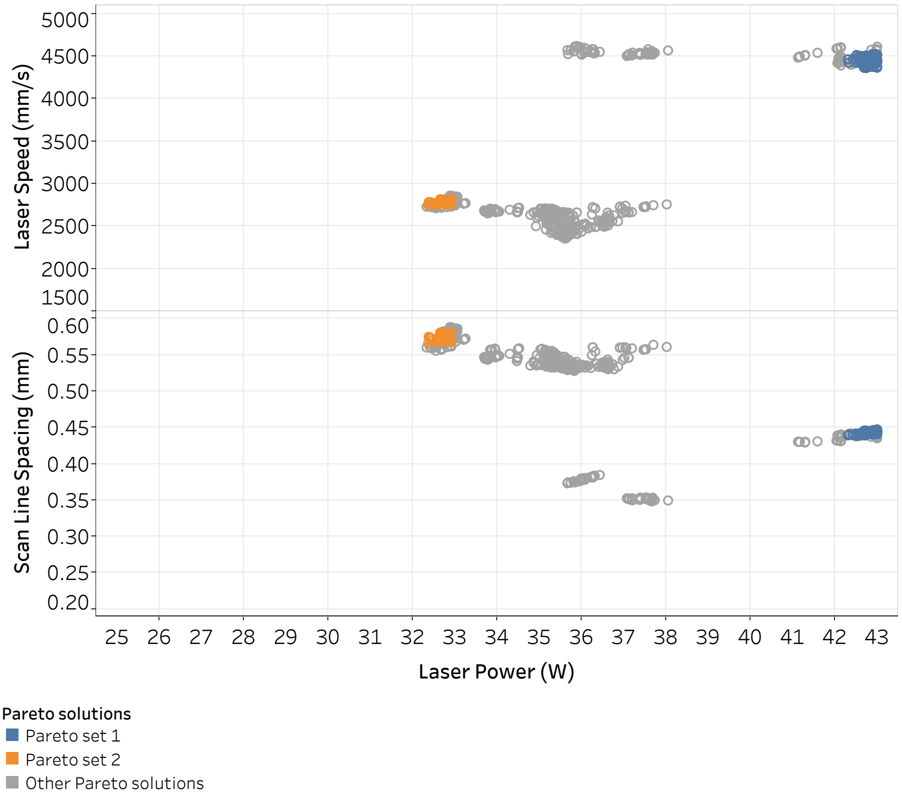

Figure 5.31 – Pareto solutions for criteria 1:laser sintering parameters.

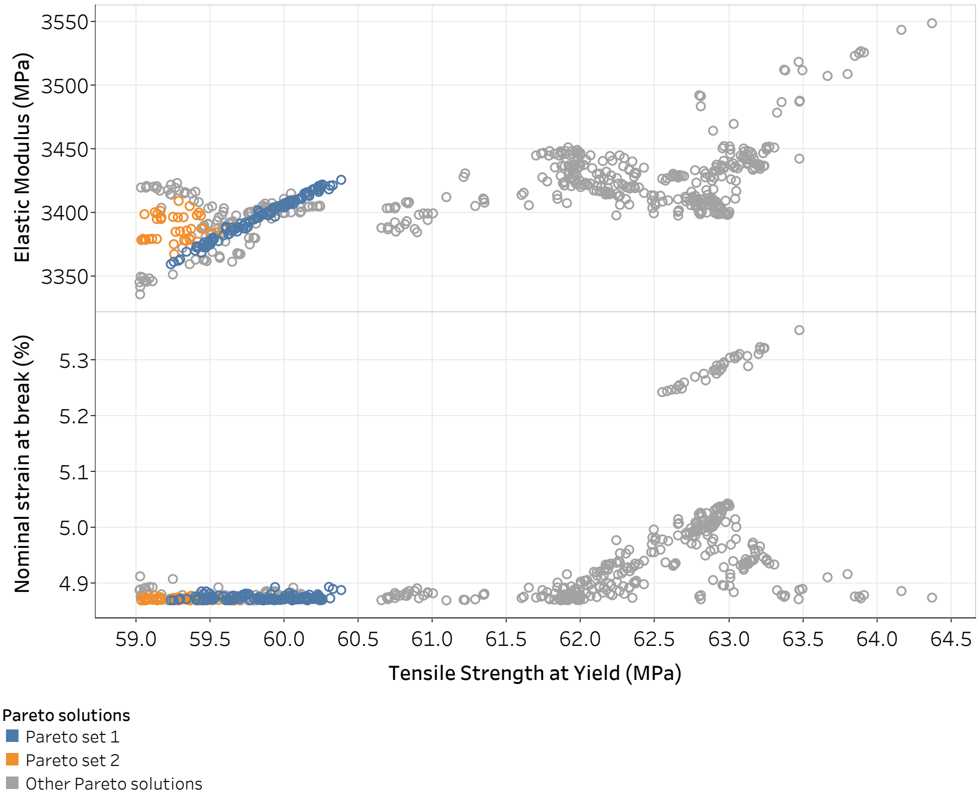

Figure 5.32 – Pareto solutions for criteria 1: elastic modulus, tensile strength at yield and nominal strength.

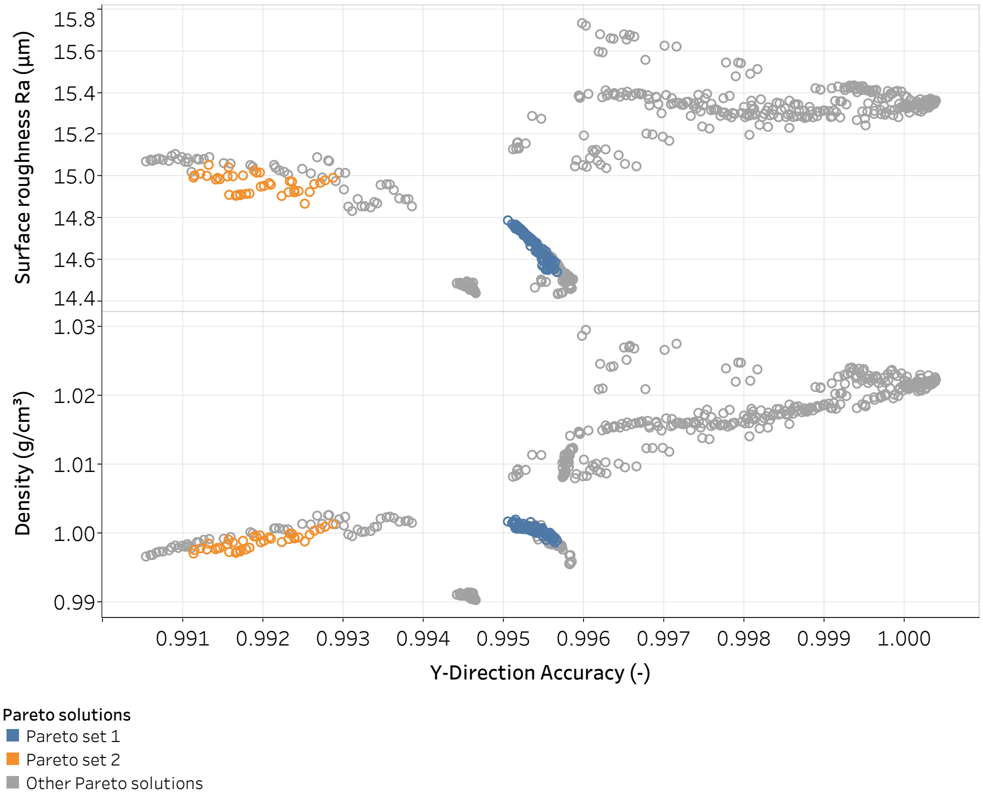

Figure 5.33 – Pareto solutions for criteria 1: surface roughness R_a, density and Y-direction accuracy.

5.3.2 Criteria 2 - Optimization of surface roughness R_a and dimensional accuracy

Optimization task with criteria 2 has the objective of minimizing surface roughness and maximizing dimensional accuracy. Yield strength was set as hard upper bound at 59 MPa, elastic modulus at 3276 MPa and nominal strain at break at 4.87 %. Normalized manufacturing time was set as a hard upper bound at 0.99, therefore no solutions with normalized manufacturing time higher than 0.99 were considered.

Figure 5.34 shows the optimization results for Pareto frontier for surface roughness R_a over Z-direction accuracy. The Pareto frontier is overall not well defined, mainly due to the poor model quality achieved by Gaussian process model training for surface roughness. Nevertheless, in order to illustrate the trade-off between solutions, three Pareto sets were defined: Pareto set 1 focused on best Z-direction accuracy values obtained at an average surface roughness below between 14.4-14.7 μm; Pareto set 2 used softer requirements for accuracy (between 0.907 and 0.91) while reducing surface roughness to values below 13.8 μm; Pareto set 3 also seeks minimum surface roughness values (between 13-13.2 μm) at a cost of lower dimensional accuracy (between 0.885-0.9).

Figure 5.35 shows laser sintering parameters at Pareto frontier. Pareto set 1 laser sintergin parameters are divided in two clusters: first cluster with high laser speed values

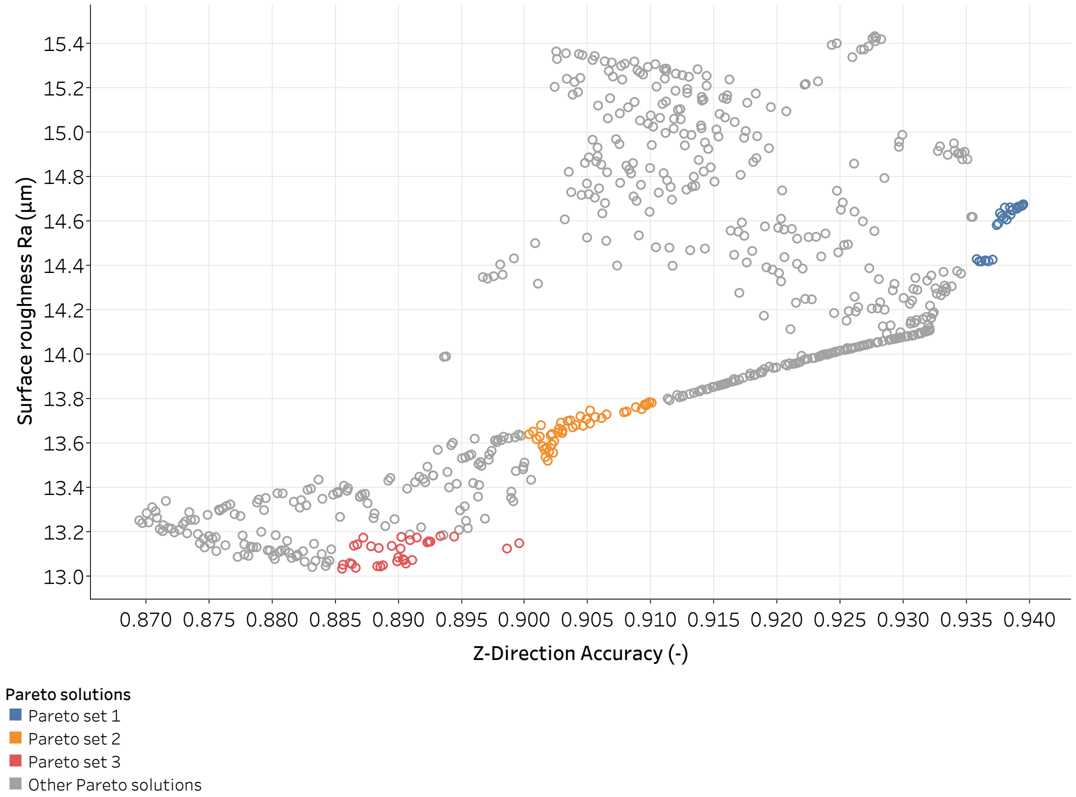

Figure 5.34 – Pareto solutions after optimization task with criteria 2.

of 4500 mm/s, laser power of 37 W and 0.39 mm scan line spacing; second cluster reduces laser speed to 2700 mm/s, combined to a reduction in laser power between 31-32 W and increase in scan line spacing to 0.55 mm. The clusters in Pareto set 1 have very close optimized objective values and give an idea on the wide parameter range that can be combined to achieved similar outputs.

Pareto set 2 gives two SLS parameters clusters: one with even lower laser speed values (near 2500 mm/s), low laser power between 26-27 W and high scan line spacing at 0.5 mm;the other cluster has higher laser power between 32-33 W, laser speed near 3400 mm/s and lower scan line spacing at 0.34 mm. Pareto set 3 achieved a wider range of laser power (between 29.5-33 W), a narrow laser speed range at 2200 mm/s and scan line spacing from 0.35-0.37 mm.

Mechanical properties at Pareto frontier for criteria 2 are depicted in Fig. 5.36. Elastic modulus for Pareto set 1 is clustered in between 3300-3400 MPa, yield strength between 59-60 MPa and nominal strain at break near 4.9 %. Pareto set 2 results in better mechanical properties, with elastic modulus at 3350 MPa, yield strength of 62 MPa and nominal strain at break between 5.2-5.3 %. The other cluster in Pareto set 2 gives even better elastic modulus (3500 MPa) and yield strength (63.5-64 MPa) but a lower nominal strain at break (4.9 %). Pareto set 3 achieved high elastic modulus (3470-3550 MPa) and yield strength (63.5-65 MPa) and nominal strain at break around 5 %.

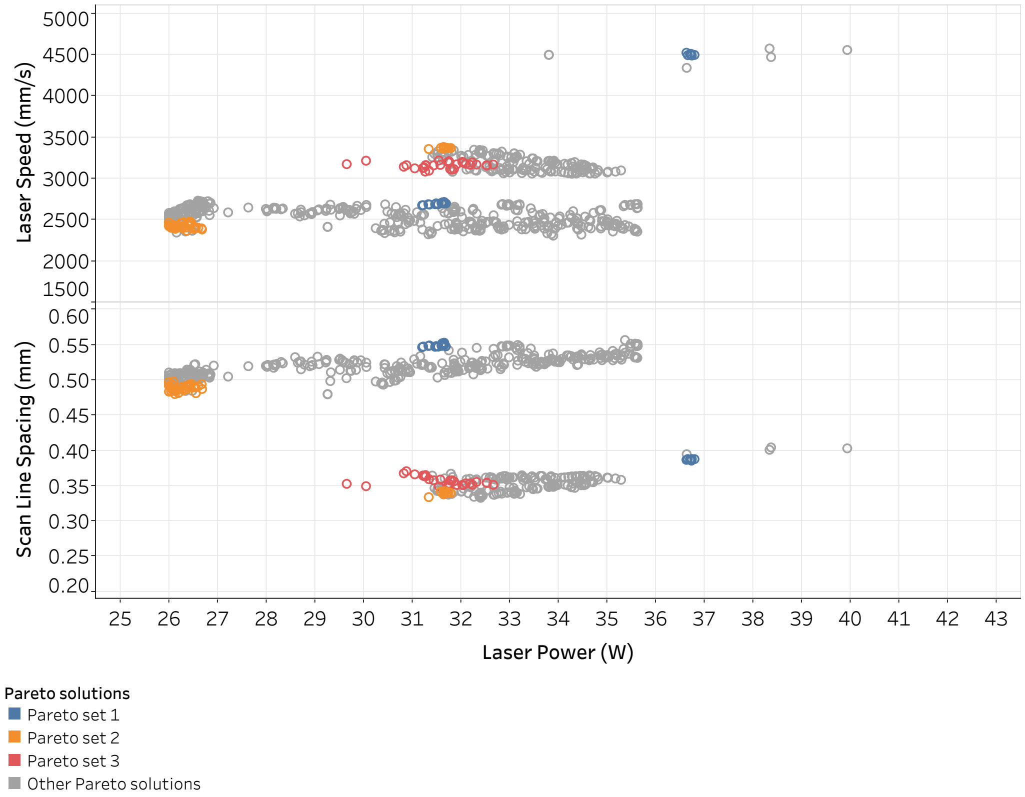

Figure 5.35 – Pareto solutions for criteria 2: laser sintering parameters.

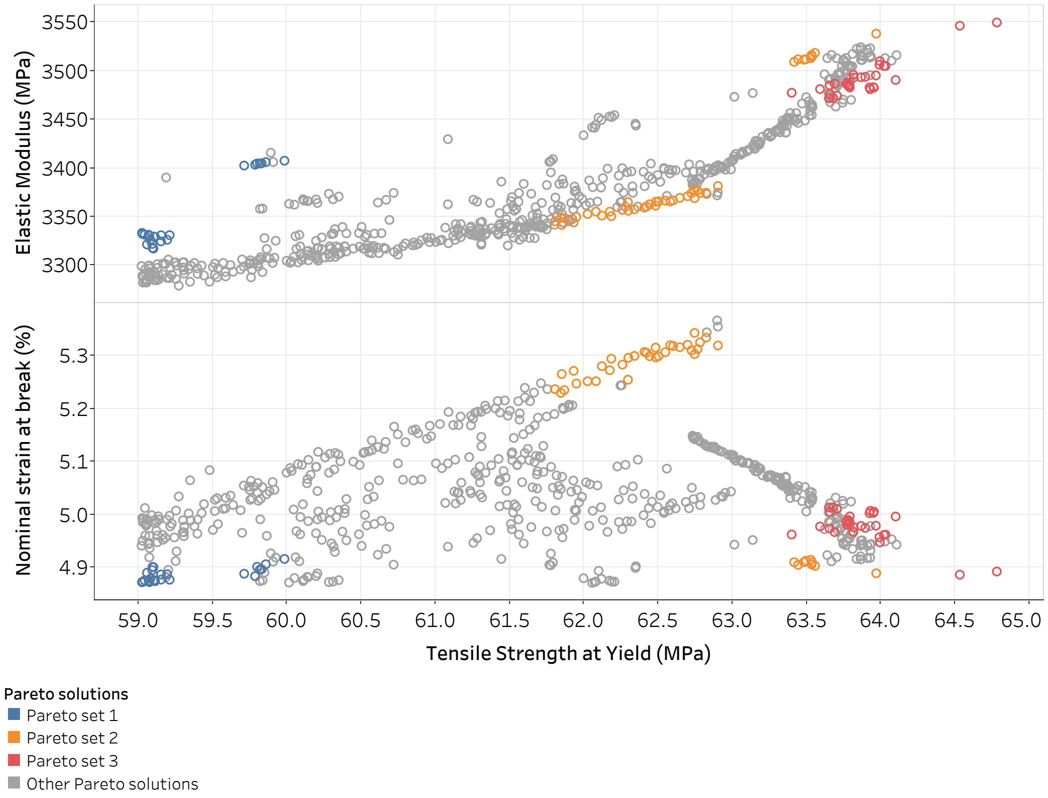

Figure 5.36 – Pareto solutions for criteria 2: elastic modulus, tensile strength at yield and nominal strength.

Density values shown in Fig. 5.37 range between 0.99-1.00 g/cm^3 for Pareto set 1 and between 1.01-1.02 g/cm^3 for Pareto set 2. Pareto set 3 gives even higher density (between 1.02-1.03 g/cm^3). Y-direction accuracy is above 0.993 for all Pareto solution sets whereas normalized manufacturing time is lower for Pareto set 1, which is clustered in two regions of 0.974 and 0.979, whereas higher values around 0.986 are found at Pareto set 2 and 3.

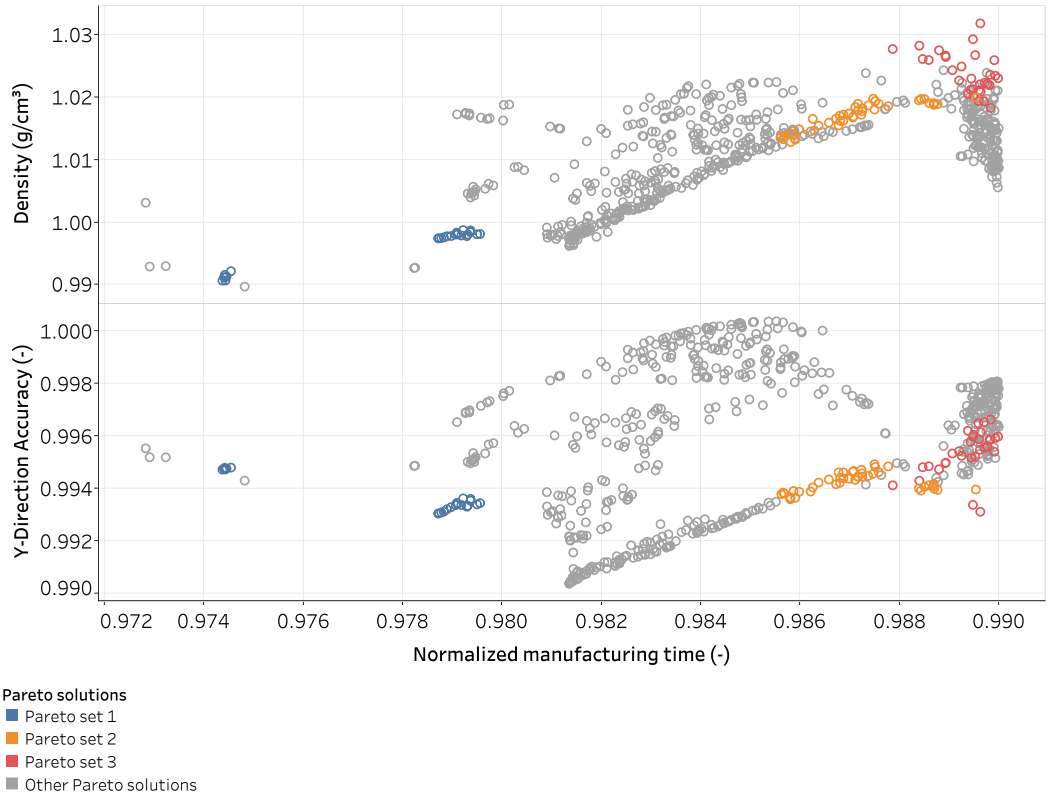

Figure 5.37 – Pareto solutions for criteria 2: density, Y-direction accuracy and normalized manufacturing time.

5.3.3 Criteria 3 - Optimization of mechanical properties and dimensional accuracy

Multi-objective optimization task with criteria 3 aims maximization of dimensional accuracy and mechanical properties. To perform this task, all main mechanical properties outputs (elastic modulus, yield strength and nominal strain at break) were maximized as well as dimensional accuracy in all directions. Normalized manufacturing time and surface roughness were set as hard upper bound at 0.99 and 16 μm respectively.

Figure 5.38 shows the Pareto frontier for yield strength and nominal strain at break over Z-direction accuracy. A well defined Pareto frontier is observed and the trade-off solutions between yield strength and Z-direction accuracy and nominal strain at break and Z-direction accuracy clearly visible. Dimensional accuracy and mechanical properties are conflicting objective functions so the choice of parameters must be carefully observed. To perform the analysis three Pareto solution sets were chosen: first Pareto set focused on high mechanical properties (yield strength above 68 MPa) in detriment of lower dimensional accuracy (between 0.91-0.92); Pareto group 2 allowed slightly lower yield strength (below 67 MPa) values to improve dimensional accuracy (Z-direction accuracy between 0.93-094); Pareto set 3 focused on maximum Z-driection accuracy values (above 0.97) at the cost of much lower mechanical properties (yield strength between 50-51 MPa); Pareto set 4 was chosen in order to maximize nominal strain at break values, which do not show direct correlation with yield strength depending on the value range.

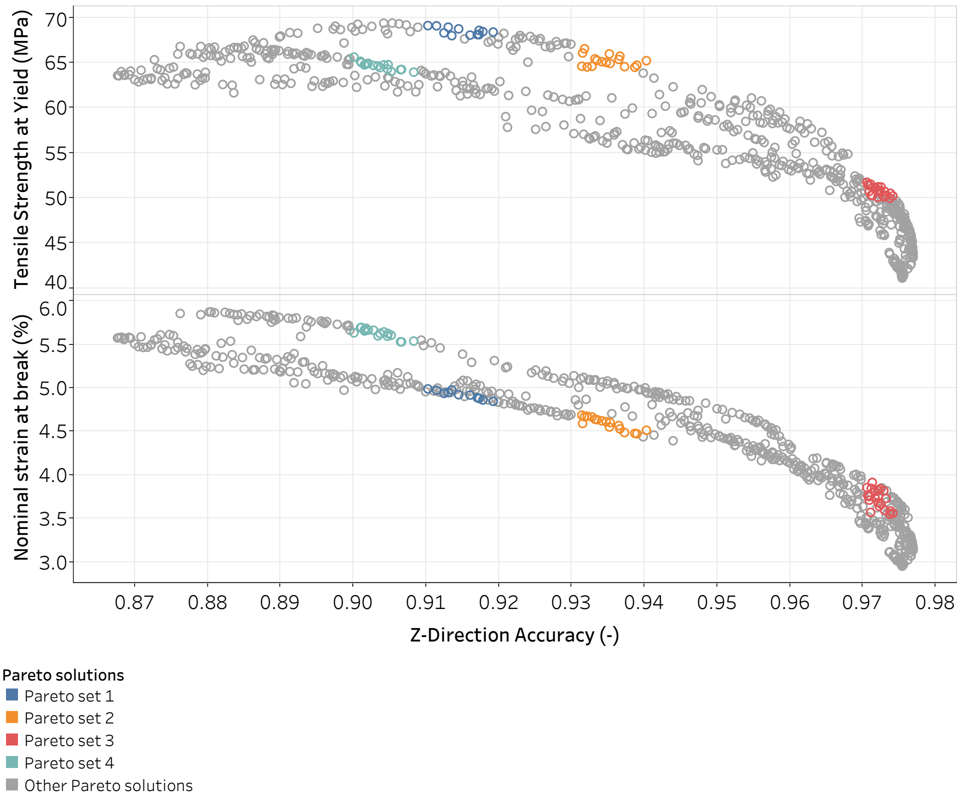

Figure 5.38 – Pareto solutions after optimization task with criteria 3.

Laser speed and scan line spacing over laser power at Pareto frontier for criteria 3 are depicted in Fig. 5.39. Each Pareto set leads to a different laser sintering parameter combination. At Pareto set 1 laser scan speed solutions are concentrated near 3000 mm/s at a laser power between 41-43 W and scan line spacing between 0.56-0.6 mm. Pareto set 2 results in similar parameters except that laser speed is higher (above 3300 mm/s) and lower scan line spacing (between 0.55-0.57 mm). Pareto set 3 is are grouped in two regions: laser power between 28-30 W, laser speed between 4300-4600 mm/s and scan line spacing between 0.38-0.4 mm; second region occurs at high laser power above 41 W, lower laser speed between 4150 and 4450 mm/s and scan line spacing ranging from 0.5-0.52 mm. At last, Pareto set 4 values are concentrated at laser power higher than 40 W, a narrow laser speed area near 4500 mm/s and scan line spacing between 0.37-0.4 mm.

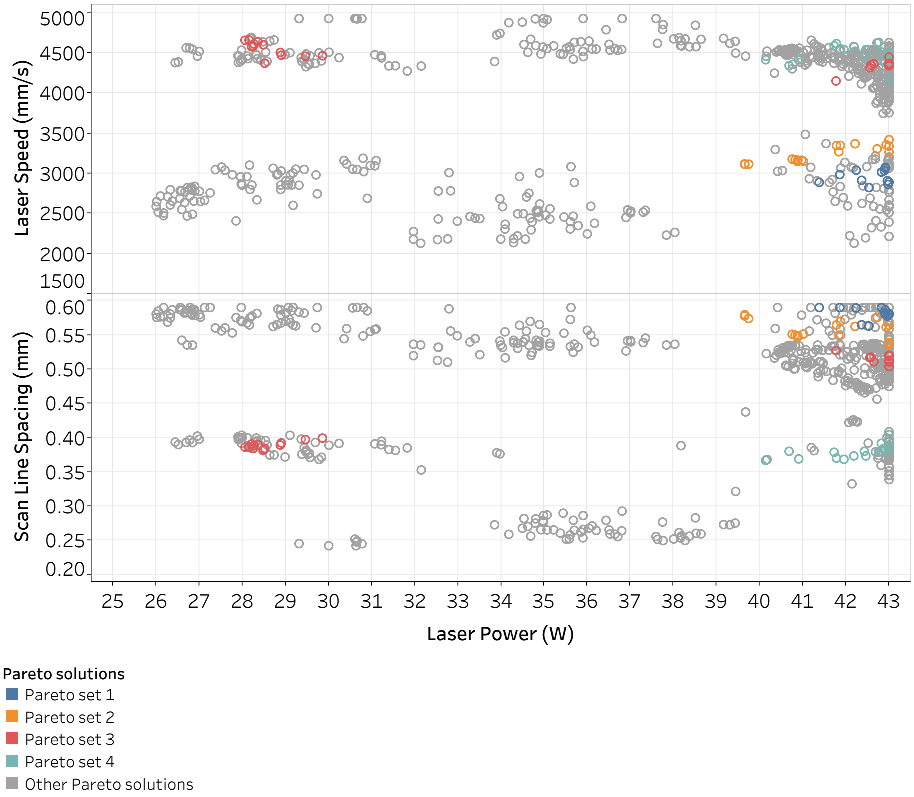

Figure 5.39 – Pareto solutions for criteria 3: laser power over laser speed and scan line spacing.

Taking a closer look at the optimized laser sintering parameters the following observations can be made: laser speed values are always atan intermediate to high level. This is in agreement with the response surfaces from Gaussian model which showed a decrease in mechanical properties at too low laser speed. There is a tendency towards higher laser power when mechanical strength is desired in the Pareto frontier. This was also observed and predicted by the Gaussian model, although high yield strength was also achieved at lower power. Scan line spacing seems decisive when higher nominal strain at break is desired, whereas higher scan line spacing are higher when yield strength is the focus. The overlapping degree may play an important role here by improving the number of laser exposures of the previously scanned area of the powder bed.

Output variables at Pareto frontier are depicted in Fig. 5.40. Values for elastic modulus, proportional limit and density at Pareto set 1 are the highest, reaching 3660 MPa, 32 MPa and 1.05 g/cm^3 respectively. Pareto set 2 results also in good mechanical properties, with slightly lower elastic modulus (3600 MPa), proportional limit (31 MPa) and density (1.02-1.03 g/cm^3). Worst mechanical properties are found at Pareto set 3, with elastic modulus near 3200 MPa, proportional limit of 25 MPa and low density of 0.94 g/cm^3. Pareto set 4 gives intermediate results with slightly lower mechanical properties than Pareto set 2 but similar density levels.

Surface roughness values shown in Fig. 5.41 were nearly the same for all Pareto

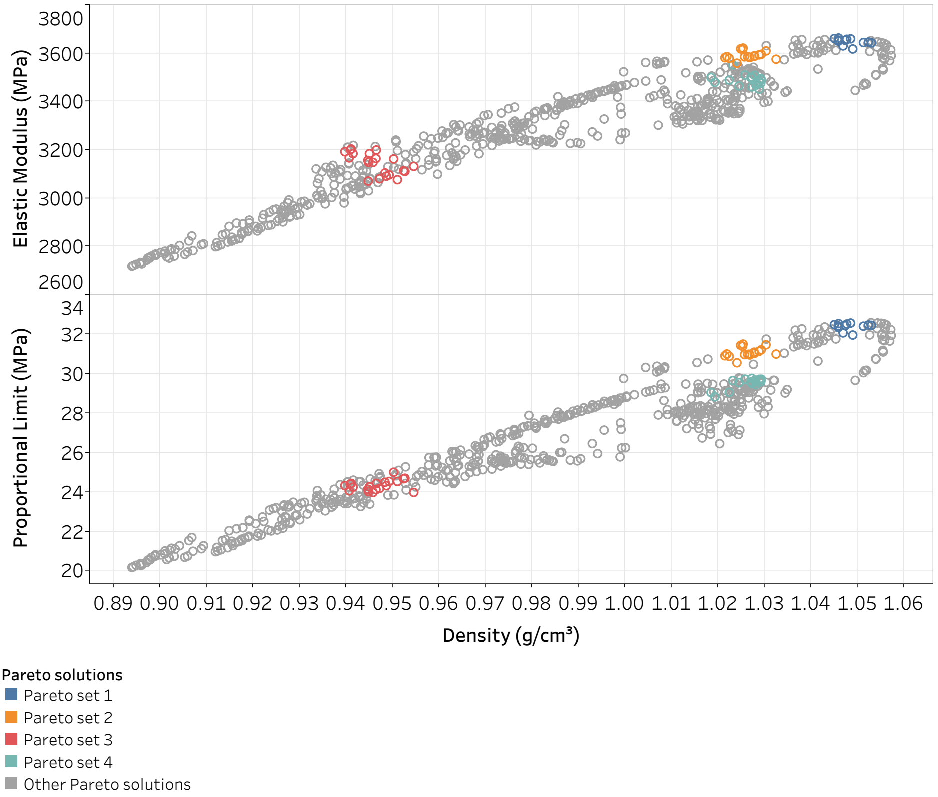

Figure 5.40 – Pareto solutions for criteria 3: elastic modulus, proportional limit and density.

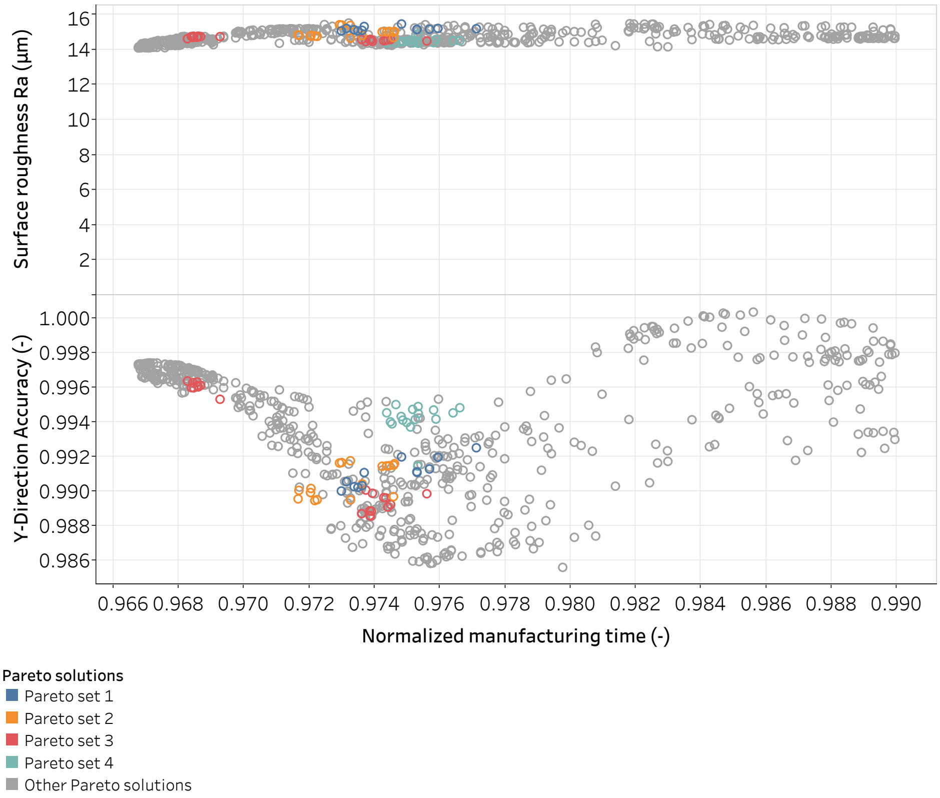

Figure 5.41 – Pareto solutions for criteria 3: normalized manufacturing time, surface roughness R_a and Y-direction accuracy.

sets (slightly above 14.5 μm). Y-direction accuracy resulted in better values for Pareto set 3 and 4, but there is a small difference compared to the other Pareto sets chosen. Normalized manufacturing times were also similar between Pareto sets chosen, ranging between 0.971-0.977, except for a solution cluster inside Pareto set 3 which exhibited lower manufacturing times of 0.968.

5.3.4 Criteria 4 - Optimization of surface roughness and normalized manufacturing time

The objective of EA optimization task with criteria 4 is minimizing surface roughness and manufacturing time while keeping adequate levels of other response variables. To perform this task, yield strength was set as hard upper bound t 59 MPa, elastic modulus at 3276 MPa and nominal strain at break at 4.87 %. Dimensional accuracy was also set as a hard lower bound at 0.88 and 0.98 for Z and Y direction.

Pareto frontier for for normalized manufacturing time over surface roughness R_a is depicted in Fig.5.42. The well defined Pareto frontier shows all possible trade-off solutions for the objective functions desired. Two sets were defined for evaluation: Pareto set 1 focus on lowest surface roughness values found (between 13.2-13.4 μm)at the cost of higher normalized manufacturing time; Pareto set 2 seeks the lowest normalized manufacturing time (0.97-0.971) in detriment of higher surface roughness (14.4 μm)

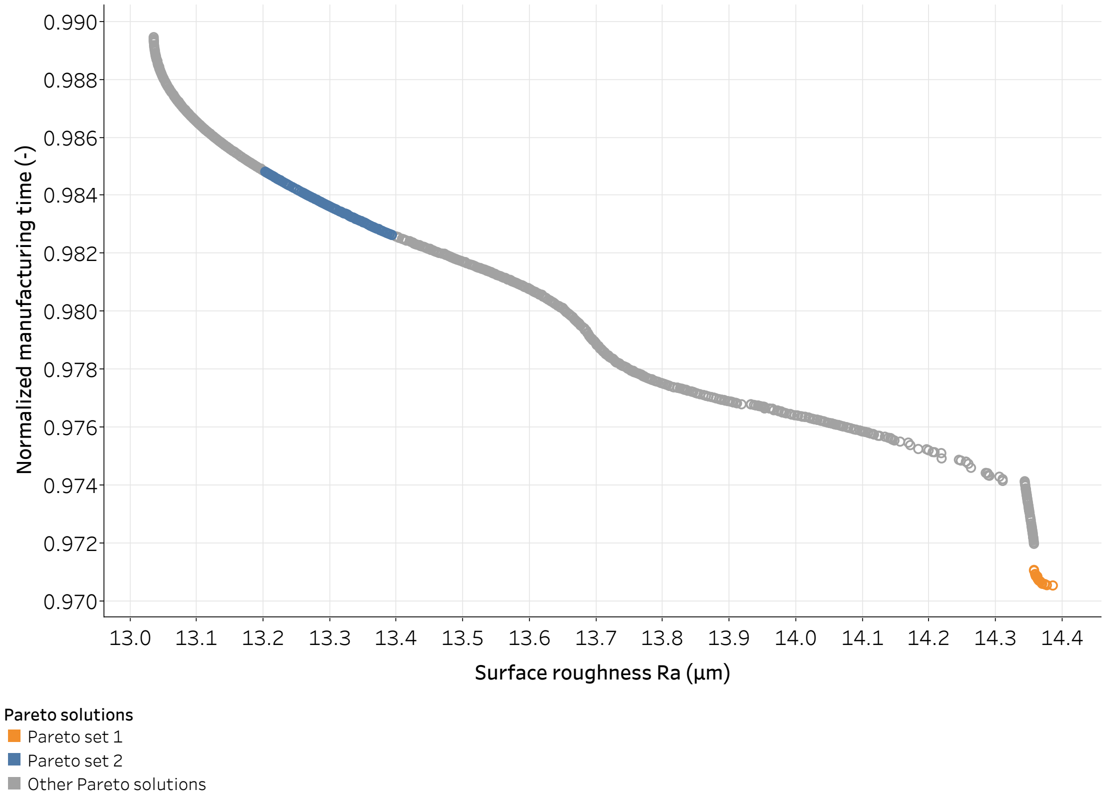

Figure 5.42 – Pareto solutions after optimization task with criteria 4.

Laser sintering parameters at Pareto frontier are depicted in Fig. 5.43. The solutions for Pareto sets are concentrated in two areas: Pareto set 1 solutions are clustered at laser power between 31-32.5 W, laser speed of 3200 mm/s and scan line spacing between 0.4-0.42 mm; Pareto set 2 moves in direction of higher laser power (between 40-43 W), higher laser speed at 4800 mm/s and scan line spacing at 0.42 mm. The solution sets found by EA are interesting as they both give similar values of scan line spacing for completely different objectives regarding surface roughness, showing here scan line spacing plays a not significant role on surface roughness properties, at least concerning the parameter range studied. The higher laser speed in Pareto set 2 is consequence of lower manufacturing times desired.

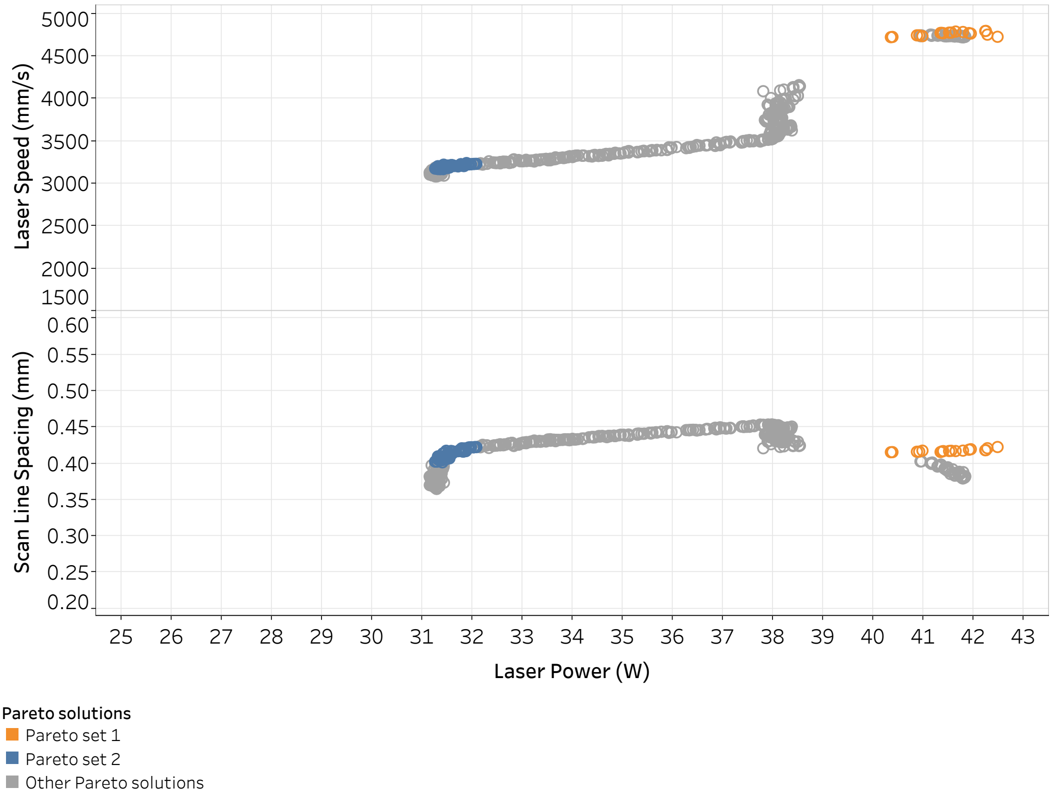

Figure 5.43 – Pareto solutions for criteria 4: laser power over laser speed and scan line spacing.

Mechanical properties resulting from Pareto frontier are given in Fig. 5.44. Elastic modulus is very similar between the two Pareto sets chosen, with values around 3300 MPa. Nominal strain has slightly better values for Pareto set 2, but the two solutions give values below 5 %. Yield strength at Pareto set 1 has a wider range between 59.6-61.5 MPa, which are better values than Pareto set 2 (59 MPa). Dimensional accuracy in Z and Y direction over density is shown in Fig. 5.45.Z-direction accuracy results in better values for Pareto set 2 (0.93) compared to Pareto set 1 (0.89). Also in Y-direction the response is slightly better for Pareto 2 (0.995). Density values for Pareto set 1 range from 1.01-1.02 g/cm^3, whereas lower values are found for Pareto set 2 (0.99-1.00 g/cm^3).

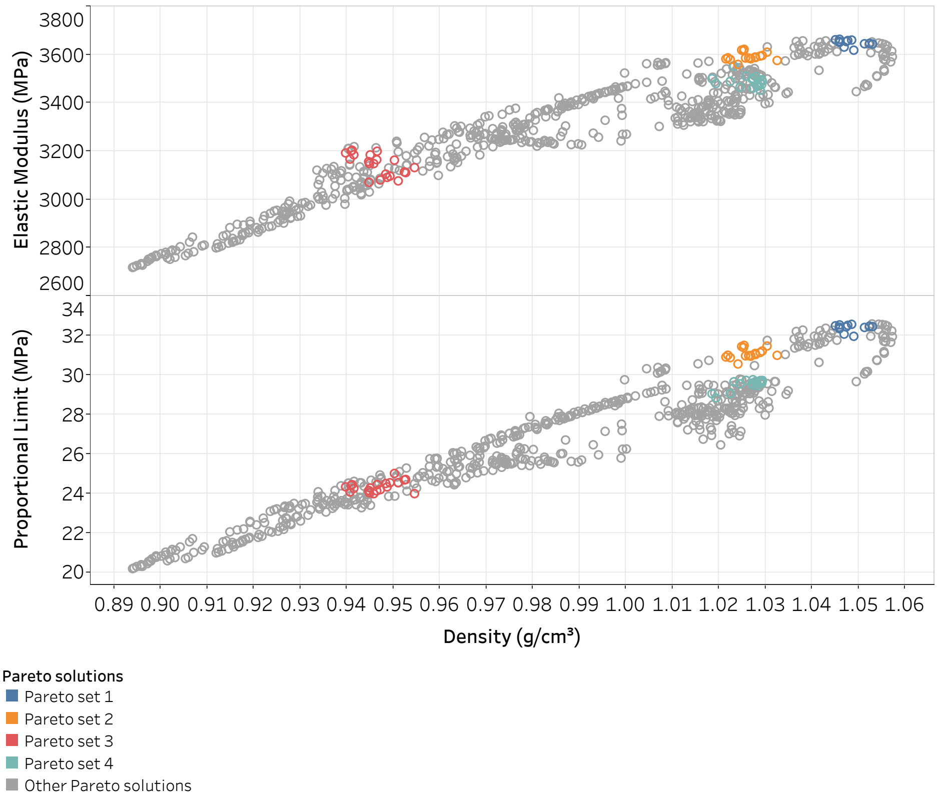

Figure 5.44 – Pareto solutions for criteria 4: elastic modulus, tensile strength at yield and nominal strain at break.

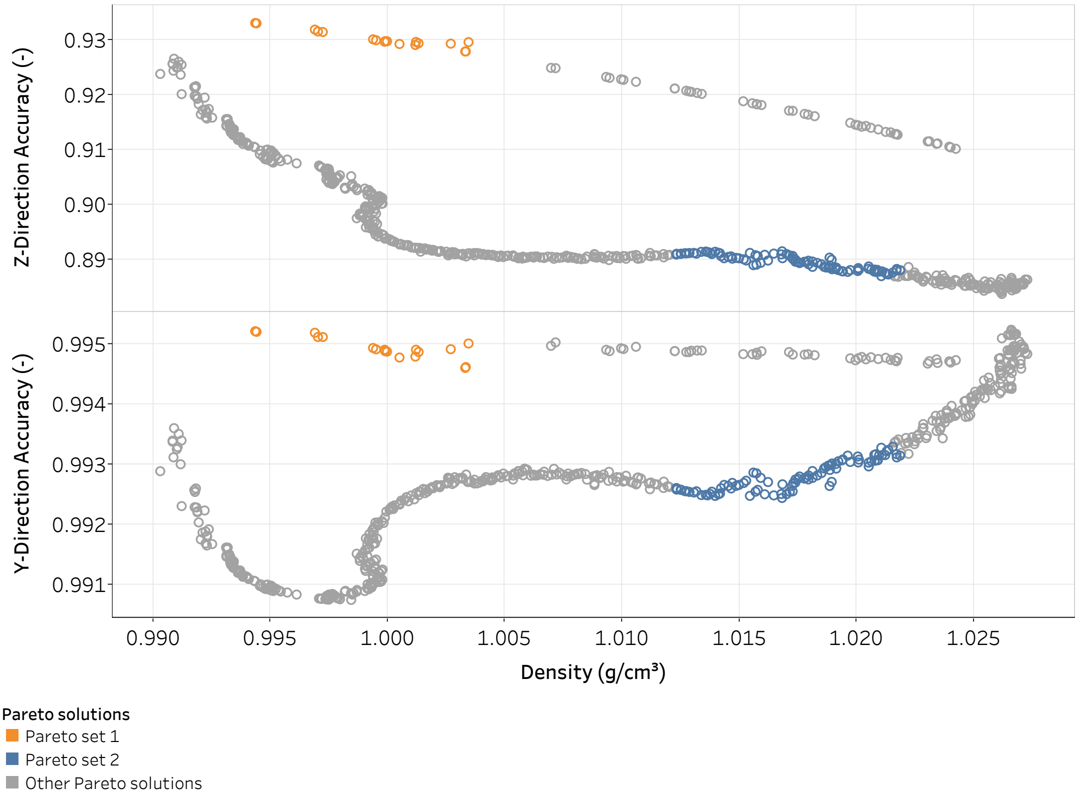

Figure 5.45 – Pareto solutions for criteria 4: density, Y-direction accuracy and Z-direction accuracy.

5.3.5 Criteria 5 - Optimization of surface roughness and mechanical properties

Optimization task criteria 5 aims the maximization of mechanical properties and minimization of surface roughness R_a. Most relevant mechanical properties parameter were maximized (yield strength, nominal strain at break and elastic modulus). Normalized manufacturing time was set as a hard upper bound, whereas Y and Z direction accuracy were set as hard lower bound at 0.98 and 0.88 respectively.

Figure 5.46 shows the Pareto frontier results for yield strength and nominal strain at break over surface roughness. The trade-off solutions are clearly distinguishable. Three Pareto sets were defined for analysis: Pareto set 1 is located at the highest yield strength values (69 MPa), at a cost of higher surface roughness (15 μm). Pareto set 2 focuses in maximizing nominal strain at break (values higher than 5.5 %) whereas Pareto set 3 aims lowest values of surface roughness (between 13-13.2 μm) at an adequate yield strength area .

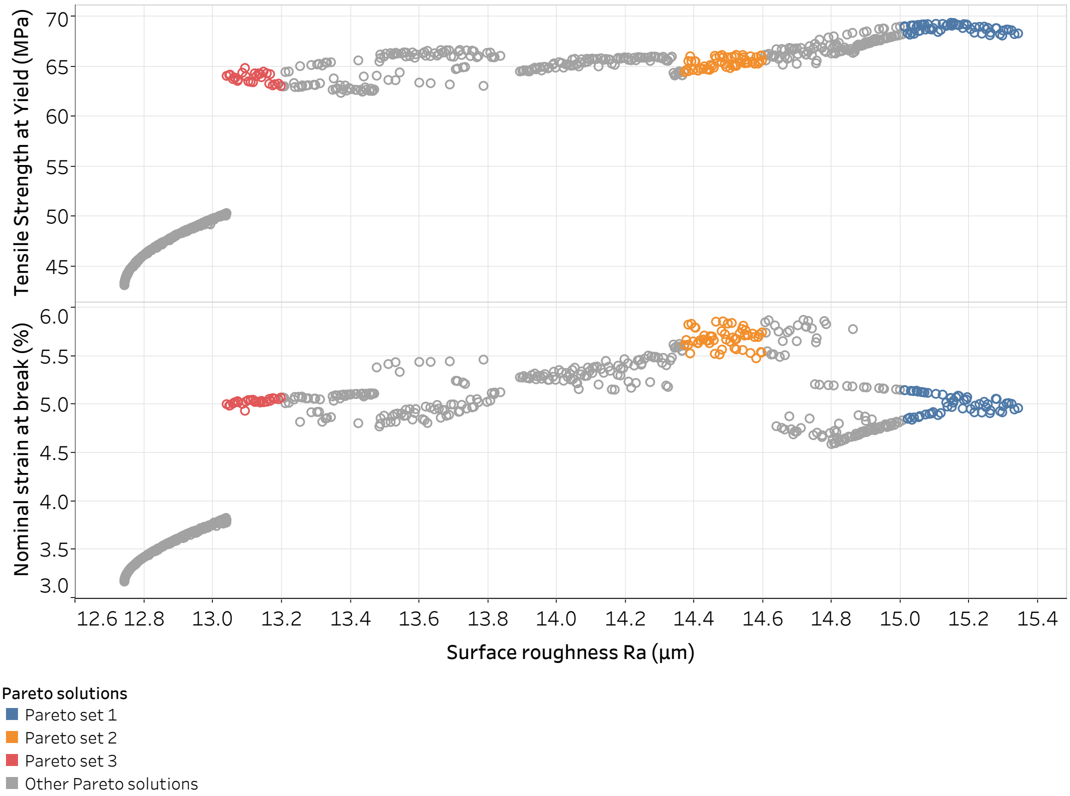

Figure 5.46 – Pareto solutions after optimization task with criteria 5.

Laser sintering parameters at Pareto frontier for optimization task with criteria 5 are depicted in Fig. 5.47. High laser power (42-43 W), laser speed between 2500-3100 mm/s and high scan line spacing (0.57-0.6 mm) are observed as solutions for Pareto set 1.Pareto set 2 results in similar levels of laser power but higher laser speed values, which are found clustered at 3700 mm/s and between 4300-4500 mm/s. Scan line spacing values are also lower at Pareto set 2 and grouped at 0.43 mm and between 0.33-0.38 mm. Pareto set 3 results are covering a wider laser power area between 30-33.5 W, whereas narrow laser speed range at 3000 mm/s and scan line spacing at 0.37 mm are observed.

The results generated via EA algorithm show distinct parameter settings are necessary even when mechanical properties maximization are the target. For instance, intermediate laser speed values and higher scan line spacing are important if yield strength is the mains objective, whereas maximum nominal strain at break is found at higher laser speed and lower scan line spacing. Although the Gaussian process model response surfaces showed such behavior for yield strength and nominal strain at break, it would be a difficult task to find the optimum parameters only via response surface analysis for both output variables, showing the benefit of using metaheuristic methods like evolutionary algorithm to perform multi-objective optimization tasks.

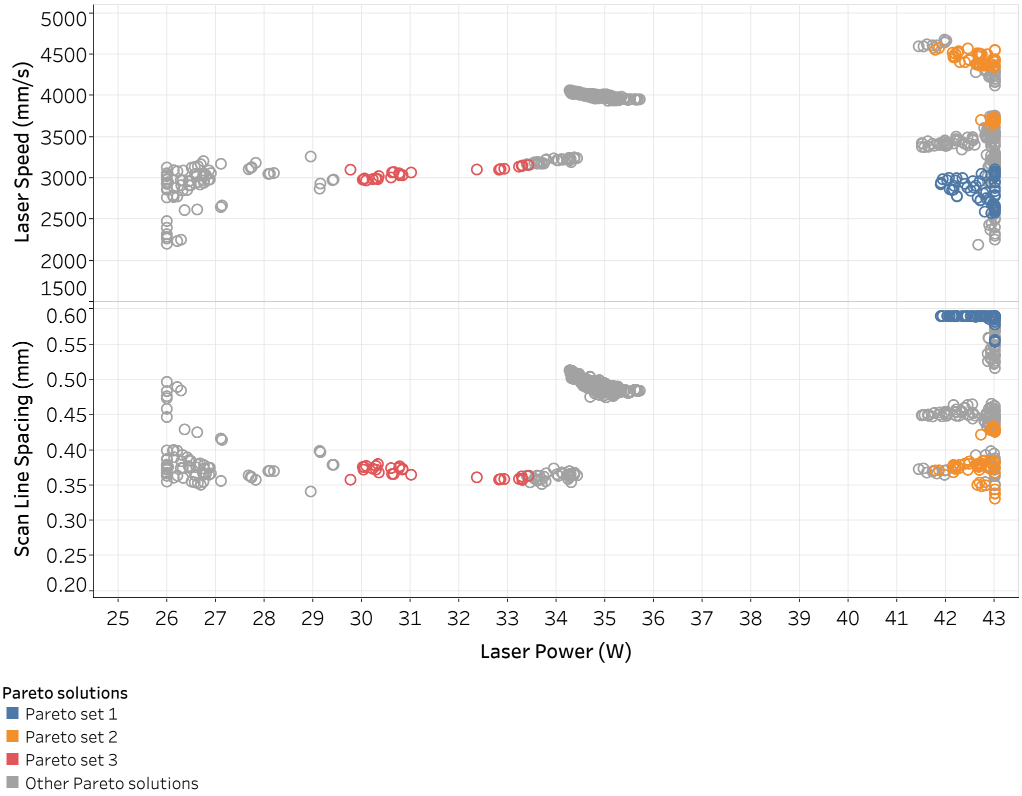

Figure 5.47 – Pareto solutions for criteria 5: laser power over laser speed and scan line spacing.

Elastic mechanical properties over density values at Pareto frontier are depicted in Fig. 5.48.Pareto set 1 results in highest values of Elastic modulus (3660 MPa),whereas Pareto sets 2 and 3 give lower results near 3500 MPa. Proportional limit is slightly higher for Pareto set 3 (maximum 33 MPa), followed by Pareto set 2 (32 MPa) and Pareto set 3 (29.6 MPa). Highest density is also found at Pareto set 1 (1.04-1.05 g/cm^3), while slightly lower values are found at Pareto set 2 and 3 (between 1.01-1.034 g/cm^3).

Figure 5.49 shows dimensional accuracy over normalized manufacturing time at Pareto frontier. Z-direction accuracy is highest for Pareto set 1 (0.9-0.92), followed by

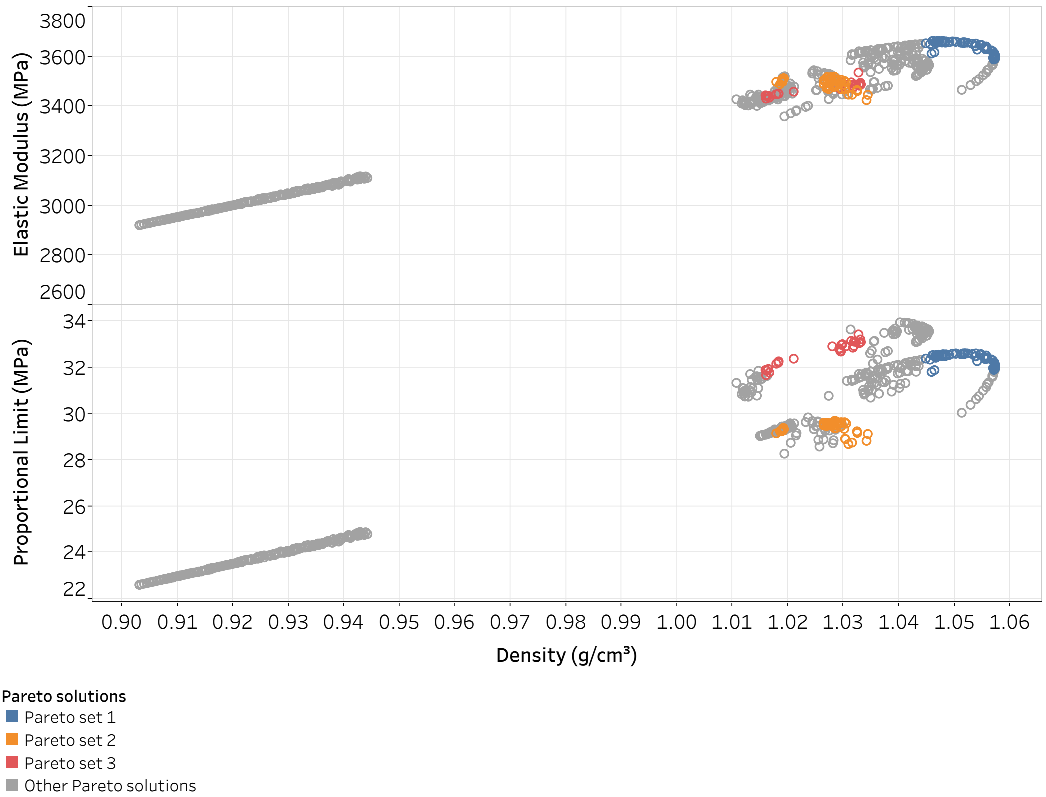

Figure 5.48 – Pareto solutions for criteria 5: elastic modulus, proportional limit and density.

Pareto set 2 (0.88-0.9) and Pareto set 3 (0.88). All Pareto sets resulted in good and close to each other Y-direction accuracy values, with Pareto set 3 presenting the highest score (above 0.994) followed by Pareto set 2 (0.992-0.994) and Pareto set 1 (0.99-0.992). Additionally, another solution cluster is with lower values for Y-direction accuracy is observed for Pareto set 2. The optimized results are in good agreement with the response surfaces. For instance, Z-direction accuracy is more sensitive to scan line spacing than laser speed and better values for this response variable are found at higher scan line spacing, in agreement with the results achieved in Pareto set 1. Laser speed was found to be more relevant for Y-direction accuracy, showing a positive correlation, in agreement with the results from Pareto set 2, which showed better Y-direction accuracy values compared to Pareto set 1.

Normalized manufacturing time for Pareto set 1 and 2 are similar, with a wider coverage for Pareto set 1 (0.972-0.979) than Pareto set 2 (0.975-0.979). Pareto set 3 gives the worst values for manufacturing time, near the upper bound set during the optimization task (0.99).

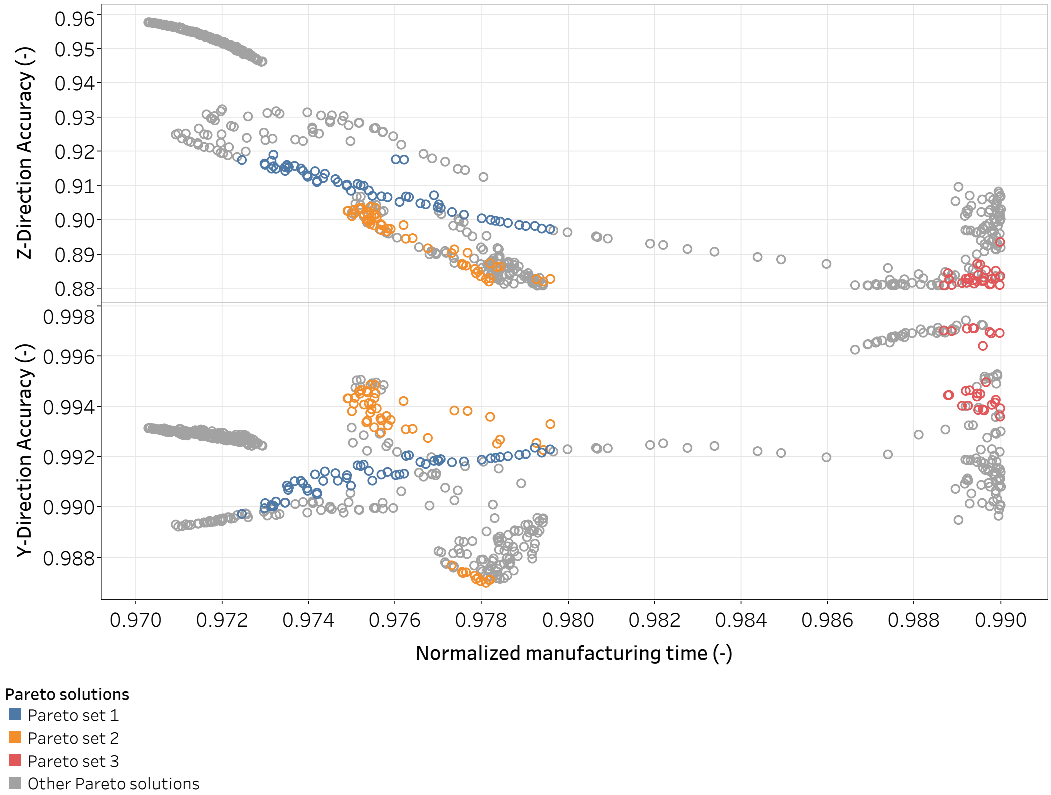

Figure 5.49 – Pareto solutions for criteria 5: Z-direction accuracy, Y-direction accuracy and normalized manufacturing time.

5.3.6 Criteria 6 - Optimization of normalized manufacturing time and mechanical properties

Optimization task 6 target is maximizing mechanical properties and normalizing manufacturing time. In order to perform the task reaching also adequate values of dimensional accuracy and surface roughness, Y and Z-direction accuracy were set as hard lower limits at 0.98 and 0.88 respectively, while surface roughness R_a was set as hard upper limit at 16 μm.

Figure 5.50 shows the Pareto frontier after EA optimization for criteria 6. The curve shows a well defined Pareto frontier with clear trade-off values.Three Pareto sets were evaluated: Pareto set 1 is focused on mechanical properties optimization with normalized manufacturing time below 0.98; Pareto set 2 is similar to Pareto set 1 but has lower yield strength target values (between 64-66.6 MPa) with highest nominal strain at break and lower range for normalized manufacturing time; Pareto set 3 has much softer values of yield strength (44-46 MPa) and nominal strain at break (3.54 %) with the benefit of lower normalized manufacturing time (0.965).

Laser sintering parameters at Pareto frontier are shown in Fig. 5.51. A different set os LS parameters is achieved depending on the specific trade-off desired. Pareto set 1 aims highest yield strength, resulting in optimized parameters clustered at high laser

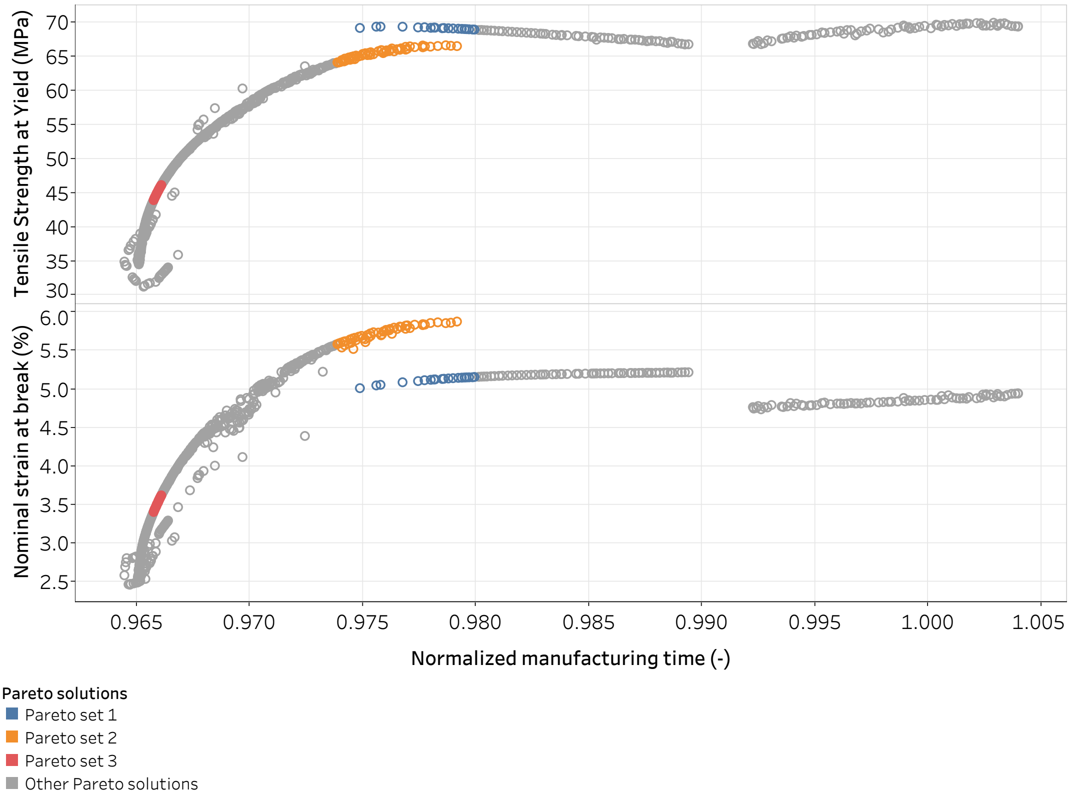

Figure 5.50 – Pareto solutions after optimization task with criteria 6.

power (43 W), intermediate laser speed between 2500-2800 mm/s and high scan line spacing at 0.6 mm. Pareto set 2 is more focused on achieving highest nominal strain, leading to higher laser speed values between 4000-4500 mm/s and lower scan line spacing between 0.35-0.41 mm while keeping the same laser power level near 43 W. Pareto set 3 seeks lowest normalized manufacturing time, therefore highest laser speed is desired (5000 mm/s) combined to also higher scan line spacing at 0.5 mm and high laser power as well.

The optimized LS parameters for criteria 6 for Pareto set 1 and 2 are very similar to the solutions found for optimization task with criteria 5, whose objective was maximization of mechanical properties as well. Comparing Pareto set 2 and 3 it can be observed that a small increase in laser speed and scan line spacing promotes a significant reduction in mechanical properties (30 % reduction in yield strength and 40 % in strain at break) at a small decrease in normalized manufacturing time (1 %).

Elastic properties over density are depicted in Fig. 5.52. Highest elastic modulus of 3600 MPa, proportional limit of 32 MPa and density of 1.05 g/cm^3 are found for Pareto set 1. Pareto set 2 gives slightly lower elastic modulus (3500 MPa), proportional limit (30 MPa) and density (1.02-1.03 g/cm^3). Pareto set 3 results in lowest elastic properties and density. Both elastic properties and density values found at each Pareto set are in accordance to the criteria defined during optimization and follows the same trend of the optimized target responses.

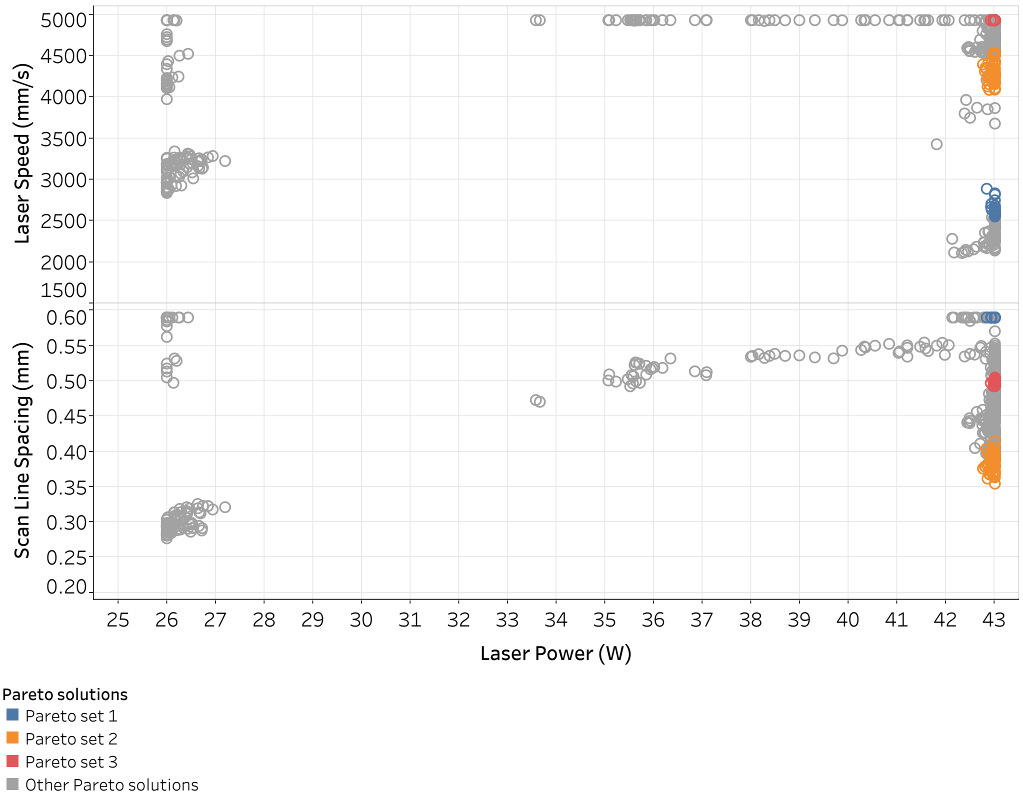

Figure 5.51 – Pareto solutions for criteria 6: laser power over laser speed and scan line spacing.

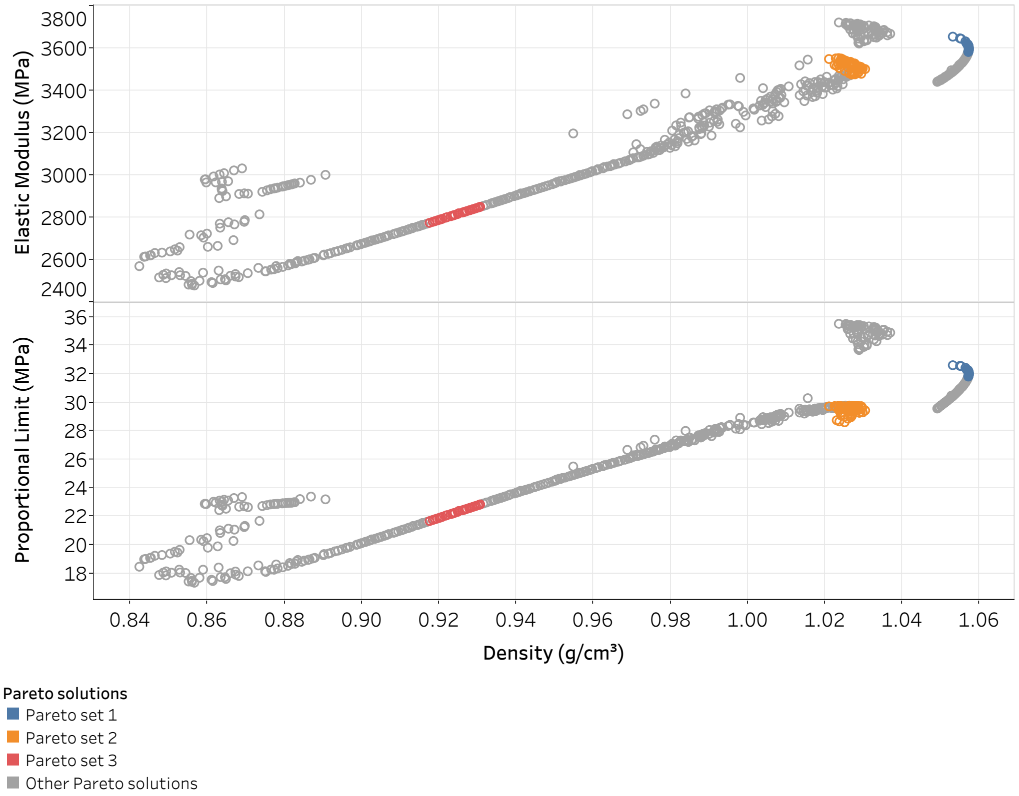

Figure 5.52 – Pareto solutions for criteria 6: elastic modulus, proportional limit and density.

Dimensional accuracy and surface roughness values at Pareto frontier are depicted in Fig. 5.53. Z- direction accuracy values are lower for Pareto set 1 and 2, ranging between 0.88-0.91, whereas Pareto set 3 gives best accuracy values of 0.96. Y-direction accuracy follows the same trend, exept for Pareto set 2 which shows some values with higher Y-direction accuracy (0.994). The variation in Y-direction accuracy is significantly lower compared to accuracy in Z-direction. Surface roughness values are slightly higher for Pareto set 1 (15 μm), whereas Pareto set 3 gives best results of 14.2 μm, although the difference here is very small and surface roughness measurements results in very noisy data.

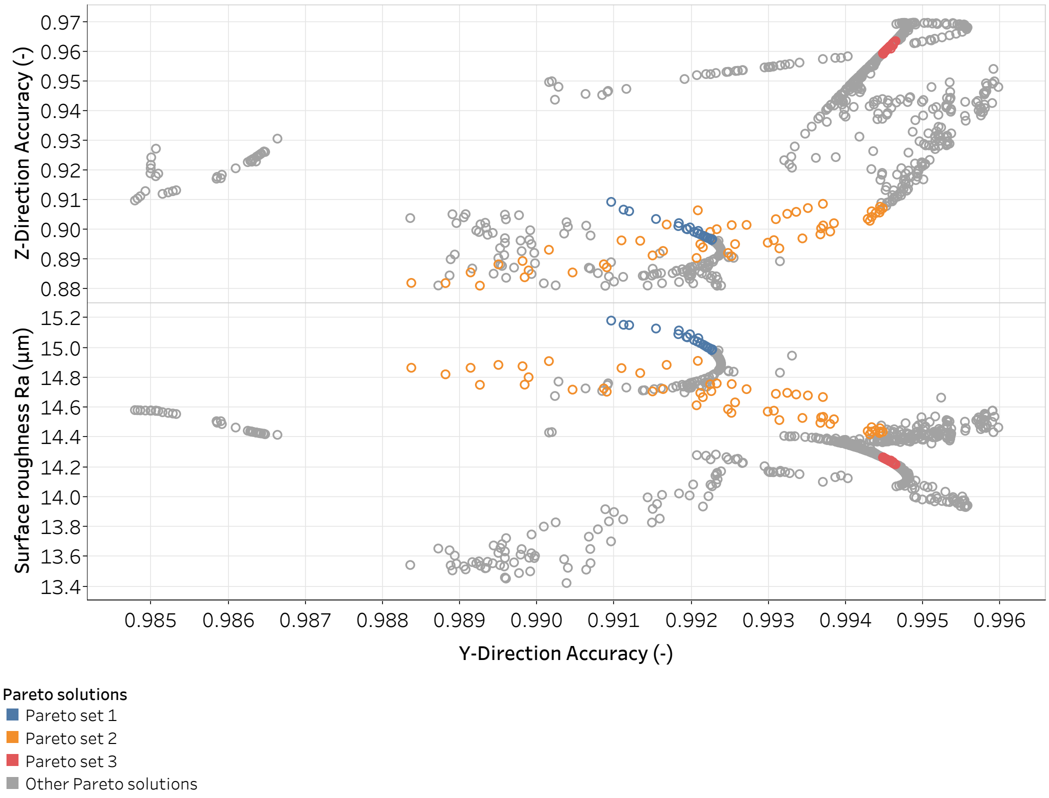

Figure 5.53 – Pareto solutions for criteria 6: Z-direction accuracy, Y-direction accuracy and surface roughness.

6 Conclusions

This work investigated the influence of the laser energy density on mechanical, surface and dimensional properties PA12 polymer and PA12-CF polymer composite materials produced by SLS. A wide parameter range was studied and the consolidation mechanism at different energy levels was studied based on microstructure and crystallization behavior of the parts. Additionally, for the first time the influence of individual laser sintering parameters on dimensional, surface, mechanical properties and manufacturing time was successfully modelled via combination of a space filling DOE method and supervised learning Gaussian Process ($\mathcal{GP}$), providing interesting results for both polymeric and composite materials. At last multi-objective stochastic optimization by means of Evolutionary Algorithm (EA) was deployed for both PA12- and PA12-CF in different criteria scenarios, aiming to understand the behavior of individual laser sintering parameters when subjected to optimization tasks.

From the investigation, the following conclusions can be drawn:

Influence of energy density on PA12:

- Highest accuracy was achieved at X-direction, which remained stable independently of the energy density applied. Y-direction accuracy remained stable at low and mid-range energy levels (up to 0.346 J/mm^3), following a similar tendency than X direction, but at high energy density range accuracy decreased significantly

- Z-direction accuracy was the lowest compared to the other directions, with highest values achieved at low energy densities. Increasing energy density led to continuously decreasing accuracy.

- Surface roughness was found to be higher at low energy density levels, which was associated to the no or negative overlapping degree between laser scan lines. Additionally, it was found that laser scan speed helped improving surface roughness when no overlapping was present. Surface morphology was similar when overlapping degree was high whereas low overlapping led to the formation of rougher surface morphology.

- Parts density increased step-wisely from very low energy density to mid-range energy until reaches more stable values oscillating between 0.91 and 0.97 g/cm^3.

- Stress behavior at elastic regimes is similar to density behavior. Inter-layer porosity plays a major role to reduce elastic properties in the low energy density range whereas a decrease in crystal fraction also reduced mechanical properties at the high energy density area.

- Mechanical plastic behavior analysis revealed a brittle fracture at low energy density, with a transition to more ductile fracture at energy level above 0.193 J/mm^3. Highest plastic strain was observed at an energy density of 0.27-0.275 J/mm^3, whereas further energy increase promoted a reduction in strain.
- SEM of the fractured surfaces revealed the transition from brittle to ductile fracture with increasing energy densities and also the lower fibril elongation at very high energy densities.
- XRD and DSC measurements corroborated the mechanical behavior observed, showing a decrease on the crystal fraction with increasing energy densities, therefore promoting better ductility, but only until an energy level of 0.275 J/mm^3, above which plastic strain decreases. I
- FTIR measurements suggested that some polymer degradation through chain scission may occur for samples processed at too high energy densities, which could explain the low plastic strain observed for samples processed at this energy level.

Gaussian process modelling for PA12:

- Gaussian process could be, for the first time, successfully applied for supervised learning regression of PA12 under a wide range of laser sintering parameters.
- Very good model quality (adequate for quantitative assessment) was achieved for the following output variables: Z-direction accuracy, density, yield strength, break strength, proportional limit, nominal strain at yield and break, elastic modulus, flexural strength, flexural modulus and normalized manufacturing time.
- Intermediate model quality (adequate for qualitative assessment) was achieved for the following output variables: Y-direction accuracy, surface roughness, nominal strain at proportional limit.
- Response surfaces showed a wide variation of topologies depending on the response variable desired, many of which with a highly non-linear shape. Gaussian process could successfully capture the non-linear effects and provide detailed information on the correlation of laser sintering parameters and output variables which can be used for both prediction and optimization of process variables.
- Relevance on individual laser sintering parameters depend strongly on the related response variable evaluated. There is no individual parameter with highest overall relevance that could be ranked.

Optimization via Evolutionary Algorithm (EA) for PA12:

- Multi-objective optimization via stochastic method Evolutionary Algorithm could be successfully deployed for several optimization tasks criteria after $\mathcal{GP}$ learning of PA12 data.
- The Pareto frontier was established for different optimization criteria and the trade-off solutions could be clearly observed in most cases.
- Laser sintering parameters at optimized Pareto frontier can be very different depending on the trade-off objective desired and the criteria used for optimization.
- Optimization task for manufacturing time and dimensional accuracy led to Pareto sets clustered at high laser power and high laser speed and lower laser power and intermediate laser speed. Layer thickness solution was kept at 150 μm and a wide range of scan line spacings available.
- Optimization of surface roughness and manufacturing time resulted in laser sintering Pareto sets at low to intermediate laser power and laser speed, layer thickness at 150 μm and intermediate scan line spacing.
- Optimization of mechanical properties and manufacturing time led to optimzed laser sintering parameters clustered at low laser power and low laser speed or high laser power and intermediate laser speed. Solutions for layer thickness were found at 150 μm and intermediate scan line spacing.
- Optimization of mechanical properties and dimensional accuracy covered a wide range of laser sintering parameters which should be tailored according to the desired trade-off.
- Optimized parameters for surface roughness and dimensional accuracy Pareto frontier were found at high laser power and laser speed or intermediate laser power and laser speed at intermediate scan line spacing and both 120-150 μm layer thickness
- Optimization of mechanical properties and surface roughness led to Pareto solutions clustered at intermediate to low laser speed and a wide range of laser power depending on laser speed used. Intermediate scan line spacing solutions were found at both 120-150 μm layer thickness's investigated.

Influence of energy density on PA12-CF:

- Highest accuracy (above 99.6 %) was achieved at X-direction, which remained stable for energy densities below 0.381 J/mm^3. Y-direction accuracy remained above 98 % and stable up to 0.212 J/mm^3, with worsening accuracy at increasing energy densities. Z-direction accuracy was the lowest measured, showing highest accuracy above 95 % at lowest energy density and decreasing step-wisely towards higher energy densities.

- No significant differences were observed on surface roughness depending on energy density applied. Even at higher scan line spacing and laser speed the surface roughness values remained very similar. Surface morphologies were very similar independently of the overlap degree used. The higher heat affected zone due to improved thermal conductivity of carbon fiber present in the system contributed to the observed surface morphologies.

- Optimum part density was reached in a mid-range energy density plateau (between 0.145-0.181 J/mm^3). Higher energy densities did not result in denser parts, which was attributed to volume increase due to increased heat affected area during SLS and polymer degradation.

- Elastic properties are improved with increasing energy densities, reaching maximum properties at 0.19 J/mm^3. Improved rearrangement phase during LPS at higher energy densities was credited to the enhanced elastic properties. At higher energy densities elastic properties diminished. A reduction in crystal fraction contributed to the observed behavior.

- Highest yield strength was found at 0.19-0.2 J/mm^3. Plastic behavior revealed a brittle fracture of PA12-CF samples regardless of the energy density used, with small values of strain at break. Improved nominal strain at break was achieved with increasing energy densities, which was attributed to the lower crystal fraction content present with increasing energy densities.

- SEM of the fractured surfaces showed a highly porous structure at interlayer regions and between PA12 and CF particles when very low energy density was applied. Increasing energy densities promoted better densification of the parts and higher plastic strain, with crack growth initiating at the interface between PA12 and CF.

- XRD measurements showed a reduction in α phase with increasing energy densities, which was associated to the better consolidation of the composites powder during SLS, reducing the overall crystal fraction of the materials. The results confirmed the improved plastic strain correlation with crystal fraction reduction assumption for PA12-CF samples processed at higher energy densities.

- Polymer degradation through chain scission was observed with FTIR measurements of samples processed at higher energy densities. The reduction of absorption at assignment bands suggest higher chain mobility of PA12. Also, carbonyl group modifications were observed at higher energy densities, which were associated to thermal degradation of oxygen groups present at CF surface, released as gas during SLS process and resulted in higher porosity of the materials and decreased mechanical properties.

Gaussian process modelling for PA12-CF:

- For the first time the modelling of SLS parameters was performed for PA12-CF. Using a DOE approach, Gaussian process was successfully applied for supervised learning regression of PA12-CF under a wide range of laser sintering parameters.
- Very good model quality (adequate for quantitative assessment) was achieved for the following output variables: Z-direction accuracy, density, yield strength, break strength, nominal strain at yield and break, elastic modulus, and normalized manufacturing time.
- Intermediate model quality (adequate for qualitative assessment) was achieved for the following output variables: density, proportional limit, Y-direction accuracy.
- Very low model quality was achieved for surface roughness, mainly due to the high noise attributed to this variable and also its low sensitivity to the laser sintering parameters.
- As with PA12,response surfaces showed a wide variation of topologies depending on the response variable desired, many of which with a highly non-linear shape. Gaussian process could successfully capture the non-linear effects and provide detailed information on the correlation of laser sintering parameters and output variables which can be used for both prediction and optimization of process variables.
- As with PA12, relevance of individual laser sintering parameters depend strongly on the related response variable evaluated. There is no individual parameter with highest overall relevance that could be ranked.
- Considering this is the first time supervised learning is applied to polymer composites manufactured by SLS, the results are relevant to provide deeper information on the influence of individual laser sintering parameters over important quality variables.

Optimization via Evolutionary Algorithm (EA) for PA12-CF:

- Multi-objective optimization via stochastic method Evolutionary Algorithm could be successfully deployed for several optimization tasks criteria after $\mathcal{GP}$ learning of PA12-CF data.
- The Pareto frontier was established for different optimization criteria and the trade-off solutions could be clearly observed in most cases.

- Laser sintering parameters at optimized Pareto frontier vary in great extent depending on the trade-off objective desired and the criteria used for optimization.

- Optimization task for manufacturing time and dimensional accuracy led to Pareto sets clustered at high laser power, high laser speed and medium to high scan line spacing or intermediate laser power and laser speed and high scan line spacing.

- Optimization of surface roughness and dimensional accuracy resulted in a wide range of laser sintering Pareto sets, but mainly located in the medium to low laser power and laser speed combined to intermediate to high scan line spacing.

- Optimization of mechanical properties and dimensional accuracy led to optimized laser sintering parameters clustered mainly at high laser power and intermediate to high laser speed. Scan line spacing varied from intermediate to high values. A clear difference was observed in SLS Pareto sets maximizing strain at break or yield strength.

- Optimization of manufacturing time and surface roughness resulted in a narrow range of laser sintering parameters, located at intermediate laser sintering values or at high laser power and speed and intermediate scan line spacing, depending on the desired trade-off solution.

- Selected values at Pareto frontier for optimized mechanical properties and surface roughness were found at high laser power and laser speed at intermediate scan line spacing; high laser power and scan line spacing at intermediate laser speed or low laser power at intermediate laser speed and scan line spacing.

- Optimization of mechanical properties and manufacturing time resulted in Pareto solutions clustered at high laser power and intermediate to high laser speed and scan line spacing, depending on the desired trade-off solution.

6.1 Directions for future research

The present work provided a detailed analysis on the influence, modelling and optimization of the main SLS process variables on important quality criteria. Significant results have been achieved and provide a relevant contribuition to the field. Nevertheless, several aspects on the field remain to be further investigated. Some directions for future research are pointed out:

- Include pre-heating temperature in the model: pre-heating temperature influence was out of the scope of this work, but it influences directly the quality parameters assessed.

- Building direction also plays an important role on quality parameters. Since this work kept the same building direction for all samples, evaluating the influence of building direction would enrich the modelling performed and extend the application range.
- Evalute in more detail the degradation mechanism occuring during SLS of PA12-CF and correlate with other measurement techniques (melt flow index or other technique).
- Run SLS trials at optimized points and correlate measurement results with modelled.
- Train the model with $\mathcal{GP}$ using less training data and using the remaining data for validation. This is similar to the cross validation approach in supervised learning but the results can be interesting to observe the differences on model quality.
- Train data with Gaussian process using different covariance functions: the function used in this work results in functions with smooth curves. It would be interesting to compare the results with GP modelling using other kernels such as Matern, which gives less smooth curves.
- Integrate the model obtained in a software platform where the optimized variables can be tailored to specific criteria and real application demands.

Bibliography

AGARWALA, M. et al. Direct selective laser sintering of metals. *Rapid Prototyping Journal*, v. 1, n. 1, p. 26–36, 1995. ISSN 1355-2546. Cited on page 25.

ALDAHSH, S. *Development of a new composite powder material of cement additive with polyamide 12 for selective laser sintering.* Tese (PhD) — Cardiff University, 2011. Disponível em: <http://orca.cf.ac.uk/10948/>. Cited on page 47.

ANESTIEV, L.; FROYEN, L. Model of the primary rearrangement processes at liquid phase sintering and selective laser sintering due to biparticle interactions. *Journal of applied physics*, v. 86, n. 7, p. 4008, 1999. ISSN 00218979. Cited 2 times on pages 41 and 147.

ASTM Standard D5947-11. Standard Test Methods for Physical Dimensions of Solid Plastics Specimens. 2011. Disponível em: <http://www.astm.org/Standards/D5947.htm>. Cited on page 66.

ASTM Standard D638-02a. Standard test method for tensile properties of plastics. 2002. Cited 3 times on pages 57, 66, and 76.

ASTM Standard D790-02. Standard Test Methods for Flexural Properties of Unreinforced and Reinforced Plastics and Electrical Insulating Materials. 2002. Cited 2 times on pages 57 and 66.

ASTM Standard F2792-12a. Standard Terminology for Additive Manufacturing Technologies. 2012. Cited 4 times on pages 15, 29, 30, and 31.

ATHREYA, S. R.; KALAITZIDOU, K.; DAS, S. Processing and characterization of a carbon black-filled electrically conductive Nylon-12 nanocomposite produced by selective laser sintering. *Materials Science and Engineering: A*, Elsevier B.V., v. 527, n. 10-11, p. 2637–2642, 2010. ISSN 09215093. Disponível em: <http://linkinghub.elsevier.com/retrieve/pii/S0921509309013318>. Cited 2 times on pages 49 and 72.

ATKINS, E.; HILL, M. J.; VELURAJA, K. Structural and morphological investigations of nylon 8 chain-folded lamellar crystals. *Polymer*, Elsevier, v. 36, n. 1, p. 35–42, jan 1995. ISSN 00323861. Disponível em: <https://www.sciencedirect.com/science/article/pii/003238619590672O>. Cited 2 times on pages 87 and 156.

BAI, J. et al. Improving the mechanical properties of laser-sintered polyamide 12 through incorporation of carbon nanotubes. *Polymer Engineering & Science*, v. 53, n. 9, p. 1937–1946, sep 2013. ISSN 00323888. Disponível em: <http://doi.wiley.com/10.1002/pen.23459>. Cited on page 51.

BAI, J. et al. Nanostructural characterization of carbon nanotubes in laser-sintered polyamide 12 by 3D-TEM. *Journal of Materials Research*, v. 29, n. 17, p. 1817–1823, 2014. ISSN 0884-2914. Disponível em: <http://www.journals.cambridge.org/abstract{_}S0884291414001>. Cited on page 51.

BAI, J. et al. Influence of carbon nanotubes on the rheology and dynamic mechanical properties of polyamide-12 for laser sintering. *Polymer Testing*, Elsevier Ltd, v. 36, p. 95–100, 2014. ISSN 01429418. Cited on page 51.

BAI, J. et al. Thermal influence of CNT on the polyamide 12 nanocomposite for selective laser sintering. *Molecules*, v. 20, n. 10, p. 19041–19050, 2015. ISSN 14203049. Cited on page 142.

BERZINS, M.; CHILDS, T.; RYDER, G. The Selective Laser Sintering of Polycarbonate. *CIRP Annals - Manufacturing Technology*, v. 45, n. 1, p. 187–190, jan 1996. ISSN 00078506. Disponível em: <http://www.sciencedirect.com/science/article/pii/S0007850607630443>. Cited on page 45.

BURNING, S. Copper Polyamide. In: K.U. LEUVEN. *2nd European SLS users meeting*. Leuven, Belgium, 1998. Cited on page 47.

CAULFIELD, B.; MCHUGH, P. E.; LOHFELD, S. Dependence of mechanical properties of polyamide components on build parameters in the SLS process. *Journal of Materials Processing Technology*, v. 182, n. 1-3, p. 477–488, 2007. ISSN 09240136. Cited 4 times on pages 26, 44, 72, and 80.

CAVAZZUTI, M. *Optimization Methods: From Theory to Design*. [S.l.]: Springer-Verlag Berlin Heidelberg, 2013. ISSN 1098-6596. ISBN 9788578110796. Cited 2 times on pages 58 and 62.

CELINA, M. et al. FTIR emission spectroscopy applied to polymer degradation. *Polymer Degradation and Stability*, Elsevier, v. 58, n. 1-2, p. 15–31, jan 1997. ISSN 0141-3910. Disponível em: <https://www.sciencedirect.com/science/article/pii/S0141391096002182>. Cited 2 times on pages 90 and 157.

CHUA, C. K.; LEONG, K. F.; LIM, C. S. *Rapid Prototyping: Principles and Applications*. 3. ed. Singapore: World Scientific, 2010. 512 p. ISBN 9812778977. Disponível em: <https://books.google.com/books?id=4OYcyiDUpsQC{&}pgi>. Cited on page 34.

CHUA, C. K. et al. Development of tissue scaffolds using selective laser sintering of polyvinyl alcohol/hydroxyapatite biocomposite for craniofacial and joint defects. *Journal of Materials Science: Materials in Medicine*, v. 15, n. 10, p. 1113–1121, 2004. ISSN 09574530. Cited on page 48.

CHUNG, H.; DAS, S. Functionally graded Nylon-11/silica nanocomposites produced by selective laser sintering. *Materials Science and Engineering: A*, v. 487, n. 1-2, p. 251–257, 2008. ISSN 09215093. Disponível em: <http://linkinghub.elsevier.com/retrieve/pii/S0921509307018096>. Cited on page 50.

DAS, S. Physical Aspects of Process Control in Selective Laser Sintering of Metals. *Advanced Engineering Materials*, v. 5, n. 10, p. 701–711, 2003. ISSN 1438-1656. Disponível em: <http://doi.wiley.com/10.1002/adem.200310099>. Cited on page 38.

DAS, S. et al. Direct laser freeform fabrication of high performance metal components. *Rapid Prototyping Journal*, v. 4, n. 3, p. 112–117, 1998. ISSN 1355-2546. Cited 2 times on pages 25 and 34.

DECKARD, C. R. *Method and apparatus for producing parts by selective sintering.* 1989. Disponível em: <http://www.google.com/patents/US4863538>. Cited on page 35.

DOLENC, A. *An Overview Of Rapid Prototyping Technologies In Manufacturing.* Helsinki, 1994. 1–23 p. Cited 2 times on pages 11 and 34.

DRUMMER, D.; WUDY, K.; DREXLER, M. Influence of energy input on degradation behavior of plastic components manufactured by selective laser melting. In: *Physics Procedia.* [s.n.], 2014. v. 56, n. C, p. 176–183. ISSN 18753892. Disponível em: <www.sciencedirect.com>. Cited on page 89.

DUPIN, S. et al. Microstructural origin of physical and mechanical properties of polyamide 12 processed by laser sintering. *European Polymer Journal*, Pergamon, v. 48, n. 9, p. 1611–1621, sep 2012. ISSN 00143057. Disponível em: <http://linkinghub.elsevier.com/retrieve/pii/S0014305712001954>. Cited 9 times on pages 25, 43, 72, 79, 80, 85, 87, 89, and 151.

EOS. *EOS P396 basic training.* 2016. Cited on page 67.

EOS. *Material Data Center.* 2020. Disponível em: <http://eos.materialdatacenter.com/eo/en>. Cited 8 times on pages 15, 55, 57, 72, 80, 82, 148, and 151.

FAN, K. M.; CHEUNG, W. L.; GIBSON, I. Fusion behavior of TrueFormTM/SiO2 composite powders during selective laser sintering. *Rapid Prototyping Journal*, v. 14, n. 2, p. 87–94, 2008. ISSN 1355-2546. Disponível em: <http://www.emeraldinsight.com/10.1108/13552540810862046>. Cited on page 47.

GERMAN, R. M. *Liquid Phase Sintering.* [S.l.]: Springer US, 1985. 244 p. Cited on page 41.

GHITA, O. et al. High Temperature Laser Sintering (HT-LS): An investigation into mechanical properties and shrinkage characteristics of Poly (Ether Ketone) (PEK) structures. *Materials & Design*, Elsevier Ltd, v. 61, p. 124–132, 2014. ISSN 02613069. Disponível em: <http://www.sciencedirect.com/science/article/pii/S0261306914003033>. Cited on page 45.

GIBSON, I.; ROSEN, D. W.; STUCKER, B. *Additive Manufacturing Technologies: Rapid Prototyping to Direct Digital Manufacturing.* [S.l.: s.n.], 2010. 484 p. ISSN 01445154. ISBN 1441911200. Cited 3 times on pages 25, 29, and 32.

GOGOLEWSKI, S.; CZERNIAWSKA, K.; GASIOREK, M. Effect of annealing on thermal properties and crystalline structure of polyamides. Nylon 12 (polyaurolactam). *Colloid & Polymer Science*, v. 258, p. 1130–1136, 1980. Cited 2 times on pages 67 and 88.

GOODRIDGE, R. et al. Processing of a Polyamide-12/carbon nanofibre composite by laser sintering. *Polymer Testing*, Elsevier Ltd, v. 30, n. 1, p. 94–100, 2011. ISSN 01429418. Disponível em: <http://linkinghub.elsevier.com/retrieve/pii/S0142941810001753>. Cited on page 50.

GOODRIDGE, R.; TUCK, C.; HAGUE, R. Laser sintering of polyamides and other polymers. *Progress in Materials Science*, Elsevier Ltd, v. 57, n. 2, p. 229–267, 2012. ISSN 00796425. Disponível em: <http://linkinghub.elsevier.com/retrieve/pii/S0079642511000648>. Cited 6 times on pages 11, 27, 40, 46, 49, and 72.

GOODRIDGE, R. D.; DALGARNO, K. W.; WOOD, D. J. Indirect selective laser sintering of an apatite-mullite glass-ceramic for potential use in bone replacement applications. *Proceedings of the Institution of Mechanical Engineers. Part H, Journal of engineering in medicine*, v. 220, n. 1, p. 57–68, 2006. ISSN 0954-4119. Cited on page 42.

GOODRIDGE, R. D.; HAGUE, R. J.; TUCK, C. J. An empirical study into laser sintering of ultra-high molecular weight polyethylene (UHMWPE). *Journal of Materials Processing Technology*, v. 210, n. 1, p. 72–80, jan 2010. ISSN 09240136. Disponível em: <http://www.sciencedirect.com/science/article/pii/S0924013609003069>. Cited on page 46.

GRIESSBACH, S.; LACH, R.; GRELLMANN, W. Structure-property correlations of laser sintered nylon 12 for dynamic dye testing of plastic parts. *Polymer Testing*, Elsevier Ltd, v. 29, n. 8, p. 1026–1030, 2010. ISSN 01429418. Disponível em: <http://dx.doi.org/10.1016/j.polymertesting.2010.09.010>. Cited 3 times on pages 26, 44, and 82.

GU, D.; SHEN, Y. Processing and microstructure of submicron WC-Co particulate reinforced Cu matrix composites prepared by direct laser sintering. *Materials Science and Engineering A*, v. 435-436, p. 54–61, 2006. ISSN 09215093. Cited on page 34.

GU, D. D. et al. Effects of processing parameters on direct laser sintering of multicomponent Cu based metal powder. *Materials Science and Technology*, v. 22, n. 12, p. 1449–1455, 2006. ISSN 02670836. Cited on page 25.

GUO, J. et al. Surface quality improvement of selective laser sintered polyamide 12 by precision grinding and magnetic field-assisted finishing. *Materials and Design*, Elsevier Ltd, v. 138, n. January, p. 39–45, jan 2018. ISSN 18734197. Cited on page 74.

GUO, N.; LEU, M. C. Additive manufacturing: technology, applications and research needs. *Frontiers of Mechanical Engineering*, v. 8, n. 3, p. 215–243, 2013. ISSN 2095-0233. Disponível em: <http://link.springer.com/10.1007/s11465-013-0248-8>. Cited on page 31.

GUO, Y.; JIANG, K.; BOURELL, D. L. Preparation and laser sintering of limestone PA 12 composite. *Polymer Testing*, Elsevier Ltd, v. 37, p. 210–215, 2014. ISSN 01429418. Disponível em: <http://dx.doi.org/10.1016/j.polymertesting.2014.06.002>. Cited 2 times on pages 27 and 47.

HAO, L. et al. Selective Laser Sintering of Hydroxyapatite Reinforced Polyethylene Composites for Bioactive Implants and Tissue Scaffold Development. *Proceedings of the Institution of Mechanical Engineers, Part H: Journal of Engineering in Medicine*, v. 220, n. 4, p. 521–531, jun 2006. ISSN 0954-4119. Disponível em: <http://pih.sagepub.com/content/220/4/521.short>. Cited 2 times on pages 46 and 48.

HERRIN, J. M.; DEMING, D. Thermal conductivity of U.S. coals. *Journal of Geophysical Research: Solid Earth*, American Geophysical Union (AGU), v. 101, n. B11, p. 25381–25386, nov 1996. ISSN 2169-9356. Cited on page 142.

HO, H. C. H.; CHEUNG, W. L.; GIBSON, L. Effects of graphite powder on the laser sintering behaviour of polycarbonate. *Rapid Prototyping Journal*, v. 8, n. 4, p. 233–242, 2002. ISSN 1355-2546. Cited 2 times on pages 45 and 47.

HOFLAND, E. C.; BARAN, I.; WISMEIJER, D. A. Correlation of Process Parameters with Mechanical Properties of Laser Sintered PA12 Parts. *Advances in Materials Science and Engineering*, v. 1, n. 1, p. 1–11, 2017. ISSN 16878442. Cited 6 times on pages 26, 44, 72, 80, 91, and 93.

HON, K.; GILL, T. Selective Laser Sintering of SiC/Polyamide Composites. *CIRP Annals - Manufacturing Technology*, v. 52, n. 1, p. 173–176, 2003. ISSN 00078506. Disponível em: <http://www.sciencedirect.com/science/article/pii/S0007850607605587>. Cited 2 times on pages 27 and 47.

HOPKINSON, N.; HAGUE, R. J.; DICKENS, P. M. *Rapid Manufacturing: An Industrial Revolution for the Digital Age*. Chichester: [s.n.], 2006. Disponível em: <http://onlinelibrary.wiley.com/book/10.1002/0470033991>. Cited on page 30.

IVANOVA, O.; WILLIAMS, C.; CAMPBELL, T. Additive manufacturing (AM) and nanotechnology: promises and challenges. *Rapid Prototyping Journal*, v. 19, n. 5, p. 353–364, 2013. ISSN 1355-2546. Disponível em: <http://www.emeraldinsight.com/doi/abs/10.1108/RPJ-12-2011-0127>. Cited on page 49.

JAIN, P. K.; PANDEY, P. M.; RAO, P. Selective laser sintering of clay-reinforced polyamide. *Polymer Composites*, v. 31, n. 4, p. 732–743, 2009. ISSN 02728397. Disponível em: <http://doi.wiley.com/10.1002/pc.20854>. Cited on page 49.

JANSSON, A.; PEJRYD, L. Characterisation of carbon fibre-reinforced polyamide manufactured by selective laser sintering. *Additive Manufacturing*, Elsevier B.V., v. 9, p. 7–13, 2016. ISSN 22148604. Disponível em: <http://dx.doi.org/10.1016/j.addma.2015.12.003>. Cited 6 times on pages 27, 48, 147, 148, 151, and 153.

JAUFFRÈS, D. et al. Sintering mechanisms involved in high-velocity compaction of nascent semicrystalline polymer powders. *Acta Materialia*, v. 57, n. 8, p. 2550–2559, 2009. ISSN 13596454. Disponível em: <www.elsevier.com/locate/actamat>. Cited 2 times on pages 79 and 151.

JING, W. et al. Surface modification of carbon fibers and the selective laser sintering of modified carbon fiber/nylon 12 composite powder. *Materials and Design*, Elsevier, v. 116, p. 253–260, feb 2017. ISSN 18734197. Disponível em: <https://www.sciencedirect.com/science/article/pii/S0264127516315544>. Cited 3 times on pages 27, 48, and 158.

KARAPATIS, N. P. et al. Thermal behavior of parts made by direct metal laser sintering. *Proceedings of the SFF Symposium*, n. Figure 1, p. 79–88, 1998. Disponível em: <http://utwired.engr.utexas.edu/lff/symposium/proceedingsArchive/pubs/Manuscripts/1998/1998-08-Karapatis.pdf>. Cited on page 35.

KIM, J.; CREASY, T. Selective laser sintering characteristics of nylon 6/clay-reinforced nanocomposite. *Polymer Testing*, v. 23, n. 6, p. 629–636, 2004. ISSN 01429418. Disponível em: <http://linkinghub.elsevier.com/retrieve/pii/S0142941804000194>. Cited on page 49.

KIMBLE, L. The materials advantage of the SLSTM selective laser sintering process. *Proceedings of the SFF Symposium*, p. 212–219, 1992. Disponível em: <http://utwired.engr.utexas.edu/lff/symposium/proceedingsArchive/pubs/Manuscripts/1992/1992-24-Kimble.pdf>. Cited 2 times on pages 25 and 35.

KOO, J. H. et al. Innovative Selective Laster Sintering Rapid Manufacturing Using Nanotechnology. In: *Proceedings of Solid Freeform Fabrication*. Austin: [s.n.], 2005. v. 11, p. 98–108. Cited on page 51.

KRUTH, J. et al. Consolidation of Polymer Powders by Selective Laser Sintering. *International Conference on Polymers and Moulds Innovations*, p. 15–30, 2008. Cited 2 times on pages 40 and 43.

KRUTH, J. et al. Lasers and materials in selective laser sintering. *Assembly Automation*, v. 23, n. 4, p. 357–371, 2003. ISSN 0144-5154. Cited 3 times on pages 25, 34, and 41.

KRUTH, J.-P. Material incress manufacturing by rapid prototyping techniques. *CIRP Annals – Manufacturing Technology*, v. 40, n. 2, p. 603–614, 1991. Cited on page 34.

KRUTH, J.-P. et al. Consolidation phenomena in laser and powder-bed based layered manufacturing. *CIRP Annals - Manufacturing Technology*, v. 56, n. 2, p. 730–759, 2007. ISSN 00078506. Disponível em: <http://linkinghub.elsevier.com/retrieve/pii/S0007850607001540>. Cited 3 times on pages 41, 72, and 150.

KRUTH, J. P. et al. Digital manufacturing of biocompatible metal frameworks for complex dental prostheses by means of SLS/SLM. *Virtual Modeling and Rapid Manufacturing: ADVANCED RESEARCH IN VIRTUAL AND RAPID PROTOTYPING*, p. 139–145, 2005. Cited on page 34.

KUMAR, S.; KRUTH, J. P. Composites by rapid prototyping technology. *Materials and Design*, v. 31, n. 2, p. 850–856, 2010. ISSN 02641275. Disponível em: <http://dx.doi.org/10.1016/j.matdes.2009.07.045>. Cited 2 times on pages 26 and 46.

LAUMER, T. et al. Optical analysis of polymer powder materials for Selective Laser Sintering. *Polymer Testing*, Elsevier, v. 56, p. 207–213, dec 2016. ISSN 01429418. Cited 3 times on pages 39, 70, and 142.

LEITE, J. L. et al. A study on morphological properties of laser sintered functionally graded blends of amorphous thermoplastics. *International Journal of Materials and Product Technology*, v. 39, n. x, p. 205, 2010. ISSN 0268-1900. Cited on page 45.

LI, R.; SHI, Y.; LIU, J. Effects of Processing Parameters on the Temperature Field of Selective Laser Melting Metal Powder. *Powder Metallurgy*, v. 48, n. 3, p. 186–195, 2009. ISSN 1068-1302. Cited on page 38.

LIU, Y. et al. Microstructure and mechanical properties of reinforced polyamide 12 composites prepared by laser additive manufacturing. *Rapid Prototyping Journal*, v. 25, n. 6, p. 1127–1134, 2019. ISSN 13552546. Disponível em: <www.emeraldinsight.com/1355-2546.htm>. Cited 3 times on pages 27, 48, and 151.

MAJEWSKI, C. E.; ZARRINGHALAM, H.; HOPKINSON, N. Effect of the degree of particle melt on mechanical properties in selective laser-sintered Nylon-12 parts. *Proceedings of the Institution of Mechanical Engineers, Part B: Journal of Engineering Manufacture*, v. 222, n. 9, p. 1055–1064, sep 2008. ISSN 0954-4054. Disponível em: <http://sffsymposium.engr.utexas.edu/Manuscripts/2008/2008-05-Majewski.pdfhttp://journals.sagepub.com/doi/10.1243/09544054JEM1122>. Cited 4 times on pages 26, 44, 79, and 85.

MAZZOLI, A.; MORICONI, G.; PAURI, M. G. Characterization of an aluminum-filled polyamide powder for applications in selective laser sintering. *Materials & Design*, v. 28, n. 3, p. 993–1000, 2007. ISSN 02613069. Disponível em: <http://linkinghub.elsevier.com/retrieve/pii/S0261306905003444>. Cited 2 times on pages 27 and 47.

NEGI, S.; DHIMAN, S.; SHARMA, R. K. Determining the effect of sintering conditions on mechanical properties of laser sintered glass filled polyamide parts using RSM. *Measurement: Journal of the International Measurement Confederation*, Elsevier, v. 68, p. 205–218, may 2015. ISSN 02632241. Disponível em: <https://www.sciencedirect.com/science/article/pii/S0263224115001219>. Cited on page 27.

NELSON, J. C. et al. Model of the selective laser sintering of bisphenol-A polycarbonate. *Industrial & Engineering Chemistry Research*, American Chemical Society, v. 32, n. 10, p. 2305–2317, oct 1993. ISSN 0888-5885. Disponível em: <http://dx.doi.org/10.1021/ie00022a014>. Cited on page 45.

PARANDOUSH, P.; LIN, D. A review on additive manufacturing of polymer-fiber composites. *Composite Structures*, Elsevier, v. 182, p. 36–53, dec 2017. ISSN 0263-8223. Disponível em: <https://www.sciencedirect.com/science/article/pii/S0263822316329063>. Cited on page 27.

POHL, H. et al. Thermal stresses in direct metal laser sintering. *Proceedings of the Solid Freeform ...*, p. 366–372, 2001. Disponível em: <http://edge.rit.edu/edge/P10551/public/SFF/SFF2001Proceedings/2001SFFPapers/41-Pohl.pdf>. Cited on page 37.

QI, F.; CHEN, N.; WANG, Q. Preparation of PA11/BaTiO3 nanocomposite powders with improved processability, dielectric and piezoelectric properties for use in selective laser sintering. *Materials & Design*, Elsevier, v. 131, p. 135–143, oct 2017. ISSN 0264-1275. Disponível em: <https://www.sciencedirect.com/science/article/pii/S0264127517305956>. Cited on page 150.

RADSTOK, E. Rapid tooling. *Rapid Prototyping Journal*, v. 5, n. 4, p. 164–169, 1999. ISSN 1355-2546. Cited on page 35.

RASMUSSEN, C. E. *Web page*. 2020. Disponível em: <http://www.gaussianprocess.org/gpml/code/matlab/doc/>. Cited on page 63.

RASMUSSEN, C. E.; WILLIAMS, C. K. I. *Rasmussen and Williams - Gaussian Processes for Machine Learning*. [s.n.], 2006. ISSN 0129-0657. ISBN 026218253X. Disponível em: <www.GaussianProcess.org/gpml>. Cited 2 times on pages 62 and 63.

RHEE, S.; WHITE, J. L. Crystal structure and morphology of biaxially oriented polyamide 12 films. *Journal of Polymer Science, Part B: Polymer Physics*, v. 40, n. 12, p. 1189–1200, 2002. ISSN 08876266. Cited 4 times on pages 15, 89, 91, and 157.

RIBEIRO, N. et al. Azo dye adsorption on anthracite : A view of thermodynamics , kinetics and cosmotropic effects Separation and Purification Technology Azo dye adsorption on anthracite : A view of thermodynamics , kinetics and cosmotropic effects. *Separation and Purification Technology*, Elsevier, v. 209, n. September, p. 806–814, 2018. ISSN 1383-5866. Disponível em: <https://doi.org/10.1016/j.seppur.2018.09.027>. Cited 2 times on pages 142 and 156.

RIETZEL, D.; WENDEL, B.; FEULNER, R. W. No Title. *Kunststoffe International*, p. 42–45, 2008. Cited on page 45.

SAVALANI, M. *Selective laser sintering of hydroxyapatite-polyamide composites*. Tese (Doutorado) — Loughborough University, 2006. Disponível em: <https://dspace.lboro.ac.uk/dspace-jspui/handle/2134/7907>. Cited on page 48.

SCHMID, M.; AMADO, A.; WEGENER, K. Materials perspective of polymers for additive manufacturing with selective laser sintering. *Journal of Materials Research*, v. 29, n. 17, p. 1824–1832, 2014. ISSN 0884-2914. Disponível em: <http://www.journals.cambridge.org/abstract{_}S0884291414001>. Cited 2 times on pages 42 and 43.

SCHMID, M. et al. Influence of the Origin of Polyamide 12 Powder on the Laser Sintering Process and Laser Sintered Parts. *Applied Sciences*, v. 7, n. 5, p. 462, 2017. Cited 2 times on pages 26 and 44.

SCHMID, M.; WEGENER, K. Additive Manufacturing: Polymers applicable for laser sintering (LS). *Procedia Engineering*, v. 149, n. 6, p. 457–464, 2016. ISSN 18777058. Disponível em: <http://dx.doi.org/10.1016/j.proeng.2016.06.692>. Cited on page 71.

SCHUEREN, B. V. D.; KRUTH, J. Powder deposition in selective metal powder sintering. *Rapid Prototyping Journal*, v. 1, n. 3, p. 23–31, 1995. ISSN 1355-2546. Cited on page 34.

SHUAI, C. et al. Fabrication of porous polyvinyl alcohol scaffold for bone tissue engineering via selective laser sintering. *Biofabrication*, v. 5, n. 1, p. 015014, 2013. ISSN 1758-5090. Disponível em: <http://www.ncbi.nlm.nih.gov/pubmed/23385303>. Cited on page 46.

SIMCHI, a.; PETZOLDT, F.; POHL, H. On the development of direct metal laser sintering for rapid tooling. *Journal of Materials Processing Technology*, v. 141, n. 3, p. 319–328, 2003. ISSN 09240136. Cited on page 37.

SIMPSON, R. L. et al. Development of a 95/5 poly(L-lactide-co-glycolide)/hydroxylapatite and beta-tricalcium phosphate scaffold as bone replacement material via selective laser sintering. *Journal of biomedical materials research. Part B, Applied biomaterials*, v. 84, n. 1, p. 17–25, jan 2008. ISSN 1552-4973. Disponível em: <http://www.ncbi.nlm.nih.gov/pubmed/17465027>. Cited 2 times on pages 46 and 48.

STICHEL, T. et al. A Round Robin study for Selective Laser Sintering of polyamide 12: Microstructural origin of the mechanical properties. *Optics and Laser Technology*, Elsevier, v. 89, n. October 2016, p. 31–40, mar 2017. ISSN 00303992. Cited 2 times on pages 26 and 43.

STICHEL, T. et al. A Round Robin study for selective laser sintering of polymers: Back tracing of the pore morphology to the process parameters. *Journal of Materials Processing Technology*, Elsevier, v. 252, p. 537–545, feb 2018. ISSN 09240136. Cited 4 times on pages 26, 43, 80, and 82.

STORN, R. M.; KENNETH, P. Differential Evolution - A simple and efficient adaptive scheme for global optimization over continuous spaces. *Journal of Global Optimization*, v. 11, n. 1, p. 341–359, 1997. Cited on page 64.

TAN, K. et al. Scaffold development using selective laser sintering of polyetheretherketone–hydroxyapatite biocomposite blends. *Biomaterials*, v. 24, n. 18, p. 3115–3123, 2003. ISSN 01429612. Disponível em: <http://linkinghub.elsevier.com/retrieve/pii/S0142961203001315>. Cited on page 48.

TAN, K. H. et al. Selective laser sintering of biocompatible polymers for applications in tissue engineering. *Bio-medical materials and engineering*, v. 15, n. 1-2, p. 113–124, 2005. ISSN 0959-2989. Cited on page 46.

TONTOWI, A. E.; CHILDS, T. H. C. Density prediction of crystalline polymer sintered parts at various powder bed temperatures. *Rapid Prototyping Journal*, MCB UP Ltd, v. 7, n. 3, p. 180–184, aug 2001. ISSN 13552546. Disponível em: <https://www.emeraldinsight.com/doi/pdfplus/10.1108/13552540110395637http://www.emeraldinsight.com/doi/10.1108/13552540110395637>. Cited on page 72.

TOWNSEND, A. et al. Surface texture metrology for metal additive manufacturing: a review. *Precision Engineering*, v. 46, p. 34–47, 2016. ISSN 01416359. Cited on page 74.

TSOTRIDIS, G.; ROTHER, H.; HONDROS, E. D. Marangoni flow and the shapes of laser-melted pools. *Naturwissenschaften*, Springer-Verlag, v. 76, n. 5, p. 216–218, may 1989. ISSN 00281042. Cited on page 41.

USHER, J. S.; GORNET, T. J.; STARR, T. L. Weibull growth modeling of laser-sintered nylon 12. *Rapid Prototyping Journal*, v. 19, n. 4, p. 300–306, oct 2013. ISSN 13552546. Disponível em: <https://www.emeraldinsight.com/doi/10.1108/13552541311323308http://www.emeraldinsight.com/doi/10.1108/13552541111184143>. Cited 2 times on pages 26 and 44.

Van Hooreweder, B. et al. On the difference in material structure and fatigue properties of nylon specimens produced by injection molding and selective laser sintering. *Polymer Testing*, Elsevier, v. 32, n. 5, p. 972–981, aug 2013. ISSN 01429418. Disponível em: <https://www.sciencedirect.com/science/article/pii/S0142941813001001>. Cited 2 times on pages 79 and 88.

VERBELEN, L. et al. Characterization of polyamide powders for determination of laser sintering processability. *European Polymer Journal*, Elsevier Ltd, v. 75, p. 163–174, feb 2016. ISSN 00143057. Disponível em: <http://dx.doi.org/10.1016/j.eurpolymj.2015.12.014https://www.sciencedirect.com/science/article/pii/S0014305715300938>. Cited 2 times on pages 26 and 44.

WAHAB, M. et al. Development of Polymer Nanocomposites for Rapid Prototyping Process. II, p. 1–6, 2010. Disponível em: <http://www.nanoarchive.org/7904/>. Cited on page 50.

WANG, X. et al. 3D printing of polymer matrix composites : A review and prospective. *Composites Part B*, Elsevier Ltd, v. 110, p. 442–458, 2017. ISSN 1359-8368. Disponível em: <http://dx.doi.org/10.1016/j.compositesb.2016.11.034>. Cited on page 27.

WANG, X. C. et al. Direct selective laser sintering of hard metal powders: Experimental study and simulation. *International Journal of Advanced Manufacturing Technology*, v. 19, n. 5, p. 351–357, 2002. ISSN 02683768. Cited on page 38.

WANG, Y.; SHI, Y.; HUANG, S. Selective laser sintering of polyamide-rectorite composite. *Proceedings of the Institution of Mechanical Engineers, Part L: Journal of Materials: Design and Applications*, v. 219, n. 1, p. 11–15, 2005. ISSN 1464-4207. Disponível em: <http://pil.sagepub.com/lookup/doi/10.1243/146442005X10229>. Cited on page 49.

WEGNER, A.; WITT, G. Correlation of Process Parameters and Part Properties in Laser Sintering using Response Surface Modeling. In: *Physics Procedia*. Elsevier, 2012. v. 39, p. 480–490. ISBN 1875-3892. ISSN 18753892. Disponível em: <https://www.sciencedirect.com/science/article/pii/S1875389212025916>. Cited 7 times on pages 26, 44, 72, 80, 82, 91, and 93.

WILLIAMS, J. D.; DECKARD, C. R. Advances in modeling the effects of selected parameters on the SLS process. *Rapid Prototyping Journal*, v. 4, n. 2, p. 90–100, 1998. ISSN 1355-2546. Cited 2 times on pages 36 and 37.

WIRIA, F. et al. Poly-ϵ-caprolactone/hydroxyapatite for tissue engineering scaffold fabrication via selective laser sintering. *Acta Biomaterialia*, v. 3, n. 1, p. 1–12, 2007. ISSN 17427061. Disponível em: <http://linkinghub.elsevier.com/retrieve/pii/S1742706106001012>. Cited on page 48.

WOHLERS, T. *Wohlers Report: Rapid Prototyping, Tooling & Manufacturing State of the Industry*. USA, 2004. Disponível em: <http://wohlersassociates.com/2004-3dp.htm>. Cited on page 29.

WOHLERS, T. *Wohlers Report: Rapid Prototyping, Tooling & Manufacturing State of the Industry*. USA, 2007. Disponível em: <http://wohlersassociates.com/2007info.htm>. Cited on page 29.

YAN, C. et al. Preparation, characterisation and processing of carbon fibre/polyamide-12 composites for selective laser sintering. *Composites Science and Technology*, Elsevier Ltd, v. 71, n. 16, p. 1834–1841, 2011. ISSN 02663538. Disponível em: <http://dx.doi.org/10.1016/j.compscitech.2011.08.013>. Cited 2 times on pages 27 and 48.

YANG, J.; SHI, Y.; YAN, C. Selective laser sintering of polyamide 12/potassium titanium whisker composites. *Journal of Applied Polymer Science*, v. 117, n. 4, p. 2196–2204, aug 2010. ISSN 00218995. Disponível em: <http://doi.wiley.com/10.1002/app.31965>. Cited on page 51.

YEONG, W. et al. Porous polycaprolactone scaffold for cardiac tissue engineering fabricated by selective laser sintering. *Acta Biomaterialia*, Acta Materialia Inc., v. 6, n. 6, p. 2028–2034, 2010. ISSN 17427061. Disponível em: <http://linkinghub.elsevier.com/retrieve/pii/S1742706109005741>. Cited on page 46.

ZARRINGHALAM, H. et al. Effects of processing on microstructure and properties of SLS Nylon 12. *Materials Science and Engineering A*, v. 435-436, p. 172–180, 2006. ISSN 09215093. Cited 2 times on pages 26 and 44.

ZHANG, J.; ADAMS, A. Understanding thermal aging of non-stabilized and stabilized polyamide 12 using 1H solid-state NMR. *Polymer Degradation and Stability*, Elsevier, v. 134, n. 1, p. 169–178, dec 2016. ISSN 01413910. Disponível em: <https://www.sciencedirect.com/science/article/pii/S0141391016303226>. Cited 2 times on pages 89 and 157.

ZHANG, Y. et al. Characterization and dynamic mechanical analysis of selective laser sintered hydroxyapatite-filled polymeric composites. *Journal of biomedical materials research. Part A*, v. 86, n. 3, p. 607–16, sep 2008. ISSN 1552-4965. Disponível em: <http://www.ncbi.nlm.nih.gov/pubmed/18022838>. Cited on page 48.

ZHENG, H. et al. Effect of core–shell composite particles on the sintering behavior and properties of nano-Al2O3/polystyrene composite prepared by SLS. *Materials Letters*, v. 60, n. 9-10, p. 1219–1223, 2006. ISSN 0167577X. Disponível em: <http://linkinghub.elsevier.com/retrieve/pii/S0167577X05010992>. Cited on page 52.

ZHOU, W. Y. et al. Selective laser sintering of porous tissue engineering scaffolds from poly(L-lactide)/carbonated hydroxyapatite nanocomposite microspheres. *Journal of Materials Science: Materials in Medicine*, v. 19, p. 2535–2540, 2008. ISSN 09574530. Cited 2 times on pages 46 and 48.